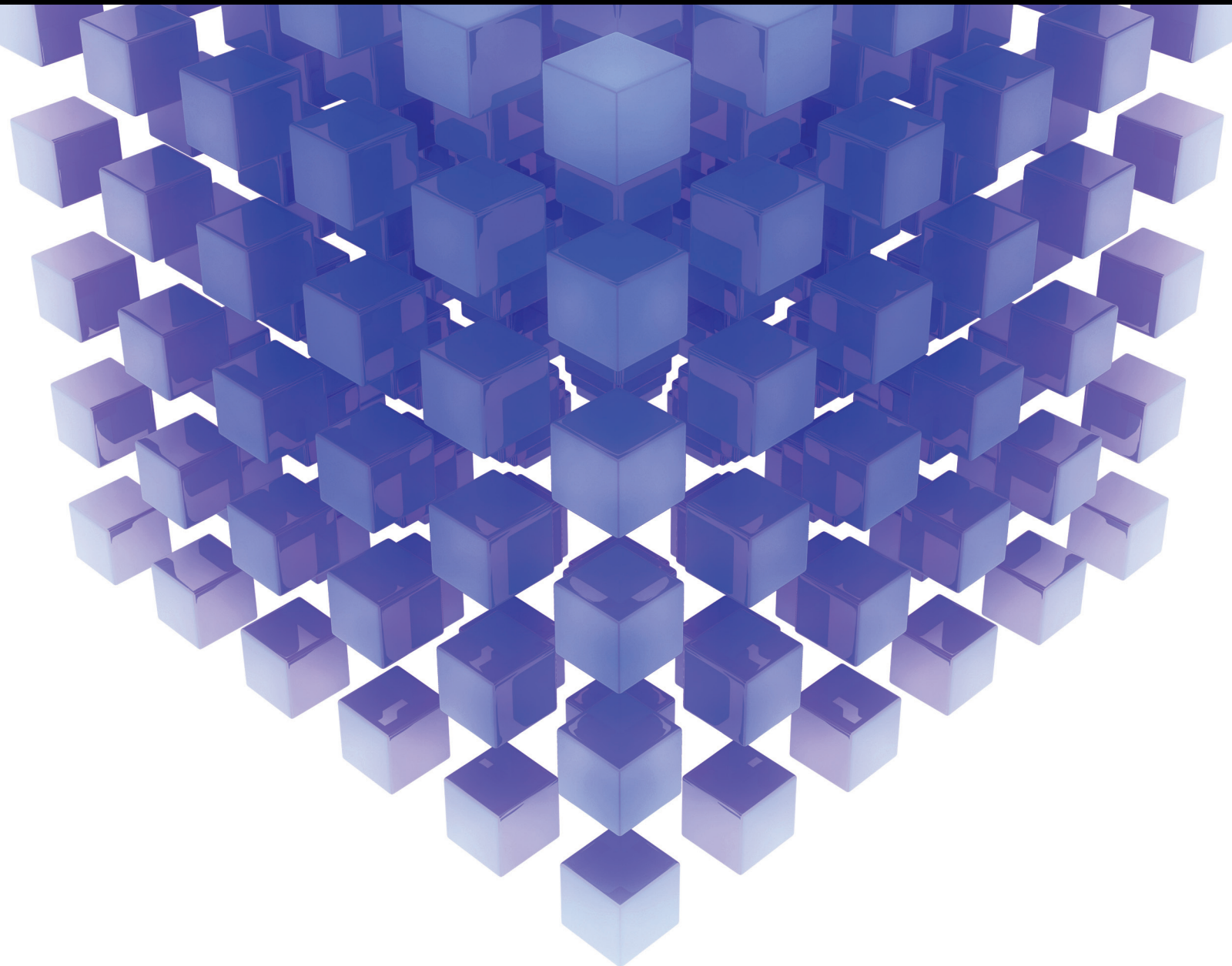


Mathematical Problems in Engineering

# Diagnostic Evaluation and Uncertainty Quantification of Earth and Environmental Systems Models

Lead Guest Editor: Shuo Wang

Guest Editors: Gordon Huang, Xander Wang, and Zoe Li





---

**Diagnostic Evaluation and Uncertainty  
Quantification of Earth and Environmental  
Systems Models**

Mathematical Problems in Engineering

---

**Diagnostic Evaluation and Uncertainty  
Quantification of Earth and Environmental  
Systems Models**

Lead Guest Editor: Shuo Wang

Guest Editors: Xander Wang and Zoe Li



---

Copyright © 2018 Hindawi. All rights reserved.

This is a special issue published in “Mathematical Problems in Engineering.” All articles are open access articles distributed under the Creative Commons Attribution License, which permits unrestricted use, distribution, and reproduction in any medium, provided the original work is properly cited.

## Editorial Board

- Mohamed Abd El Aziz, Egypt  
AITOUCHE Abdelouhab, France  
Leonardo Acho, Spain  
José A. Acosta, Spain  
Daniela Addressi, Italy  
Paolo Adesso, Italy  
Claudia Adduce, Italy  
Ramesh Agarwal, USA  
Francesco Aggoggeri, Italy  
J. C. Agüero, Australia  
Ricardo Aguilar-López, Mexico  
Tarek Ahmed-Ali, France  
Elias Aifantis, USA  
Muhammad N. Akram, Norway  
Guido Ala, Italy  
Andrea Alaimo, Italy  
Reza Alam, USA  
Nicholas Alexander, UK  
Salvatore Alfonzetti, Italy  
Mohammad D. Aliyu, Canada  
Juan A. Almendral, Spain  
José Domingo Álvarez, Spain  
Cláudio Alves, Portugal  
Juan P. Amezcua-Sanchez, Mexico  
Lionel Amodeo, France  
Sebastian Anita, Romania  
Renata Archetti, Italy  
Felice Arena, Italy  
Sabri Arik, Turkey  
Francesco Aristodemo, Italy  
Fausto Arpino, Italy  
Alessandro Arsie, USA  
Edoardo Artioli, Italy  
Fumihiko Ashida, Japan  
Farhad Aslani, Australia  
Mohsen Asle Zaem, USA  
Romain Aubry, USA  
Matteo Aureli, USA  
Richard I. Avery, USA  
Viktor Avrutin, Germany  
Francesco Aymerich, Italy  
T. P. Azevedo Perdicoulis, Portugal  
Sajad Azizi, Belgium  
Michele Baccocchi, Italy
- Seungik Baek, USA  
Adil Bagirov, Australia  
Khaled Bahlali, France  
Laurent Bako, France  
Pedro Balaguer, Spain  
Stefan Balint, Romania  
Ines Tejado Balsera, Spain  
Alfonso Banos, Spain  
Jerzy Baranowski, Poland  
Roberto Baratti, Italy  
Andrzej Bartoszewicz, Poland  
David Bassir, France  
Chiara Bedon, Italy  
Azeddine Beghdadi, France  
Denis Benasciutti, Italy  
Ivano Benedetti, Italy  
Rosa M. Benito, Spain  
Elena Benvenuti, Italy  
Giovanni Berselli, Italy  
Giorgio Besagni, Italy  
Michele Betti, Italy  
Jean-Charles Beugnot, France  
Pietro Bia, Italy  
Carlo Bianca, France  
Simone Bianco, Italy  
Vincenzo Bianco, Italy  
Vittorio Bianco, Italy  
Gennaro N. Bifulco, Italy  
David Bigaud, France  
Antonio Bilotta, Italy  
Paul Bogdan, USA  
Guido Bolognesi, UK  
Rodolfo Bontempo, Italy  
Alberto Borboni, Italy  
Paolo Boscariol, Italy  
Daniela Boso, Italy  
Guillermo Botella-Juan, Spain  
Boulaïd Boulkroune, Belgium  
Fabio Bovenga, Italy  
Francesco Braghin, Italy  
Ricardo Branco, Portugal  
Maurizio Brocchini, Italy  
Julien Bruchon, France  
Matteo Bruggi, Italy
- Michele Brun, Italy  
Vasilis Burganos, Greece  
Tito Busani, USA  
Raquel Caballero-Águila, Spain  
Filippo Cacace, Italy  
Pierfrancesco Cacciola, UK  
Salvatore Caddemi, Italy  
Roberto Caldelli, Italy  
Alberto Campagnolo, Italy  
Eric Campos-Canton, Mexico  
Marko Canadija, Croatia  
Salvatore Cannella, Italy  
Francesco Cannizzaro, Italy  
Javier Cara, Spain  
Ana Carpio, Spain  
Caterina Casavola, Italy  
Sara Casciati, Italy  
Federica Caselli, Italy  
Carmen Castillo, Spain  
Inmaculada T. Castro, Spain  
Miguel Castro, Portugal  
Giuseppe Catalanotti, UK  
Nicola Caterino, Italy  
Alberto Cavallo, Italy  
Gabriele Cazzulani, Italy  
Luis Cea, Spain  
Song Cen, China  
Miguel Cerrolaza, Venezuela  
M. Chadli, France  
Gregory Chagnon, France  
Ludovic Chamoin, France  
Ching-Ter Chang, Taiwan  
Qing Chang, USA  
Michael J. Chappell, UK  
Kacem Chehdi, France  
Peter N. Cheimets, USA  
Xinkai Chen, Japan  
Luca Chiapponi, Italy  
Francisco Chicano, Spain  
Nicholas Chileshe, Australia  
Adrian Chmielewski, Poland  
Ioannis T. Christou, Greece  
Hung-Yuan Chung, Taiwan  
Simone Cinquemani, Italy

Roberto G. Citarella, Italy  
Joaquim Ciurana, Spain  
John D. Clayton, USA  
Francesco Clementi, Italy  
Piero Colajanni, Italy  
Giuseppina Colicchio, Italy  
Vassilios Constantoudis, Greece  
Enrico Conte, Italy  
Francesco Conte, Italy  
Alessandro Contento, USA  
Mario Cools, Belgium  
José A. Correia, Portugal  
Jean-Pierre Corriou, France  
J.-C. Cortés, Spain  
Carlo Cosentino, Italy  
Paolo Crippa, Italy  
Andrea Crivellini, Italy  
Frederico R. B. Cruz, Brazil  
Erik Cuevas, Mexico  
Maria C. Cunha, Portugal  
Peter Dabnichki, Australia  
Luca D'Acierno, Italy  
Weizhong Dai, USA  
Andrea Dall'Asta, Italy  
Purushothaman Damodaran, USA  
Bhabani S. Dandapat, India  
Farhang Daneshmand, Canada  
Giuseppe D'Aniello, Italy  
Sergey Dashkovskiy, Germany  
Fabio De Angelis, Italy  
Samuele De Bartolo, Italy  
Abílio De Jesus, Portugal  
Pietro De Lellis, Italy  
Alessandro De Luca, Italy  
Stefano de Miranda, Italy  
Filippo de Monte, Italy  
Maria do Rosário de Pinho, Portugal  
Michael Defoort, France  
Alessandro Della Corte, Italy  
Xavier Delorme, France  
Laurent Dewasme, Belgium  
Angelo Di Egidio, Italy  
Roberta Di Pace, Italy  
Ramón I. Diego, Spain  
Yannis Dimakopoulos, Greece  
Zhengtao Ding, UK  
M. Djemai, France  
Alexandre B. Dolgui, France  
Georgios Dounias, Greece  
Florent Duchaine, France  
George S. Dulikravich, USA  
Bogdan Dumitrescu, Romania  
Horst Ecker, Austria  
Saeed Eftekhari Azam, USA  
Ahmed El Hajjaji, France  
Antonio Elipe, Spain  
Fouad Erchiqui, Canada  
Anders Eriksson, Sweden  
R. Emre Erkmen, Australia  
G. Espinosa-Paredes, Mexico  
Leandro F. F. Miguel, Brazil  
Andrea L. Facci, Italy  
Giacomo Falcucci, Italy  
Giovanni Falsone, Italy  
Hua Fan, China  
Nicholas Fantuzzi, Italy  
Yann Favennec, France  
Fiorenzo A. Fazzolari, UK  
Giuseppe Fedele, Italy  
Roberto Fedele, Italy  
Arturo J. Fernández, Spain  
Jesus M. Fernandez Oro, Spain  
Massimiliano Ferraioli, Italy  
Massimiliano Ferrara, Italy  
Francesco Ferrise, Italy  
Eric Feulvarch, France  
Barak Fishbain, Israel  
S. Douwe Flapper, Netherlands  
Thierry Floquet, France  
Eric Florentin, France  
Alessandro Formisano, Italy  
Francesco Franco, Italy  
Elisa Francomano, Italy  
Tomonari Furukawa, USA  
Juan C. G. Prada, Spain  
Mohamed Gadala, Canada  
Matteo Gaeta, Italy  
Mauro Gaggero, Italy  
Zoran Gajic, USA  
Erez Gal, Israel  
Jaime Gallardo-Alvarado, Mexico  
Ugo Galvanetto, Italy  
Akemi Gálvez, Spain  
Rita Gamberini, Italy  
Maria L. Gandarias, Spain  
Arman Ganji, Canada  
Zhiwei Gao, UK  
Zhong-Ke Gao, China  
Giovanni Garcea, Italy  
Luis Rodolfo Garcia Carrillo, USA  
Jose M. Garcia-Aznar, Spain  
Akhil Garg, China  
Alessandro Gasparetto, Italy  
Oleg V. Gendelman, Israel  
Stylianos Georgantzinou, Greece  
Fotios Georgiades, UK  
Mergen H. Ghayesh, Australia  
Georgios I. Giannopoulos, Greece  
Agathoklis Giaralis, UK  
Pablo Gil, Spain  
Anna M. Gil-Lafuente, Spain  
Ivan Giorgio, Italy  
Gaetano Giunta, Luxembourg  
Alessio Gizzi, Italy  
Jefferson L.M.A. Gomes, UK  
Emilio Gómez-Déniz, Spain  
Antonio M. Gonçalves de Lima, Brazil  
David González, Spain  
Chris Goodrich, USA  
Rama S. R. Gorla, USA  
Kannan Govindan, Denmark  
Antoine Grall, France  
George A. Gravvanis, Greece  
Fabrizio Greco, Italy  
David Greiner, Spain  
Simonetta Grilli, Italy  
Jason Gu, Canada  
Federico Guarracino, Italy  
Michele Guida, Italy  
Zhaoxia Guo, China  
José L. Guzmán, Spain  
Quang Phuc Ha, Australia  
Petr Hájek, Czech Republic  
Weimin Han, USA  
Zhen-Lai Han, China  
Thomas Hanne, Switzerland  
Mohammad A. Hariri-Ardebili, USA  
Xiao-Qiao He, China  
Luca Heltai, Italy  
Nicolae Herisanu, Romania  
Alfredo G. Hernández-Díaz, Spain

M.I. Herreros, Spain  
Eckhard Hitzer, Japan  
Paul Honeine, France  
Jaromir Horacek, Czech Republic  
Muneo Hori, Japan  
András Horváth, Italy  
S. H. Hosseinnia, Netherlands  
Mengqi Hu, USA  
Gordon Huang, Canada  
Sajid Hussain, Canada  
Asier Ibeas, Spain  
Orest V. Iftime, Netherlands  
Przemyslaw Ignaciuk, Poland  
Giacomo Innocenti, Italy  
Emilio Insfran Pelozo, Spain  
Alessio Ishizaka, UK  
Nazrul Islam, USA  
Benoit lung, France  
Benjamin Ivorra, Spain  
Payman Jalali, Finland  
Mahdi Jalili, Australia  
Łukasz Jankowski, Poland  
Samuel N. Jator, USA  
Juan C. Jauregui-Correa, Mexico  
Reza Jazar, Australia  
Khalide Jbilou, France  
Piotr Jędrzejowicz, Poland  
Isabel S. Jesus, Portugal  
Linni Jian, China  
Bin Jiang, China  
Zhongping Jiang, USA  
Emilio Jiménez Macías, Spain  
Ningde Jin, China  
Xiaoliang Jin, USA  
Liang Jing, Canada  
Dylan F. Jones, UK  
Palle E. Jorgensen, USA  
Vyacheslav Kalashnikov, Mexico  
Tamas Kalmár-Nagy, Hungary  
Tomasz Kapitaniak, Poland  
Julius Kaplunov, UK  
Haranath Kar, India  
Konstantinos Karamanos, Belgium  
Krzysztof Kecik, Poland  
Jean-Pierre Kenne, Canada  
Chaudry M. Khalique, South Africa  
Do Wan Kim, Republic of Korea  
Nam-Il Kim, Republic of Korea  
Jan Koci, Czech Republic  
Ioannis Kostavelis, Greece  
Sotiris B. Kotsiantis, Greece  
Manfred Krafczyk, Germany  
Frederic Kratz, France  
Petr Krysl, USA  
Krzysztof S. Kulpa, Poland  
Shailesh I. Kundalwal, India  
Jurgen Kurths, Germany  
Cedrick A. K. Kwimiy, USA  
Kyandoghere Kyamakya, Austria  
Davide La Torre, Italy  
Risto Lahdelma, Finland  
Hak-Keung Lam, UK  
Giovanni Lancioni, Italy  
Jimmy Lauber, France  
Antonino Laudani, Italy  
Hervé Laurent, France  
Aimé Lay-Ekuakille, Italy  
Nicolas J. Leconte, France  
Dimitri Lefebvre, France  
Eric Lefevre, France  
Marek Lefik, Poland  
Yaguo Lei, China  
Kauko Leiviskä, Finland  
Thibault Lemaire, France  
Roman Lewandowski, Poland  
Chen-Feng Li, China  
Jian Li, USA  
En-Qiang Lin, USA  
Zhiyun Lin, China  
Peide Liu, China  
Peter Liu, Taiwan  
Wanquan Liu, Australia  
Bonifacio Llamazares, Spain  
Alessandro Lo Schiavo, Italy  
Jean Jacques Loiseau, France  
Francesco Lolli, Italy  
Paolo Lonetti, Italy  
Sandro Longo, Italy  
António M. Lopes, Portugal  
Sebastian López, Spain  
Pablo Lopez-Crespo, Spain  
Luis M. López-Ochoa, Spain  
Ezequiel López-Rubio, Spain  
Vassilios C. Loukopoulos, Greece  
Jose A. Lozano-Galant, Spain  
Helen Lu, Australia  
Gabriel Luque, Spain  
Valentin Lychagin, Norway  
Antonio Madeo, Italy  
José María Maestre, Spain  
Alessandro Magnani, Italy  
Fazal M. Mahomed, South Africa  
Noureddine Manamanni, France  
Paolo Manfredi, Italy  
Didier Maquin, France  
Giuseppe Carlo Marano, Italy  
Damijan Markovic, France  
Francesco Marotti de Sciarra, Italy  
Rui Cunha Marques, Portugal  
Luis Martínez, Spain  
Rodrigo Martínez-Bejar, Spain  
Guiomar Martín-Herrán, Spain  
Denizar Cruz Martins, Brazil  
Benoit Marx, France  
Elio Masciari, Italy  
Franck Massa, France  
Paolo Massioni, France  
Alessandro Mauro, Italy  
Fabio Mazza, Italy  
Laura Mazzola, Italy  
Driss Mehdi, France  
Roderick Melnik, Canada  
Pasquale Memmolo, Italy  
Xiangyu Meng, USA  
Jose Merodio, Spain  
Alessio Merola, Italy  
Mahmoud Mesbah, Iran  
Luciano Mescia, Italy  
Laurent Mevel, France  
Mariusz Michta, Poland  
Aki Mikkola, Finland  
Giovanni Minafò, Italy  
Hiroyuki Mino, Japan  
Pablo Mira, Spain  
D. Mitsotakis, New Zealand  
Vito Mocella, Italy  
Sara Montagna, Italy  
Roberto Montanini, Italy  
Francisco J. Montáns, Spain  
Luiz H. A. Monteiro, Brazil  
Gisele Mophou, France

Rafael Morales, Spain  
Marco Morandini, Italy  
Javier Moreno-Valenzuela, Mexico  
Simone Morganti, Italy  
Caroline Mota, Brazil  
Aziz Moukrim, France  
Dimitris Mourtzis, Greece  
Emiliano Mucchi, Italy  
Josefa Mula, Spain  
Jose J. Muñoz, Spain  
Giuseppe Muscolino, Italy  
Marco Mussetta, Italy  
Hakim Naceur, France  
Alessandro Naddeo, Italy  
Hassane Naji, France  
Mariko Nakano-Miyatake, Mexico  
Keivan Navaie, UK  
AMA Neves, Portugal  
Luís C. Neves, UK  
Dong Ngoduy, New Zealand  
Nhon Nguyen-Thanh, Singapore  
Tatsushi Nishi, Japan  
Xesús Nogueira, Spain  
Ben T. Nohara, Japan  
Mohammed Nouari, France  
Mustapha Nourelfath, Canada  
Włodzimierz Ogryczak, Poland  
Roger Ohayon, France  
Krzysztof Okarma, Poland  
Mitsuhiro Okayasu, Japan  
Alberto Olivares, Spain  
Enrique Onieva, Spain  
Calogero Orlando, Italy  
Alejandro Ortega-Moñux, Spain  
Sergio Ortobelli, Italy  
Naohisa Otsuka, Japan  
Erika Ottaviano, Italy  
Pawel Packo, Poland  
Arturo Pagano, Italy  
Alkis S. Paipetis, Greece  
Roberto Palma, Spain  
Alessandro Palmeri, UK  
Pasquale Palumbo, Italy  
Jürgen Pannek, Germany  
Elena Panteley, France  
Achille Paolone, Italy  
George A. Papakostas, Greece  
Xosé M. Pardo, Spain  
Vicente Parra-Vega, Mexico  
Manuel Pastor, Spain  
Petr Páta, Czech Republic  
Pubudu N. Pathirana, Australia  
Surajit Kumar Paul, India  
Sitek Paweł, Poland  
Luis Payá, Spain  
Alexander Paz, USA  
Igor Pažanin, Croatia  
Libor Pekař, Czech Republic  
Francesco Pellicano, Italy  
Marcello Pellicciari, Italy  
Haipeng Peng, China  
Mingshu Peng, China  
Zhengbiao Peng, Australia  
Zhi-ke Peng, China  
Marzio Pennisi, Italy  
Maria Patrizia Pera, Italy  
Matjaz Perc, Slovenia  
A. M. Bastos Pereira, Portugal  
Ricardo Perera, Spain  
Francesco Pesavento, Italy  
Ivo Petras, Slovakia  
Francesco Petrini, Italy  
Lukasz Pieczonka, Poland  
Dario Piga, Switzerland  
Paulo M. Pimenta, Brazil  
Antonina Pirrotta, Italy  
Marco Pizzarelli, Italy  
Vicent Pla, Spain  
Javier Plaza, Spain  
Kemal Polat, Turkey  
Dragan Poljak, Croatia  
Jorge Pomares, Spain  
Sébastien Poncet, Canada  
Volodymyr Ponomaryov, Mexico  
Jean-Christophe Ponsart, France  
Mauro Pontani, Italy  
Cornelio Posadas-Castillo, Mexico  
Francesc Pozo, Spain  
Christopher Pretty, New Zealand  
Luca Pugi, Italy  
Krzysztof Puszynski, Poland  
Giuseppe Quaranta, Italy  
Vitomir Racic, Italy  
Jose Ragot, France  
Carlo Rainieri, Italy  
K. Ramamani Rajagopal, USA  
Ali Ramazani, USA  
Higinio Ramos, Spain  
Alain Rassinoux, France  
S.S. Ravindran, USA  
Alessandro Reali, Italy  
Jose A. Reinoso, Spain  
Oscar Reinoso, Spain  
Fabrizio Renno, Italy  
Nidhal Rezg, France  
Ricardo Riaza, Spain  
Francesco Riganti-Fulginei, Italy  
Gerasimos Rigatos, Greece  
Francesco Ripamonti, Italy  
Jorge Rivera, Mexico  
Eugenio Roanes-Lozano, Spain  
Bruno G. M. Robert, France  
Ana Maria A. C. Rocha, Portugal  
José Rodellar, Spain  
Luigi Rodino, Italy  
Rosana Rodríguez López, Spain  
Ignacio Rojas, Spain  
Alessandra Romolo, Italy  
Debasish Roy, India  
Gianluigi Rozza, Italy  
Jose de Jesus Rubio, Mexico  
Rubén Ruiz, Spain  
Antonio Ruiz-Cortes, Spain  
Ivan D. Rukhlenko, Australia  
Mazen Saad, France  
Kishin Sadarangani, Spain  
Andrés Sáez, Spain  
Mehrddad Saif, Canada  
John S. Sakellariou, Greece  
Salvatore Salamone, USA  
Vicente Salas, Spain  
Jose Vicente Salcedo, Spain  
Nunzio Salerno, Italy  
Miguel A. Salido, Spain  
Roque J. Saltarén, Spain  
Alessandro Salvini, Italy  
Sylwester Samborski, Poland  
Ramon Sancibrian, Spain  
Giuseppe Sanfilippo, Italy  
Miguel A. F. Sanjuan, Spain  
Vittorio Sansalone, France

José A. Sanz-Herrera, Spain  
 Nickolas S. Sapidis, Greece  
 Evangelos J. Sapountzakis, Greece  
 Luis Saucedo-Mora, Spain  
 Marcelo A. Savi, Brazil  
 Andrey V. Savkin, Australia  
 Roberta Sburlati, Italy  
 Gustavo Scaglia, Argentina  
 Thomas Schuster, Germany  
 Oliver Schütze, Mexico  
 Lotfi Senhadji, France  
 Junwon Seo, USA  
 Joan Serra-Sagrsta, Spain  
 Gerardo Severino, Italy  
 Ruben Sevilla, UK  
 Stefano Sfarra, Italy  
 Mohamed Shaat, Egypt  
 Mostafa S. Shadloo, France  
 Leonid Shaikhet, Israel  
 Hassan M. Shanechi, USA  
 Bo Shen, Germany  
 Suzanne M. Shontz, USA  
 Babak Shotorban, USA  
 Zhan Shu, UK  
 Nuno Simões, Portugal  
 Christos H. Skiadas, Greece  
 Konstantina Skouri, Greece  
 Neale R. Smith, Mexico  
 Bogdan Smolka, Poland  
 Delfim Soares Jr., Brazil  
 Alba Sofi, Italy  
 Francesco Soldovieri, Italy  
 Raffaele Solimene, Italy  
 Jussi Sopanen, Finland  
 Marco Spadini, Italy  
 Bernardo Spagnolo, Italy  
 Paolo Spagnolo, Italy  
 Ruben Specogna, Italy  
 Vasilios Spitas, Greece  
 Sri Sridharan, USA  
 Ivanka Stamova, USA  
 Rafał Stanisławski, Poland  
 Florin Stoican, Romania  
 Salvatore Strano, Italy  
 Yakov Strelniker, Israel  
 Guang-Yong Sun, China  
 Ning Sun, China  
 Sergey A. Suslov, Australia  
 Thomas Svensson, Sweden  
 Andrzej Swierniak, Poland  
 Andras Szekrenyes, Hungary  
 Kumar K. Tamma, USA  
 Yang Tang, Germany  
 Hafez Tari, USA  
 Alessandro Tasora, Italy  
 Sergio Teggi, Italy  
 Ana C. Teodoro, Portugal  
 Alexander Timokha, Norway  
 Gisella Tomasini, Italy  
 Francesco Tornabene, Italy  
 Antonio Tornambe, Italy  
 Javier Martinez Torres, Spain  
 Mariano Torrisi, Italy  
 George Tsiatas, Greece  
 Antonios Tsourdos, UK  
 Federica Tubino, Italy  
 Nerio Tullini, Italy  
 Andrea Tundis, Italy  
 Emilio Turco, Italy  
 Vladimir Turetsky, Israel  
 Mustafa Tutar, Spain  
 Ilhan Tuzcu, USA  
 Efstratios Tzirtzilakis, Greece  
 Filippo Ubertini, Italy  
 Francesco Ubertini, Italy  
 Mohammad Uddin, Australia  
 Hassan Ugail, UK  
 Giuseppe Vairo, Italy  
 Eusebio Valero, Spain  
 Pandian Vasant, Malaysia  
 Marcello Vasta, Italy  
 Carlos-Renato Vázquez, Mexico  
 Miguel E. Vázquez-Méndez, Spain  
 Josep Vehi, Spain  
 Martin Velasco Villa, Mexico  
 K. C. Veluvolu, Republic of Korea  
 Fons J. Verbeek, Netherlands  
 Franck J. Vernerey, USA  
 Georgios Veronis, USA  
 Vincenzo Vespri, Italy  
 Renato Vidoni, Italy  
 V. Vijayaraghavan, Australia  
 Anna Vila, Spain  
 Rafael J. Villanueva, Spain  
 Francisco R. Villatoro, Spain  
 Uchechukwu E. Vincent, UK  
 Gareth A. Vio, Australia  
 Francesca Vipiana, Italy  
 Stanislav Vitek, Czech Republic  
 Thuc P. Vo, UK  
 Jan Vorel, Czech Republic  
 Michael Vynnycky, Sweden  
 Hao Wang, USA  
 Liliang Wang, UK  
 Shuming Wang, China  
 Yongqi Wang, Germany  
 Roman Wan-Wendner, Austria  
 Jaroslaw Wąs, Poland  
 P.H. Wen, UK  
 Waldemar T. Wójcik, Poland  
 Changzhi Wu, Australia  
 Desheng D. Wu, Sweden  
 Hong-Yu Wu, USA  
 Yuqiang Wu, China  
 Michalis Xenos, Greece  
 Guangming Xie, China  
 Xue-Jun Xie, China  
 Gen Q. Xu, China  
 Hang Xu, China  
 Joseph J. Yame, France  
 Xinggang Yan, UK  
 Jixiang Yang, Canada  
 Mijia Yang, USA  
 Yongheng Yang, Denmark  
 Luis J. Yebra, Spain  
 Peng-Yeng Yin, Taiwan  
 Qin Yuming, China  
 Elena Zaitseva, Slovakia  
 Arkadiusz Zak, Poland  
 Daniel Zaldivar, Mexico  
 Francesco Zammori, Italy  
 Vittorio Zampoli, Italy  
 Rafal Zdunek, Poland  
 Ibrahim Zeid, USA  
 Huaguang Zhang, China  
 Kai Zhang, China  
 Qingling Zhang, China  
 Xianming Zhang, Australia  
 Xuping Zhang, Denmark  
 Zhao Zhang, China  
 Yifan Zhao, UK



---

Jian G. Zhou, UK  
Quanxin Zhu, China

Mustapha Zidi, France  
Gaetano Zizzo, Italy

Zhixiang Zou, Germany

# Contents

## **Diagnostic Evaluation and Uncertainty Quantification of Earth and Environmental Systems Models**

Shuo Wang , Xander Wang, and Zoe Li

Editorial (2 pages), Article ID 5308012, Volume 2018 (2018)

## **Inexact Fuzzy Chance-Constrained Fractional Programming for Sustainable Management of Electric Power Systems**

C. Y. Zhou , G. H. Huang , J. P. Chen, and X. Y. Zhang

Research Article (13 pages), Article ID 5794016, Volume 2018 (2018)

## **Planning of Electric Power Systems Considering Virtual Power Plants with Dispatchable Loads Included: An Inexact Two-Stage Stochastic Linear Programming Model**

Changyu Zhou, Guohe Huang , and Jiapei Chen

Research Article (12 pages), Article ID 7049329, Volume 2018 (2018)

## **Connectivity Evaluation and Planning of a River-Lake System in East China Based on Graph Theory**

Jing Chen , Chenguang Xiao , and Dan Chen 

Research Article (12 pages), Article ID 1361867, Volume 2018 (2018)

## **A Tidal Level Prediction Approach Based on BP Neural Network and Cubic B-Spline Curve with Knot Insertion Algorithm**

Wenjuan Wang and Hongchun Yuan 

Research Article (9 pages), Article ID 9835079, Volume 2018 (2018)

## **Application of Surface Spline Interpolation Method in Parameter Estimation of a PM<sub>2.5</sub> Transport Adjoint Model**

Ning Li, Xianqing Lv , and Jicai Zhang 

Research Article (11 pages), Article ID 6231271, Volume 2018 (2018)

## **Economic and Environmental Effects of Public Transport Subsidy Policies: a Spatial CGE Model of Beijing**

Ping Xu , Weiyu Wang, and Chunxia Wei 

Research Article (12 pages), Article ID 3843281, Volume 2018 (2018)

## **Study on Viscoelastic Deformation Monitoring Index of an RCC Gravity Dam in an Alpine Region Using Orthogonal Test Design**

Yaoying Huang  and Zhiyong Wan 

Research Article (12 pages), Article ID 8743505, Volume 2018 (2018)

## **A Complete MCDM Model for NPD Performance Assessment in an LED-Based Lighting Plant Factory**

Wen-Chin Chen , Yen-Fu Lin, Kai-Ping Liu, Hui-Pin Chang, Li-Yi Wang , and Pei-Hao Tai 

Research Article (24 pages), Article ID 7049208, Volume 2018 (2018)

## **Effect of Shaft Pillar Extraction on Stability of Main Shaft: A Case Study at Xincheng Gold Mine, China**

Xige Liu, Wancheng Zhu , Kai Guan, and Hongxun Zhang

Research Article (16 pages), Article ID 1652312, Volume 2018 (2018)

## **Analytical Solution and Application for One-Dimensional Consolidation of Tailings Dam**

Hai-ming Liu , Gan Nan, Wei Guo, Chun-he Yang, and Chao Zhang

Research Article (9 pages), Article ID 4573780, Volume 2018 (2018)

## Editorial

# Diagnostic Evaluation and Uncertainty Quantification of Earth and Environmental Systems Models

Shuo Wang <sup>1</sup>, Xander Wang,<sup>2</sup> and Zoe Li<sup>3</sup>

<sup>1</sup>Department of Land Surveying and Geo-Informatics, Hong Kong Polytechnic University, Kowloon, Hong Kong

<sup>2</sup>School of Climate Change and Adaptation, University of Prince Edward Island, Charlottetown, Canada

<sup>3</sup>Department of Civil Engineering, McMaster University, Hamilton, Canada

Correspondence should be addressed to Shuo Wang; [shuo.s.wang@polyu.edu.hk](mailto:shuo.s.wang@polyu.edu.hk)

Received 19 November 2018; Accepted 20 November 2018; Published 2 December 2018

Copyright © 2018 Shuo Wang et al. This is an open access article distributed under the Creative Commons Attribution License, which permits unrestricted use, distribution, and reproduction in any medium, provided the original work is properly cited.

Earth and Environmental Systems (EES) models play a crucial role in facilitating the research and development in science and engineering disciplines. To better conceptualize the EES by using mathematical equations, models are becoming more complex with increasingly more sources of uncertainty, including the characterization of initial and boundary conditions, the errors in observation data, the difficulty in obtaining accurate parameter estimates, and model structural deficiencies. Therefore, it is necessary to address complexities and uncertainties propagated through the EES models in order to advance the understanding of nonlinear dynamics and chaos in the EES and to enhance the reliability of model results.

The aim of this special issue is to gather contributions on both theory and application of diagnostic analysis and uncertainty quantification of the EES models. Researchers and scientists are invited to propose recent advances in methodologies, models, and tools for solving complex engineering problems. This special issue has received a total of 27 manuscripts, 10 of which have been accepted for publication. The accepted papers involve a variety of modelling techniques and contribute to a wide range of application areas. A brief introduction for each contribution is provided as follows.

The paper entitled “Planning of Electric Power Systems Considering Virtual Power Plants with Dispatchable Loads Included: An Inexact Two-Stage Stochastic Linear Programming Model” by C. Zhou et al. proposes an inexact

two-stage stochastic linear programming method for supporting sustainable management of electric power systems under uncertainty. The proposed method is applied to solve a typical planning problem of power systems considering virtual power plants.

The paper entitled “Inexact Fuzzy Chance-constrained Fractional Programming for Sustainable Management of Electric Power Systems” by C. Y. Zhou et al. presents an inexact fuzzy chance-constrained fractional programming model for the planning of electric power systems under uncertainty. The proposed model can not only deal with multiple uncertainties but also tackle potential tradeoffs between conflicting objectives in terms of greenhouse gas mitigation and profit maximization.

The paper entitled “Connectivity Evaluation and Planning of a River-Lake System in East China Based on Graph Theory” by J. Chen et al. introduces a connectivity evaluation index method based on graph theory. The proposed method is applied for evaluating the connectivity of the stream network and for planning a river-lake system located in Eastern China.

The paper entitled “A Tidal Level Prediction Approach Based on BP Neural Network and Cubic B-Spline Curve with Knot Insertion Algorithm” by W. Wang and H. Yuan introduces a new method that merges the strengths of the BP neural network and the cubic B-spline curve with the knot insertion algorithm for predicting the tide levels of storm surge caused by typhoons. The predictive performance is

validated against historical tide level and typhoon data at Luchaogang, China.

The paper entitled “Application of Surface Spline Interpolation Method in Parameter Estimation of a  $PM_{2.5}$  Transport Adjoint Model” by N. Li et al. proposes a new method for estimating initial conditions in a  $PM_{2.5}$  transport adjoint model. The field of initial conditions is constructed by interpolating values at independent points using the surface spline interpolation method. The adjoint model combined with the surface spline interpolation is evaluated for optimizing initial conditions of the  $PM_{2.5}$  transport simulation.

The paper entitled “Economic and Environmental Effects of Public Transport Subsidy Policies: A Spatial CGE Model of Beijing” by P. Xu et al. proposes a Spatial Computable General Equilibrium (SCGE) model to examine the economic and environmental effects of public transport subsidy policies. By using a benchmark equilibrium calibrated for Beijing, the SCGE model is used to simulate social welfare, population distribution, and travel-related  $CO_2$  emission effects under different subsidy policies, including fare subsidy, cash grant, road expansion, and public transport speedup.

The paper entitled “Study on Viscoelastic Deformation Monitoring Index of an RCC Gravity Dam in an Alpine Region Using Orthogonal Test Design” by Y. Huang and Z. Wan presents a new method for determining viscoelastic deformation monitoring index of a Roller-compacted concrete (RCC) gravity dam in an alpine region. The state of viscoelasticity for the dam is illustrated followed by an investigation and designation of adverse load cases using the orthogonal test method. Water pressure component is then calculated by the finite element method, while temperature, time effect, and frost heave components are obtained through a deformation statistical model.

The paper entitled “A Complete MCDM Model for NPD Performance Assessment in An LED-Based Lighting Plant Factory” by W.-C. Chen et al. proposes a hybrid multicriteria decision-making model for assessing the performance of the new product development in the light-emitting diode- (LED-) based lighting plant factory. The feasibility of the proposed model is validated in a Taiwanese LED-based lighting plant factory.

The paper entitled “Effect of Shaft Pillar Extraction on Stability of Main Shaft: A Case Study at Xincheng Gold Mine, China” by X. Liu et al. presents a comprehensive investigation on the effects of mining activates on the stability of the main mine shaft at the Xincheng Gold Mine in China by means of in situ monitoring and numerical simulation. This study is useful for achieving reasonable predictions of shaft deformation and for providing valuable suggestions to mining operations.

The paper entitled “Analytical Solution and Application for One-Dimensional Consolidation of Tailings Dam” by H. Liu et al. proposes a partial differential equation for reasonably estimating the pore water pressure based on the assumption of 1D consolidation and small strain of tailings material. The analytic solutions can be obtained by solving the partial differential equation, which is useful for providing meaningful insights into the stability of the tailings dam.

We hope that the readers will find this special issue interesting and the published papers will stimulate further advancement in diagnostic evaluation and uncertainty quantification of Earth and Environmental Systems Models.

### Conflicts of Interest

We declare that there are no conflicts of interest regarding the publication of this editorial.

### Acknowledgments

We would like to express our gratitude to all the authors for their contributions and also the reviewers for their efforts to provide valuable comments and feedback.

*Shuo Wang  
Xander Wang  
Zoe Li*

## Research Article

# Inexact Fuzzy Chance-Constrained Fractional Programming for Sustainable Management of Electric Power Systems

C. Y. Zhou <sup>1</sup>, G. H. Huang <sup>2</sup>, J. P. Chen,<sup>3</sup> and X. Y. Zhang<sup>3</sup>

<sup>1</sup>*School of Control and Computer Engineering, North China Electric Power University, Beijing 102206, China*

<sup>2</sup>*Institute for Energy, Environment and Sustainability Research, UR-NCEPU, North China Electric Power University, Beijing 102206, China*

<sup>3</sup>*Institute for Energy, Environment and Sustainable Communities, UR-BNU, 3737 Wascana Parkway, Regina, SK, Canada S4S 0A2*

Correspondence should be addressed to G. H. Huang; [huang@iseis.org](mailto:huang@iseis.org)

Received 14 April 2018; Accepted 8 July 2018; Published 19 November 2018

Academic Editor: Ching-Ter Chang

Copyright © 2018 C. Y. Zhou et al. This is an open access article distributed under the Creative Commons Attribution License, which permits unrestricted use, distribution, and reproduction in any medium, provided the original work is properly cited.

An inexact fuzzy chance-constrained fractional programming model is developed and applied to the planning of electric power systems management under uncertainty. An electric power system management system involves several processes with socioeconomic and environmental influenced. Due to the multiobjective, multilayer and multiperiod features, associated with these various factors and their interactions extensive uncertainties, may exist in the study system. As an extension of the existing fractional programming approach, the inexact fuzzy chance-constrained fractional programming can explicitly address system uncertainties with complex presentations. The approach can not only deal with multiple uncertainties presented as random variables, fuzzy sets, interval values, and their combinations but also reflect the tradeoff in conflicting objectives between greenhouse gas mitigation and system economic profit. Different from using least-cost models, a more sustainable management approach is to maximize the ratio between clean energy power generation and system cost. Results of the case study indicate that useful solutions for planning electric power systems management practices can be generated.

## 1. Introduction

Sustainable development of electric power systems (EPS) plays a significant role in urban planning. At the present, the major energy sources for electricity generation in many countries are still nonrenewable fossil fuels, which are considered as one of the major contributors to the greenhouse gases emissions. Renewable energy, as an alternative energy source, has the characteristics of cleanliness, nondepletion, and easier operation and maintenance, however, its cost of generating electricity is higher and the energy source is intermittent and unreliable. Thus, there are many challenges to identify sustainable management plans for EPS. Among them, most importantly, decision-makers need to consider the tradeoff between economic cost and environmental impacts, the reflection of dynamic characteristics of facility capacity issues, as well as uncertainties of input information, such as the forecast values of electricity demands and renewable resource availabilities. Due to these complexities,

inexact systems analysis techniques are desired to assist in developing long-term EPS management plans. There are many techniques to handle system uncertainties, such as interval parameter programming (IPP) [1–3], stochastic mathematical programming (SMP) [4–7], and fuzzy possibilistic programming (FPP) [8–12].

In past decades, many inexact optimization methods were developed for energy system planning and management [13–20]. Classically, some models were formulated as single-objective Linear Programming (LP) problems aimed at minimization of system cost under specific levels of environmental requirements [21–23]. For example, Sun et al. [23] utilized a static deterministic linear model for planning China's electric power systems development, in which real energy use patterns among interregional energy spillover effects were examined. Since the early 1980s, for better reflecting the multidimensionality of the sustainability goal, it was increasingly popular to represent the EPS management problems within a Multiple Objective Programming (MOP)

framework [24–30]. For example, Han et al. [27] presented a multiobjective model for the EPS planning to maximize the expected system total profit and minimize the financial risk of handling uncertain environments. Meza et al. [26] propose a long-term multiobjective model for the power generation expansion planning of Mexican electric power system, which can optimize simultaneously multiple objectives (i.e., minimizes costs, environmental impact, imported fuel, and fuel price risks). Nevertheless, the tradeoff of multiple objectives was neglected and the system complexities could not be adequately reflected. In order to deal with the conflict objectives between the economic development and environmental protection, Fractional Programming (FP) was used in many management problems [31–34]. For instance, Wang et al. [34] developed a multistage joint-probabilistic chance-constrained fractional programming (MJCFP) approach of Saskatchewan, Canada. The MJCFP approach aimed to help tackle various uncertainties involved in typical electric power systems and thus facilitate risk-based management for climate change mitigation. Chen et al. [32] advanced a nonlinear fractional programming approach for addressing the environmental/economic power dispatch problems in the thermal power systems. Zhang et al. [33] put forward a fuzzy linear fractional programming approach for optimal irrigation water allocation under uncertainty.

FP has the advantages of better reflecting the real problems by optimizing the ratio between the economic and the environmental aspects over the conventional single-objective or multiobjective optimization programming methods. However, few of the earlier studies about EPS are focused on analyzing interactive relationships among multiple objectives, the randomness of the parameters, and uncertainties existed in multiple levels. In addition, chance-constrained programming (CCP) with the dual uncertainties (i.e., an interval number with fuzzy boundaries) parameters is seldom integrated into the FP optimization framework to deal with the violation of system constraints exists in the optimization model.

Therefore, this study aims to develop an inexact fuzzy chance-constrained fractional power system planning (IFCF-PSP). IFCF-PSP model will integrate chance-constrained programming, fuzzy programming, and interval-parameter programming within a fractional programming framework. Results will provide decision support for (i) achieving tradeoffs among system violation risk, environmental requirement, and system cost; (ii) generating flexible capacity expansion strategies under different risk levels; (iii) providing a variety of power generation and capacity expansion alternatives that can help support decision making under changing conditions; and (iv) helping decision-makers identify the optimal EPS management strategies and gain deeper insights into system efficiency, system cost and system risk under different CO<sub>2</sub> emission targets.

## 2. Methodology

The tradeoff of conflicting objectives between CO<sub>2</sub> mitigation and system economic profit is important to power systems planning (PSP). The linear fractional programming

(LFP) method can be effective in balancing two conflicting objectives and addressing randomness in the right-hand parameters. A general LFP problem can be expressed as follows:

$$\max f = \frac{\sum_{j=1}^n c_j x_j + \alpha}{\sum_{j=1}^n d_j x_j + \beta} \quad (1a)$$

$$\text{subject to: } \sum_{j=1}^n a_{ij} x_j \leq b_i, \quad i = 1, 2, \dots, m \quad (1b)$$

$$x_j \geq 0, \quad j = 1, 2, \dots, n \quad (1c)$$

where  $X$  is a vector of interval decision variables,  $a_{ij}$  are technical coefficients, and  $b_i$  are right-hand-side parameters;  $\alpha$  and  $\beta$  are constants.

In a power system, many data available are imprecise. Parameters in the model can be represented as interval numbers and/or fuzzy membership functions, such that the uncertainties can be directly communicated into the optimization process and resulting solution. Interval linear programming (ILP) is an effective method to deal with uncertainties existing as interval values without distribution information. The ILP method is integrated into the LFP method to reflect the uncertainty of the model parameters. Interval linear fractional programming (ILFP) can be an effective tool to tackle dual-objective optimization problems under uncertainty, especially when distribution information is not known exactly, and merely lower and upper bounds are available. A general ILFP problem can be expressed as follows:

$$\max f^\pm = \frac{\sum_{j=1}^n c_j^\pm x_j^\pm + \beta^\pm}{\sum_{j=1}^n d_j^\pm x_j^\pm + \gamma^\pm} \quad (2a)$$

$$\text{subject to: } \sum_{j=1}^n a_{ij}^\pm x_j^\pm \leq b_i^\pm, \quad i = 1, 2, \dots, m \quad (2b)$$

$$x_j^\pm \geq 0, \quad j = 1, 2, \dots, n \quad (2c)$$

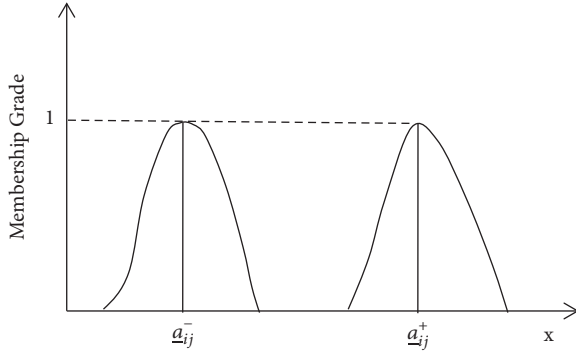
If  $b_i^\pm$  is a random right-hand-side parameter, the constraints (2b) can be transformed as follows:

$$\Pr \left\{ \sum_{j=1}^n a_{ij}^\pm x_j^\pm \leq b_i^\pm \right\} \geq \delta_i, \quad i = 1, 2, \dots, m \quad (3)$$

This means that the possible region of occurrence for the left-hand side of each constraint should be contained within a satisfactory or tolerable region as defined by the corresponding right-hand side. Thus, by incorporating tolerance measures  $\delta_i$  ( $0 \leq \delta_i \leq 1$ ) and utilizing the chance-constrained approach, the stochastic constraints of (3) can be transformed to their deterministic equivalents as follows:

$$\sum_{j=1}^n a_{ij}^\pm x_j^\pm \leq b_i^{\pm(p_i)}, \quad i = 1, 2, \dots, m \quad (4)$$

where  $b_i^{\pm(p_i)} = F_i^{-1}(p_i)$ ,  $i = 1, 2, \dots, m$ ;  $p_i = 1 - \delta_i$ , given the cumulative distribution function of  $b_i$  (i.e.,  $F_i(b_i)$ ) and


 FIGURE 1: Fuzzy boundaries for interval  $a^\pm$ .

the probability of violating constraint (4) ( $p_i$ ). The constraint of the model in the optimization process is changed from “rigid satisfaction” to “flexible response.” Therefore, the scheme can meet the optimization target with flexibility and maneuverability.

However, the problem with constraints (4) can only reflect the case when A is deterministic. In many real-world problems, the lower and upper bounds of some interval parameters can rarely be acquired as deterministic values. Instead, they may often be given as subjective information that can only be expressed as fuzzy sets. This leads to dual uncertainties as shown in Figure 1. If both A and B are uncertain, the set of feasible constraints may become more complicated. To generate a precise analysis of decision-making, multiple uncertainties need to be tackled. For example, the total carbon dioxide emissions in a certain region can be described as probability distributions, and the statistics of such a random parameter can be expressed as fuzzy sets. This results in dual uncertainties, which can be represented by the concept of distribution with fuzzy probability (DFP). In order to deal with the hybrid uncertainty resulting from fuzzy and stochastic information in constraints and parameters, CCP is then integrated into the ILFP method to reflect probability distribution of fuzzy numbers. Models (2a), (2b), and (2c) can be further improved by incorporating fuzzy and chance-constrained techniques. Therefore, let  $\mathfrak{R}^\pm$  be the set of intervals with fuzzy lower and upper bounds, and  $\psi^\pm$  denotes a set of fuzzy random numbers for fuzzy lower and upper bounds.

$$\sum_{j=1}^n \tilde{a}_{ij}^\pm x_j^\pm \leq \tilde{b}_i^{\pm(p_i)}, \quad i = 1, 2, \dots, m \quad (5)$$

Let  $\underline{U}_j$  and  $\underline{V}$  be base variables imposed by fuzzy subsets  $A_j$  and B, then

$$\mu_{A_j} : \underline{U}_j \longrightarrow [0, 1] \quad (6a)$$

$$\mu_B : \underline{V} \longrightarrow [0, 1] \quad (6b)$$

where  $\mu_{A_j}$  indicates the possibility of consuming a specific amount of resource by activity  $j$  and  $\mu_B$  indicates the possible

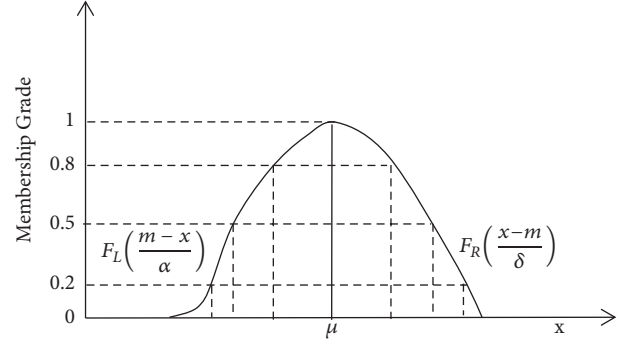


FIGURE 2: L-R fuzzy membership function.

availability of resource B.  $\leq$  means fuzzy inequality. Fuzzy subset  $N$  can be expressed as a L-R fuzzy number [35]:

$$\mu_N(x) = \begin{cases} F_L\left(\frac{m-x}{\alpha}\right), & \text{if } -\infty < x < m, \alpha > 0, \\ 1, & \text{if } x = m, \\ F_R\left(\frac{x-m}{\delta}\right), & \text{if } m < x < +\infty, \delta > 0. \end{cases} \quad (7a)$$

where  $F_L$  and  $F_R$  are the shape functions (Figure 2). For a linear case, fuzzy subset  $N$  can be defined as the following general format:

$$\mu_N(x) = \begin{cases} 0, & \text{if } x < \underline{\alpha} \text{ or } x > \bar{\alpha}, \\ 1, & \text{if } x = m, \\ 1 - \frac{2|m-x|}{\bar{\alpha} - \underline{\alpha}}, & \text{if } \underline{\alpha} < x < \bar{\alpha}. \end{cases} \quad (7b)$$

where  $[\underline{\alpha}, \bar{\alpha}]$  is an interval imposed by fuzzy subset  $N$ . Based on the method from Nie et al. [36] and Leung et al. [37], the fuzzy constraints in (5) can be replaced by the following  $2k$  precise inequalities, in which  $k$  denotes the number of  $\alpha$ -cut levels:

$$\sum_{j=1}^n \overline{a}_{ij}^{\pm s} x_j^\pm \leq \overline{b}_i^{\pm s(p_i)}, \quad i = 1, 2, \dots, m; \quad s = 1, 2, \dots, k \quad (8a)$$

$$\sum_{j=1}^n \underline{a}_{ij}^{\pm s} x_j^\pm \geq \underline{b}_i^{\pm s(p_i)}, \quad i = 1, 2, \dots, m; \quad s = 1, 2, \dots, k \quad (8b)$$

where

$$\overline{a}_{ij}^{\pm s} = \sup(a_{ij}^{\pm s}), \quad a_{ij}^{\pm s} \in (A_j)_{\alpha_s} \quad (8c)$$

$$\underline{a}_{ij}^{\pm s} = \inf(a_{ij}^{\pm s}), \quad a_{ij}^{\pm s} \in (A_j)_{\alpha_s} \quad (8d)$$

$$\overline{b}_i^{\pm s} = \sup(b_i^{\pm s}), \quad b_i^{\pm s} \in B_{\alpha_s} \quad (8e)$$

$$\underline{b}_i^{\pm s} = \inf(b_i^{\pm s}), \quad b_i^{\pm s} \in B_{\alpha_s} \quad (8f)$$

$\alpha_s \in (0, 1]$  ( $s = 1, 2, \dots, k$ ),  $\sup(t)$  represents the superior limit value among set  $t$ , and  $\inf(t)$  denotes the inferior limit value among set  $t$ .

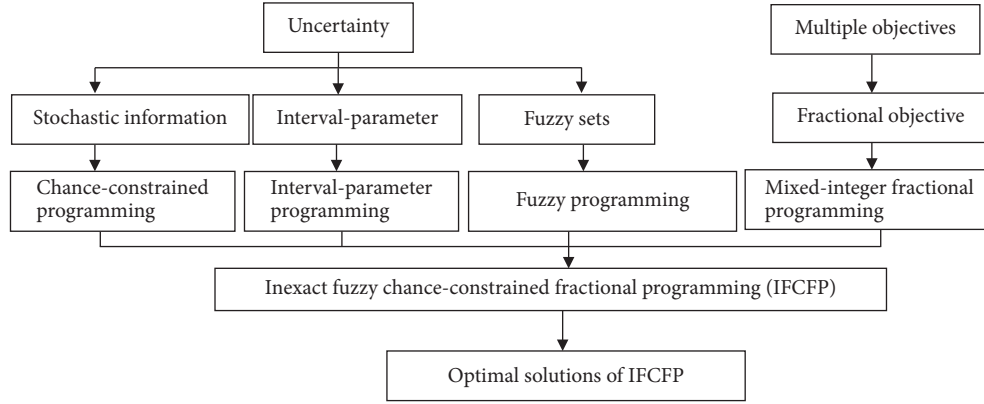


FIGURE 3: Framework of the IFCFP approach.

Figure 3 presents the framework of the IFCFP method. Give a set of certain values of the  $\alpha$  – cut level to fuzzy parameters  $\tilde{a}_{ij}$ ,  $\tilde{b}_i$ , and  $\tilde{p}_i$ , and solve models (1a), (1b), and (1c) through the IFCFP approach. According to interactive transform algorithm proposed by Zhu et al. [31], the IFCFP model can be transformed into two submodels and then can be solved through the branch-and-bound algorithm and the method proposed by Charnes et al. [38]. Compared with the existing optimization methods, the proposed IFCFP approach has three characteristics: (i) it can tackle ratio optimization problems; (ii) it can handle uncertainties with unknown distribution information by interval parameters and variables; and (iii) it can deal with uncertain parameters presented as fuzzy sets in the objective and the left hand side, as well as dual uncertainties expressed as the distribution with fuzzy probability.

### 3. Case Study

To demonstrate its advantages, the proposed IFCFP method is applied to a typical regional electric system management problem with representative cost and technical data within a Chinese context. In the study system, it is assumed that there is an independent regional electricity grid, where one nonrenewable resource (coal) and four clean energy resources (natural gas, wind, solar, and hydro) are available for electricity generation. The decision-makers are responsible for arranging electricity production from those five types of power-generation to meet the demand of end users. To reflect the dynamic features of the study system, three-time periods (5 years for each period) are considered in a 15-year planning horizon.

A sufficient electricity supply at minimum cost is important to the electric generation expansion planning. The system cost  $C^\pm$  is formulated as a sum of the following:

$$C^\pm = f_1^\pm + f_2^\pm + f_3^\pm + f_4^\pm + f_5^\pm \quad (9a)$$

(1) the total cost for primary energy supply:

$$f_1^\pm = \sum_{t=1}^T \sum_{j=1}^I CPE_{tj}^\pm \times APE_{tj}^\pm \quad (9b)$$

where  $t$  is equal to index for the time periods ( $t = 1, 2, \dots, T$ );  $j$  is equal to index for the power-generation technology ( $j = 1, 2, \dots, J$ ),  $I$  is the number of nonrenewable power-generation technology (e.g.,  $j = 1$  coal power,  $j = 2$  natural gas, and  $I < J$ );  $CPE_{tj}^\pm$  is equal to cost for local primary energy supply for power-generation technology  $j$  in period  $t$  ( $10^3$  \$/TJ);  $APE_{tj}^\pm$  is equal to decision variable and represents local supply of primary energy resource for power-generation technology  $j$  in period  $t$  (TJ).

(2) fixed and variable operating costs for power generation:

$$f_2^\pm = \sum_{t=1}^T \sum_{j=1}^J CPG_{tj}^\pm \times APG_{tj}^\pm \quad (9c)$$

where  $APG_{tj}^\pm$  is equal to decision variable and represents electricity generation from power-generation technology  $j$  in period  $t$  (GWh);  $CPG_{tj}^\pm$  is equal to fixed and variable operation costs for generating electricity via technology  $j$  in period  $t$  ( $10^3$  \$/GWh);

(3) cost for capacity expansions:

$$f_3^\pm = \sum_{t=1}^T \sum_{j=1}^J \sum_{m=1}^M CEP_{tj}^\pm \times ECA_{tjm}^\pm \times Y_{tjm} \quad (9d)$$

where  $m$  is equal to index for the capacity expansion options ( $m = 1, 2, \dots, M$ ).  $CEP_{tj}^\pm$  is equal to cost for expanding capacity for generating electricity via technology  $j$  in period  $t$ . ( $10^6$  \$/GW).  $ECA_{tjm}^\pm$  is equal to capacity expansion option of power-generation technology  $j$  under different expansion program  $m$  in period  $t$  (GW);  $Y_{tjm}$  is equal to binary variable of capacity option  $m$  for power-generation technology  $j$  in period  $t$ .

(4) cost for importing electricity:

$$f_4^\pm = \sum_{t=1}^T CIE_t^\pm \times AIE_t^\pm \quad (9e)$$

where  $CIE_t^\pm$  is equal to cost of importing electricity in period  $t$  ( $10^3$  \$/GWh);  $AIE_t^\pm$  is equal to decision variable and

represents the shortage amount of electricity needs to be imported in period  $t$ (GWh).

(5) cost for pollutant mitigation:

$$f_5^\pm = \sum_{t=1}^T \sum_{j=1}^I CPM_{tj}^\pm \times APG_{tj}^\pm \times \eta_t^\pm \quad (9f)$$

where  $CPM_{tj}^\pm$  is equal to cost of pollution mitigation of power-generation technology  $j$  in period  $t$ ( $10^3$  \$/ton);  $\eta_t^\pm$  CO<sub>2</sub> emission factor in period  $t$ ( $10^3$  ton/GWh).

Renewable energy resources are intermittent and unreliable, which are subject to spatial and/or temporal

fluctuations. The natural gas generation with low carbon dioxide emissions can stabilize the risk of the intermittent and unpredictable nature of renewable energy generation. In this study, we assumed natural gas resources as the clean energy power generation. Therefore, the objective of this study is to maximize the ratio between clean energy generation (including the natural gas) and system cost, while a series of constraints define the interrelationships among the decision variables and system conditions/factors. The inexact fuzzy chance-constrained fractional power systems planning (IFCF-PSP) can be formulated as follows:

$$\begin{aligned} \max f^\pm &= \frac{CG^\pm}{C^\pm} \\ &= \frac{\sum_{t=1}^T \sum_{j=I+1}^J APG_{tj}^\pm + \sum_{t=1}^T APG_{t2}^\pm}{\sum_{t=1}^T \sum_{j=1}^I CPE_{tj}^\pm \times APE_{tj}^\pm + \sum_{t=1}^T \sum_{j=1}^I CPG_{tj}^\pm \times APG_{tj}^\pm + \sum_{t=1}^T \sum_{j=1}^I \sum_{m=1}^M CEP_{tjm}^\pm \times ECA_{tjm}^\pm \times Y_{tjm} + \sum_{t=1}^T CIE_t^\pm \times AIE_t^\pm + \sum_{t=1}^T \sum_{j=1}^I CPM_{tj}^\pm \times APG_{tj}^\pm \times \eta_t^\pm} \end{aligned} \quad (10a)$$

where the clean energy power generation ( $CG^\pm$ ) consists of the renewable energies such as wind power, solar energy, and hydropower ( $APG_{tj}^\pm$  and  $j = I + 1, \dots, J$ ) and the natural gas generation in period  $t$ .

The constraints are listed as follows:

(1) electricity demand constraints:

$$\sum_{j=1}^J APG_{tj}^\pm + AIE_t^\pm \geq DM_t^\pm \times (1 + \theta_t^\pm), \quad \forall t \quad (10b)$$

where  $DM_t^\pm$  is equal to local electricity demand (GWh);  $\theta_t^\pm$  is equal to transmission loss in period  $t$ .

(2) capacity limitation constraints for power-generation facilities:

$$APG_{tj}^\pm \leq \left( RCA_{tj}^\pm + \sum_{m=1}^M ECA_{tjm}^\pm \times Y_{tjm} \right) \times STM_{tj}^\pm, \quad \forall t, j \quad (10c)$$

where  $RCA_{tj}^\pm$  is equal to the current capacity of power-generation technology  $j$  in period  $t$ (GW);  $STM_{tj}^\pm$  is equal to the maximum service time of power-generation technology  $j$  in period  $t$ (hour).

(3) primary energy availability constraints:

$$APE_{tj}^\pm \leq UPE_{tj}^\pm, \quad \forall t, j \quad (10d)$$

$$APG_{tj}^\pm \times rf_{tj}^\pm \leq APE_{tj}^\pm, \quad \forall t, j \quad (10e)$$

where  $UPE_{tj}^\pm$  is equal to available primary energy  $j$  in period  $t$  ( $j = 1, 2; TJ$ );  $rf_{tj}^\pm$  is equal to energy consumption conversion rate by power-generation technology  $j$  in period  $t$  ( $j = 1, 2; TJ/GWh$ ).

(4) capacity expansion constraints:

$$RCA_{tj}^\pm + \sum_{m=1}^M ECA_{tjm}^\pm \times Y_{tjm} \leq UCA_{tj}^\pm, \quad \forall t, j \quad (10f)$$

where  $UCA_{tj}^\pm$  is equal to maximum capacity of generation technology  $j$  in period  $t$ (GW).

(5) expansion options constraints:

$$\sum_{m=1}^M Y_{tjm} \leq 1, \quad \forall t, j \quad (10g)$$

$Y_{tjm} = 1$ , if capacity expansion is undertaken  
 $Y_{tjm} = 0$ , otherwise

(6) import electricity constraints:

$$AIE_t^\pm \leq UIE_t^\pm, \quad \forall t \quad (10h)$$

where  $UIE_t^\pm$  is equal to maximum import amount of electricity imports in period  $t$  (GWh).

(7) renewable energy availability constraints:

$$\sum_{j=I+1}^J APG_{tj}^\pm \geq \left( \sum_{j=1}^I APG_{tj}^\pm \right) \sigma_t^\pm, \quad \forall t \quad (10i)$$

where  $\sigma_t^\pm$  is equal to the minimum proportion of electricity generation by renewable energy in the whole power-generation. Currently, the Renewable Portfolio Standard (RPS) mechanisms have been adopted in several countries, including the United Kingdom (Renewables Obligation in the UK), Italy, Poland, Sweden, and Belgium, and 29 out of 50 US states, etc. According to the government's requirement, a certain percentage of the electricity generation of the power enterprises will come from renewable energy sources. The proportion of electricity from renewable sources will usually increase year by year. Thus, in the model,  $\sigma_t^\pm$  is used to represent the lowest ratio of the RPS.

(8) pollutants emission constraints:

$$\sum_{j=1}^I APG_{tj}^\pm \times \eta_{tj}^\pm \times (1 - \tilde{\xi}_t^\pm) \leq E\tilde{M}_t^{\pm(p_i)}, \quad \forall t \quad (10j)$$

TABLE 1: Cost of energy supply and conversion parameters.

	Period		
	t=1	t=2	t=3
Energy supply cost ( $10^3$ \$/TJ)			
Coal	[2.56, 3.06]	[3.26, 3.76]	[3.96, 4.46]
Natural gas	[6.76, 6.96]	[7.57, 7.77]	[8.38, 8.58]
Units of energy carrier per units of electricity generation (TJ/GWh)			
Coal	[11.12, 11.7]	[10.68, 11.16]	[10.15, 10.62]
Natural gas	[8.38, 8.82]	[7.54, 7.92]	[6.79, 7.38]

TABLE 2: Fuzzy subsets for efficiency coefficient under different  $\alpha$  - cut levels.

$\alpha$ - cut level	period	efficiency coefficient			
		$\underline{\rho}^+$	$\overline{\rho}^+$	$\underline{\rho}^-$	$\overline{\rho}^-$
0	t=1	0.125	0.235	0.12	0.23
	t=2	0.14	0.175	0.136	0.17
	t=3	0.119	0.149	0.116	0.145
0.2	t=1	0.135	0.223	0.13	0.218
	t=2	0.142	0.17	0.138	0.165
	t=3	0.12	0.144	0.117	0.14
0.5	t=1	0.15	0.205	0.145	0.2
	t=2	0.144	0.162	0.14	0.157
	t=3	0.123	0.138	0.119	0.134
0.8	t=1	0.165	0.187	0.16	0.182
	t=2	0.147	0.154	0.143	0.15
	t=3	0.125	0.131	0.122	0.127
1	t=1	0.175	0.175	0.17	0.17
	t=2	0.149	0.149	0.145	0.145
	t=3	0.126	0.126	0.123	0.123

Note. efficiency coefficient ( $\overline{\rho}_t^+ = 1 - \overline{\xi}_t^+$ ).

where  $EM_t$  is equal to the permitted  $\text{CO}_2$  emission in period  $t$  ( $10^3$  ton).  $\overline{\xi}_t^\pm$  is equal to the efficiency of chemical absorption or capture and storage of  $\text{CO}_2$  in period  $t$ .  $p_i$  = the risk confidence levels.

(9) nonnegativity constraints:

$$APE_{tj}^\pm, APG_{tj}^\pm, AIE_t^\pm \geq 0 \quad \forall t, j \quad (10k)$$

Interval parameters are adopted to address imprecise uncertainties, which are generally associated with electricity demands, prices of energy resources, costs of capacity expansion, and many other constraints. The real research data are used as input data of the model. The detailed descriptions of cost for energy supply and relative conversion parameters were illustrated in Table 1. Table 2 gives fuzzy subsets for efficiency coefficient under different  $\alpha$ -cut levels. Table 3 lists the capacity expansion options and capital investment costs for each facility.

## 4. Results and Discussion

In Figure 4, coal-fired electricity supply would increase steadily and still play an important role in the power system due to its high availability and competitive price over the study planning horizon. However, increasingly stringent emission limits result in idle coal-fired facilities. More economical and environmentally friendly power generation facilities will be prioritized. The risk confidence level ( $p_i$ ) is employed to the constraints of  $\text{CO}_2$  emission requirement. The decision-maker can adjust the value of the  $p_i$  level according to actual needs. We assumed that violations of emission constraints are allowed under three given  $p_i$  levels ( $p_i = 0.01, 0.05$ , and  $0.1$ , which are normally adopted as the significance levels) [39]. The higher credibility level would correspond to a tight environment requirement, thus leading to a lower  $\text{CO}_2$  emission, while the lower credibility level would correspond to a relatively relaxed environment requirement, thus resulting in a higher  $\text{CO}_2$  emission. Therefore, changes in  $p_i$ -level have an impact on coal-fired power

TABLE 3: Capacity expansion options and costs for power-generation facilities.

		Period		
		t=1	t=2	t=3
Capacity-expansion options (GW)				
Coal	m=1	0.05	0.05	0.05
	m=2	0.10	0.10	0.10
	m=3	0.15	0.15	0.15
Natural gas	m=1	0.10	0.10	0.10
	m=2	0.15	0.15	0.15
	m=3	0.20	0.20	0.20
Wind power	m=1	0.05	0.05	0.05
	m=2	0.15	0.15	0.15
	m=3	0.20	0.20	0.20
Solar energy	m=1	0.05	0.05	0.05
	m=2	0.15	0.15	0.15
	m=3	0.20	0.20	0.20
Hydropower	m=1	0.15	0.15	0.15
	m=2	0.20	0.20	0.20
	m=3	0.25	0.25	0.25
Capacity expansion cost ( $10^6$ \$/GW)				
Coal		[577, 607]	[547, 577]	[517, 547]
Natural gas		[726, 756]	[676, 726]	[626, 676]
Wind power		[1256, 1306]	[1156, 1206]	[1056, 1106]
Solar energy		[2668, 2768]	[2468, 2568]	[2268, 2368]
Hydropower		[1597, 1697]	[1497, 1597]	[1397, 1497]

generation. The total supply of coal-fired generation would decrease from  $[480.69, 507.20] \times 10^9$  GWh when  $p_i = 0.1$  to  $[471.75, 506.85] \times 10^9$  GWh when  $p_i = 0.05$ , and reach  $[459.38, 503.13] \times 10^9$  GWh when  $p_i = 0.01$ . In contrast, clean energy generation will increase. For example, solar power generation of three periods would rise from  $[24.38, 27.68] \times 10^9$  GWh when  $p_i = 0.1$  to  $[25.62, 27.68] \times 10^9$  GWh when  $p_i = 0.05$  and reach  $[26.25, 27.69] \times 10^9$  GWh when  $p_i = 0.01$ . As shown in Figure 4, the generation of solar power and natural gas in clean power facilities are mainly affected by emission constraints. When  $p_i = 0.01$ , the solar power generation is the largest and the power generation from natural gas is the lowest in the three-study  $p_i$ -levels. This is the result of the tradeoff between carbon dioxide emissions and system costs. Developing natural gas electricity requires a relatively low capital cost but leads to more CO<sub>2</sub> emissions, and the solar energy technology needs a low operational cost but an extremely high capital cost. Similarly, the results under other  $p_i$  levels ( $p_i = 0.05$  and  $p_i = 0.1$ ) can be interpreted. During the entire planning horizon, the ratio objective between clean energy generation and the total system cost would be  $[2.15, 3]$  GWh per  $10^6$ , which also represents the range of the system efficiency. When the electricity-generation pattern varies under different  $p_i$  levels and within the interval solution ranges, the system efficiency would also fluctuate within its solution range correspondingly. Thus, the IFCF-PSP results can create multiple decision alternatives through adjusting

different combinations of the solutions. Table 4 presents the typical alternatives, where combinations of upper/lower bound values for  $APE_{ij}^{\pm}, APG_{ij}^{\pm}, Y_{tjm}^{\pm}, (j = 1, \forall t, m)$  and  $APG_{ij}^{\pm}, Y_{tjm}^{\pm}, (j = 2, 3, 4, 5, \forall t, m)$  are examined. Under the same power generation alternative, interval solution of the system cost can be obtained according to interval price parameters and corresponds to the interval solution of system efficiency. Based on the result of the total electricity generated, we divided the 12 alternatives into three groups (high: A3, A4, A8, and A12; medium: A1, A5, A7, and A9; low: A2, A6, A10, and A11) to meet the future high, medium, or low electricity demand.

The comparison of the system efficiency under different  $p_i$  levels shows that  $A11 > A6 > A10 > A2$  under low-level total power generation group. Alternative A11 (corresponding to f+) would lead to the most sustainable option with a system efficiency as much as  $[2.714, 2.999]$  GWh per  $10^6$ , which corresponds to the highest amount of clean energy electricity ( $0.478 \times 10^6$  GWh) and a moderate cost ( $[159.36, 176.12] \times 10^9$  \$). Additionally, lower-level electricity demands will be satisfied by a total power generation of  $1.856 \times 10^6$  GWh. Therefore, Alternative A11 is a desirable choice from the point of view of resources conservation and environmental protection when electricity demand is at the low level. Alternative A6 would also meet low electricity demand and reached the lowest system cost ( $[151.42, 167.85] \times 10^9$  \$). When Alternative A10 is adopted, all the power generation

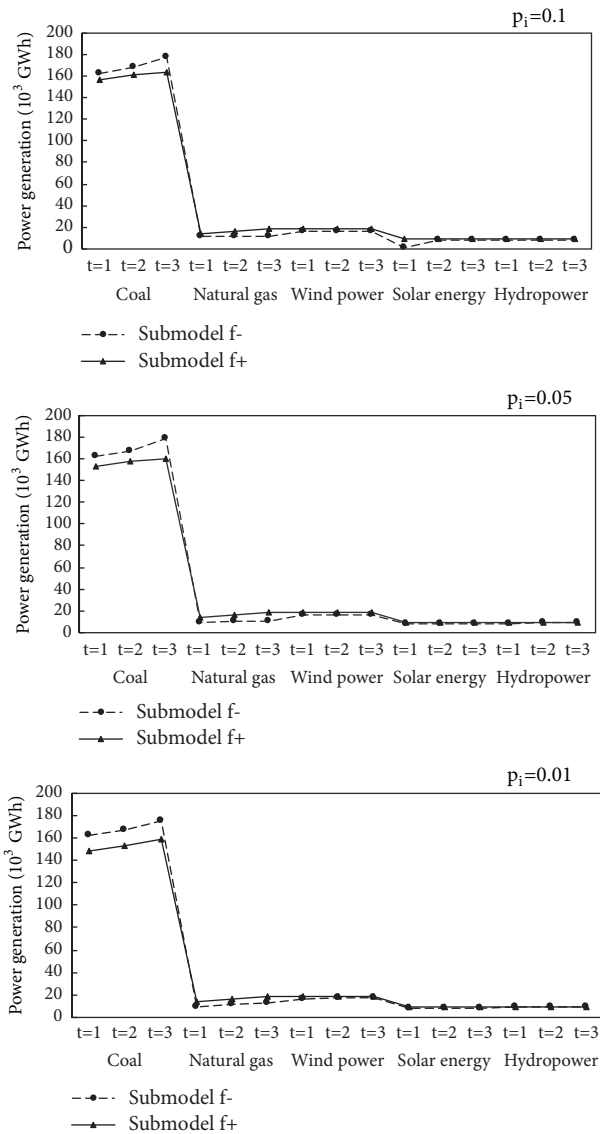


FIGURE 4: Power generation loads for EPS through the IFCF-PSP model.

activities will reach their lower bound levels, leading to the lowest power generation ( $1.764 \times 10^6$  GWh). Compared with Alternative A6, this alternative may be of less interest to decision-makers due to its lower system efficiency and higher system cost. However, it is the solution that is obtained under the most stringent emission constraints (i.e.,  $p_i = 0.01$ ). Alternative A2 is a moderate solution in this group. Its system cost, system efficiency, total power generation, and clean energy power generation are  $[152.95, 169.54] \times 10^9$  \$,  $[2.206, 2.445]$  GWh per  $10^6$ ,  $1.816 \times 10^6$  GWh, and  $0.374 \times 10^6$  GWh.

In middle-level total power generation group, the comparison of the system efficiency under different  $p_i$  levels shows that alternative  $A7 > A5 > A9 > A1$ . In alternative A7, middle-level electricity demands will be satisfied by a total power generation of  $1.893 \times 10^6$  GWh. In addition, Alternative

A7 has the highest system efficiency ( $[2.661, 2.941]$  GWh per  $10^6$  \$) and the largest amount of clean energy power generation ( $0.478 \times 10^6$  GWh) in this group. Thus, Alternative A7 is considered to be a desirable choice. Alternatives A5 and A9 would lead to the same total power generation solution ( $1.895 \times 10^6$  GWh). They are the two-moderate solutions in this group. The system cost obtained from the A1 is the lowest ( $[157.18, 174.13] \times 10^9$  \$) in this group. It would lead to the lowest system efficiency ( $[2.148, 2.379]$  GWh per  $10^6$  \$), but due to the largest proportion of fossil-fired power generation, A1 has the maximum security for energy supply.

In high-level total power generation group, the comparison of the system efficiency under different  $p_i$  levels shows that alternative  $A3 > A12 > A8 > A4$ . The same clean energy power generation obtained from the 4 alternatives is  $0.478 \times 10^6$  GWh. In Alternative A4, all the power generation activities will be equal to their upper-bound values at the same time. It would lead to the highest system cost ( $[169.01, 186.76] \times 10^9$  \$), but the moderate system efficiency ( $[2.559, 2.828]$  GWh per  $10^6$  \$). In comparison, Alternative A3 would lead to the minimum system cost ( $[164.78, 182.16] \times 10^9$  \$) and the highest system efficiency ( $[2.624, 2.901]$  GWh per  $10^6$  \$) in this group. In addition, this alternative would also provide the highest clean energy power generation. Therefore, this alternative is a desirable sustainable option under the high electricity demand level. Alternatives A8 and A12 can provide modest system efficiencies, which would be  $[2.561, 2.83]$  and  $[2.575, 2.845]$  GWh per  $10^6$  \$, respectively, and lower system costs, which would be  $[168.92, 186.66]$  and  $[168.00, 185.64] \times 10^9$  \$. Therefore, decision-makers who pay attention to the stability of the system may be interested in these two alternatives.

The above alternatives represent various options between economic and environmental tradeoffs. Willingness to accept high system cost will guarantee meeting the objective of increasing the proportion of clean energy. A strong desire to acquire low system cost will cause the risk of violating emission constraints. In general, the above research results were favored by decision makers due to their flexibility and preference for practical-making decision processes. The feasible ranges for decision variables under different  $p_i$  levels were useful for decision makers to justify the generated alternatives directly.

Besides the scenario of maximizing the proportion of clean energy, another scenario of minimizing the system cost is also analyzed to evaluate the effects of different energy supply policies. The optimal-ratio problem presented in Models (10a)–(10k) can be converted into a least-cost problem with the following objective:

$\min f = \text{system cost}$

$$\begin{aligned}
 &= \sum_{t=1}^T \sum_{j=1}^J CPE_{tj}^{\pm} \times APE_{tj}^{\pm} + \sum_{t=1}^T \sum_{j=1}^J CPG_{tj}^{\pm} \times APG_{tj}^{\pm} \\
 &+ \sum_{t=1}^T \sum_{j=1}^J \sum_{m=1}^M CEP_{tj}^{\pm} \times ECA_{tjm}^{\pm} \times Y_{tjm}
 \end{aligned}$$

TABLE 4: Typical decision alternatives obtained from the IFCF-PSP model solutions.

Alternative	$APE_{ij}^{\pm}, APG_{ij}^{\pm}, Y_{ijm}^{\pm}$ ( $j=1, \forall t, m$ )	$APG_{ij}^{\pm}, Y_{ijm}^{\pm}$ ( $j=2,3,4,5, \forall t, m$ )	System efficiency (GWh per $10^6$ \$)	System cost ( $10^9$ \$)	Total power generation ( $10^6$ GWh)	Clean energy power generation ( $10^6$ GWh)
$p_i = 0.1$						
A1	+	-	[2.148,2.379] (#12)	[157.18,174.13] (#4)	1.895 (#6)	0.374 (#11)
A2	-	-	[2.206,2.445] (#9)	[152.95,169.54] (#3)	1.816 (#10)	0.374 (#11)
A3	-	+	[2.624,2.901] (#3)	[164.78,182.16] (#9)	1.92 (#4)	0.478 (#1)
A4	+	+	[2.559,2.828] (#6)	[169.01, 186.76] (#12)	2 (#1)	0.478 (#1)
$p_i = 0.05$						
A5	+	-	[2.236,2.477] (#8)	[157.83,174.87] (#5)	1.912 (#5)	0.391 (#7)
A6	-	-	[2.329,2.582] (#7)	[151.42,167.85] (#1)	1.807 (#11)	0.391 (#7)
A7	-	+	[2.661,2.941] (#2)	[162.51,179.63] (#8)	1.893 (#8)	0.478 (#1)
A8	+	+	[2.561,2.83] (#5)	[168.92,186.66] (#11)	1.999 (#2)	0.478 (#1)
$p_i = 0.01$						
A9	+	-	[2.174, 2.406] (#11)	[160.40, 177.57] (#7)	1.895 (#6)	0.386 (#9)
A10	-	-	[2.297,2.543] (#8)	[151.76, 168.06] (#2)	1.764 (#12)	0.386 (#9)
A11	-	+	[2.714,2.999] (#1)	[159.36,176.12] (#6)	1.856 (#9)	0.478 (#1)
A12	+	+	[2.575,2.845] (#4)	[168.00, 185.64] (#10)	1.987 (#3)	0.478 (#1)

TABLE 5: The proportion of clean energy power generation from IFCF-PSP and LS models.

Clean power generation ratio (%)	IFCF-PSP			LS		
	t=1	t=2	t=3	t=1	t=2	t=3
$p_i = 0.1$	[18.02, 24.32]	[20.89, 24.93]	[19.86, 25.40]	[16.23, 18.70]	[16.81, 17.19]	[15.15, 16.38]
$p_i = 0.05$	[20.67, 24.65]	[20.93, 25.28]	[20.10, 25.78]	[16.24, 18.70]	[16.81, 17.19]	[16.32, 18.69]
$p_i = 0.01$	[21.55, 25.30]	[21.58, 25.96]	[21.41, 25.96]	[16.48, 18.93]	[16.79, 17.52]	[19.97, 22.24]

$$\begin{aligned}
 & + \sum_{t=1}^T CIE_t^{\pm} \times AIE_t^{\pm} \\
 & + \sum_{t=1}^T \sum_{j=1}^I CPM_{tj}^{\pm} \times APG_{tj}^{\pm} \times \eta_t^{\pm}
 \end{aligned} \tag{11}$$

Figure 5 shows the proportion of different power generation technologies from the IFCF-PSP and LS models under  $p_i = 0.01$  over three planning periods. The IFCF-PSP model leads to a relatively higher percentage of natural gas power generation; in comparison, the LS model leads to relatively higher percentages of coal-fired electricity supplies. According to the solutions from IFCF-PSP model, the percent of electricity generated by natural gas facilities would be [5, 6] %, [7, 8] %, and [5, 8] % in periods 1, 2, and 3, respectively. The LS model achieves the slightly lower percent (i.e. 0%, 0% and [5, 6] % in periods 1, 2, and 3.) Similarly, the results under other  $p_i$  levels ( $p_i = 0.05$  and  $p_i = 0.1$ ) can be interpreted.

According to Table 5, the differences can be found between the results of two models under different  $p_i$  levels. The proportion of clean energy power generation from IFCF-PSP model is higher than that of the LS model. For example, under  $p_i = 0.01$ , clean energy power generation of the entire region occupied [21.55, 25.30], [21.58, 25.96], and [21.41, 25.96]% of the total electricity generation in

the three study periods from IFCF-PSP model, which are higher than the LS model [16.48, 19.93], [16.79, 17.52] and [19.97, 22.24]%, respectively. Similarly, the results under other  $p_i$  levels ( $p_i = 0.05$  and  $p_i = 0.1$ ) can be interpreted. An increased  $p_i$  level represents a higher admissible risk, leading to a decreased strictness for the emission constraints and hence an expanded decision space. Therefore, under typical conditions, as the risk level becomes lower, the proportion of clean energy power generation or renewable power generation would increase. For example, in period 2, when the  $p_i$  level is dropped from 0.1 to 0.01, the proportion of clean energy power generation from IFCF-PSP model would be increased from [20.89, 24.93]% to [21.58, 25.96]%. Likewise, the results under other periods can be similarly analyzed. The confidence level of constraints satisfaction is more reliable because the risk level is lower. Therefore, in this case, the decision-makers will be more conservative in the EPS management. There is no capacity-expansion would be conducted for the coal-fired facility in three periods, since its high carbon dioxide emissions and increasingly stringent emission limits. On the other hand, clean energy electricity supply would be insufficient for the future energy demands. According to Table 6, when  $p_i$  takes different values (i.e.,  $p_i = 0.01$ ,  $p_i = 0.05$ , and  $p_i = 0.1$ ), differences of capacity-expansion option can be found between the results of two models. In both models, when the risk of violating the constraints of carbon emission target is decreased (i.e., the value of  $p_i$ -level

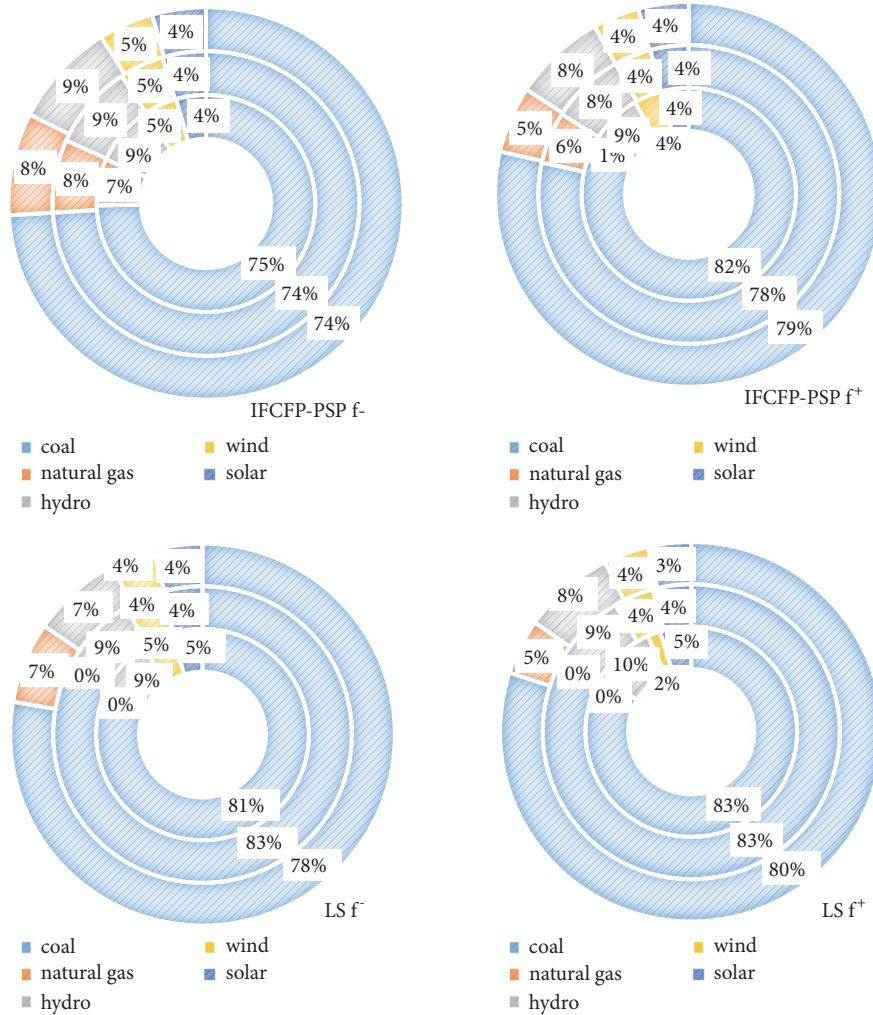


FIGURE 5: Comparison of power-generation patterns from IFCFP-PSP and least-system-cost (LS) models under  $p_i$ -level 0.01. Note that the innermost circle in the pie chart represents the first planning period.

is larger), the demand for expansion of clean energy will increase. On the other hand, the total demand of capacity expansion in the lower bound model is lower than the upper bound model. One of the reasons for this result is that the annual utilization hours of various power generation facilities in the lower bound model are higher than the corresponding parameter settings of the upper bound model.

The result of LS model has shown that, under the corresponding lower bound parameter settings, the capacity of 0.15 GW would be added to the hydropower facility in period 3 when  $p_i = 0.01$  and  $p_i = 0.05$ . Only a capacity of 0.15 GW would be added to the wind power facility in period 3. While under the corresponding upper bound parameter settings, natural gas, and solar energy facilities expansions are not required, that is because the former resource is under penalty of CO<sub>2</sub> emission and the capacity cost of the solar power expansion is much higher.

In the IFCF-PSP model, clean energy will be given more development opportunities. Take  $p_i = 0.01$  as an example (corresponding to  $f^-$ ), with a capacity expansion of 0.2

GW at the beginning of period 1 and period 2, electricity generation of wind power facility would rise from  $16.4 \times 10^3$  GW in period 1 to  $16.8 \times 10^3$  GW in period 2; and with another capacity expansion of 0.2 GW at the beginning of period 3, its total electricity generation capacity would reach  $17.2 \times 10^3$  GW. Likewise, to meet the growing energy demand, the capacity of 0.2 GW would be added to the natural gas-fired facility in period 1, period 2, and period 3; as a result, its total generation capacity would rise from  $9.54 \times 10^3$  GW in period 1 to  $11.9 \times 10^3$  GW in period 2 and reach  $12.4 \times 10^3$  GW in period 3. In the planning period 1, due to more lenient emission policies and more economical cost strategies, some of the natural gas power generation facilities are idle. The capacities of 0.25 GW would be added to the hydropower facility in three periods, and the corresponding power generation capacity would be  $8.12 \times 10^3$  GW,  $8.75 \times 10^3$  GW, and  $9.37 \times 10^3$  GW. Generating electricity from solar energy facility is more expensive than other power generation facilities; thus when the emission limits and electricity demand are relatively low, solar energy facility would not be expanded during first two periods. 0.15

TABLE 6: Binary solutions of capacity expansions.

$P_i$ -level	Power-generation facility	Capacity-expansion option	IFCF-PSP			LS		
			t=1	t=2	t=3	t=1	t=2	t=3
0.1	Natural gas	m=1	0	0	0	0	0	0
		m=2	0	0	0	0	0	0
		m=3	1	[0, 1]	[0, 1]	0	0	0
	Wind power	m=1	0	0	0	0	0	0
		m=2	0	[0, 1]	0	0	[0, 1]	1
		m=3	[0, 1]	[0, 1]	[0, 1]	0	0	0
	Solar energy	m=1	0	0	0	0	0	0
		m=2	0	0	0	0	0	0
		m=3	0	0	0	0	0	0
Hydropower	m=1	[0, 1]	[0, 1]	0	0	0	[0, 1]	
	m=2	0	0	0	0	0	0	
	m=3	[0, 1]	[0, 1]	0	[0, 1]	[0, 1]	0	
0.05	Natural gas	m=1	0	0	0	0	0	0
		m=2	0	0	0	0	0	0
		m=3	[0, 1]	[0, 1]	[0, 1]	0	0	0
	Wind power	m=1	[0, 1]	[0, 1]	0	0	0	0
		m=2	0	0	0	0	[0, 1]	1
		m=3	[0, 1]	[0, 1]	0	0	0	0
	Solar energy	m=1	0	0	0	0	0	0
		m=2	0	0	0	0	0	0
		m=3	0	0	0	0	0	0
Hydropower	m=1	0	0	0	0	[0, 1]	[0, 1]	
	m=2	0	0	0	0	0	0	
	m=3	1	1	0	[0, 1]	[0, 1]	0	
0.01	Natural gas	m=1	0	0	0	0	0	0
		m=2	0	0	0	0	0	0
		m=3	1	1	1	[0, 1]	[0, 1]	[0, 1]
	Wind power	m=1	0	0	0	0	0	0
		m=2	0	0	0	0	0	[0, 1]
		m=3	1	1	[0, 1]	[0, 1]	[0, 1]	[0, 1]
	Solar energy	m=1	0	0	0	0	0	0
		m=2	0	0	[0, 1]	0	0	0
		m=3	0	0	0	0	0	0
Hydropower	m=1	0	0	0	0	[0, 1]	0	
	m=2	0	0	0	0	0	0	
	m=3	1	1	[0, 1]	[0, 1]	[0, 1]	[0, 1]	

GW of capacity would only be added to the solar energy facility in period 3.

Apparently, with the successful application of IFCI-PSP within a typical regional electric system management problem, solutions obtained could provide useful decision alternatives under different policies and various energy availabilities. Compared with the least-cost model, the IFCF-PSP model is an effective tool for providing environmental management schemes with dual objectives. In addition, the IFCF-PSP has following advantages over the conventional programming methods: (a) balancing multiple conflicting

objectives, (b) reflecting interrelationships among system efficiency, economic cost, and system reliability (c) effectively dealing with randomness in both the objective and constraints, and (d) assisting the analysis of diverse decision schemes associated with various energy demand levels.

### 5. Conclusions

An inexact fuzzy chance-constrained fractional programming approach is developed for optimal electric power systems management under uncertainties. In the developed

model, fuzzy chance-constrained programming is incorporated into a fractional programming optimization framework. The obtained results are useful for supporting EPS management. The IFCF-PSP approach is capable of (i) balancing the conflict between two objectives; (ii) reflecting different electricity generation and capacity expansion strategies; (iii) presenting optimal solutions under different constraint violating conditions; and (iv) introducing the concept of fuzzy boundary interval, with which the complexity of dual uncertainties can be effectively handled. The results of IFCF-PSP model show that (i) a higher confidence level corresponds to a higher proportion of clean energy power generation and a lower economic productivity, and (ii) as a result of encouraging environment-friendly energies, the generation capacities for the natural gas, wind-power, solar energy, and hydropower facilities would be significantly increased. The solutions obtained from the IFCF-PSP approach could provide specific energy options for power system planning and provide effective management solution of the electric power system for identifying electricity generation and capacity expansion schemes.

This study attempts to develop a modeling framework for ratio problems involving fuzzy uncertainties to deal with electric power systems management problem. The results suggest that it is also applicable to other energy management problems. In the future practice, IFCF-PSP could be further improved through considering more impact factors. For instance, the fuzzy membership functions and the confidence level are critical in the decision-making process, and this requires effective ways to provide appropriate choices for decision making. Such challenges desire further investigations. Future research can be aimed at applying the advanced approach to a more complex real-world electric power system.

### Data Availability

The data used to support the findings of this study are available from the corresponding author upon request.

### Conflicts of Interest

The authors declare that they have no conflicts of interest.

### Acknowledgments

This research was supported by the Fundamental Research Funds for the Central Universities, NCEPU (2018BJ0293), the State Scholarship Fund (201706735025), the National Key Research and Development Plan (2016YFC0502800), the Natural Sciences Foundation (51520105013, 51679087), and the III Program (B14008). The data used to support the findings of this study are available from the corresponding author upon request.

### References

- [1] G. H. Huang, "A hybrid inexact-stochastic water management model," *European Journal of Operational Research*, vol. 107, no. 1, pp. 137–158, 1998.
- [2] A. Grosfeld-Nir and A. Tishler, "A stochastic model for the measurement of electricity outage costs," *Energy*, pp. 157–174, 1993.
- [3] S. Wang, G. Huang, and B. W. Baetz, "An Inexact Probabilistic-Possibilistic Optimization Framework for Flood Management in a Hybrid Uncertain Environment," *IEEE Transactions on Fuzzy Systems*, vol. 23, no. 4, pp. 897–908, 2015.
- [4] G. H. Huang and D. P. Loucks, "An inexact two-stage stochastic programming model for water resources management under uncertainty," *Civil Engineering and Environmental Systems*, vol. 17, no. 2, pp. 95–118, 2000.
- [5] K. Darby-Dowman, S. Barker, E. Audsley, and D. Parsons, "A two-stage stochastic programming with recourse model for determining robust planting plans in horticulture," *Journal of the Operational Research Society*, vol. 51, no. 1, pp. 83–89, 2000.
- [6] J. Hu, L. Sun, C. H. Li, X. Wang, X. L. Jia, and Y. P. Cai, "Water Quality Risk Assessment for the Laoguanhe River of China Using a Stochastic Simulation Method," *Journal of Environmental Informatics*, vol. 31, no. 2, pp. 123–136, 2018.
- [7] S. Wang and G. H. Huang, "A multi-level Taguchi-factorial two-stage stochastic programming approach for characterization of parameter uncertainties and their interactions: An application to water resources management," *European Journal of Operational Research*, vol. 240, no. 2, pp. 572–581, 2015.
- [8] S. Chanas and P. Zieliński, "On the equivalence of two optimization methods for fuzzy linear programming problems," *European Journal of Operational Research*, vol. 121, no. 1, pp. 56–63, 2000.
- [9] J. Mula, D. Peidro, and R. Poler, "The effectiveness of a fuzzy mathematical programming approach for supply chain production planning with fuzzy demand," *International Journal of Production Economics*, vol. 128, no. 1, pp. 136–143, 2010.
- [10] B. Chen, P. Li, H. J. Wu, T. Husain, and F. Khan, "MCFP: A monte carlo simulation-based fuzzy programming approach for optimization under dual uncertainties of possibility and continuous probability," *Journal of Environmental Informatics (JEI)*, vol. 29, no. 2, pp. 88–97, 2017.
- [11] C. Z. Huang, S. Nie, L. Guo, and Y. R. Fan, "Inexact fuzzy stochastic chance constraint programming for emergency evacuation in Qinshan nuclear power plant under uncertainty," *Journal of Environmental Informatics (JEI)*, vol. 30, no. 1, pp. 63–78, 2017.
- [12] U. S. Sakalli, "Optimization of Production-Distribution Problem in Supply Chain Management under Stochastic and Fuzzy Uncertainties," *Mathematical Problems in Engineering*, vol. 2017, Article ID 4389064, 29 pages, 2017.
- [13] A. Charnes and W. W. Cooper, "Programming with linear fractional functionals," *Naval research logistics (NRL)*, pp. 181–186, 1962.
- [14] N. I. Voropai and E. Y. Ivanova, "Multi-criteria decision analysis techniques in electric power system expansion planning," *International Journal of Electrical Power & Energy Systems*, vol. 24, no. 1, pp. 71–78, 2002.
- [15] M. Chakraborty and S. Gupta, "Fuzzy mathematical programming for multi objective linear fractional programming problem," *Fuzzy Sets and Systems*, vol. 125, no. 3, pp. 335–342, 2002.
- [16] Y. Deng, "A threat assessment model under uncertain environment," *Mathematical Problems in Engineering*, vol. 2015, Article ID 878024, 12 pages, 2015.
- [17] W. Li, Z. Bao, G. H. Huang, and Y. L. Xie, "An Inexact Credibility Chance-Constrained Integer Programming for Greenhouse

- Gas Mitigation Management in Regional Electric Power System under Uncertainty,” in *Journal of Environmental Informatics*, 2017.
- [18] M. Paunovic, N. M. Ralevic, V. Gajovic et al., “Two-Stage Fuzzy Logic Model for Cloud Service Supplier Selection and Evaluation,” *Mathematical Problems in Engineering*, 2018.
- [19] S. Wang, G. H. Huang, B. W. Baetz, and B. C. Ancell, “Towards robust quantification and reduction of uncertainty in hydrologic predictions: Integration of particle Markov chain Monte Carlo and factorial polynomial chaos expansion,” *Journal of Hydrology*, vol. 548, pp. 484–497, 2017.
- [20] S. Wang, B. C. Ancell, G. H. Huang, and B. W. Baetz, “Improving Robustness of Hydrologic Ensemble Predictions Through Probabilistic Pre- and Post-Processing in Sequential Data Assimilation,” *Water Resources Research*, 2018.
- [21] M. G. Iskander, “A suggested approach for possibility and necessity dominance indices in stochastic fuzzy linear programming,” *Applied Mathematics Letters*, vol. 18, no. 4, pp. 395–399, 2005.
- [22] A. Rong and R. Lahdelma, “Fuzzy chance constrained linear programming model for optimizing the scrap charge in steel production,” *European Journal of Operational Research*, vol. 186, no. 3, pp. 953–964, 2008.
- [23] X. Sun, J. Li, H. Qiao, and B. Zhang, “Energy implications of China’s regional development: New insights from multi-regional input-output analysis,” *Applied Energy*, vol. 196, pp. 118–131, 2017.
- [24] M. A. Quaddus and T. N. Goh, “Electric power generation expansion: Planning with multiple objectives,” *Applied Energy*, vol. 19, no. 4, pp. 301–319, 1985.
- [25] C. H. Antunes, A. G. Martins, and I. S. Brito, “A multiple objective mixed integer linear programming model for power generation expansion planning,” *Energy*, vol. 29, no. 4, pp. 613–627, 2004.
- [26] J. L. C. Meza, M. B. Yildirim, and A. S. M. Masud, “A model for the multiperiod multiobjective power generation expansion problem,” *IEEE Transactions on Power Systems*, vol. 22, no. 2, pp. 871–878, 2007.
- [27] J.-H. Han, Y.-C. Ahn, and I.-B. Lee, “A multi-objective optimization model for sustainable electricity generation and CO<sub>2</sub> mitigation (EGCM) infrastructure design considering economic profit and financial risk,” *Applied Energy*, vol. 95, pp. 186–195, 2012.
- [28] M. Rezik, A. Abdelkafi, and L. Krichen, “A micro-grid ensuring multi-objective control strategy of a power electrical system for quality improvement,” *Energy*, vol. 88, pp. 351–363, 2015.
- [29] A. Azadeh, Z. Raoofi, and M. Zarrin, “A multi-objective fuzzy linear programming model for optimization of natural gas supply chain through a greenhouse gas reduction approach,” *Journal of Natural Gas Science and Engineering*, vol. 26, pp. 702–710, 2015.
- [30] K. Li, L. Pan, W. Xue, H. Jiang, and H. Mao, “Multi-objective optimization for energy performance improvement of residential buildings: a comparative study,” *Energies*, vol. 10, no. 2, p. 245, 2017.
- [31] H. Zhu, W. W. Huang, and G. H. Huang, “Planning of regional energy systems: An inexact mixed-integer fractional programming model,” *Applied Energy*, vol. 113, pp. 500–514, 2014.
- [32] F. Chen, G. H. Huang, Y. R. Fan, and R. F. Liao, “A nonlinear fractional programming approach for environmental-economic power dispatch,” *International Journal of Electrical Power & Energy Systems*, vol. 78, pp. 463–469, 2016.
- [33] C. Zhang and P. Guo, “FLFP: A fuzzy linear fractional programming approach with double-sided fuzziness for optimal irrigation water allocation,” *Agricultural Water Management*, vol. 199, pp. 105–119, 2018.
- [34] L. Wang, G. Huang, X. Wang, and H. Zhu, “Risk-based electric power system planning for climate change mitigation through multi-stage joint-probabilistic left-hand-side chance-constrained fractional programming: A Canadian case study,” *Renewable & Sustainable Energy Reviews*, vol. 82, pp. 1056–1067, 2018.
- [35] D. Dubois and H. Prade, “Operations on fuzzy numbers,” *International Journal of Systems Science*, vol. 9, no. 6, pp. 613–626, 1978.
- [36] X. H. Nie, G. H. Huang, Y. P. Li, and L. Liu, “IFRP: A hybrid interval-parameter fuzzy robust programming approach for waste management planning under uncertainty,” *Journal of Environmental Management*, vol. 84, no. 1, pp. 1–11, 2007.
- [37] Y. Leung, *Spatial analysis and planning under imprecision*, Elsevier, 1st edition, 2013.
- [38] A. Charnes, W. W. Cooper, and M. J. L. Kirby, “Chance-constrained programming: an extension of statistical method,” in *Optimizing methods in statistics*, pp. 391–402, Academic Press, 1971.
- [39] Y. P. Cai, G. H. Huang, Z. F. Yang, and Q. Tan, “Identification of optimal strategies for energy management systems planning under multiple uncertainties,” *Applied Energy*, vol. 86, no. 4, pp. 480–495, 2009.

## Research Article

# Planning of Electric Power Systems Considering Virtual Power Plants with Dispatchable Loads Included: An Inexact Two-Stage Stochastic Linear Programming Model

Changyu Zhou,<sup>1</sup> Guohe Huang ,<sup>2</sup> and Jiapei Chen<sup>3</sup>

<sup>1</sup>School of Control and Computer Engineering, North China Electric Power University, Beijing 102206, China

<sup>2</sup>Institute for Energy, Environment and Sustainability Research, UR-NCEPU, North China Electric Power University, Beijing 102206, China

<sup>3</sup>Institute for Energy, Environment and Sustainable Communities, UR-BNU, 3737 Wascana Parkway, Regina, SK, Canada S4S 0A2

Correspondence should be addressed to Guohe Huang; [huang@iseis.org](mailto:huang@iseis.org)

Received 14 April 2018; Revised 2 July 2018; Accepted 25 July 2018; Published 30 August 2018

Academic Editor: Paolo Manfredi

Copyright © 2018 Changyu Zhou et al. This is an open access article distributed under the Creative Commons Attribution License, which permits unrestricted use, distribution, and reproduction in any medium, provided the original work is properly cited.

In this study, an inexact two-stage stochastic linear programming (ITSLP) method is proposed for supporting sustainable management of electric power system under uncertainties. Methods of interval-parameter programming and two-stage stochastic programming were incorporated to tackle uncertainties expressed as interval values and probability distributions. The dispatchable loads are integrated into the framework of the virtual power plants, and the support vector regression technique is applied to the prediction of electricity demand. For demonstrating the effectiveness of the developed approach, ITSLP is applied to a case study of a typical planning problem of power system considering virtual power plants. The results indicate that reasonable solutions for virtual power plant management practice have been generated, which can provide strategies in mitigating pollutant emissions, reducing system costs, and improving the reliability of power supply. ITSLP is more reliable for the risk-averse planners in handling high-variability conditions by considering peak-electricity demand and the associated recourse costs attributed to the stochastic event. The solutions will help decision makers generate alternatives in the event of the insufficient power supply and offer insight into the tradeoffs between economic and environmental objectives.

## 1. Introduction

Due to the shortage of fossil fuel and the resulting of environmental pollution problems from energy combustion, renewable energy power generation has caught worldwide attention. However, there are many challenges in the processes of environment-friendly power systems planning. The availabilities of renewable energy resources highly rely on natural and meteorological conditions, which may further intensify the complexity of the decision-making process. Many technologies and measures have been proposed to solve the instability of renewable energy power generation. Among them, virtual power plants (VPPs) is proposed as an innovative technology of the power system, and it can effectively integrate, aggregate, and manage both conventional and renewable energy power plants to achieve rational power

allocation with limited and changeable resource availabilities [1–6]. VPPs refers to heterogeneous power plants, which usually include renewable energy power plants, traditional fossil-fuel-fired power plants, energy storage facilities, and dispatchable loads (shown in Figure 1). Through the coordination of the VPPs, the impact of fluctuations in renewable energy generation can be abated. Previously, there were few studies focused on the optimization model of power systems with consideration of VPPs with dispatchable loads. Furthermore, many economic, environmental, and political factors dynamically affect system planning processes, resulting in uncertainties in some key system parameters (e.g., renewable energy availability, load demands, and energy prices). These uncertainties and their latent interactions might further intensify the complexity of the decision-making process. Previous research on VPPs rarely considered these uncertainties.

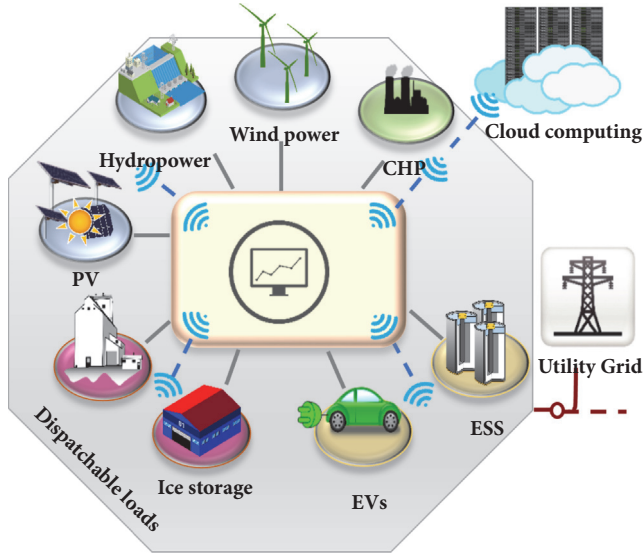


FIGURE 1: The composition of heterogeneous VPPs. Note. PVs: photovoltaic units; ESS: energy storage system; DLs: dispatchable loads; EVs: electric vehicles; CHP: combined heat and power.

Therefore, efficient mathematical programming techniques for planning electric power systems with consideration of uncertainties and complexities are desired.

Optimization techniques have played an important role in helping decision makers manage planning problems in an effective and efficient way [7–13]. In past decades, a multitude of optimization methods were proposed for dealing with electric power systems management problems. In these research work, some techniques were used to handle various uncertainties existing in the electric power systems. Among these techniques, stochastic programming (SP) have received extensive attention since they could directly integrate uncertain information expressed as probability distributions into the optimization framework. For example, Cai et al. [14] proposed an inexact chance-constrained community-scale energy model for long-term renewable energy management. Li et al. [15] developed an interval-parameter credibility constrained programming model for the electric power system planning and greenhouse gas (GHG) emission mitigation. Koltsaklis and Georgiadis [16] developed a stochastic multi-regional multiperiod mixed-integer linear programming approach for Greek generation expansion planning.

Some limitation of the conventional SP methods is that they are incapable of considering the variability of the recourse values since it is assumed that the decision maker is risk neutral. However, the decision maker might be risk-averse under high-variability conditions. In fact, electric power systems are often associated with various system-failure risks (e.g., renewable energy supply risk) due to multiple uncertainties and unpredictable events. Desired energy allocation patterns might vary from time to time under high-variability conditions. Such unstable power supply might result in a high risk of electricity shortage, particularly when electricity demand-level is high. Two-stage stochastic programming (TSP) can take corrective actions

after a random event occurs. In TSP, a first-stage decision is made before the occurrence of a random event, and then a second-stage decision can be made after the random events have happened. This could minimize losses that may appear due to any system failure [17–19]. However, TSP method could merely deal with uncertainties described in one single format. It has difficulties in addressing uncertainties existing in multiple levels, especially when knowledge is insufficient to obtain probability distributions. Interval programming (IP) can reflect interval information in the coefficients of the objective function and constraints, without knowing distribution information [20, 21]. Interval solutions can also be obtained in objective function and decision variables, which is helpful for decision makers to interpret and adjust decision schemes according to practical situations. Thus, TSP and IP can be integrated to enhance the capability of addressing multiple uncertainties in power system planning with VPPs.

Therefore, the objective of this study is to develop an inexact two-stage stochastic linear programming model for planning the electric power system including VPPs in a hybrid uncertain environment. ITSLP-VPP will integrate two-stage stochastic programming and interval-parameter programming in an energy system planning framework with consideration of virtual power plants. Results will provide the following decision support: (a) reflecting uncertain interactions among multiple random variables and disclosing their impacts on system outputs; (b) achieving tradeoffs between environmental conservation and system costs; (c) evaluating the economic impacts and CO<sub>2</sub> emission mitigation benefits of the energy scheme alternatives due to the introduction of VPPs.

This paper is organized as follows. Section 2 presents the development of ITSLP-VPP model. Section 3 introduces the basic structure of VPP and describes case studies and simulation results of electric power systems considering VPPs, where solutions under the different scenarios and uncertainty analysis are analyzed. Section 4 presents conclusions and future works.

## 2. Model Development

**2.1. Interval Two-Stage Stochastic Linear Programming.** Two-stage stochastic programming model can reflect the tradeoffs between pre-regulated policy and the associated economic penalty due to any infeasible event, and the fundamental concept includes recourse and adaptive adjustments. A general TSP model can be formulated as follows:

$$\min f = C^T X + E_{\omega \in \Omega} [Q(X, \omega)] \quad (1a)$$

subject to

$$AX \geq B \quad (1b)$$

$$X \geq 0 \quad (1c)$$

where  $C$  is the vector of coefficients;  $X$  is the first-stage decision variable;  $\omega$  is the random variable;  $E[\bullet]$  is the expected value of the random variable; and the inequalities

(1b) and (1c) are constraints of the model, where  $A$  and  $B$  are technical coefficient.  $Q(X, \omega)$  can be written as follows:

$$Q(X, \omega) = \min q(Y, \omega) \quad (1d)$$

$$D(\omega) y \geq h(\omega) + T(\omega) x \quad (1e)$$

$$\begin{aligned} x &\in X, \\ y &\in Y \end{aligned} \quad (1f)$$

where  $Y$  is the second-stage decision variable;  $q(Y, \omega)$  denotes the second-stage cost function; and  $\{D(\omega), T(\omega), h(\omega) \mid \omega \in \Omega\}$  are random model parameters corresponding to their dimensions; they are the functions of the random variable  $\omega$ . By letting random variables (i.e.,  $\omega$ ) take discrete values  $\omega_h$  with probability levels  $p_h$  ( $h = 1, 2, \dots, v$  and  $\sum p_h = 1$ ), Model (1a), (1b), (1c), (1d), (1e), and (1f) can be equivalently formulated as a linear programming model [22, 23].

$$\min f = C^T X + \sum_{h=1}^v p_h D^T Y \quad (2a)$$

subject to

$$A_r X \geq B_r, \quad r = 1, 2, \dots, m_1 \quad (2b)$$

$$A_t X + A'_t Y \geq \omega_h, \quad t = 1, 2, \dots, m_2 \quad (2c)$$

$$\begin{aligned} x_j &\geq 0, \\ x_j &\in X, \end{aligned} \quad (2d)$$

$$j = 1, 2, \dots, n_1$$

$$\begin{aligned} y_{jh} &\geq 0, \\ y_{jh} &\in Y, \end{aligned} \quad (2e)$$

$$j = 1, 2, \dots, n_2, \quad h = 1, 2, \dots, v$$

where  $r$  is the number of general constraints and  $t$  is the number of constraints associated with the random variables.

Model (2a), (2b), (2c), (2d), and (2e) can effectively reflect uncertainties in resources (such as solar energy and wind energy) availability. An extended consideration is for uncertainties in the other parameters. For example, some economic data may not be available as deterministic values. In many practical problems, the quality of information that can be obtained for these uncertainties is mostly not good enough to be presented as probability distributions. Interval-parameter linear programming is efficient in coping with uncertain information expressed as interval numbers with known lower and upper bounds but unknown distribution functions. Based on the above consideration, interval parameters are introduced into the TSP framework to communicate uncertainties in technical coefficients into the optimization process. This leads to a hybrid inexact TSP (or ITSLP) model as follows:

$$\min f^\pm = C_{T_1}^\pm X + \sum_{h=1}^v p_h D_{T_2}^\pm Y^\pm \quad (3a)$$

subject to

$$A_r^\pm X^\pm \geq B_r^\pm, \quad r = 1, 2, \dots, m_1 \quad (3b)$$

$$A_t^\pm X^\pm + A'_t{}^\pm Y^\pm \geq \omega_h^\pm, \quad t = 1, 2, \dots, m_2 \quad (3c)$$

$$\begin{aligned} x_j^\pm &\geq 0, \\ x_j^\pm &\in X^\pm, \end{aligned} \quad (3d)$$

$$j = 1, 2, \dots, n_1$$

$$\begin{aligned} y_{jh}^\pm &\geq 0, \\ y_{jh}^\pm &\in Y^\pm, \end{aligned} \quad (3e)$$

$$j = 1, 2, \dots, n_2, \quad h = 1, 2, \dots, v.$$

Model (3a), (3b), (3c), (3d), and (3e) can be transformed into two deterministic submodels that correspond to the lower and upper bounds of desired objective function value. This transformation process is based on an interactive algorithm, which is different from the best/worst case analysis [24, 25]. The submodel corresponding to the lower bound  $f^-$  should be first solved when the objective function is to minimize  $f^\pm$  and can be formulated as follows:

$$\begin{aligned} \min f^- &= \sum_{j=1}^{k_1} c_j^- x_j^- + \sum_{j=k_1+1}^{n_1} c_j^- x_j^+ + \sum_{j=1}^{k_2} \sum_{h=1}^v p_h d_j^- y_{jh}^- \\ &+ \sum_{j=k_2+1}^{n_2} \sum_{h=1}^v p_h d_j^- y_{jh}^+ \end{aligned} \quad (4a)$$

subject to

$$\sum_{j=1}^{k_1} |a_{rj}^\pm|^+ \text{sign}(a_{rj}^\pm) x_j^- \quad (4b)$$

$$+ \sum_{j=k_1+1}^{n_1} |a_{rj}^\pm|^- \text{sign}(a_{rj}^\pm) x_j^+ \leq b_r^-, \quad \forall r$$

$$\begin{aligned} \sum_{j=1}^{k_1} |a_{tj}^\pm|^+ \text{sign}(a_{tj}^\pm) x_j^- + \sum_{j=k_1+1}^{n_1} |a_{tj}^\pm|^- \text{sign}(a_{tj}^\pm) x_j^+ \\ + \sum_{j=1}^{k_2} |a_{tj}^\pm|^+ \text{sign}(a_{tj}^\pm) y_{jh}^- \end{aligned} \quad (4c)$$

$$+ \sum_{j=k_2+1}^{n_2} |a_{tj}^\pm|^- \text{sign}(a_{tj}^\pm) y_{jh}^+ \leq \omega_h^-, \quad \forall t, h$$

$$x_j^- \geq 0, \quad j = 1, 2, \dots, k_1 \quad (4d)$$

$$x_j^+ \geq 0, \quad j = k_1 + 1, k_1 + 2, \dots, n_1 \quad (4e)$$

$$y_{jh}^- \geq 0, \quad j = 1, 2, \dots, k_2; \quad \forall h \quad (4f)$$

$$y_{jh}^+ \geq 0, \quad j = k_2 + 1, k_2 + 2, \dots, n_2; \quad \forall h. \quad (4g)$$

Based on the above solutions, the second submodel for  $f^+$  can be formulated as follows:

$$\begin{aligned} \min f^+ = & \sum_{j=1}^{k_1} c_j^+ x_j^+ + \sum_{j=k_1+1}^{n_1} c_j^+ x_j^- + \sum_{j=1}^{k_2} \sum_{h=1}^v p_h d_j^+ y_{jh}^+ \\ & + \sum_{j=k_2+1}^{n_2} \sum_{h=1}^v p_h d_j^+ y_{jh}^- \end{aligned} \quad (5a)$$

subject to

$$\begin{aligned} \sum_{j=1}^{k_1} |a_{rj}^{\pm}|^- \text{sign}(a_{rj}^{\pm}) x_j^+ + \sum_{j=k_1+1}^{n_1} |a_{rj}^{\pm}|^+ \text{sign}(a_{rj}^{\pm}) x_j^- \\ \leq b_r^+, \quad \forall r \end{aligned} \quad (5b)$$

$$\begin{aligned} \sum_{j=1}^{k_1} |a_{tj}^{\pm}|^- \text{sign}(a_{tj}^{\pm}) x_j^+ + \sum_{j=k_1+1}^{n_1} |a_{tj}^{\pm}|^+ \text{sign}(a_{tj}^{\pm}) x_j^- \\ + \sum_{j=1}^{k_2} |a_{tj}^{\pm}|^- \text{sign}(a_{tj}^{\pm}) y_{jh}^+ \end{aligned} \quad (5c)$$

$$+ \sum_{j=k_2+1}^{n_2} |a_{tj}^{\pm}|^+ \text{sign}(a_{tj}^{\pm}) y_{jh}^- \leq \omega_h^+, \quad \forall t, h$$

$$x_j^+ \geq x_{jopt}^-, \quad j = 1, 2, \dots, k_1 \quad (5d)$$

$$x_{jopt}^+ \geq x_j^- \geq 0, \quad j = k_1 + 1, k_1 + 2, \dots, n_1 \quad (5e)$$

$$y_{jh}^+ \geq y_{jhopt}^-, \quad j = 1, 2, \dots, k_2; \quad \forall h \quad (5f)$$

$$y_{jhopt}^+ \geq y_{jh}^- \geq 0, \quad j = k_2 + 1, k_2 + 2, \dots, n_2; \quad \forall h. \quad (5g)$$

Therefore, the following solutions for the ITSLP Model (3a), (3b), (3c), (3d), and (3e) can be obtained:

$$f_{opt}^{\pm} = [f_{opt}^-, f_{opt}^+] \quad (6a)$$

$$x_{jopt}^{\pm} = [x_{jopt}^-, x_{jopt}^+] \quad (6b)$$

$$y_{jhopt}^{\pm} = [y_{jhopt}^-, y_{jhopt}^+]. \quad (6c)$$

**2.2. Development of ITSLP-VPP Model.** The decision makers are responsible for allocating electricity-supply patterns, capacity expansions, and pollutant mitigation with a minimum system cost over a mid-term planning horizon. Five types of electricity-conversion facilities are considered,

namely, coal-fired and natural gas-fired plants, photovoltaic power, hydropower station, and wind power farm. In order to tackle such multiple formats of uncertainties in electric power systems considering virtual power plants, interval linear programming and two-stage stochastic programming methods are incorporated within a general planning model, leading to an inexact two-stage stochastic linear programming model. The objective of the model is to minimize the system cost, while a set of constraints are formulated to define the relationships among the system factors/conditions and decision variables. The ITSLP-VPP can be formulated as follows:

$$\min f^{\pm} = \min (f_1^{\pm} + f_2^{\pm} + f_3^{\pm} + f_4^{\pm}). \quad (7a)$$

The system cost includes the cost for energy resource purchase, the cost for electricity generation from conventional power plants and VPPs, and the cost for pollutant treatment. Due to the intermittent and unreliability of renewable energy power generation, the actual generation deviates from the planned generation. When random events occur, the dispatchable loads (such as large-scale ice storage, hot-spring facilities, and energy storage system) can be used as an important part of regulating power generation deviations. Therefore, deviation economic costs and the compensation costs of the dispatchable loads are included in the cost of power generation as the cost of the second-stage. In detail, the system cost is a sum of the following items:

(1) *The Total Cost for Purchasing Primary Energy*

$$f_1^{\pm} = \sum_{t=1}^3 \sum_{k=1}^2 AER_{t,k}^{\pm} \times CER_{t,k}^{\pm} \quad (7b)$$

(2) *Fixed and Variable Generation Costs for Conventional Power Plants*

$$\begin{aligned} f_2^{\pm} = & \sum_{t=1}^3 \sum_{s=1}^4 \sum_{d=1}^4 \sum_{i=1}^2 AEG_{t,s,d,i}^{\pm} \times CVG_{t,i}^{\pm} + \sum_{t=1}^3 \sum_{i=1}^2 CFM_{t,i}^{\pm} \\ & \times ICA_{t,i}^{\pm} \end{aligned} \quad (7c)$$

(3) *Generation and Operating Costs of the VPPs*

$$f_3^{\pm} = f_{3,1}^{\pm} + f_{3,2}^{\pm} \quad (7d)$$

where

$$f_{3,1}^{\pm} = \sum_{t=1}^3 \sum_{s=1}^4 \sum_{d=1}^4 \sum_{j=1}^3 AR_{t,s,d,j}^{\pm} \times CAR_{t,j}^{\pm} \quad (7e)$$

$$\begin{aligned} f_{3,2}^{\pm} = & \sum_{t=1}^3 \sum_{s=1}^4 \sum_{d=1}^4 (E[GE_{t,s,d}^{(\omega)\pm}] \times CR_{t,s,d}^{\pm}) \\ = & \sum_{t=1}^3 \sum_{s=1}^4 \sum_{d=1}^4 \left( \sum_{m=1}^3 P_m (GEW_{t,s,d}^{(\omega)\pm} \times CRW_{t,s,d}^{\pm} + GES_{t,s,d}^{(\omega)\pm} \times CRS_{t,s,d}^{\pm} + GEH_{t,s,d}^{(\omega)\pm} \times CRH_{t,s,d}^{\pm} + ACS_{t,s,d}^{(\omega)\pm} \times CCS_{t,s,d}^{\pm}) \right) \end{aligned} \quad (7f)$$

## (4) Pollutants Emission Costs

$$f_4^\pm = \sum_{t=1}^3 \sum_{s=1}^4 \sum_{d=1}^4 \sum_{i=1}^2 AEG_{t,s,d,i}^\pm \times cf_{t,i}^\pm \times \eta_{t,i}^\pm \times CCR_{t,i}^\pm \quad (7g)$$

subject to the following.

## (1) Electricity Demand Constraints

$$\begin{aligned} & \sum_{s=1}^4 \sum_{d=1}^4 \sum_{i=1}^2 AEG_{t,s,d,i}^\pm + \sum_{s=1}^4 \sum_{d=1}^4 \sum_{j=1}^3 AR_{t,s,d,j}^\pm \\ & \geq DM_t^\pm \times (1 + \theta_t^\pm), \quad \forall t \end{aligned} \quad (7h)$$

## (2) Capacity Limitation Constraint for Power Generation Facilities

$$\sum_{s=1}^4 \sum_{d=1}^4 \sum_{i=1}^2 AEG_{t,s,d,i}^\pm \leq \sum_{i=1}^2 ICA_{t,i} \times STM_{t,i}^\pm, \quad \forall t \quad (7i)$$

 (3) CO<sub>2</sub> Emission Constraints

$$\sum_{s=1}^4 \sum_{d=1}^4 \sum_{i=1}^2 AEG_{t,s,d,i}^\pm \times cf_{t,i}^\pm \times (1 - \eta_{t,i}^\pm) \leq EM_t, \quad \forall t \quad (7j)$$

## (4) Electricity Peak-Load Demand Constraints

$$\begin{aligned} & \sum_{i=1}^2 AEG_{t,s,d,i}^\pm + \sum_{j=1}^3 AR_{t,s,d,j}^\pm - GES_{t,s,d,m}^{(\omega)\pm} - GEW_{t,s,d,m}^{(\omega)\pm} \\ & - GEH_{t,s,d,m}^{(\omega)\pm} \geq PLOAD_{t,s,d}^\pm - ACS_{t,s,d,m}^{(\omega)\pm}, \end{aligned} \quad (7k)$$

$\forall t, s, d$

## (5) Renewable Energy Availability Constraints

$$\begin{aligned} & \sum_{d=1}^4 \left( AR_{t,s,d,1}^\pm + GEW_{t,s,d,m}^{(\omega)\pm} + GEH_{t,s,d,m}^{(\omega)\pm} - ACS_{t,s,d,m}^{(\omega)\pm} \right) \\ & \leq AVS_{t,s,m}^{(\omega)\pm}, \quad \forall t, s, m \end{aligned} \quad (7l)$$

Electricity generated from solar energy equal to or less than its total availability

$$\begin{aligned} & \sum_{d=1}^4 \left( AR_{t,s,d,2}^\pm + GES_{t,s,d,m}^{(\omega)\pm} + GEH_{t,s,d,m}^{(\omega)\pm} - ACS_{t,s,d,m}^{(\omega)\pm} \right) \\ & \leq AVW_{t,s,m}^{(\omega)\pm}, \quad \forall t, s, m \end{aligned} \quad (7m)$$

Electricity generated from wind energy equal to or less than its total availability

$$\begin{aligned} & \sum_{d=1}^4 \left( AR_{t,s,d,3}^\pm + GES_{t,s,d,m}^{(\omega)\pm} + GEW_{t,s,d,m}^{(\omega)\pm} - ACS_{t,s,d,m}^{(\omega)\pm} \right) \\ & \leq AVH_{t,s,m}^{(\omega)\pm}, \quad \forall t, s, m \end{aligned} \quad (7n)$$

Electricity generated from hydropower equal to or less than its total availability

## (6) Dispatchable Loads Regulation Constraints

$$\sum_{d=1}^4 ACS_{t,s,d,m}^\pm \leq \sum_{d=1}^4 \left( \frac{QCS_{t,s,d}^\pm}{COP_{t,s,d}^\pm} \right) \times ST_{t,s}^\pm \times TOR_{t,s}^\pm, \quad (7o)$$

$\forall t, s, m$

## (7) Electricity Deficiency Equal to or Less Than the Predefined Targets

$$\begin{aligned} & GES_{t,s,d,m}^{(\omega)\pm} + GEW_{t,s,d,m}^{(\omega)\pm} + GEH_{t,s,d,m}^{(\omega)\pm} + ACS_{t,s,d,m}^{(\omega)\pm} \\ & \leq \sum_{j=1}^3 AR_{t,s,d,j}^\pm, \quad \forall t, s, d, m \end{aligned} \quad (7p)$$

## (8) Primary Energy Sources Availability Constraints

$$AER_{t,k}^\pm \leq UP_{t,k}, \quad \forall t, k \quad (7q)$$

$$\sum_{s=1}^4 \sum_{d=1}^4 AEG_{t,s,d,i}^\pm \times rf_{t,i}^\pm \leq AER_{t,k}^\pm, \quad \forall t, i \quad (7r)$$

## (9) Nonnegativity Constraints

$$\begin{aligned} & AEG_{t,s,d,i}^\pm, ACS_{t,s,d,m}^{(\omega)\pm}, AER_{t,k}^\pm, GES_{t,s,d,m}^{(\omega)\pm}, GEH_{t,s,d,m}^{(\omega)\pm}, \\ & GEW_{t,s,d,m}^{(\omega)\pm} \geq 0 \end{aligned} \quad (7s)$$

The specific nomenclatures for variables and parameters are provided in Nomenclature. All the decision variables in the ITSLP-VPP model are considered as interval values.

The annual electricity demand forecast is an important part of power system planning, which is influenced by economic and social uncertainties. Support vector regression (SVR) can be applied to the prediction problem in the case of finite samples. Thus, SVR can be used for predicting electricity demand.

$$DM_t = \sum_{i=1}^k (\alpha_i^* - \alpha_i) K(x_i, x) + b^* \quad (8)$$

where  $\alpha_i^*$ ,  $\alpha_i$  are the Lagrangian multipliers.  $K(x_i, x)$  is called the kernel function, whose value equals the inner product of two vectors (such as  $x_i$  and  $x$ ) in the feature space.  $b^*$  is constant. SVM aims to minimize the empirical risk. Selecting and determining the parameters of the kernel function require knowledge based on the application domain and reflect the distribution of the input training data as much as possible. There are many kernel functions commonly used, such as polynomial kernel function, Gaussian radial basis function (RBF), kernel function, and the Sigmoid kernel function. RBF kernel is easier to implement and able to nonlinearly map the training data into an infinite

dimensional space, and it is suitable to deal with nonlinear relationship problems. Thus, this study used RBF kernel to predict the electricity demand, radial basis function (RBF) with a width of  $\sigma$  :  $K(x_i, x_j) = \exp(-\|x_i - x_j\|^2 / 2\sigma^2)$ . SVR generalization performance depends on a good setting of regularization constant  $C$ , precision parameter  $\varepsilon$ , and the kernel parameters  $\sigma$  [26]. In this study, the optimal values of parameters  $C$ ,  $\varepsilon$ , and  $\sigma$  are determined by employing a grid-search in a  $n$ -fold cross-validation approach which can prevent the overfitting problem [27, 28]. The mean absolute percent error (MAPE) is a commonly used forecasting error metric for quantifying and assessing the accuracy of the predicted output values. Meanwhile, the average relative error strengthens the function of the large error term in the indicator. Therefore, this study adopts the average relative error as the judgment basis of each prediction result. Three kinds of accuracy criteria (i.e., prediction accuracy: PA, Fitting accuracy: FA, and overall accuracy: OA) were used to assess the performance of the SVR model [26, 29, 30].

$$PA = 1 - \frac{\sum_{t=n+1}^{n+m} |(y_t - \hat{y}_t) / y_t|}{m} \times 100\% \quad (9a)$$

$$FA = 1 - \frac{\sum_{t=1}^n |(y_t - \hat{y}_t) / y_t|}{n} \times 100\% \quad (9b)$$

$$OA = 1 - \frac{\sum_{t=1}^{n+m} |(y_t - \hat{y}_t) / y_t|}{n + m} \times 100\% \quad (9c)$$

$PA$  is used to compare actual electricity consumption values and predicted electricity consumption values during the test period.  $FA$  is used to compare the actual electricity consumption values and the predicted electricity consumption values of all the training points time periods.  $OA$  is used to compare actual electricity consumption values and to predict electricity consumption values over all time periods, including training and testing time periods.

### 3. Case Study and Result Analysis

To demonstrate its advantages, the proposed ITSLP-VPP method is applied to a case study of a typical regional electric power systems management problem with representative cost and technical data within a Chinese context.

**3.1. Overview of the Study System.** Renewable energy (e.g., hydro, wind, and solar) is naturally replenished and much more sustainable and cleaner in contrast with fossil fuels. Nevertheless, wind and solar power could not provide continuous power supply to end-users without backup power generation facilities or energy storage, due to intermittence of input energy, instability of weather condition, and flaw of technical restriction. Large-scale ice storage (LIS), freezers in supermarkets, or refrigerators and freezers in private homes can be viewed as storage electrical power facilities that store electricity in cold form. Hot-spring convalescent facilities using cogeneration systems store electricity in hot form, and electric cars in cities can also be used as energy storage devices in the Smart Grid. These facilities all have sponge-like properties; they can play a role of energy storage when

the power load is at a low point (i.e., the generating capacity is higher than the load), absorbing and storing electricity, and when the load is at a peak period (i.e., the generating capacity is less than the load); it is like energy storage device that begins to release electricity, such as ice storage; even if the power is cut off, the temperature drop is very slow, in a certain temperature and time range, and will not lead to the deterioration of the quality of storage goods. When the wind power is strong, solar energy is abundant, and electricity market price is low, the smart control system can start the ice storage or reduce the set temperature of refrigerated in operation, to store a certain amount of electricity in 'cold' form. In the period of electricity shortage, lack of wind or solar energy, and high price in the electricity market, smart system can suspend the operation of ice storage, run the frequency converter, or increase the set temperature, to reduce the power consumption and play the role of peak-load shifting. Therefore, this study combines the LIS and renewable energy power plants to form virtual power plants. In the power shortage periods, the VPPs in some special areas can play an active role in regulation, such as areas having high reliance on renewable energy sources and port cities that have numerous LIS bases.

For each power-conversion technology, an electricity-generation target is preplanned. If the target is not exceeded, the system will encounter the regular costs; otherwise, the system will be subject to costs for the extra operation and maintenance, or the compensation costs of the dispatchable loads. The problems under consideration include (1) how to achieve the minimized total system cost with potential low carbon emissions, (2) how to assign scientific electricity-generation schemes, (3) how to deal with the uncertainties and random information existing in both the objective and constraints, and (4) how to identify the effective scheme of the dispatchable loads in the virtual power plant to achieve potential low carbon emissions and low system cost. A variety of uncertainties exist in these problems, increasing the complexity of the decision-making process. ITSLP-VPP is considered to be a promising approach for dealing with this electric power system management problem.

**3.2. Data Collection and Result Analysis.** Table 1 contains part of attributes for SVR prediction. The increasing power consumption in cities can be attributed to industrial development, economic improvement, and population growth. The first, second, and tertiary industry and industrial products are the main factors determining the use of electricity. Gross domestic product (GDP) is a broad parameter that reveals the prosperity of the urban economy, which provides a quantitative indicator of the average living standard, indicating the capacity to produce and consume electricity. We refer to the historical data of an administrative area and establish the analog input data of the model. Table 2 provides the costs for electricity generation expressed as interval values.

Figure 2 presents the observation, prediction, and error of electricity demand of the administrative district. Three kinds of accuracy criteria (i.e., PA, FA, and OA) were used to assess the performance of the SVR model, and the SVR parameters can be searched by the grid-search method. When the values

TABLE 1: The attributes for SVR prediction.

GDP (10 <sup>2</sup> million \$)	Primary industry (10 <sup>2</sup> million \$)	Secondary industry	Tertiary industry	Industry	Electricity consumption (10 <sup>2</sup> GWh)
42.82	2.79	23.82	16.2	21.50	67.24
78.19	3.39	39.69	35.12	36.11	70.97
88.17	3.62	44.06	40.49	39.93	75.14
98.81	3.87	49.12	45.83	44.49	84.30
118.44	4.13	61.44	52.88	55.95	93.90
142.92	4.84	77.45	60.63	71.19	105.29
179.43	5.16	98.09	76.18	89.95	115.45
205.03	4.75	112.88	87.40	103.90	130.10
241.32	5.06	132.89	103.37	122.29	148.41
308.68	5.63	170.44	132.62	157.07	154.77
345.57	5.92	183.21	156.44	166.41	165.05
423.79	6.69	222.37	194.73	202.64	193.72
519.48	7.34	272.36	239.78	249.50	208.55
592.37	7.88	306.15	278.34	281.30	222.96
663.49	8.66	335.75	319.09	307.19	238.34
722.52	9.18	355.22	358.12	325.23	247.18
759.79	9.59	353.95	396.26	320.80	255.34

TABLE 2: Cost for power generation.

	Period 1	Period 2	Period 3
Cost for purchasing fossil fuels (10 <sup>3</sup> \$/TJ)			
Coal	[0.32,0.38]	[0.30,0.36]	[0.28,0.34]
Natural gas	[0.35,0.42]	[0.33,0.40]	[0.31,0.38]
Variable cost for power generation (10 <sup>3</sup> \$/GWh)			
Coal	[1.62, 1.87]	[1.54,1.78]	[1.46,1.69]
Natural gas	[2.19,2.52]	[2.08,2.39]	[1.98,2.27]
Solar	[4.90,5.10]	[4.66,4.84]	[4.42,4.60]
Wind	[8.64,9.19]	[8.21,8.68]	[7.8,8.19]
Hydro	[6.58,7.80]	[6.25,7.41]	[5.94,7.03]

of the parameters  $C$ ,  $\epsilon$ , and  $\sigma$  are  $2^7$ ,  $2^{-7}$ , and 1.0 respectively, the PA, FA, and OA values of the SVR model are 95.42%, 91.36%, and 93.53%, respectively, and the predicted results are satisfactory. The predicting values of electricity demand are 263.34, 274.69, and 286.04 (10<sup>2</sup> GWh) from 2017 to 2019.  $p^-$  is prediction  $-\epsilon$ .  $p^+$  is prediction  $+\epsilon$ . The forecast results are used to set the interval of electricity demand. Figure 3 shows the power generation of various generating technologies in the three study periods (corresponding to  $f^-$ ). Over the planning horizon, the coal-fired power supply would gradually decline, but due to its high availability and competitive price, it still plays an important role in the power system. For example, during the spring, when  $d=1$ , the total coal-fired generation would be 1307,1166.82, and 1102 GWh in three periods, respectively. Likewise, the results during other times and seasons can be analyzed similarly to those. Renewable energy generation steadily increases during the planning periods. For instance, when  $d=1$ , wind power generation over the four seasons would be 360, 408.67, and 466.13 GWh in spring;

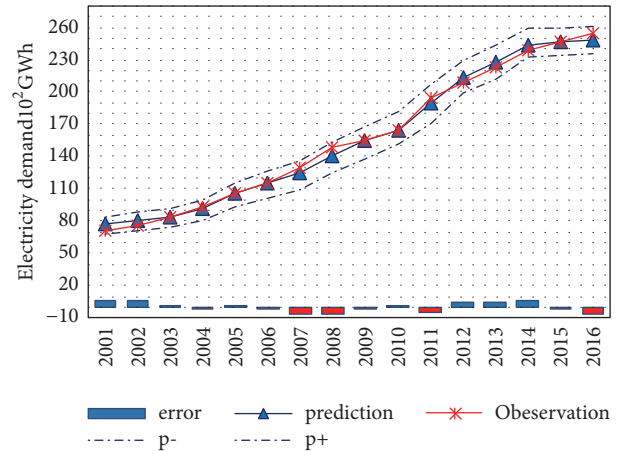


FIGURE 2: Comparison of the prediction and actual value with a SVR model.

396, 447.55, and 497.3 GWh in summer; 396, 447.55, and 508.9 GWh in autumn; and 396, 447.55, and 508.9 in winter, respectively. Similarly, the obtained results of other power generation technologies can be interpreted. In addition, the power consumption of businesses and residents has changed a lot in 24 hours a day. The overall average load during summer high demand period and peak demand period was 29.36% higher than that in the general period. It would lead to the increase of electricity supply during high demand period and peak demand period (i.e.,  $d=3$ ,  $d=4$ ). For example, hydropower supply in period 3 would rise from 84.17 GWh when  $d=3$  to 148.32 GWh when  $d=4$ , which would be higher than 41.33 GWh when  $d=1$  and 40.03 GWh when  $d=2$ . Moreover, renewable energy generation in the summer is

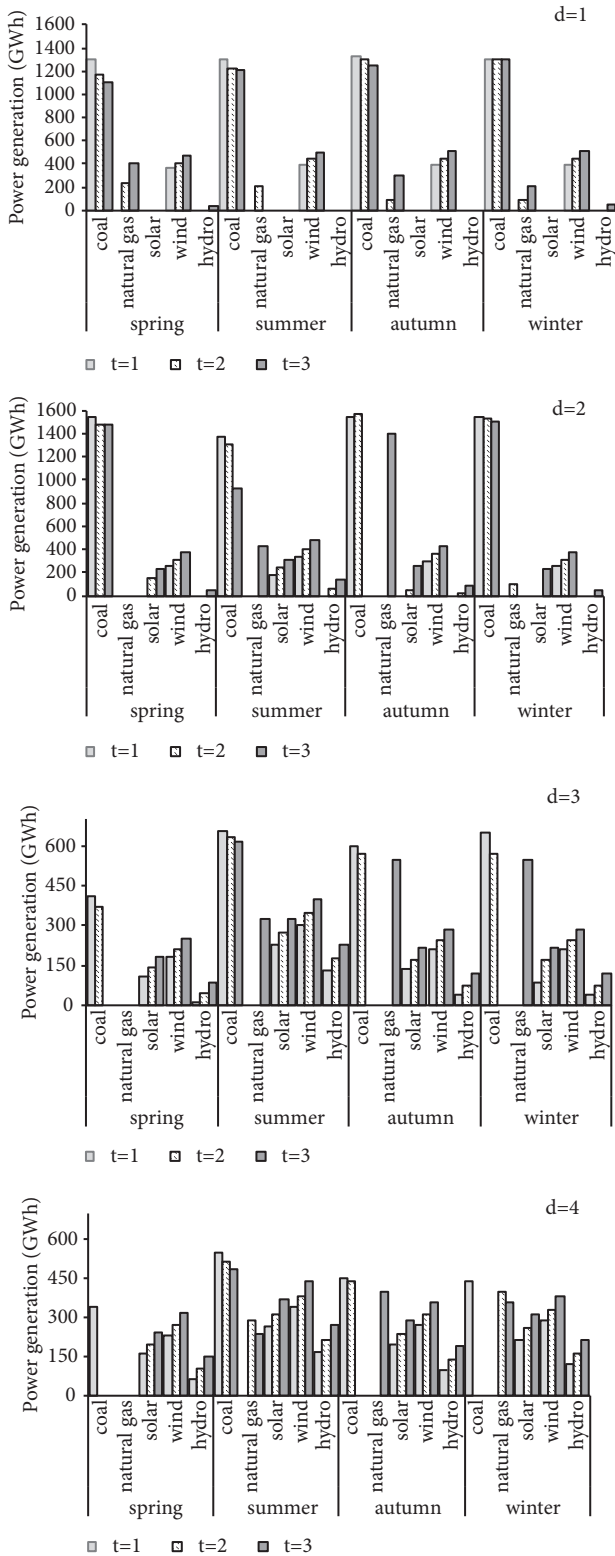


FIGURE 3: Power generation of various generating technologies in different periods ( $f$ ).

higher than other seasons. This is related to the climate of the area corresponding to the reference data. Therefore, renewable energy generation arrangements have increased.

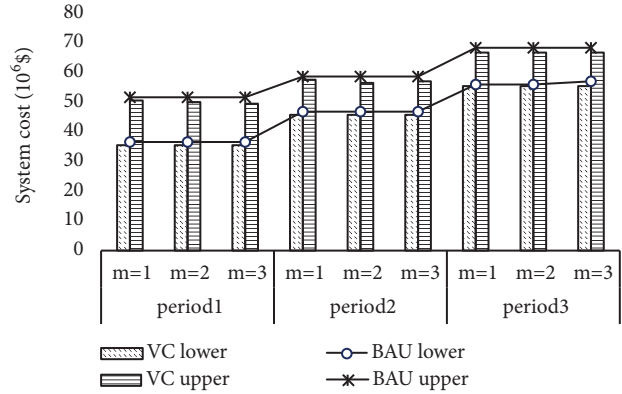


FIGURE 4: Comparison of expected costs between two scenarios. Note. BAU: business as usual; VC: VPP case.

On the other hand, with the decline of thermal power, in three planning periods, renewable energy generation proportion gradually increased, accounting for the total generation of 32.73%, 40.78%, and 42.67%.

Table 3 shows the dispatchable loads regulation amount under different renewable energy availability levels. The high, medium, and low resource availability levels correspond to  $m=1$ ,  $m=2$ , and  $m=3$ , respectively. During different seasons, when the electricity-generation pattern varies under different  $m$  levels and within interval solution ranges, the dispatchable loads regulation amount would also fluctuate within its solution range correspondingly, which would be  $[0.43, 58.08]$  GWh. The results show that the VPP's adjustable electricity is quite different at different times of different seasons. For example, when  $d = 4$ , the dispatchable load in VPP is only regulated in winter (50.16 GWh). This is because, unlike other seasons, the outdoor temperature in winter is low, and even if a part of the power of refrigeration equipment of LIS is cut off, the temperature drop would be very slow. The operation of the refrigeration equipment can be more flexibly started or stopped in a temperature range where the quality of stored goods does not deteriorate. Therefore, the dispatchable loads can play a considerable role in regulation during various time periods in winter. In comparison, the impact of the availability of renewable energy on the amount of regulation of controllable loads is less pronounced than that of seasons and time periods. For instance, during spring 1st time period, the amounts of electricity regulation are almost the same under the three  $m$  levels, which would be  $[47.38, 58.08]$ ,  $[47.38, 58.08]$ , and  $[47.38, 50.16]$  GWh, respectively. Nevertheless, when the availabilities of renewable energy resources are insufficient to meet the energy demand, the LIS in VPP can play a positive regulatory role. The maximum ratio of LIS regulation to power generation shortage during the three planning periods is 94.16%, the minimum is 15.01%, and the average is 39.13%.

Figure 4 compares the system cost corresponding to BAU (business as usual, i.e., no dispatchable loads being included) and VC (VPP case) scenarios over the planning horizon. The power generation cost of the VC scenario is slightly lower than that of BAU. The system costs obtained from

TABLE 3: Dispatchable loads adjusting quantity.

Time	Period	p=1	p=2	p=3
<b>Spring</b>				
1	t=1	[47.38,58.08]	[47.38,58.08]	[47.38,50.16]
	t=2	[0,47.38]	[0,47.38]	[0,47.38]
	t=3	[0.43,20]	[0,0.43]	[0,0.43]
2	t=1	[0,50.16]	[0,50.16]	[0,50.16]
	t=2	[0,58.08]	[0,58.08]	[0,58.08]
	t=3	[27.38,57.65]	[38.08,57.65]	[13.85,57.65]
3	t=1	[0,57.65]	[0,57.65]	[0,57.65]
	t=2	0	0	0
	t=3	0	0	0
4	t=1	0	0	0
	t=2	0	0	0
	t=3	0	0	0
<b>Summer</b>				
1	t=1	[0,58.08]	[47.38,58.08]	0
	t=2	[0,58.08]	[0,58.08]	[47.38,58.08]
	t=3	[0,43.2]	[43.2,47.38]	[0,43.2]
2	t=1	[0,47.38]	0	[0,47.38]
	t=2	[0,47.38]	[0,47.38]	0
	t=3	[0,14.88]	[0,14.88]	[14.88,43.76]
3	t=1	[0,58.08]	[0,58.08]	[0,58.08]
	t=2	[0,58.08]	[0,58.08]	[0,58.08]
	t=3	[0,47.38]	0	0
4	t=1	0	0	0
	t=2	0	0	0
	t=3	0	0	0
<b>Autumn</b>				
1	t=1	0	0	0
	t=2	[0,22.36]	0	0
	t=3	[0,20]	0	0
2	t=1	[47.38,49.84]	47.38,49.84]	47.38,49.84]
	t=2	[25.02,58.08]	[47.38,58.08]	[47.38,58.08]
	t=3	[0,27.38]	[0,47.38]	[0,47.38]
3	t=1	[0,58.08]	[0,58.08]	[0,58.08]
	t=2	0	0	0
	t=3	[0,58.08]	[0,58.08]	[0,58.08]
4	t=1	0	0	0
	t=2	0	0	0
	t=3	0	0	0
<b>Winter</b>				
1	t=1	[47.38,58.08]	[47.38,58.08]	[0,47.38]
	t=2	[47.38,58.08]	[47.38,58.08]	[0,47.38]
	t=3	0	0	[0,20]
2	t=1	0	0	[0,58.08]
	t=2	0	0	[0,58.08]
	t=3	[0,7.38]	[0,47.38]	[27.38,58.08]
3	t=1	0	0	0
	t=2	0	0	0
	t=3	[0,40]	0	0
4	t=1	0	0	0
	t=2	[0,50.16]	[0,50.16]	[0,50.16]
	t=3	0	0	0

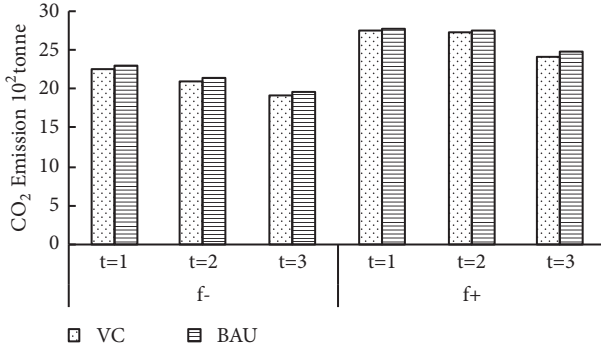


FIGURE 5: Carbon dioxide emissions in different scenarios.

these two scenarios would both increase with the planning period changes. For example, under VC scenario, when  $p=3$ , the total system cost for the three planning periods would be  $[35.41, 49.48]$ ,  $[45.47, 56.67]$ , and  $[55.41, 66.63] \times 10^6$  \$, respectively. The solution results are lower than the system costs obtained for the BAU scenario, which are  $[36.41, 51.34]$ ,  $[46.47, 58.42]$ , and  $[56.96, 68.34] \times 10^6$  \$, respectively. Similarly, the results under other  $m$  levels ( $m=1$  and  $m=2$ ) can be interpreted. In the optimal scheme of interval solution, the system cost of the VC scenario would be decreased at least by 1.98% lower than the BAU scenario, the highest is 3.63%, and the average decrease is 2.34%. The cost decline is not obvious because the scale of the dispatchable loads in the case is limited. With the development of energy Internet technology, the increase of the proportion of dispatchable loads is expected to bring more cost reduction space for the electric power system.

Figure 5 shows a comparison of carbon dioxide emissions conventional from conventional power generation scenario and from dispatchable loads as alternative scenarios in VPP. In detail, the BAU scenario leads to slightly higher CO<sub>2</sub> emissions than the VC scenario under all levels. The CO<sub>2</sub> emissions from BAU scenario are  $[23.13, 27.84] \times 10^6$  ton in period 1,  $[21.38, 27.65] \times 10^6$  ton in period 2, and  $[19.53, 24.84] \times 10^6$  ton in period 3. In comparison, the VC scenario would lead to the lower CO<sub>2</sub> emissions ( $[22.47, 27.65]$ ,  $[20.93, 27.34]$ ,  $[19.07, 24.23] \times 10^6$  ton, respectively). When the availabilities of renewable energy resources are limited, more electricity would be generated from conventional facilities, leading to higher CO<sub>2</sub> emissions. In comparison, the dispatchable loads in VPP can adjust its own electricity demand during these periods, shift to other time periods, and therefore lead to less CO<sub>2</sub> emissions. In addition, increasingly stringent emission limits would lead to a drop in overall emissions levels. For example, under VC scenario (corresponding to  $f^-$ ), the CO<sub>2</sub> emissions would decrease from 22.47  $10^6$  ton in period 1 to 20.93  $10^6$  ton in period 2 and reach 19.07  $10^6$  ton in period 3. The VC scenario may be of more interest to decision makers due to its lower system cost and CO<sub>2</sub> emissions.

The solutions obtained from the above two cases (BAU and VC) could provide useful decision alternatives under different policies and various energy availabilities. Compared with the BAU model, the ITSLP-VPP model could be

an effective tool for providing environmental management schemes under various system conditions.

## 4. Conclusions

An inexact two-stage stochastic linear programming approach is developed for optimal electric power systems management with VPP under uncertainties. In the developed model, two-stage stochastic programming is incorporated into a two-stage programming optimization framework. The obtained results are useful for supporting electric power system management. The ITSLP-VPP approach is capable of (a) adjustment or justification of allocation patterns of renewable energy resources and services; (b) evaluation of the impact of intermittency of the renewable energy on the power system management; (c) decision support of local policies on energy use, economic development, and energy structures; (d) analysis of the interaction between economic costs, system reliability, and energy supply shortages.

This study attempts to develop a modeling framework for optimization problems involving uncertainties to deal with the electric power systems management problem with VPP. In the future practice, the proposed method could be further improved through considering more impact factors, for instance, the stability of the smart composite system, the peak-shaving risk caused by the uncertainty of the forecast of wind power and PV power generation, the effect of price-based policy and the incentive policy on the flexible response of VPP, and the integration of energy storage facilities.

## Nomenclature

- $t$ : Period (1 year for each period,  $t=1,2,3$ )
- $i$ : Resource type, including coal and natural gas ( $i=1,2$ )
- $j$ : Renewable energy generation type, including Solar, wind power, and hydro ( $j=1,2,3$ )
- $s$ : Season, namely, spring, summer, autumn, or winter ( $s=1,2,3,4$ )
- $m$ : The availability level of renewable energy ( $m=1$  high,  $m=2$  medium, and  $m=3$  low.)
- $d$ : Time (where  $d=1$  for the trough period, a total of 8 hours (23:00-7:00);  $d=2$  for the general period, 8 hours (7:00-8:00 and 11:00-18:00);  $d=3$  (8:00-10:00, 18:00-19:00, and 21:00-23:00);  $d=4$  (10:00-11:00 and 19:00-21:00), respectively, the high demand period and peak demand period, 4 hours)
- $AER_{t,k}^{\pm}$ : The supply of fossil fuels  $k$  for the generation in period  $t$  (TJ)
- $AEG_{t,s,d,i}^{\pm}$ : Electricity-generation amount via electricity-generation technology  $i$  in period  $t$  season  $s$  time  $d$

$AR_{t,s,d}^{\pm}$ :	The target for electricity generation from renewable energy $j$ under season $s$ time $d$ period $t$ that is determined at the first stage, which is the first-stage decision variable (GWh)	$GEW_{t,s,d}$ :	The amount of wind energy by which the target of $AR$ is not met in period $t$ (GWh)
$ACS_{t,s,d}^{\pm}$ :	The amount of the dispatchable loads (GWh)	$GEH_{t,s,d}$ :	The amount of hydropower by which the target of $AR$ is not met in period $t$ (GWh)
$AVH_{t,s,m}$ :	Availability of hydropower in period $t$ season $s$ under probability level $m$ (GWh)	$ICA_{t,i}^{\pm}$ :	The current capacity of power generation technology $i$ in period $t$ (GW)
$AVS_{t,s,m}$ :	Availability of photovoltaic power in period $t$ season $s$ under probability level $m$ (GWh)	$PLOAD_{t,s,d}^{\pm}$ :	Peak-load electricity demand (GWh)
$AVW_{t,s,d}$ :	Availability of wind power in period $t$ season $s$ under probability level $m$ (GWh)	$QCS_{t,s,d}^{\pm}$ :	Cooling capacity of ice storage during period $d$ of the typical day in season $s$ (BTU/h)
$CER_{t,k}^{\pm}$ :	Cost of purchasing primary energy $k$ in period $t$ ( $10^3$ \$/TJ)	$STM_{t,i}^{\pm}$ :	Maximum service time of electricity-generation technology $i$ in period $t$ (hour)
$CVG_{t,i}^{\pm}$ :	Variable cost for generating electricity via electricity-generation technology $i$ in period $t$ ( $10^3$ \$/GWh)	$ST_{t,s}^{\pm}$ :	Average running time of ice storage
$CFM_{t,i}^{\pm}$ :	Fixed cost for generating electricity via electricity-generation technology $i$ in period $t$ ( $10^3$ \$/GWh)	$TOR_{t,s}^{\pm}$ :	Maximum tolerated cooling deficiency rate
$CAR_{t,j}^{\pm}$ :	Average cost for renewable energy $j$ electricity production when energy is sufficient ( $10^3$ \$/GWh)	$UP_{t,k}$ :	Available resource $k$ in period $t$
$CR_{t,s,d}^{\pm}$ :	Average recourse cost for the shortage of electricity production ( $10^3$ \$/GWh)	$cf_{t,i}^{\pm}$ :	Carbon dioxide emission coefficient
$CRS_{t,s,d}^{\pm}$ :	Average recourse cost for the shortage of electricity production from solar energy ( $10^3$ \$/GWh)	$\eta_{t,i}^{\pm}$ :	$CO_2$ emission factor in period $t$ ( $10^3$ ton/GWh)
$CRH_{t,s,d}^{\pm}$ :	Average recourse cost for the shortage of electricity production from hydropower ( $10^3$ \$/GWh)	$\theta_t^{\pm}$ :	Transmission loss in period $t$
$CRW_{t,s,d}^{\pm}$ :	Average recourse cost for the shortage of electricity production from wind energy ( $10^3$ \$/GWh)	$rf_{t,i}^{\pm}$ :	Energy consumption rate of electricity-conversion technology $i$
$CCS_{t,s,d}^{\pm}$ :	Compensation cost of dispatchable loads ( $10^3$ \$/GWh)		
$CCR_{t,i}^{\pm}$ :	Cost of pollution mitigation of power generation technology $i$ in period $t$ ( $10^3$ \$/ton)		
$COP_{t,s,d}^{\pm}$ :	Coefficient of performance of ice storage (BTU/GWh)		
$DM_t^{\pm}$ :	Total electricity demand in period $t$ (GWh)		
$EM_t$ :	The maximum permitted $CO_2$ emission in period $t$ ( $10^3$ ton)		
$GE_{t,s,d}^{\pm}$ :	The amount of renewable energy by which the target of $AR$ is not met in period $t$ , which is the second-stage decision variable (GWh)		
$GES_{t,s,d}$ :	The amount of solar energy by which the target of $AR$ is not met in period $t$ (GWh)		

## Data Availability

The data used to support the findings of this study are available from the corresponding author upon request.

## Conflicts of Interest

The authors declare that they have no conflicts of interest.

## Acknowledgments

This research was supported by the Fundamental Research Funds for the Central Universities, NCEPU (JB2017042), the State Scholarship Fund (201706735025), the National Key Research and Development Plan (2016YFC0502800), the Natural Sciences Foundation (51520105013, 51679087), and the III Program (B14008).

## References

- [1] M. Rekik, Z. Chtourou, N. Mitton, and A. Atieh, "Geographic routing protocol for the deployment of virtual power plant within the smart grid," *Sustainable Cities and Society*, vol. 25, pp. 39–48, 2016.
- [2] S. M. Nosratabadi, R.-A. Hooshmand, and E. Gholipour, "Stochastic profit-based scheduling of industrial virtual power plant using the best demand response strategy," *Applied Energy*, vol. 164, pp. 590–606, 2016.
- [3] M. Loßner, D. Böttger, and T. Bruckner, "Economic assessment of virtual power plants in the German energy market — A scenario-based and model-supported analysis," *Energy Economics*, vol. 62, pp. 125–138, 2017.

- [4] Y. Li, W. Gao, and Y. Ruan, "Feasibility of virtual power plants (VPPs) and its efficiency assessment through benefiting both the supply and demand sides in Chongming country, China," *Sustainable Cities and Society*, vol. 35, pp. 544–551, 2017.
- [5] M. Kolenc, P. Nemček, C. Gutsch, N. Suljanović, and M. Zajc, "Performance evaluation of a virtual power plant communication system providing ancillary services," *Electric Power Systems Research*, vol. 149, pp. 46–54, 2017.
- [6] M. M. Othman, Y. G. Hegazy, and A. Y. Abdelaziz, "Electrical energy management in unbalanced distribution networks using virtual power plant concept," *Electric Power Systems Research*, vol. 145, pp. 157–165, 2017.
- [7] Y. Deng, "A threat assessment model under uncertain environment," *Mathematical Problems in Engineering*, vol. 2015, Article ID 878024, 12 pages, 2015.
- [8] U. S. Sakalli, "Optimization of Production-Distribution Problem in Supply Chain Management under Stochastic and Fuzzy Uncertainties," *Mathematical Problems in Engineering*, vol. 2017, Article ID 4389064, 29 pages, 2017.
- [9] C. Z. Huang, S. Nie, L. Guo, and Y. R. Fan, "Inexact fuzzy stochastic chance constraint programming for emergency evacuation in Qinshan nuclear power plant under uncertainty," *Journal of Environmental Informatics (JEI)*, vol. 30, no. 1, pp. 63–78, 2017.
- [10] B. Chen, P. Li, H. J. Wu, T. Husain, and F. Khan, "MCFP: A monte carlo simulation-based fuzzy programming approach for optimization under dual uncertainties of possibility and continuous probability," *Journal of Environmental Informatics (JEI)*, vol. 29, no. 2, pp. 88–97, 2017.
- [11] S. Wang, G. H. Huang, B. W. Baetz, and B. C. Ancell, "Towards robust quantification and reduction of uncertainty in hydrologic predictions: Integration of particle Markov chain Monte Carlo and factorial polynomial chaos expansion," *Journal of Hydrology*, vol. 548, pp. 484–497, 2017.
- [12] S. Wang, B. C. Ancell, G. H. Huang, and B. W. Baetz, "Improving robustness of hydrologic ensemble predictions through probabilistic pre- and post- processing in sequential data assimilation," *Water Resources Research*, vol. 54, pp. 2129–2151, 2018.
- [13] J. Hu, L. Sun, C. H. Li, X. Wang, X. L. Jia, and Y. P. Cai, "Water Quality Risk Assessment for the Laoguanhe River of China Using a Stochastic Simulation," *Method. of Environmental Informatics*, vol. 31, no. 2, pp. 123–136, 2018.
- [14] Y. P. Cai, G. H. Huang, Q. Tan, and Z. F. Yang, "Planning of community-scale renewable energy management systems in a mixed stochastic and fuzzy environment," *Journal of Renewable Energy*, vol. 34, no. 7, pp. 1833–1847, 2009.
- [15] W. Li, Z. Bao, G. H. Huang, and Y. L. Xie, "An Inexact Credibility Chance-Constrained Integer Programming for Greenhouse Gas Mitigation Management," in *Regional Electric Power System under Uncertainty of Environmental Informatics*, 2017.
- [16] N. E. Koltsaklis, P. Liu, and M. C. Georgiadis, "An integrated stochastic multi-regional long-term energy planning model incorporating autonomous power systems and demand response," *Energy*, vol. 82, pp. 865–888, 2015.
- [17] S. Wang, G. Huang, and B. W. Baetz, "An Inexact Probabilistic-Possibilistic Optimization Framework for Flood Management in a Hybrid Uncertain Environment," *IEEE Transactions on Fuzzy Systems*, vol. 23, no. 4, pp. 897–908, 2015.
- [18] C. Zhang and P. Guo, "An inexact CVaR two-stage mixed-integer linear programming approach for agricultural water management under uncertainty considering ecological water requirement," *Ecological Indicators*, 2016.
- [19] M. Paunovic, N. M. Ralevic, V. Gajovic et al., "Two-Stage Fuzzy Logic Model for Cloud Service Supplier Selection and Evaluation," *Mathematical Problems in Engineering*, 2018.
- [20] G. H. Huang, "A hybrid inexact-stochastic water management model," *European Journal of Operational Research*, vol. 107, no. 1, pp. 137–158, 1998.
- [21] Y. Han, Y.-F. Huang, G.-Q. Wang, and I. Maqsood, "A Multi-objective Linear Programming Model with Interval Parameters for Water Resources Allocation in Dalian City," *Water Resources Management*, vol. 25, no. 2, pp. 449–463, 2011.
- [22] S. Ahmed, "Mean-risk objectives in stochastic programming," 2004.
- [23] S. Wang and G. H. Huang, "A multi-level Taguchi-factorial two-stage stochastic programming approach for characterization of parameter uncertainties and their interactions: An application to water resources management," *European Journal of Operational Research*, vol. 240, no. 2, pp. 572–581, 2015.
- [24] G. Huang, B. W. Baetz, and G. G. Patry, "A grey linear programming approach for municipal solid waste management planning under uncertainty," *Civil Engineering Systems*, vol. 9, no. 4, pp. 319–335, 1992.
- [25] Y. R. Fan and G. H. Huang, "A robust two-step method for solving interval linear programming problems within an environmental management context," *Journal of Environmental Informatics (JEI)*, vol. 19, no. 1, pp. 1–9, 2012.
- [26] W.-C. Hong, Y. Dong, L.-Y. Chen, and S.-Y. Wei, "SVR with hybrid chaotic genetic algorithms for tourism demand forecasting," *Applied Soft Computing*, vol. 11, no. 2, pp. 1881–1890, 2011.
- [27] V. Cherkassky and Y. Ma, "Practical selection of SVM parameters and noise estimation for SVM regression," *Neural Networks*, vol. 17, no. 1, pp. 113–126, 2004.
- [28] G.-F. Lin, G.-R. Chen, P.-Y. Huang, and Y.-C. Chou, "Support vector machine-based models for hourly reservoir inflow forecasting during typhoon-warning periods," *Journal of Hydrology*, vol. 372, no. 1–4, pp. 17–29, 2009.
- [29] A. Kulkarni, V. K. Jayaraman, and B. D. Kulkarni, "Support vector classification with parameter tuning assisted by agent-based technique," *Computers & Chemical Engineering*, vol. 28, no. 3, pp. 311–318, 2004.
- [30] A. A. Levis and L. G. Papageorgiou, "Customer demand forecasting via support vector regression analysis," *Chemical Engineering Research and Design*, vol. 83, no. 8 A, pp. 1009–1018, 2005.

## Research Article

# Connectivity Evaluation and Planning of a River-Lake System in East China Based on Graph Theory

Jing Chen <sup>1</sup>, Chenguang Xiao <sup>1</sup>, and Dan Chen <sup>1,2</sup>

<sup>1</sup>Key Laboratory of Efficient Irrigation-Drainage and Agricultural Soil-Water Environment in Southern China (Ministry of Education), College of Water Conservancy and Hydropower Engineering, Hohai University, Nanjing 210098, China

<sup>2</sup>Department of Agricultural and Biological Engineering, The University of Florida, Gainesville, FL 32611, USA

Correspondence should be addressed to Chenguang Xiao; [xiaochenguang@hhu.edu.cn](mailto:xiaochenguang@hhu.edu.cn) and Dan Chen; [23543458@qq.com](mailto:23543458@qq.com)

Received 13 March 2018; Accepted 10 July 2018; Published 18 July 2018

Academic Editor: Xander Wang

Copyright © 2018 Jing Chen et al. This is an open access article distributed under the Creative Commons Attribution License, which permits unrestricted use, distribution, and reproduction in any medium, provided the original work is properly cited.

The connectivity of the stream network plays an important role in water-mediated transport and river environments, which are threatened by the rugged development process in China. In this study, based on graph theory, a connectivity evaluation index system was built, which includes the Edge Connectivity, Edge-Node rate, Connectivity Reliability, and Edge Weight. The new evaluation standard and calculation method of each index is presented. The river-lake system of Fenhu industrial park in Jiangsu China is simplified to an Edge-Node graph and evaluated by the index system as a case study. The results indicate that the river-lake system of the research area has low Edge Connectivity, a high Edge-Node rate, and high reliability in the current connectivity level. In addition, the Edge Weight index of several channels does not satisfy the standard of the Basic Edge Weight. To solve the connectivity problems, specific project plans include broadening the unqualified channel and building canals linked with the low-connectivity lakes. The results show that, after the planning, the connectivity of the stream network in Fenhu industrial park will increase, and the connectivity evaluation index system is useful in the study area.

## 1. Introduction

The interconnection of a stream system is notably important, which ensures that the stream network delivers water, nutrients, and sediment through the basin and accelerates the self-cleaning ability of the system [1]. In recent years, with the rapid social and economic development in China, the rugged developing mode makes some towns or villages have serious water connectivity problems [2]. On one hand, the natural sedimentation, block, and drought retard the flow and cause the water exchange ability to decline. On the other hand, because of the pursuit of high utilization rate of land in the urbanization construction process [3], many rivers were filled or truncated to provide more construction land, which artificially intensifies the disconnected situation of the stream network and causes drainage difficulty, water quality deterioration, poor ecological environment, and many types of water problems [4–6]. Hence, studies about the interconnection of stream systems in China's urbanization process are emerging.

In recent years, the amount of research regarding stream network connectivity from different perspectives has constantly increased. From the hydrology perspective, connectivity refers to the water-mediated transport of matter, energy, and organisms within or between elements of the hydrologic cycle [7, 8]; from the ecology perspective, river-to-lake connectivity plays an important role in water renewal and aquatic habitat diversity [9, 10]; from the dynamics perspective, connectivity is important to the stream flow and runoff response [11]. To improve the hydraulic relationship between rivers and lakes, many engineering and nonengineering measures such as connecting project and hydrologic dispatch are used in China.

Graph theory is a theoretical model that uses an abstract method to represent the mutual relations among the study objects. The graphs in graph theory do not have characteristics such as size, shape, or mass except objects (represented by nodes) and their relations (represented by edges). The Edge-Node structure in the graph theory system is highly

similar to the actual stream network [12]. The rivers in an actual stream network can be simplified to edges, and the lakes and junctions (points where two channels combine into one) can be simplified to nodes [13, 14]. According to the structure characteristic of a stream network and the graph theory method, the stream network can be generalized mathematics [15]. A simplified network can be evaluated by some analysis methods of graph theory, where the connectivity of the stream network can be quantitatively analyzed. Many previous studies examined the stream network analysis using graph theory [16]. Zhao et al. evaluated the connectivity of a channel-beach system using graph theory and provided the Edge Connectivity calculation process [17]. Xu et al. combined graph theory and flow resistance theory, defined a calculation of the Edge Weight, and compared the connectivity before and after channel dredging in Taihu Basin in China [18]; Wang and Xu et al. analyzed the river system connectivity of Wuxi's central urban area based on graph theory and found that the river system had a decreasing trend [19]; Yang extracted the river network in Jiaodong, China, and evaluated its connectivity based on graph theory [20]. Tejedor et al. presented a framework based on the spectral graph theory and constructed vulnerability maps in the river deltas using the framework [21].

However, in previous studies, most researchers used single indicators to analyze the connectivity of stream networks, which introduced many problems caused by the limitations of individual indices. For example, the Edge Connectivity index can reflect the interrelationship of the nodes but cannot reflect the size of the rivers, and the Edge Weight index is the opposite. Nevertheless, different indicators of graph theory are rarely combined to make a comprehensive analysis of stream systems. In addition, little attention has been paid to the connectivity evaluation for river-lake systems (stream networks with numerous lakes) and the specific project guidance after the evaluation.

The objectives of this study are to (1) select a typical stream network with numerous lakes and abstract it based on graph theory, (2) establish a multidimension evaluation method to estimate the interconnectivity level of the river-lake system, and (3) use specific projects to improve the connectivity of the study area. First, we select the river-lake system of Fenhu industrial park in China as the study area and simplify it to an Edge-Node graph. Second, we build a connectivity evaluation index system that includes the Edge Connectivity, Edge-Node rate, Connectivity Reliability, and Edge Weights, and we explain the meaning and evaluation criterion of each index. Finally, we evaluate the connectivity of the river-lake system in Fenhu using the evaluation system and provide specific project planning to solve the connectivity problems.

## 2. Study Area and Methods

**2.1. Study Area.** We use Fenhu industrial park in Jiangsu province, East China, as the research area (Figure 1). Fenhu industrial park belongs to Taihu Basin with an area of 258 km<sup>2</sup> and a population of 250 thousand. It has subtropical monsoon climate with plenty of rainfall and four distinct seasons [22].

The area is located on the flood plain with a ground elevation of 2.20-5.20 m and mostly belongs to polder areas. Because of the natural factors, the water level, flow direction, and velocity of the stream often vary.

The study area has a typical stream network structure in flood plains in China with flat, shallow, and narrow channels, a disordered river-lake system, deficient connectivity between rivers and lakes, serious sedimentation, and low draining capability. In addition, because the area is located in the downstream location of Taihu Lake (China's second largest lake), it is easily threatened by flood disasters. Thus, Fenhu industrial park consists of several polder areas to prevent the inner polder areas from being threatened by flooding. The stream system of each polder area is separated by the dike, sluice, and dam, which make the inner polder area independent from the outside. This setting also introduces many problems such as insufficient flood control and drainage ability, standard-exceeding of water quality, and ecosystem destruction. Because of the relative independence of the inner polder area, in this study, we ignore the inner area and select the outer polder area as the research object (Figure 2).

**2.2. River-Lake System Simplification.** In this study, we focus on the connectivity of the stream network outside the polder area; we only identify and extract the outer rivers and lakes on the map using labels. As shown in Figure 3(a), following the principle of graph theory, we use numbers to represent lakes and junctions and circled numbers to represent rivers.

After identifying the research objects, we simplify the lakes and river junctions to nodes and the rivers to edges. Because the flow direction in the study area often changes with the climate and rainfall, we define the rivers as undirected edges [23]. As shown in Figure 3(b), there is a simplified, undirected stream network graph that reflects the relationship between rivers and lakes. The research below is based on the simplified stream network graph.

**2.3. Connectivity Evaluation Index System.** Many indices in graph theory can evaluate the connectivity, for example, the Edge Connectivity, Edge-Node rate, Actual Ring Formation rate, Network Connection degree, and Edge Weights. Currently, there is no unified and complete evaluation index system to perfectly and synthetically evaluate the connectivity of a stream network. In this paper, based on the principles of comprehensiveness, diversity, and operability, four indices (Edge Connectivity, Edge-Node rate, Connectivity Reliability, and Edge Weights) are set as a connectivity evaluation index system (Table 1). In the system, the indices of Edge Connectivity, Edge-Node rate, and Edge Weights are generally used in the graph theory; the Connectivity Reliability is created in this paper for the first time. Through this connectivity evaluation index system, the connectivity of the stream network can be better evaluated. We will introduce the meaning, calculation, and evaluation standard of each index in this system below.

**2.3.1. Edge Connectivity.** The Edge Connectivity is equal to the minimum number of edges, which must be removed to make an unconnected graph, with notation  $\lambda$ . The Edge

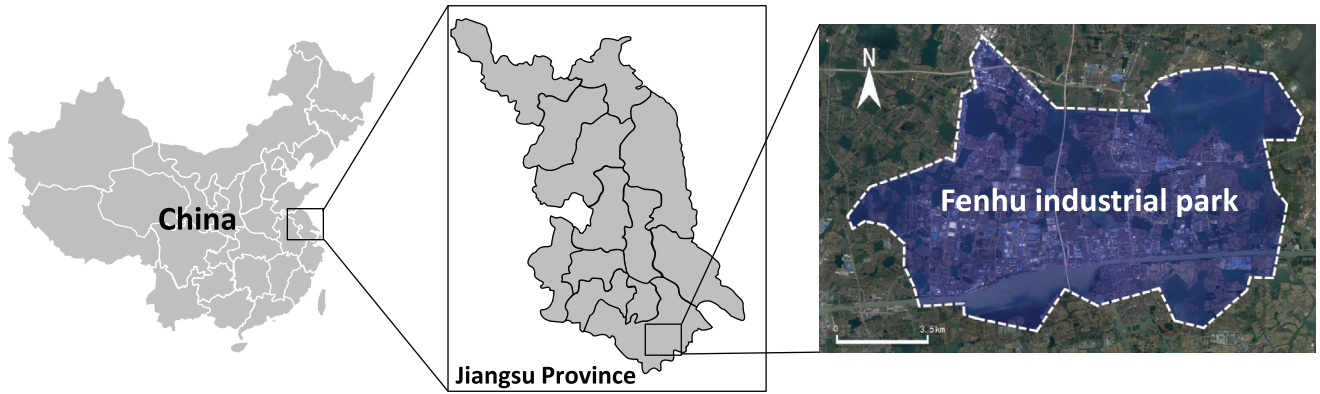


FIGURE 1: Location of the study area in Jiangsu province, East China.

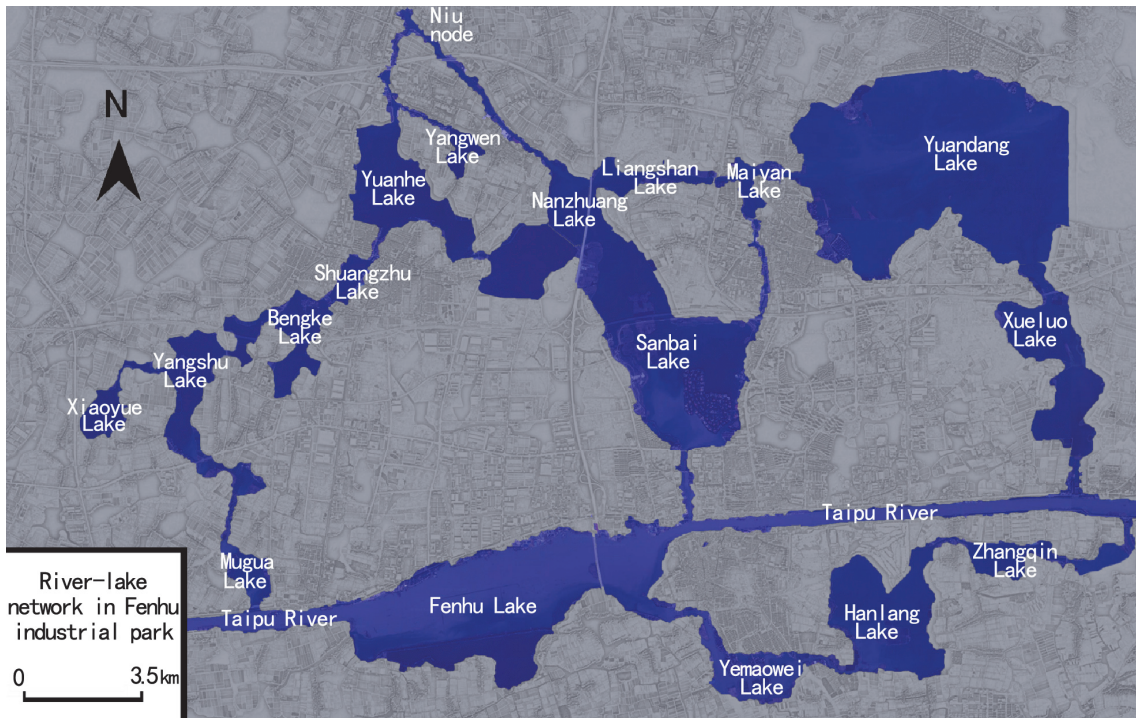


FIGURE 2: River-lake system of Fenhu industrial park; the blue portion is outer polder area.

TABLE 1: Connectivity evaluation index system.

Classification	Index	Meaning	Evaluation content
<b>Determinant index</b>	Edge Connectivity $\lambda$	The minimum number of edges that must be removed to make a graph unconnected.	Evaluate the connectivity of the entire stream network.
	Edge-Node rate $\beta$	Divide the number of rivers by the number of lakes and junctions.	Evaluate the number of rivers that each node occupies.
<b>Evaluative index</b>	Connectivity Reliability $P_\lambda$	The possibility of the Edge Connectivity remains unchanged if one edge is randomly disconnected in a system with Edge Connectivity $\lambda$ .	Evaluate the reliability of a stream network in the current Edge Connectivity level. The range is from 0 to 1
	Edge Weights $A$ ( $m^2$ )	River section.	Evaluate the discharge capacity of rivers.

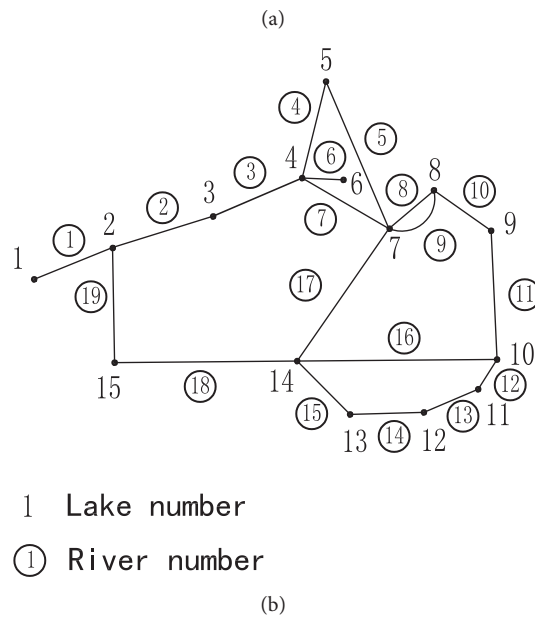
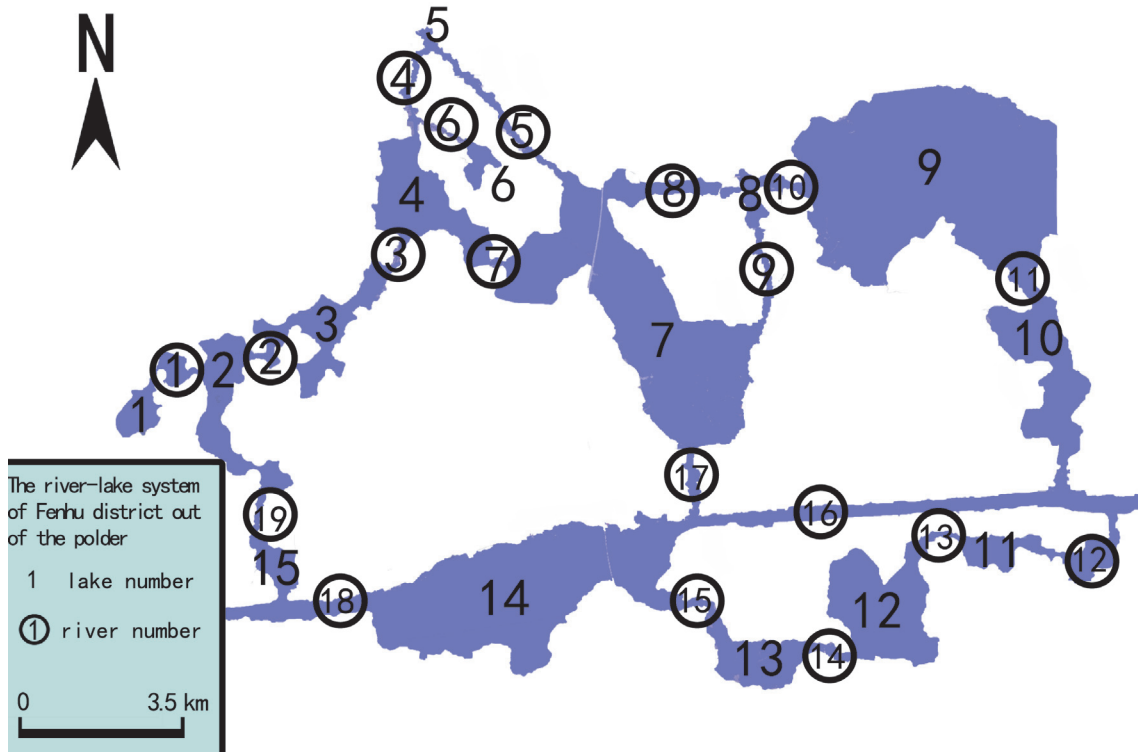


FIGURE 3: (a) River-lake system of the research area outside the polder. (b) Simplified stream network graph of Fenhu industrial park.

Connectivity of an unconnected graph is zero. Graphs with high Edge Connectivity must remove more edges to become an unconnected graph; they have strong connectivity and are difficult to break. In an actual drainage basin, the poor connectivity of a small area always becomes the source of weak flood control ability, deteriorative water quality, and poor ecosystem of the entire basin. The Edge Connectivity index can precisely reflect the extent of the weakest link

area in the stream network and use it to represent the connectivity of the entire system. The Edge Connectivity is the determinant index in an evaluation system, by which we classified the networks.

The unconnected stream networks contain isolated lakes, ponds, or independent small subnetworks (e.g., node  $n_1$  in Figure 4(a)). The connectivity of these parts is notably poor, and they almost cannot have water exchange with one

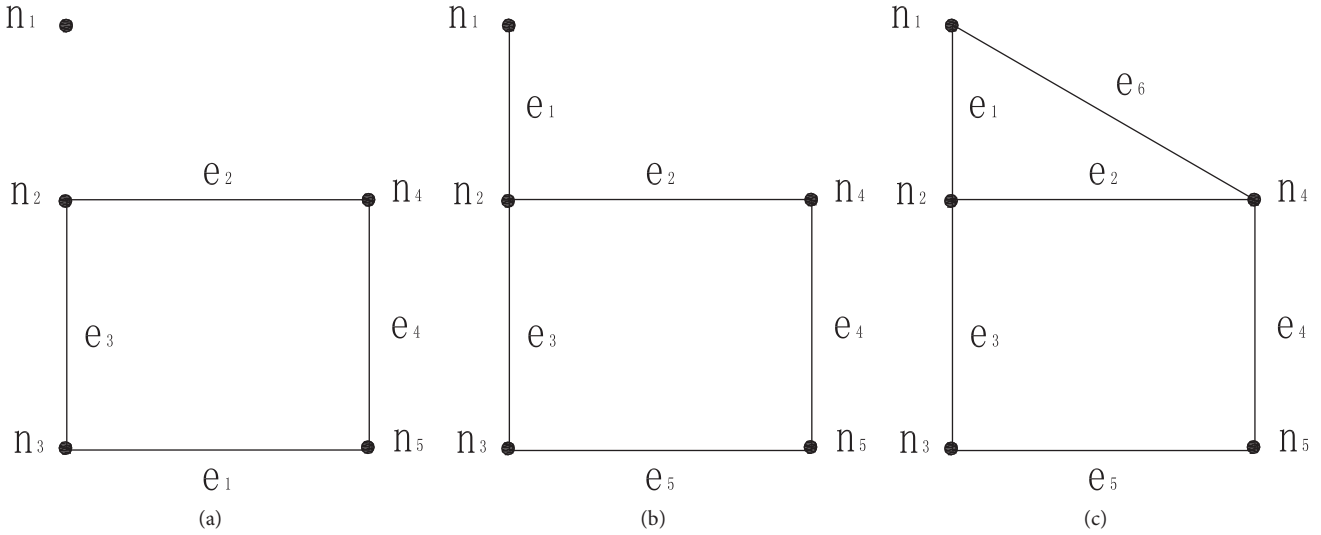


FIGURE 4: (a) Unconnected graph. (b) Connected graph with an Edge Connectivity of 1. (c) Connected graph with an Edge Connectivity of 2.

another. Thus, an unconnected stream network has a notably poor interconnectivity, which is the unacceptable drainage structure form.

To the stream network, where the Edge Connectivity is 1 (Figure 4(b)), the connectivity of the network remains poor. The lakes whose degree (number of edges that link with the node) is 1 cannot smoothly exchange water with other lakes (e.g., node  $n_1$  in Figure 4(b)). It may cause water quality deterioration and allow the deteriorating water to be transmitted to the entire stream network. Thus, a system with an Edge Connectivity of 1 is also unacceptable.

To the stream network, when the Edge Connectivity is 2 (Figure 4(c)), every lake is at least linked with two other lakes as part of a closed loop. The in-out water-delivering channel of the lakes can be build. The pollutant in the stream network will be self-cleaned by a cycle in the loop. Thus, the system with an Edge Connectivity of 2 is acceptable.

To the stream network with Edge Connectivity at 3 or more, the connect abilities between lakes are generally more perfect. The water exchange is smooth, so it is the ideal stream network structure.

**2.3.2. Edge-Node Rate.** The Edge-Node rate is obtained by dividing the number of rivers by the number of lakes as follows:

$$\beta = \frac{L}{N} \tag{1}$$

where  $\beta$  is the Edge-Node rate,  $L$  is the number of rivers, and  $N$  is the number of lakes or junctions. The Edge-Node rate can reflect the relative density of rivers. This important index can evaluate the connectivity of the entire system. The system with a high Edge-Node rate commonly has a developed stream network, and each lake occupies more rivers.

For the connected network, an Edge-Node rate less than 1 indicates that the stream network is too thin, each lake

averagely occupies less than 1 river, and there is no ring structure to circulate water in the network. Hence, it is an unacceptable Edge-Node rate number. When the Edge-Node rate is equal to 1, there is one ring structure in the system (e.g., Figure 4(b)). When the Edge-Node rate is larger than 1, there are two or more ring structures in the system, and the structure of the stream network is more complex (e.g., Figure 4(c)). Thus, the Edge-Node rate should be larger than one to satisfy the connectivity requirement.

**2.3.3. Connectivity Reliability.** The common connectivity index sometimes cannot reflect the different structures of two similar-size systems, so the Connectivity Reliability index has been created.

The Connectivity Reliability is the possibility of the Edge Connectivity remaining unchanged if one edge randomly disconnects; for a network whose Edge Connectivity is  $\lambda$  (formula (2)), we have

$$P_\lambda = \frac{E}{L} \quad (0 \geq P_\lambda > 1) \tag{2}$$

where  $P_\lambda$  is the Connectivity Reliability of the network with an Edge Connectivity of  $\lambda$ ,  $E$  is the number of edges that can be removed while keeping the Edge Connectivity invariable, and  $L$  is the number of all edges in the system.

The Connectivity Reliability has a notably adaptive practical significance: it can simulate the possibility of connectivity reducing by river blocking because of perennial sedimentation or geological disasters. At a certain Edge Connectivity, the stream network structure will become more reliable when the Connectivity Reliability index approaches 1 and more unreliable when it approaches 0. The systems with high Connectivity Reliabilities have a strong ability to resist river breaking; that is, even if a river breaks, the impact will be small. When the Connectivity Reliability is equal to 1, the Edge Connectivity will increase by a level. The Connectivity

TABLE 2: Connectivity Reliability evaluation scale.

Connectivity Reliability	[0.00, 0.25)	[0.25, 0.50)	[0.50, 0.85)	[0.85, 1.00)
Rating	Very unreliable	Unreliable	Reliable	Very reliable

Reliability cannot be compared when the systems have two different Edge Connectivity levels.

According to statistical analysis and experience, the relationship between the Connectivity Reliability index and the actual stream network is built (Table 2).

**2.3.4. Edge Weights.** In graph theory, many river characteristics such as the length, width, and depth have been neglected. However, in actual stream networks, some characteristics have obvious effects on the interconnectivity. Thus, the Edge Weight index is developed and can be used to simulate the actual river forms. Many characteristics can affect the river discharge capacity, such as the flow section area, flow velocity, geometrical shape, length, slope, roughness, and evaporation. However, because the research area is flat, the slope tends to be zero, and the flow velocity is notably slow; other characteristics are subordinate and difficult to precisely measure in actual situations. Thus, the flow section of rivers is set as the Edge Weights, which is denoted by  $A_e$ . This index has the largest effect on the river discharge capacity.

Rivers with high Edge Weights have large flow section and high discharge capacity to improve the connectivity of the stream network. There are different standards of Edge Weights in different research areas and situations. In this paper, for the lakes concentration areas south of Jiangsu, an evaluation criterion of Edge Weights is created, respectively, from the view of lakes and rivers.

*(1) Basic Total River Flow Section to Lakes.* The sum of the river flow section areas that are linked with lake  $n$  is called the Total River Flow Section of lake  $n$ , which is denoted by  $M_n$ . Lakes with larger  $M_n$  have greater water exchange capacity and self-cleaning ability. A lake with more water commonly requires larger  $M_n$ . Thus, to analyze whether  $M_n$  satisfies the lake connectivity requirement, the Basic Total River Flow Section is created and denoted by  $M_{kn}$ . Its relationship with the water volumes is given in the following formula:

$$M_{kn} = \omega V_n \quad (3)$$

where  $M_{kn}$  is the Basic Total River Flow Section linked with lake  $n$  ( $\text{m}^2$ );  $\omega$  is the Total River Flow Section Coefficient ( $\text{m}^2/\text{m}^3$ );  $V_n$  is the water volume of lake  $n$  ( $\text{m}^3$ ), calculated by the ordinary water level.  $M_{kn}$  is the minimum  $M_n$  that the lakes require. When  $M_n$  is greater than  $M_{kn}$ , the basic connectivity of the lake satisfies the demand. When  $M_n$  is less than  $M_{kn}$ , the system cannot satisfy the basic connectivity demand and must be improved. Coefficient  $\omega$  must be adjusted according to the specific situation of the study area.

*(2) Basic Edge Weight.* The Basic Edge Weight is the minimum flow section area that the rivers must have to satisfy the connectivity demand and is denoted by  $A_{ke}$ . Lakes connect with other lakes through rivers or channels; because of different

water transmission quantities, the connection between large lakes commonly requires a large river flow section. The river flow section and size of lakes linked with the river have a strong positive correlation. Thus, their relationship can be built to find the Basic Edge Weights as follows:

$$A_{ka} = \frac{M_{ka} V_b}{\sum V_{ta}}$$

$$A_{kb} = \frac{M_{kb} V_a}{\sum V_{tb}} \quad (4)$$

$$A_{ke} = \max(A_{ka}, A_{kb})$$

where  $a, b$  are the numbers of lakes connected by river  $e$ ;  $A_{ka}$  is the Basic Edge Weight of river  $e$  calculated from lake  $a$  ( $\text{m}^2$ );  $A_{kb}$  is the Basic Edge Weight of river  $e$  calculated from lake  $b$  ( $\text{m}^2$ );  $M_{ka}$  is the Basic Total River Flow Section of Lake  $a$  ( $\text{m}^2$ );  $M_{kb}$  is the Basic Total River Flow Section of lake  $b$  ( $\text{m}^2$ );  $V_a$  is the volume of lake  $a$  ( $\text{m}^3$ );  $V_b$  is the volume of lake  $b$  ( $\text{m}^3$ );  $\sum V_{ta}$  is the total volume of all lakes connected with lake  $a$  ( $\text{m}^3$ );  $\sum V_{tb}$  is the total volume of all lakes connected with lake  $b$  ( $\text{m}^3$ );  $A_{ke}$  is the Basic Edge Weight of river  $e$  ( $\text{m}^2$ ). The formula is calculated, respectively, from two lakes linked by river  $e$ . Firstly, We assign  $M_{ka}$  and  $M_{kb}$  to river  $e$  to obtain  $A_{ka}$  and  $A_{kb}$ ; then we take the maximum of those two as  $A_{ke}$  (Figure 5(a)).

When the realistic flow section of a river is larger than the Basic Edge Weight, we consider that the river satisfies the demand of basic connectivity. If every River Flow Section in the system is larger than the Basic Edge Weight, the entire stream system is considered to be smoothly running.

A special drainage structure will sometimes affect the accuracy of the calculation. For example, when two large lakes are connected by a notably small lake, the calculation results may be small and do not affect the actual situation (Figure 5(b)). Thus, we must make some adjustments according to the actual condition in the calculation, such as ignoring the small lakes and directly selecting two large lakes as the research lakes.

**2.4. Research Procedure.** The research method is summarized in three steps. (1) According to the actual river-lake relationship, abstract the stream network to a nodes-edges graph based on graph theory; (2) bring characteristic data into the connectivity evaluation index system to estimate the connectivity level of the river-lake system; and (3) develop connectivity planning including specific projects to improve the connectivity of the study area (Figure 6).

### 3. Results and Discussion

#### 3.1. Connectivity Evaluation of Fenhu Industrial Park

**3.1.1. Edge Connectivity.** In the simplified stream network graph (Figure 3(b)), every node links to others and makes

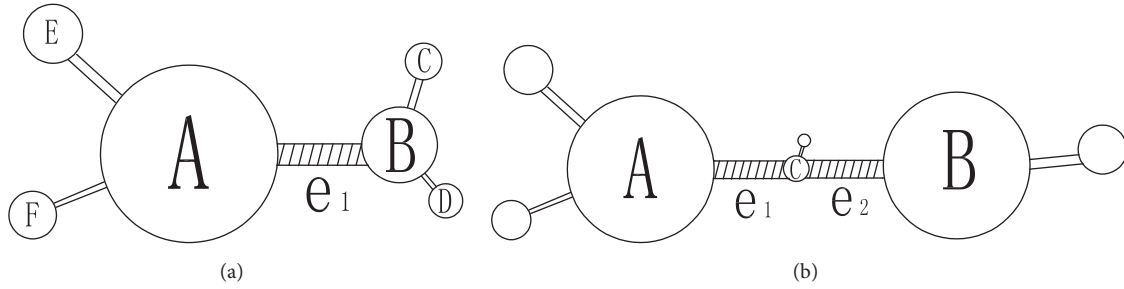


FIGURE 5: (a) Basic Edge Weight calculation illustration. (b) Basic Edge Weight calculation illustration in a special situation.

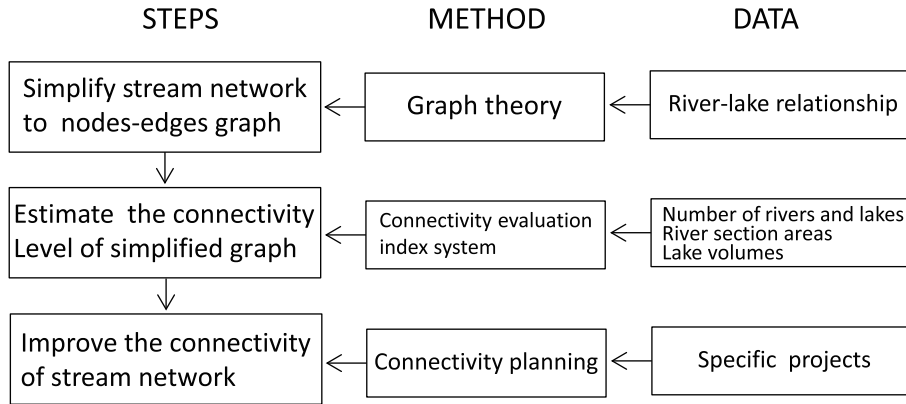


FIGURE 6: Flowchart.

the graph a connected graph. If we remove one specific edge (edge 1 or edge 6), node 1 or node 6 will be separated from the entire network, which makes the system disconnected. Thus, the Edge Connectivity of the current network is 1.

**3.1.2. Node-Edge Rate.** There are 15 nodes and 19 edges in the graph. According to formula (1), the Node-Edge Rate is 1.27, which indicates that the stream network construction is complex and has more than two cyclic structures.

**3.1.3. Connectivity Reliability.** After we remove edge 1 or edge 6, the Edge Connectivity will be reduced to 0, and other rivers will not affect the Edge Connectivity if any one of them is removed. According to formula (2), the Connectivity Reliability  $P_1$  is 0.89, which is in the range of [0.85, 1.00]; that is, the stream network is notably reliable in the current connectivity level (Table 2).

**3.1.4. Edge Weight.** The Edge Weight of each river is its river section area, as listed in Table 4. To avoid the influence of river and lake sizes varying and ensure the accuracy of the calculation, all the data we used are up to date. To determine whether the flow sections satisfy the evaluation standard, we should calculate  $M_{kn}$  and  $A_{ke}$ .

(1) *Calculation of the Basic Total River Flow Section of Lakes  $M_{kn}$ .* The Total River Flow Section of lake  $n$  ( $M_n$ ) is calculated by adding all connected river sections of lake  $n$ . According to the practical situation in the study area and research

experience, the Total River Flow Section Coefficient  $\omega$  is defined as  $0.00006 \text{ m}^2/\text{m}^3$ , which implies that every 100000 cubic meters of water need 6 square meters of flow section area to ensure that the lake smoothly runs. Using formula (3), we can obtain  $M_{kn}$  of each lake, from which we subtract  $M_n$  to obtain the Shortage of Total River Flow Section  $M_\Delta$  (Table 3).

When  $M_\Delta$  is positive, the lake does not have sufficient drainage channel area, and we must increase  $M_n$  to  $M_{kn}$ . When  $M_\Delta$  is negative,  $M_n$  need not be changed. According to Table 3, lakes 1, 2, 3, 6, 7, and 12 should adjust the flow section around them to satisfy the basic requirement of  $M_{kn}$ .

(2) *Calculation of Basic Edge Weight  $A_{ke}$ .* Based on formula (4), we can find two sets of Basic Edge Weight and select the larger one as  $A_{ke}$ , which subtract the current river section to obtain the Shortage of River Section ( $A_\Delta$ ), as shown in Table 4.

When we calculate the Basic Edge Weights of rivers 8, 9, and 10, we select node 7 (Sanbai Lake) and node 9 (Yuan Lake) as lake  $a$  and lake  $b$  and ignore the small lake 8 (Maiyan) to ensure a correct and reasonable result. When  $A_\Delta$  is positive, the River Flow Section is not sufficiently large and we must increase  $A_e$  to  $A_{ke}$ . When  $A_\Delta$  is negative,  $A_e$  need not be changed. According to Table 4, rivers 1, 2, 3, 6, 7, 14, 17, and 19 have different insufficient situations in the river section area.

The above calculation and analysis show that the connectivity condition of the river-lake network in Fenhu industrial park is not sufficient. The problems of low Edge Connectivity, narrow channel, and insufficient flow section threaten the local water security and water environment. Therefore, the

TABLE 3: Calculation of Total River Flow Section of lakes.

Lake number $n$	Lake name	Volume of lake $nV_n$ ( $m^3$ )	Total River Flow Section of lake $nM_n$ ( $m^2$ )	Basic Total River Flow Section of lake $nM_{kn}$ ( $m^2$ )	Shortage of Total River Flow Section $M_\Delta$ ( $m^2$ )
1	Xiaoyue Lake	310000	7.42	18.60	11.18
2	Shaobo Lake, etc.	750000	17.51	45.00	27.49
3	Bengke Lake, etc.	580000	34.69	34.80	0.11
4	Yuanhe Lake	1830000	172.61	109.80	-62.81
5	Niu Node	30000	149.52	1.80	-147.72
6	Yangwen Lake	180000	10.42	10.80	0.38
7	Sanbai Lake, etc.	7386666	564.17	443.20	-121.0
8	Maiyan lake	320000	582.42	19.20	-563.22
9	Yuan Lake	9930000	689.10	595.80	-93.3
10	Xueluo Lake	982000	961.39	58.92	-902.47
11	Zhangqing Lake	450000	102.03	27.00	-75.03
12	Hanlang Lake	2150000	101.94	129.00	27.06
13	Yemaowei Lake	250000	91.67	15.00	-76.67
14	Fenhu Lake	3150000	1982.61	189.00	-1793.61
15	Mugua Lake	520000	952.02	31.20	-920.82

TABLE 4: Calculation of Basic Edge Weight.

River number $e$	River section area $A_e$ ( $m^2$ )	Basic Edge Weight of river $eA_{ke}$ ( $m^2$ )	Shortage of river section $A_\Delta$ ( $m^2$ )
1	7.42	18.60	11.18
2	10.09	29.33	19.24
3	24.60	24.68	0.09
4	65.95	0.40	-65.55
5	83.57	1.44	-82.12
6	10.42	10.80	0.38
7	71.64	99.19	27.55
8	269.64	288.40	-24.38
9	43.14	288.40	-24.38
10	269.64	11.48	-258.16
11	136.37	43.23	-93.14
12	15.36	8.47	-6.89
13	86.68	82.93	-3.75
14	15.26	46.07	30.81
15	76.41	8.92	-67.49
16	926.57	17.79	-908.77
17	96.18	133.71	37.53
18	933.78	9.42	-924.36
19	13.72	26.29	12.57

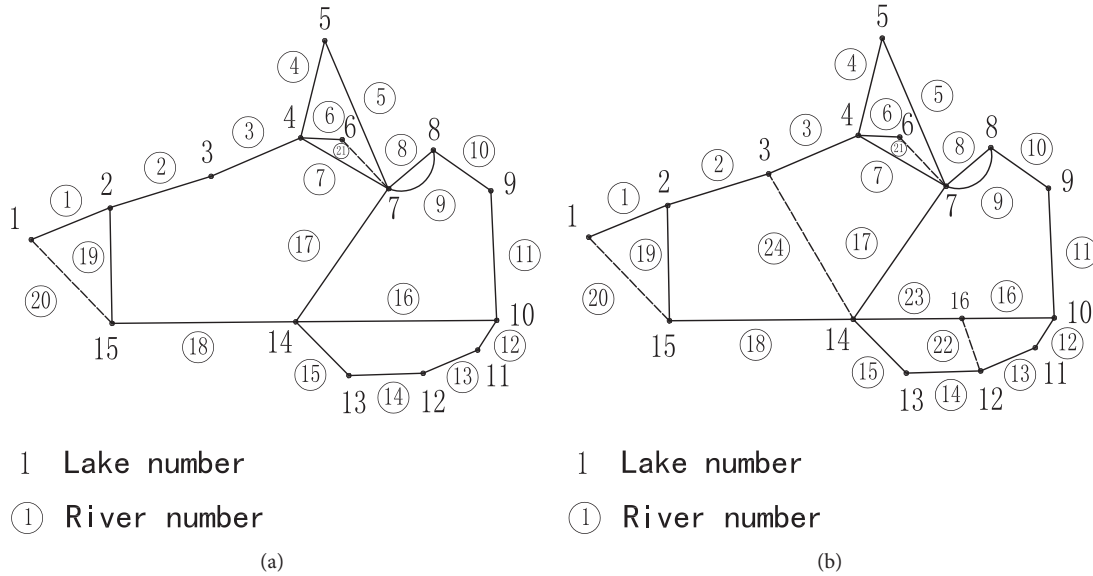


FIGURE 7: (a) Simplified stream network after the first-phase planning. (b) Simplified stream network after the second-phase planning.

transformation plan targeted on the river-lake system in the study area to enhance the current connectivity situation is urgently required.

**3.2. Transform Plan of the River-Lake System in Fenhu Industrial Park.** Based on the current connectivity evaluation in Section 3.1, a connectivity improvement plan is provided with two phases. The first phase aims to make the stream network essentially unimpeded under the limited manpower, material resources, and financial resources. The second phase aims to solve most connected problems to make the river-lake network more unimpeded and smooth. The connectivity condition in the study area will be improved after the two phases.

**3.2.1. First-Phase Planning.** In Fenhu industrial park, the Edge Connectivity of the river-lake network is 1, which is unacceptable. Because the insufficient connection of nodes 1 and 6 may cause a part of stream network to decrease in water exchange efficacy and deterioration of water quality, which will affect the regional water environment, we must increase the Edge Connectivity. In addition, the Connectivity Reliability is sufficiently large, so a few connection projects can improve the Edge Connectivity, and the plan is feasible.

More specifically, we should focus on linking Xiaoyue Lake (node 1) and Yangwen Lake (node 6) to the entire stream network to increase the Edge Connectivity. According to the design philosophy of low work quantity and respecting the natural river morphology, we attempt to minimize digging new rivers, demolition, and immigration in the project process. Based on the local situation, we connect the water channels between Xiaoyue Lake (node 1) and Mugua Lake (node 15) and between Yangwen Lake (node 6) and Sanbai Lake (node 7). The new water channels are constituted by the surrounding unconnected rivers and lakes in the polder.

Figure 7(a) shows the simplified graph after the connection; the new channels are named edge 20 and edge 21 as shown with dotted lines. After the primary improvement, the Edge Connectivity of the system has been increased to 2, which is acceptable.

**3.2.2. Second-Phase Planning.** After the first phase, the stream network is relatively unobstructed but can be further improved. Because of the difficulty of adding new rivers to increase the Edge Connectivity to 3 and because 2 is an acceptable Edge Connectivity value, we decide to improve the connectivity using other indices.

*(1) Improve the Connectivity by Increasing the Connectivity Reliability.* After the first phase, the Connectivity Reliability  $P_2$  becomes 0.33, which belongs to the unreliable scale and should be improved (Table 2). Following the principle of best comprehensive benefits, we select the edge that can increase the Connectivity Reliability as much as possible and minimize the damage on the local original channel. Thus, we link Bengke Lake (node 3) with Fenhu Lake (node 14) and Hanlang Lake (node 12) with Taipu River (new node 16). Both projects use the existing rivers and lakes in the polder to avoid the disturbance. The simplified graph is shown in Figure 7(b), and the new channels are named edge 22 and edge 24 as shown with dotted lines.

*(2) Improve the Connectivity by Increasing the Edge Weight.* According to the analysis of Table 3,  $M_{\Delta}$  of some lakes are positive, which implies that the rivers around these lakes must be widened to satisfy the  $M_{kn}$  requirement. According to the analysis of Table 4,  $A_{\Delta}$  of some rivers are positive, which implies that we must broaden these rivers to satisfy the  $A_{ke}$  requirement.

The narrow rivers mainly appear around Shaobo Lake (node 2) and Sanbai Lake (node 7). Based on the calculation,

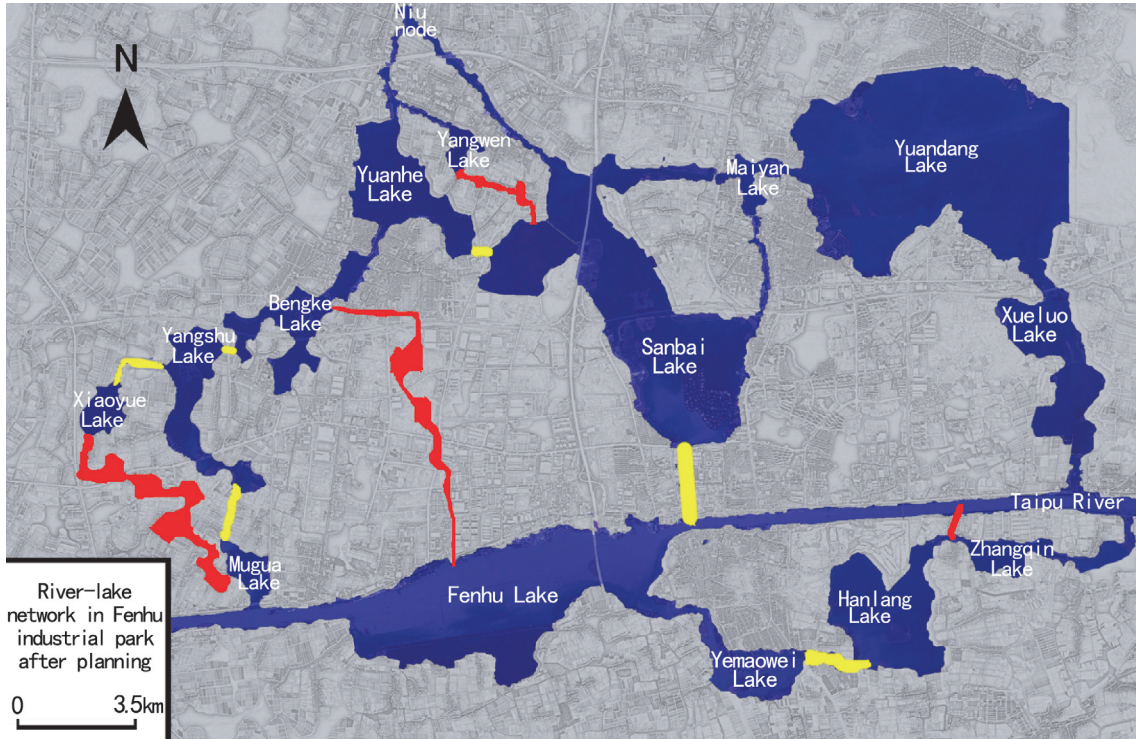


FIGURE 8: River-lake network in Fenhu industrial park after planning. The red line represents the connecting projects, and the yellow line represents the widening projects.

we must desilt the rivers that link Xiaoyue Lake (node 1), Bengke Lake (node 3), and Mugua Lake (node 15) with Shaobo Lake (node 2) and broaden the rivers that link Yuanhe Lake (node 4) and Fenhu Lake (node 14) with Sanbai Lake (node 7). In addition, the flow section between Yemaowei Lake (node 13) and Hanlang Lake (node 12) is not sufficiently large and must be desilted. Thus, 6 rivers (river 1, river 2, river 7, river 14, river 17, and river 19) must be desilted or broadened. Because the new rivers 21 and 24 reduce the drainage stress of rivers 3 and 6, after the connecting projects, those two narrow rivers can satisfy the standard. After several specific project measures, the flow section of those rivers will be as follows: river 1:  $16.52 \text{ m}^2$ ; river 2:  $30.24 \text{ m}^2$ ; river 7:  $116.34 \text{ m}^2$ ; river 14:  $39.05 \text{ m}^2$ ; river 17:  $138.18 \text{ m}^2$ ; river 19:  $27.18 \text{ m}^2$ .

**3.3. Discussion.** After two phases, the connectivity indices of the study area are changed. The Edge Connectivity is changed to 2, which implies that every lake is at least linked with two other lakes to compose a closed loop. The in-out water-delivering channel of each lake can be built, and the pollutant in the stream network will be self-cleaned by the cycle in the loop; there are 24 edges and 16 nodes in the graph, so the Edge-Node rate is 1.5; that is, the structure becomes more complex and more conducive to water exchange. Among all 24 edges, if we remove any edge in a group of 12 edges (edges 2, 3, 7, 8, 9, 16, 17, 18, 19, 22, 23, and 24), the Edge Connectivity will not change. Hence, in the situation where Edge Connectivity is 2, the index of Connectivity Reliability  $P_2$  is 0.5, which is in the reliable range. Two new edges

(edges 20 and 21) are added to the Edge Weight index. The calculation results show that both  $M_\Delta$  and  $A_\Delta$  are negative after the projects, which indicates that all rivers satisfy the demand of minimum flow section area. All projects in planning are shown in Figure 8, including 4 connecting projects and 6 widening projects. All indices satisfy the standard requirements according to the connectivity evaluation index system. The connectivity between rivers and lakes is unobstructed, and the water security and water environment goals can be basically achieved.

The results show that the connectivity planning is effective. However, if the size of the river-lake system changes due to erosion and so forth in the future, we should use the evaluation system and the new data to reevaluate its connectivity. We still need to further validate the effectiveness of the evaluation system by investigating the actual connectivity of study area after the completion of the specific projects. In addition, more statistical analysis is needed to cross-validate the evaluation in the future to verify the universal applicability.

## 4. Conclusion

In this paper, based on the graph theory, we have built a connectivity evaluation index system of the river-lake system and introduced the calculation method of each index. The standard of a smooth river-lake network is as follows: the Edge Connectivity is larger than 2, the Edge-Node rate is larger than 1, the Connectivity Reliability is larger than 0.5,

and the Edge Weights are larger than the Basic Edge Weight. According to different evaluation results, we can provide different planning schemes. For the stream networks with Edge Connectivity below 2, we add new channel to the systems to enhance the Edge Connectivity. For the river networks whose Edge Connectivity are larger than 2, we can enhance the Edge-Node rate, Connectivity Reliability, and Edge Weights, which is an effective method to improve the connection level.

We used the river-lake network of Fenhu industrial park in Suzhou China as an example and analyzed the connection situation using the established evaluation methodology. The result indicates that the river-lake network in Fenhu industrial park has several connectivity problems: low Edge Connectivity, narrow flow section, lack of Total River Flow Section of some lakes, and so forth. Hence, specific planning advice was provided, which includes designing new channels to link the isolated or low-node-degree lakes (such as Xiaoyue Lake and Yangwen Lake) and broadening the present narrow rivers (including 6 specific rivers). According to the calculation, after two phases of connecting plan are implemented, all connectivity indices will satisfy the standard requirements, and the connectivity of the river-lake system in Fenhu industrial park will be efficiently promoted.

The evaluation index system and planning method are notably useful in our study area. However, a limitation is worth noting. The Total River Flow Section Coefficient  $\omega$  reflects the relationship between the lake volume and the Total River Flow Section of the lake; in our case study, it is defined by the interview of the front-line governor of Fenhu and our research experience. This index can be accurately calculated in future research.

## Data Availability

The river data of Fenhu river-lake system were provided by Wujiang district water conservancy bureaus, which included the width, average surface elevation, bed elevation, and side slope ratio of each river. The flow section of each river was calculated from the basic river data. The lake volume data were obtained from the planning document of Wujiang Lakes Protection Planning and Basic Statistics of Lake over 50 mu. Requests for access to these data should be made to Chenguang Xiao (xiaochengguang@hhu.edu.cn).

## Conflicts of Interest

The authors declare that there are no conflicts of interest.

## Acknowledgments

This study has been supported by the National Key Research and Development Program of China (2017YFC040320502), a Project Funded by the Priority Academic Program Development of Jiangsu Higher Education Institutions (PAPD), and Australian Research Council for Discovery Project (Grant DPI170104138).

## References

- [1] E. Wohl, "The significance of small streams," *Frontiers of Earth Science*, vol. 11, no. 3, pp. 447–456, 2017.
- [2] X. Deng, Y. Xu, L. Han et al., "Impacts of urbanization on river systems in the Taihu Region, China," *Water (Switzerland)*, vol. 7, no. 4, pp. 1340–1358, 2015.
- [3] H. Zhang, Q. Wang, G. Li, H. Zhang, and J. Zhang, "Losses of ecosystem service values in the Taihu Lake Basin from 1979 to 2010," *Frontiers of Earth Science*, vol. 11, no. 2, pp. 310–320, 2017.
- [4] P. Passalacqua, "The Delta Connectome: A network-based framework for studying connectivity in river deltas," *Geomorphology*, vol. 277, pp. 50–62, 2017.
- [5] L. Feng, D. Wang, and B. Chen, "Water quality modeling for a tidal river network: A case study of the Suzhou River," *Frontiers of Earth Science*, vol. 5, no. 4, pp. 428–431, 2011.
- [6] Q. Tian, Q. Wang, and Y. Liu, "Geomorphic change in Dingzi Bay, East China since the 1950s: impacts of human activity and fluvial input," *Frontiers of Earth Science*, vol. 11, no. 2, pp. 385–396, 2017.
- [7] M. C. Freeman, C. M. Pringle, and C. R. Jackson, "Hydrologic connectivity and the contribution of stream headwaters to ecological integrity at regional scales," *JAWRA Journal of the American Water Resources Association*, vol. 43, no. 1, pp. 5–14, 2007.
- [8] E. C. Drago, A. R. Paira, and K. M. Wantzen, "Channel-floodplain geomorphology and connectivity of the lower paraguay hydrosystem," *Ecohydrology & Hydrobiology*, vol. 8, no. 1, pp. 31–48, 2008.
- [9] L. F. W. Lesack and P. Marsh, "River-to-lake connectivities, water renewal, and aquatic habitat diversity in the Mackenzie River Delta," *Water Resources Research*, vol. 46, no. 12, 2010.
- [10] B. O. L. Demars, G. Wiegand, D. M. Harper, U. Bröring, H. Brux, and W. Herr, "Aquatic plant dynamics in lowland river networks: Connectivity, management and climate change," *Water (Switzerland)*, vol. 6, no. 4, pp. 868–911, 2014.
- [11] R. W. Phillips, C. Spence, and J. W. Pomeroy, "Connectivity and runoff dynamics in heterogeneous basins," *Hydrological Processes*, vol. 25, no. 19, pp. 3061–3075, 2011.
- [12] G. Rincón, J. Solana-Gutiérrez, C. Alonso, S. Saura, and D. García de Jalón, "Longitudinal connectivity loss in a riverine network: accounting for the likelihood of upstream and downstream movement across dams," *Aquatic Sciences*, vol. 79, no. 3, pp. 573–585, 2017.
- [13] J. D. Phillips, W. Schwanghart, and T. Heckmann, "Graph theory in the geosciences," *Earth-Science Reviews*, vol. 143, pp. 147–160, 2015.
- [14] P. Segurado, P. Branco, and M. T. Ferreira, "Prioritizing restoration of structural connectivity in rivers: A graph based approach," *Landscape Ecology*, vol. 28, no. 7, pp. 1231–1238, 2013.
- [15] Z. Cui, V. Koren, N. Cajina, A. Voellmy, and F. Moreda, "Hydroinformatics advances for operational river forecasting: Using graphs for drainage network descriptions," *Journal of Hydroinformatics*, vol. 13, no. 2, pp. 181–197, 2011.
- [16] A. E. Ilaya-Ayza, C. Martins, E. Campbell, and J. Izquierdo, "Implementation of DMAs in Intermittentwater supply networks based on equity criteria," *Water (Switzerland)*, vol. 9, no. 11, 2017.
- [17] J. Zhao, Z. Dong, and Z. Huo, "Evaluation of connectivity in channel-beach system based on graph theory," *Journal of Hydraulic Engineering*, vol. 42, no. 5, pp. 537–543, 2011.

- [18] G. Xu, Y. Xu, and Y. Wang, "Evaluation of river network connectivity base on flow resistance and graph theory," *Advances in Water Science*, vol. 23, no. 6, pp. 776–781, 2012.
- [19] L. Y. Wang, Y. P. Xu, and M. J. Yu, "River System Connectivity Analysis of Wuxi's Central Urban Area Based on Graph Theory," *Applied Mechanics and Materials*, vol. 212-213, pp. 543–548, 2012.
- [20] X. Yang, *Study on Water System Connectivity Evaluation Based on Graph Theory Research in Jiaodong Area*, University of Jinan, 2014.
- [21] A. Tejedor, A. Longjas, I. Zaliapin, and E. Foufoula-Georgiou, "Delta channel networks: 1. A graph-theoretic approach for studying connectivity and steady state transport on deltaic surfaces," *Water Resources Research*, vol. 51, no. 6, pp. 3998–4018, 2015.
- [22] M.-N. Yang, Y.-P. Xu, G.-B. Pan, and L.-F. Han, "Impacts of urbanization on precipitation in Taihu Lake Basin, China," *Journal of Hydrologic Engineering*, vol. 19, no. 4, pp. 739–746, 2014.
- [23] A. Abed-Elmdoust, A. Singh, and Z.-L. Yang, "Emergent spectral properties of river network topology: An optimal channel network approach," *Scientific Reports*, vol. 7, no. 1, 2017.

## Research Article

# A Tidal Level Prediction Approach Based on BP Neural Network and Cubic B-Spline Curve with Knot Insertion Algorithm

Wenjuan Wang<sup>1,2</sup> and Hongchun Yuan <sup>1</sup>

<sup>1</sup>College of Information Technology, Shanghai Ocean University, Shanghai, China

<sup>2</sup>Key Laboratory of Fisheries Information, Ministry of Agriculture, Shanghai, China

Correspondence should be addressed to Hongchun Yuan; [hcyuan@shou.edu.cn](mailto:hcyuan@shou.edu.cn)

Received 2 February 2018; Revised 26 March 2018; Accepted 10 June 2018; Published 11 July 2018

Academic Editor: Xander Wang

Copyright © 2018 Wenjuan Wang and Hongchun Yuan. This is an open access article distributed under the Creative Commons Attribution License, which permits unrestricted use, distribution, and reproduction in any medium, provided the original work is properly cited.

Tide levels depend on both long-term astronomical effects that are mainly affected by moon and sun and short-term meteorological effects generated by severe weather conditions like storm surge. Storm surge caused by typhoons will impose serious security risks and threats on the coastal residents' safety in production, property, and life. Due to the challenges of nonperiodic and incontinuous tidal level record data and the influence of multimeteorological factors, the existing methods cannot predict the tide levels affected by typhoons precisely. This paper targets to explore a more advanced method for forecasting the tide levels of storm surge caused by typhoons. First, on the basis of successive five-year tide level and typhoon data at Luchaogang, China, a BP neural network model is developed using six parameters of typhoons as input parameters and the relevant tide level data as output parameters. Then, for an improved forecasting accuracy, cubic B-spline curve with knot insertion algorithm is combined with the BP model to conduct smooth processing of the predicted points and thus the smoothed prediction curve of tidal level has been obtained. By using the data of the fifth year as the testing sample, the predicted results by the two methods are compared. The experimental results have shown that the latter approach has higher accuracy in forecasting tidal level of storm surge caused by typhoons, and the combined prediction approach provides a powerful tool for defending and reducing storm surge disaster.

## 1. Introduction

The phenomenon of local sea-level turbulence or non-periodical abnormal sea-level rise or decline due to strong winds and fast pressure changes caused by tropical cyclones, extratropical cyclones, and coastal squall lines is referred to as storm surge [1]. Storm surge is a severe natural disaster which will lead to abnormal rise of sea level in a short period of time. Located in the estuary of the Yangtze River, with the East China Sea to the east, Shanghai is frequently attached by typhoons. Storm surge caused by typhoons will impose serious security risks and threats on the coastal residents' safety in production, property, and life.

At present, there exist some methods for predicting tidal levels, such as time series analysis, finite difference method, harmonic analysis, probability, and statistics, and so forth. However, both time series analysis and harmonic analysis put too much emphasis on the periodicity of the data; the

algorithm of finite difference method for solving nonlinear problems is too complex; probability and statistics cannot solve the issue of data continuity [2–6]. In order to overcome the challenges of nonperiodic and incontinuous tidal level record data, and the influence of multifactors, the neural network method has first been applied by many researchers to predict periodic tidal levels depending on long-term astronomical effects that are mainly affected by moon and sun [7–15]; then it has also been employed to predict tidal levels with short-term meteorological effects generated by severe weather conditions like storm surge [16–21].

Latest research has tried to improve the prediction accuracy by employing a mixed approach or improved algorithm. For example, Supharatid [22] optimized the neural network-based tidal level predicting model with the Levenberg-Marquardt algorithm and found that the dry period had stronger influences on tide levels than the flood period. Further, through comparison between harmonic analysis

method, BP neural network method, and BP neural network method based on self-adapting particle swarm optimization algorithm, Zhang et al. [23] have revealed that the conventional harmonic method performs with the lowest accuracy in predicting tidal level with meteorological effects. French et al. [24] combined ANN with computational hydrodynamics for predicting short-term tidal levels at estuarine ports and they have found that the ANN-hydrodynamic model can generate realistic flood extents that can inform port resilience planning. Moreover, Rahman et al. [25] proposed a satisfactory vertically integrated shallow model for computing water levels due to the nonlinear interaction of tide and surge associated with some storms that hit the coast of Bangladesh. In order to select data samples with most representing ability and construct appropriate sampling pool, Yin and Wang [26] combined conventional harmonic analysis with the online sequential extreme learning machine based on improved Gath-Geva fuzzy segmentation algorithm, and their simulation results demonstrated the feasibility and effectiveness of the combined method for dynamic tidal level prediction. Further, El-Diasty et al. [27] developed a hybrid harmonic analysis and wavelet network (HA-and-WN) model for accurate sea-level prediction and their validation experiments have revealed that the overall performance of the hybrid HA-and-WN model is superior to the HA-only model by 85% and outperforms the WN-only model by about 20% based on the overall root mean square.

Although numerous techniques have been employed to forecast tide levels, there exist large forecasting errors no less than 11 cm [28–30]. In order to achieve an improved forecast accuracy and adapt to severe weather caused by meteorological components, this paper will explore an effective and feasible model for predicting tidal level of storm surge caused by typhoons. On the basis of observation data of long-term tidal levels and typhoons, this study first attempts to develop a BP neural network-based model for predicting tidal level. In the early published work of [20], in order to select a most accurate tidal level prediction approach, we compared three methods, linear regression, BP neural network, and RBF neural network using the same testing data and the experimental results have demonstrated that BP model outweighs the other two approaches in forecasting the tidal level of storm surge caused by typhoons.

However, the tide levels predicted by BP model are isolated points. Due to the fact that tidal level changes gradually not suddenly, there is probability that the highest tidal level appears between two predicted points. Therefore, the second step of this study is to optimize the BP prediction model using cubic B-spline curve with knot insertion algorithm (KIA) [31, 32], BP-KIA model for short, which will conduct curve simulation and smooth processing of the forecasted data points, thus to accurately predict the highest tide level and its time of occurrence. The proposed BP model and its optimized BP-KIA model are tested with the same historic tidal level data of Luchaogang, China.

This paper is organized in the following way. In the second section, the main methods are introduced. In Section 3, the details of experiments are delineated. Section 4 presents the

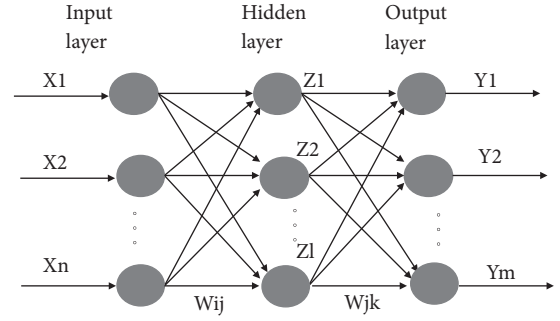


FIGURE 1: A classical three-layer BP network model.

major experimental results and related discussion. Section 5 provides a conclusion of this paper.

## 2. Methods

**2.1. BP Neural Network.** ANN is an intelligent system that can simulate the information processing functions of biological neural networks by interconnecting many simple neurons. ANN is an adaptive nonlinear dynamic system which is mutually connected by a large amount of neurons. BP neural network is the most prevalent and effective learning model of ANN. Compared with other conventional models, BP neural network has better durability and timely predictability. BP uses the gradient descent method to correct the weights of the interconnective neurons and it can easily handle the interaction of processing elements by adding hidden layers. In the learning process of BP, the interconnection weights are adjusted using an error convergence technique to obtain a desired output for a given input.

A typical BP neural network is composed by three layers: input layer, hidden layer, and output layer. Theoretically, it can approach a continuous function with any precision. A classical three-layer BP network model is shown in Figure 1.

$n$  is the input layer nodes,  $l$  is the hidden layer nodes,  $m$  is the output layer nodes,  $W_{ij}$  is called input-hidden layer link weight, and  $W_{jk}$  is called hidden-output layer link weight.

Then the output value of hidden layer is expressed as follows:

$$H_j = f\left(\sum_{i=1}^n w_{ij}x_i - \theta_j\right), \quad j = 1, 2, \dots, l \quad (1)$$

where  $\theta_j$  is the threshold of the hidden layer nodes and  $f(\cdot)$  is a nonlinear transfer function. The Sigmoid function:  $f(x) = 1/(1 + e^{-x})$  is commonly adopted as the nonlinear transfer function.

Thus, the actual outputs of BP network can be obtained:

$$O_k = \sum_{j=1}^l H_j w_{jk} - a_k, \quad k = 1, 2, \dots, m \quad (2)$$

where  $a_k$  is the threshold of the output layer nodes.

According to the actual output  $O$  and the desired network outputs  $Y$ , the network error  $e$  can be obtained through the following:

$$e_k = \frac{1}{2} \sum_{k=1}^m (Y_k - O_k)^2, \quad k = 1, 2, \dots, m \quad (3)$$

If the number of learning sample is  $p$ , the global error  $E$  is defined as

$$E = \frac{1}{2p} \sum_{q=1}^p \sum_{k=1}^m (Y_k - O_k)^2, \quad (4)$$

$$k = 1, 2, \dots, m, \quad q = 1, 2, \dots, p$$

If  $E$  is less than allowed error  $\varepsilon$ , the learning process terminates; otherwise, there is a need to calculate the output deviation of each layer to conduct error back propagation in order to modify the values of weights and thresholds of BP neural network. Repeat this process until the global error  $E$  reaches the allowed error  $\varepsilon$ , then record all weight values and threshold values, the network training terminates. The prediction values can be obtained if inputting the samples data at this moment.

2.2. *Cubic B-Spline Curve Based on KIA.* The derivation process of cubic B-spline curve based on KIA is depicted as follows.

The curve segment  $n - k + 1$  of  $K$ -degree B-spline curve in definition domain  $t \in [t_k, t_{n+1}]$  takes the following form:

$$P(t) = \sum_{j=i-k}^i p_j N_{j,k}(t), \quad t \in [t_k, t_{n+1}] \quad (5)$$

$K$ -degree B-spline curve  $P(t)$  is a continuous spline curve composed of multi-segment polynomial in the definition domain. Therefore, conduct simple parameter transformation:  $t = t(x) = t_i + x$ , and set  $r = i - k$  which represents the curve  $r$ , then the equation of  $K$ -degree B-spline curve is transformed as follows:

$$S_r(x) = P(t(x)) = \begin{bmatrix} x^k & x^{k-1} & \dots & x & 1 \end{bmatrix} M_k \begin{bmatrix} p_r \\ p_{r+1} \\ \dots \\ p_{r+k} \end{bmatrix} \quad (6)$$

where  $0 \leq x \leq 1, r = 0, 1, \dots, n - k$ .

In terms of cubic B-spline curve, it is inferred from (6) that cubic B-spline curve is composed of  $n-2$  curve segments, the first curve segment takes the following form:

$$S(x) = \frac{1}{6} * \begin{bmatrix} x^3 & x^2 & x & 1 \end{bmatrix} \begin{bmatrix} -1 & 3 & -3 & 1 \\ 3 & -6 & 3 & 0 \\ -3 & 0 & 3 & 0 \\ 1 & 4 & 1 & 0 \end{bmatrix} \begin{bmatrix} p_0 \\ p_1 \\ p_2 \\ p_3 \end{bmatrix} \quad 0 \leq x \leq 1 \quad (7)$$

Set

$$M_3 = \frac{1}{6} * \begin{bmatrix} -1 & 3 & -3 & 1 \\ 3 & -6 & 3 & 0 \\ -3 & 0 & 3 & 0 \\ 1 & 4 & 1 & 0 \end{bmatrix}, \quad (8)$$

$$[c_0 \ c_1 \ c_2 \ c_3]^T = M_3 [p_0 \ p_1 \ p_2 \ p_3]^T,$$

Equation (7) can be converted into the following form:

$$S(x) = [x^3 \ x^2 \ x \ 1] [c_0 \ c_1 \ c_2 \ c_3]^T \quad 0 \leq x \leq 1 \quad (9)$$

Divide the interval  $[0, 1]$  into  $m$  segments equally, set  $x_i = i/m$  ( $i = 0, 1, \dots, m$ ), and  $S(x_i)$  represents the unknown points of the curve segments after inserting nodes.

Inferring from Taylor series of the function, we obtain the following equation:

$$S(x+h) = S(x) + S'(x)h + \frac{S''(x)}{2}h^2 + \frac{S'''(x)}{6}h^3 \quad (10)$$

If we set  $S_i = S(x_i), SP_i = S'(x_i)h, SPP2_i = S''(x_i)h^2/2, SPPP6_i = S'''(x_i)h^3/6$ , the following equation can be drawn from (10):

$$S_{i+1} = S_i + SP_i + SPP2_i + SPPP6_i \quad (11)$$

Therefore, as long as we acquire the iterative formulas of  $SP_i, SPP2_i, SPPP6_i$ , the iterative formula of  $S_i$  can be calculated from (11).

After Taylor series of expansion of  $S'(x+h)$ , we can obtain  $S'(x+h) = S'(x) + S''(x)h + (S'''(x)/2)h^2$ . If multiplied by  $h$  on its two sides, and set  $SPP_i = S''(x_i)h^2, SPPP2_i = S'''(x_i)h^3/2$ , the following equation can be achieved:

$$SP_{i+1} = SP_i + SPP_i + SPPP2_i \quad (12)$$

After Taylor series of expansion of  $S''(x+h)$ , we can obtain  $S''(x+h) = S''(x) + S'''(x)h$ . If multiplied by  $h^2$  on its two sides, and set  $SPPP_i = S'''(x_i)h^3$ , the following equation can be obtained:

$$SPP_{i+1} = SPP_i + SPPP_i \quad (13)$$

$$SPP2_{i+1} = SPP2_i + SPPP2_i \quad (14)$$

$S(x)$  is cubic polynomial curve,  $SPPP_i, SPPP2_i, SPPP6_i$  are constants. After  $S_0, SP_0, SPP_0, SPPP2_0$ , and  $SPPP6_0$  are computed, other points  $S_i$  on the curve can be collectively calculated by (11), (12), (13), and (14).

2.3. *The Proposed Tidal Level Prediction Model.* Based on aforementioned theories, the proposed tidal level prediction model, based on BP neural network and cubic B-spline curve with KIA, BP-KIA model is derived. First, the preliminary predicted data are drawn from BP model, then insert nodes using knot insertion algorithm, and finally the smoothed tidal level prediction curve is gained. The proposed BP-KIA tidal level prediction model is depicted in Figure 2.

$x_1, x_2, x_3, x_4, x_5$ , and  $x_6$  represent the latitude and longitude of the typhoon, distance from the observation point to the typhoon, strength of the typhoon, pressure of the

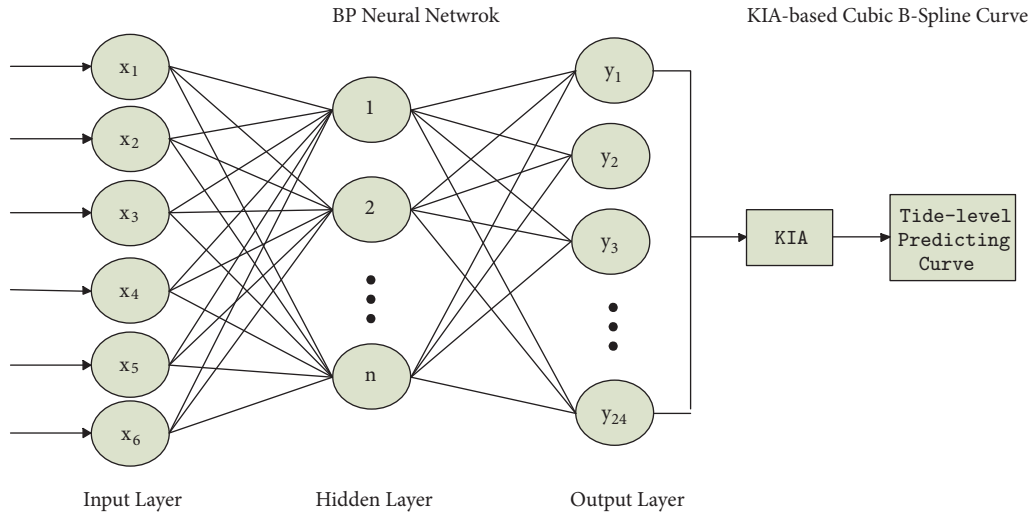


FIGURE 2: The structure of proposed BP-KIA tidal level prediction model.

typhoon, and speed of the typhoon. The parameters of  $y_1, y_2, y_3 \dots, y_{24}$  represent the predicted tidal levels from today's midday 12 until midday 12 the next day.

### 3. Experiments

**3.1. Experimental Procedures.** In order to develop a tidal level prediction model for Luchaogang, the first step is to normalize the six parameters of typhoon. Next, the normalized data are taken as the inputs of the BP model. After training of the BP model is completed, the predicted tide levels in 24 hours from today's midday 12 until midday 12 the next day are acquired. Then, cubic B-spline curve with KIA is employed to conduct smooth processing of the predicted data in 24 hours. Finally, the tidal level prediction curve is obtained. The detailed experimental procedures are illustrated in Figure 3.

**3.2. Source of Data.** The typhoon data and tidal level data in this study are provided by Pudong Hydrological Bureau. There are 137952 groups of tidal level observation data, 360 groups of typhoon data, and 10143 groups of astronomical tide data at Luchaogang, from 2008 to 2012. The first step is to match the tidal level data and typhoon data occur simultaneously, and then 360 groups of typhoon data and correspondingly tidal level data are summarized. Next, tidal level data under the influence of typhoon are acquired by subtraction between the annual tidal level observation data and the corresponding astronomical tide data. The latitude and longitude of the typhoon, distance from the observation point to the typhoon, strength of the typhoon, pressure of the typhoon, and speed of the typhoon are employed as the input parameters; the corresponding tidal level data are adopted as the output parameters.

**3.3. Data Normalization of Input Parameters.** Because the measurement units and formats of the parameters of typhoon are not inconsistent, they cannot be directly used as the input layer of BP model: they must be normalized. For

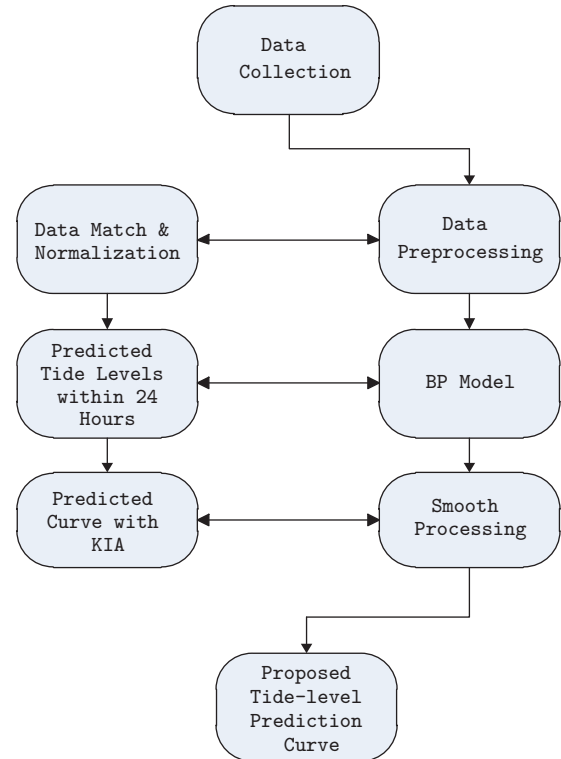


FIGURE 3: The experimental procedures.

normalization, there is no need for complex calculation of unit conversion. Normalization is a method of turning the absolute value of real data into relative value, which is an effective means to simplify computing and reduce value. Linear function transformation is used in this paper to normalize the parameters of typhoon, which is expressed as follows:

$$y = \frac{(y_{max} - y_{min}) \times (x - x_{min})}{(x_{max} - x_{min})} + y_{min} \quad (15)$$

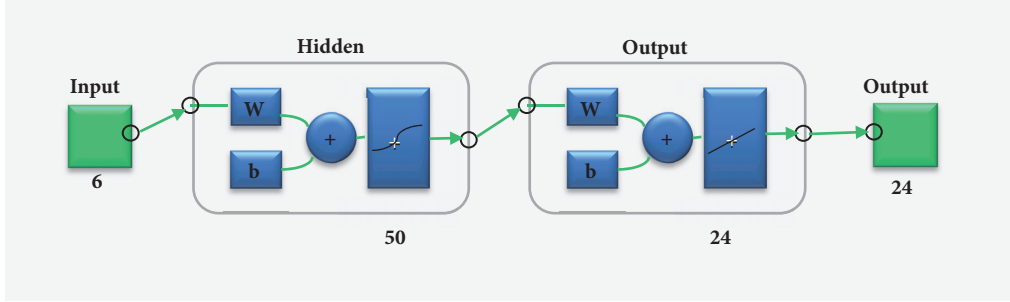


FIGURE 4: The structure of BP neural network in Matlab.

where  $x$  are the parameters of typhoon. In order to make the input parameters of typhoon between  $[-1, 1]$ , based on the requirements of data normalization,  $y_{max}$  and  $y_{min}$  are defined as follows:

$$y_{max}=1 \tag{16}$$

$$y_{min}=-1 \tag{17}$$

**3.4. Design of BP Neural Network.** In the proposed BP model, some of the training parameters are set with the Matlab neural network toolbox-MatlabR2014a. For MatlabR2014a, the default transformation function is Sigmoid. After a series of test, it is found that when the number of neurons in the hidden layer is more than 40, the model has better convergence, with a relatively small *MSE*. Therefore, the number of nodes in the hidden layer is set as 50. The conjugate gradient method is selected as the training function due to its advantages of avoiding slow convergence and computational complexity. In addition, the learning rate is 0.05; the number of training iterations is 1000. The six normalized parameters of typhoons, latitude, longitude, distance, strength, pressure, and speed, from 2008 to 2011 are used as the input parameters, and the corresponding tidal level data are used as the output parameters. A BP neural network model is obtained by training, as shown in Figure 4.

**3.5. The BP-KIA Tidal Level Prediction Model.** The tide levels predicted by BP neural network model are isolated points. However, the changes of actual tide levels are gradual not sudden. Due to the limitation of observed sample data, there is probability that the highest tidal level occurs between two predicted points. Therefore, this study employs KIA-based cubic B-spline curve to optimize the proposed BP prediction model and conduct smooth processing of the predicted points. Thus the smoothed curve can predict continuous changes of tide levels and the peak of tidal level sequence.

Through running the code of cubic B-spline curve based on KIA in MatlabR2014a, the tidal level data predicted by BP model are conducted with smooth processing and the tidal level curve within 24 hours can be obtained as shown in Figure 5. In Figure 5, the broken line comprised by discrete points is the results predicted by BP model, and the curve is the results predicted by the BP-KIA model. The  $x$ -axis represents 24 hours from today's midday 12 until midday 12

TABLE 1: The degree of influence by “Damrey” “Haikui” “Tembin” and “Sanba”.

Name of typhoon	Influence date	Influence degree to Shanghai
Damrey	2nd Aug. -4th Aug.	Strong
Haikui	3rd Aug. - 9th Aug.	Very Strong
Tembin	19th Aug. -28th Aug.	Slightly weaker
Sanba	11th Sep.-19th Sep.	Very weak

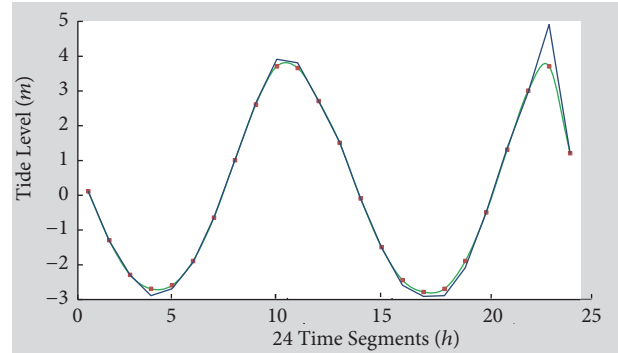


FIGURE 5: The tidal level prediction curve.

the next day, while the  $y$ -axis represents the height of tide level in the measurement unit of meters.

## 4. Results and Discussion

**4.1. Analysis of Predicted Highest Tide Levels.** The highest predicted tide level is the maximum value of predicted tide levels in 24 hours. All predicted tide levels in one day can be obtained through curve simulation and smoothing. In order to compare the prediction accuracy between BP model and BP-KIA prediction model, we extracted the highest tidal level data in given dates in 2012 from the documents provided by Pudong Hydrological Bureau. Then four typhoons, Damrey, Haikui, Tembin, and Sanba, were, respectively, adopted as testing cases to inspect applicability of the proposed prediction models. Those four typhoons have different impacts on Shanghai's tide levels (see Table 1 for details).

Subsequently, the prediction models were employed to predict tide levels in selected dates. Table 2 lists the real

TABLE 2: The comparison of BP model and BP-KIA model with influence of Haikui.

Date	Real tide levels [m]	Tide levels predicted by BP model [m]	Tide levels predicted by BP-KIA model [m]	date	Real tide levels [m]	Tide levels predicted by BP model [m]	Tide levels predicted by BP-KIA model [m]
8.1-2	4.28	4.25	4.25	8.24-25	4.13	4.10	4.11
8.2-3	4.50	4.35	4.47	8.25-26	3.99	3.98	3.98
8.3-4	4.92	5.71	5.72	8.26-27	4.05	4.01	4.02
8.4-5	4.83	5.35	5.35	8.27-28	4.73	4.65	4.66
8.5-6	4.64	4.71	4.72	9.11-12	3.67	3.65	3.67
8.6-7	4.51	4.45	4.52	9.12-13	3.99	3.96	3.97
8.7-8	4.81	4.46	4.46	9.13-14	4.21	4.21	4.25
8.19-20	4.51	4.01	4.04	9.14-15	4.48	4.41	4.55
8.20-21	4.47	4.21	4.22	9.15-16	4.76	4.48	4.63
8.21-22	4.32	4.22	4.24	9.16-17	4.98	5.25	5.28
8.22-23	4.35	4.39	4.39	9.17-18	4.82	4.81	4.81
8.23-24	4.16	4.15	4.15	9.18-19	4.55	5.02	5.03

TABLE 3: The comparison of *MSE* and *RMSE* for the highest tide levels by BP model and BP-KIA model.

Error type	Prediction by BP model [m]	Prediction by BP-KIA model [m]
<i>MSE</i>	0.074	0.070
<i>RMSE</i>	0.271	0.265

highest tide levels, as well as the corresponding highest tide levels predicted by BP model and BP-KIA model, respectively, with the influence of typhoon Haikui in 2012 (retaining two decimal fractions).

Data in Table 2 were divided into two groups for further analysis. One group was real tide levels and tide levels predicted by BP model, and the other group was real tide levels and tide levels predicted by BP-KIA model. Matlab was adopted to calculate *MSE* and *RMSE* of the two groups, and the results are displayed in Table 3.

It can be inferred from Table 3 that the prediction accuracy of the highest tide level has been enhanced by adding KIA. Both BP tidal level prediction model and BP-KIA model have higher prediction accuracy than linear regression model with *MSE* of 4.9734 m [20], RBF model with *MSE* of 0.2526 m [20], and conventional harmonic analysis method with the mean error of 0.2-0.3 m [23]. The *MSE* of 0.070 m and *RMSE* of 0.265 m demonstrate that the method of combining BP neural network and cubic B-spline curve with KIA has great significance and applicability in predicting tide levels when typhoons approach.

**4.2. Analysis of Predicted Time of Tidal Level Peak.** When a typhoon occurs, not only is accurate prediction of upcoming highest tide level needed, the precise analysis of the time when the highest tide level appears is also critical.

In the proposed BP-KIA tidal level prediction model, the time segments of tide-level prediction data commence from today's midday 12 until midday 12 the next day. In order to

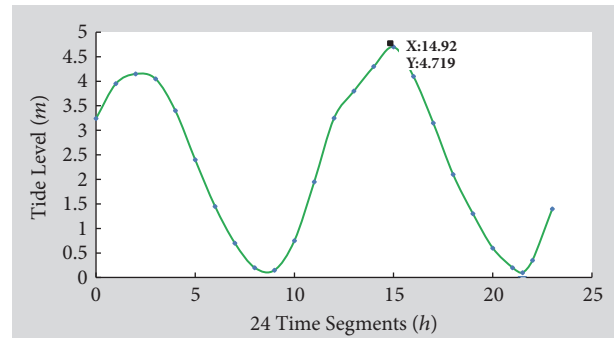


FIGURE 6: The tidal level prediction curve with time.

simplify computation, we use 24 integers to represent the time segments; for instance, 0 corresponds to today's midday 12 and 1 corresponds to 1pm today, and so on. The highest tide level and its time of occurrence can be obtained by calculating the horizontal ordinate and vertical coordinate values of the peak of the tidal level prediction curve. For instance, in Figure 6, the highest tide level is 4.719 m and its occurring time is 14.92. Because the predicted time is processed by decimal system, a conversion formula is needed to compute the real time. Therefore, by setting  $a$  as the integer bit of the horizontal ordinate and  $b$  as its decimal place, the formula to obtain the accurate time  $t$  can be summarized as follows:

$$t = \begin{cases} (12 - a) : [0.6 \ b] & (0 \leq a < 12) \\ (a - 12) : [0.6 \ b] & (12 \leq a < 23) \end{cases} \quad (18)$$

Through formula (18), it can be calculated that the horizontal ordinate 14.92 represents 2:55 am the next day. The complete 24-hour prediction curve (see Figure 6) can be obtained through running the optimized tidal level prediction model based on BP and cubic B-spline curve with KIA in Matlab.

TABLE 4: The corresponding date and time of tidal level peak.

Date	Time of the highest tide level	Predicted time of the highest tide level	Date	Time of the highest tide level	Predicted time of the highest tide level
8.1-2	11.68	12.56	8.24-25	4.75	4.81
8.2-3	12.08	13.22	8.25-26	5.58	5.92
8.3-4	13.33	13.69	8.26-27	7.17	7.12
8.4-5	14.08	14.12	8.27-28	8.33	8.81
8.5-6	14.58	14.92	9.11-12	8.50	8.69
8.6-7	15.33	15.34	9.12-13	9.75	9.81
<b>8.7-8</b>	<b>15.83</b>	<b>4</b>	9.13-14	10.75	10.69
<b>8.19-20</b>	<b>13.75</b>	<b>1.61</b>	9.14-15	11.33	10.69
<b>8.20-21</b>	<b>14.33</b>	<b>1.82</b>	9.15-16	12.25	10.80
<b>8.21-22</b>	<b>14.83</b>	<b>2.8</b>	9.16-17	12.75	13.92
<b>8.22-23</b>	<b>3.17</b>	<b>14.23</b>	9.17-18	0.25	1.00
8.23-24	3.83	3.92	9.18-19	13.25	14.69

TABLE 5: The second highest tide level.

Date	Real time of the second highest tide level	Predicted time of the highest tide level
8.7-8	3.75	4
8.19-20	1.58	1.61
8.20-21	2.08	1.82
8.21-22	2.67	2.8
8.22-23	15.50	14.23

Afterwards, the error between the real time when the highest tidal levels occurred from 1 August to 19 September in 2012 and the corresponding time predicted by the proposed BP-KIA model was analyzed (see details in Table 4). It is noted that, in order to conduct effective comparison, the real occurrence time of the highest tide level provided by the documents from Pudong Hydrological Bureau had to be decimalized.

Table 4 demonstrates that there is a bigger error of the predicted time of tidal level peak when the typhoon comes or leaves (see the bold numbers). According to the rhythm of the tides, there are twice second highest tidal levels per day, which are approaching the highest tidal level, called second highest tide level. It is inferred from sample data that there is no big difference between the second highest tidal level and the highest tidal level, with a maximum error of 0.3 m. Replace the real time of the highest tide level with the real occurring time of the second highest tide level, which can be obtained by the documents provided by Pudong Hydrological Bureau; Table 5 is obtained.

It is inferred from Table 5 that, through the replacement, the accuracy of predicted time of highest tidal level has been significantly enhanced. Therefore, the method of using the proposed model to predict occurrence time of the second highest tidal level has higher accuracy and has more practical significance.

Consequently, the *MSE* and *RMSE* between the real time when the highest tide level occurs and its occurring time

TABLE 6: The comparison of *MSE* and *RMSE* in the predicted time of tide level peak.

	Prediction by BP model[ <i>h</i> ]	Prediction by BP-KIA model[ <i>h</i> ]
<i>MSE</i>	0.8564	0.5084
<i>RMSE</i>	0.9254	0.7130

predicted by BP model and the *MSE* and *RMSE* between the real occurrence time of the highest tidal level and its occurring time predicted by BP-KIA model are displayed in Table 6.

It can be inferred from Table 6 that the accuracy of predicting the occurring time of highest tide level has been enhanced by adding KIA. The *MSE* of 0.5084 h and *RMSE* of 0.7130 h have demonstrated that the method of combining BP neural network and cubic B-spline curve with KIA has greater significance and applicability in predicting the occurring time of highest tide level when typhoons approach.

## 5. Conclusions

In order to explore an effective method to predict tidal level with a typhoon effect at Luchaogang, two tidal level prediction models, based on unique BP neural network and on a combination of BP neural network and KIA-based cubic B-spline curve, were introduced. Then, using the data from Pudong Hydrological Bureau, experiments on the two models were conducted with six parameters of typhoon as the input parameters and corresponding tidal level data as the output parameters. The comparison results have showed that the BP-KIA model is superior to the unique BP neural network model. This optimized model has not only improved the prediction accuracy of the highest tide level but also has accurate prediction results on time when the tidal level peak occurs. Through the BP-KIA prediction model, the trend of tide levels in 24 hours can be forecasted in real time. Based on the BP-KIA tidal level prediction model developed in

this study, protective measures can be taken in advance to effectively reduce the impact of typhoon disasters.

However, there are still some weaknesses in the proposed BP-KIA model. The training process, the learning rate, and some other parameters need to be continuously adjusted; there is randomness in the setting of the parameters. How to automatically and scientifically set these parameters is a problem that needs to be addressed in future research. In addition, more real data should be included to examine the validity of curve simulation in order to ensure the reliability of the model. Furthermore, as stated earlier, the four testing cases are experimented separately, and how to accurately predict the tidal level when multiple typhoons occur has not been covered by this study yet and will be explored in future study.

### Data Availability

The data used to support the findings of this study are available from the corresponding author upon request.

### Conflicts of Interest

The authors declare that there are no conflicts of interest regarding the publication of this article.

### Acknowledgments

This work is supported by the Supporting Program of Shanghai Municipal Science and Technology Commission (14391901400) and by the Key Program of National Natural Science Foundation of China (41776142). Their support is gratefully acknowledged.

### References

- [1] T. Yasuda, S. Nakajo, S. Kim, H. Mase, N. Mori, and K. Horsburgh, "Evaluation of future storm surge risk in East Asia based on state-of-the-art climate change projection," *Coastal Engineering Journal*, vol. 83, pp. 65–71, 2014.
- [2] D. F. Liu and H. Jiang, "Prediction method of exam sea level induced by typhoon," *Periodical of Ocean University of China*, vol. 39, no. 30, pp. 516–520, 2009.
- [3] R. Weisse, D. Bellafiore, M. Menéndez et al., "Changing extreme sea levels along European coasts," *Coastal Engineering Journal*, vol. 87, pp. 4–14, 2014.
- [4] S. Xu and W. Huang, "An improved empirical equation for storm surge hydrographs in the Gulf of Mexico, U.S.A.," *Ocean Engineering*, vol. 75, pp. 174–179, 2014.
- [5] J. A. Major and J. J. Mangano, "Selecting among rules induced from a hurricane database," *Journal of Intelligent Information Systems*, vol. 4, no. 1, pp. 39–52, 1995.
- [6] G. C. Paul, S. Senthilkumar, and R. Pria, "An efficient approach to forecast water levels owing to the interaction of tide and surge associated with a storm along the coast of Bangladesh," *Ocean Engineering*, vol. 148, pp. 516–529, 2018.
- [7] M. Vaziri, "Predicting Caspian sea surface water level by ANN and ARIMA models," *Journal of Waterway, Port, Coastal, and Ocean Engineering*, vol. 123, no. 4, pp. 158–162, 1997.
- [8] M. C. Deo and G. Chaudhari, "Tide prediction using neural networks," *Computer-Aided Civil and Infrastructure Engineering*, vol. 13, no. 2, pp. 113–120, 1998.
- [9] T. L. Lee, C. P. Tsai, D. S. Jeng, and R. J. Shieh, "Neural network for the prediction and supplement of tidal record in Taichung Harbor, Taiwan," *Advances in Engineering Software*, vol. 33, no. 6, pp. 329–338, 2002.
- [10] T.-L. Lee, "Back-propagation neural network for long-term tidal predictions," *Ocean Engineering*, vol. 31, no. 2, pp. 225–238, 2004.
- [11] C.-P. Tsai and T.-L. Lee, "Back-propagation neural network in tidal-level forecasting," *Journal of Waterway, Port, Coastal, and Ocean Engineering*, vol. 125, no. 4, pp. 195–202, 1999.
- [12] T.-L. Lee, O. Makarynsky, and C.-C. Shao, "A combined harmonic analysis-artificial neural network methodology for tidal predictions," *Journal of Coastal Research*, vol. 23, no. 3, pp. 764–770, 2007.
- [13] E. Sertel, H. K. Cigizoglu, and D. U. Sanli, "Estimating daily mean sea level heights using artificial neural networks," *Journal of Coastal Research*, vol. 24, no. 3, pp. 727–734, 2008.
- [14] S. Rajasekaran, K. Thiruvenkatasamy, and T.-L. Lee, "Tidal level forecasting using functional and sequential learning neural networks," *Applied Mathematical Modelling*, vol. 30, no. 1, pp. 85–103, 2006.
- [15] A. M. Salim, G. S. Dwarakish, K. V. Liju, J. Thomas, G. Devi, and R. Rajeesh, "Weekly prediction of tides using neural networks," *Procedia Engineering*, 116, no. 2016, pp. 678–682, 11.
- [16] W. Huang, C. Murray, N. Kraus, and J. Rosati, "Development of a regional neural network for coastal water level predictions," *Ocean Engineering*, vol. 30, no. 17, pp. 2275–2295, 2003.
- [17] H.-K. Chang and L.-C. Lin, "Multi-point tidal prediction using artificial neural network with tide-generating forces," *Coastal Engineering Journal*, vol. 53, no. 10, pp. 857–864, 2006.
- [18] D. T. Cox, P. Tissot, and P. Michaud, "Water level observations and short-term predictions including meteorological events for entrance of Galveston Bay, Texas," *Journal of Waterway, Port, Coastal, and Ocean Engineering*, vol. 128, no. 1, pp. 21–29, 2002.
- [19] T.-L. Lee, "Neural network prediction of a storm surge," *Ocean Engineering*, vol. 33, no. 3-4, pp. 483–494, 2006.
- [20] H. Yuan, M. Tan, and W. Wang, "Selection of methods for predicting tidal levels with a typhoon surge effect," *Journal of Coastal Research*, pp. 337–341, 2015.
- [21] W. Wang, H. Yuan, and M. Tan, "Application of BP Neural Network in Monitoring of Ocean Tide Level," in *Proceedings of the 2015 International Conference on Computational Intelligence and Communication Networks (CICN)*, pp. 1238–1240, Jabalpur, India, December 2015.
- [22] S. Supharatid, "Tidal-level forecasting and filtering by neural network model," *Coastal Engineering Journal*, vol. 45, no. 1, pp. 119–137, 2003.
- [23] Z. Zhang, J. Yin, C. Liu, and X. Zhang, "Short-term tidal level forecasting based on self-adapting PSO-BP neural network model," in *Proceedings of the 2016 Chinese Control and Decision Conference (CCDC)*, pp. 3069–3074, Yinchuan, China, May 2016.
- [24] J. French, R. Mawdsley, T. Fujiyama, and K. Achuthan, "Combining machine learning with computational hydrodynamics for prediction of tidal surge inundation at estuarine ports," *Procedia IUTAM*, vol. 25, pp. 28–35, 2017.
- [25] M. M. Rahman, G. C. Paul, and A. Hoque, "A shallow water model for computing water level due to tide and surge along

- the coast of Bangladesh using nested numerical schemes,” *Mathematics and Computers in Simulation*, vol. 132, pp. 257–276, 2017.
- [26] J. Yin and N. Wang, “An online sequential extreme learning machine for tidal prediction based on improved Gath-Geva fuzzy segmentation,” *Neurocomputing*, vol. 174, pp. 85–98, 2016.
- [27] M. El-Diasty, S. Al-Harbi, and S. Pagiatakis, “Hybrid harmonic analysis and wavelet network model for sea water level prediction,” *Applied Ocean Research*, vol. 70, pp. 14–21, 2018.
- [28] J. Xu, L. Ruan, Z. Li et al., “Characterization of four hemocyanin isoforms in *Litopenaeus vannamei*,” *Acta Oceanologica Sinica*, vol. 34, no. 2, pp. 36–44, 2015.
- [29] Q. Zhang, Z. Liu, Z. Bao, H. Wu, and Z. Du, “Flood forecasting model correction in tidal reach of Yalu River,” *Journal of Liaodong University: Natural Sciences*, vol. 19, no. 2, pp. 94–97, 2012 (Chinese).
- [30] H. Jiang, Y. Fei, and Y. Ying, “Tidal harmonic analysis using the Matlab fitting toolbox,” *Ocean Technology*, vol. 31, no. 3, pp. 33–36, 2012 (Chinese).
- [31] S. Ma, J. Ma, and Z. Liu, “A smoothing approach based on cubic B-spline curve with knot insertion algorithm,” *Computer Era*, vol. 12, p. 47, 2008 (Chinese).
- [32] R. Pan and Z. Yao, “A fast algorithm for inserting a series of knots into a B-spline curve simultaneously,” *Mini-Micro Systems*, vol. 24, no. 12, pp. 2295–2298, 2003 (Chinese).

## Research Article

# Application of Surface Spline Interpolation Method in Parameter Estimation of a PM<sub>2.5</sub> Transport Adjoint Model

Ning Li,<sup>1,2</sup> Xianqing Lv ,<sup>2</sup> and Jicai Zhang <sup>3</sup>

<sup>1</sup>*School of Science, Dalian Jiaotong University, Dalian 116028, China*

<sup>2</sup>*Physical Oceanography Laboratory/CIMST, Ocean University of China and Qingdao National Laboratory for Marine Science and Technology, Qingdao 266003, China*

<sup>3</sup>*Institute of Physical Oceanography, Ocean College, Zhejiang University, Zhoushan 316000, China*

Correspondence should be addressed to Jicai Zhang; [jicai\\_zhang@163.com](mailto:jicai_zhang@163.com)

Received 31 March 2018; Accepted 21 June 2018; Published 5 July 2018

Academic Editor: Shuo Wang

Copyright © 2018 Ning Li et al. This is an open access article distributed under the Creative Commons Attribution License, which permits unrestricted use, distribution, and reproduction in any medium, provided the original work is properly cited.

A new method for the estimation of initial conditions (ICs) in a PM<sub>2.5</sub> transport adjoint model is proposed in this paper. In this method, we construct the field of ICs by interpolating values at independent points using the surface spline interpolation. Compared to the traditionally used linear interpolation, the surface spline interpolation has an advantage for reconstructing continuous smooth surfaces. The method is verified in twin experiments, and the results indicate that this method can produce better inverted ICs and less simulation errors. In practical experiments, simulation results show good agreement with the ground-level observations during the 22nd Asia-Pacific Economic Cooperation summit period, demonstrating that the new method is effective in practical application fields.

## 1. Introduction

In recent years, air pollution has escalated to hazardous levels in Chinese cities. Among numerous types of air pollution, PM<sub>2.5</sub> (fine particles with diameter of 2.5 μm or less) is considered the most threatened kind to life expectancy and public health (e.g., [1–4]). Therefore, simulation and prediction of PM<sub>2.5</sub> pollution are always an area of interest to researchers.

An increasing number of atmospheric numerical models have been conducted and publicly available in various studies for more in-depth understanding of the physical, chemical, and dynamical processes concerned with PM<sub>2.5</sub> pollution (e.g., [5–12]). Initial condition (IC) plays an important role in the model researches. Providing the best possible ICs is essential for the success of the models. Existing studies presented several methods to obtain the IC. The initial condition was obtained from the National Meteorological Center (NMC) global data and enhanced by rawinsonde and surface observations by Liu et al. [11]. A background value (a small constant) was given to the model with the first few

days as the spin-up period to minimize the influence of initial conditions by Fu et al. [12]. Another efficient and accurate way to estimate the ICs is through data assimilation using the adjoint method (e.g., [13–17]).

Data assimilation provides a configuration for combining observations and models to form an optimal initial model state. In this method, uncertain model parameters can be constrained by minimizing the distance between the model simulations and observations. In practice, how to reduce the influence of ill-posedness caused by excessive control parameters has been a key part of data assimilation and parameter estimation. Several studies have proved that it can be effectively solved by applying independent point scheme (IPS) (e.g., [13–17]). In detail, several grids are selected as independent points (IPs) in the space domain; values of the ICs at the IPs can be optimized, while those at other grids can be calculated through a certain interpolation method with the values at the IPs. Thus interpolation is another important problem that remains to be studied.

Referring to previous studies, Cressman interpolation (hereafter abbreviated as CI) is preferred for the adjoint

model due to easy accessibility. Although the adjoint model with the CI leads to satisfying results in general, the reconstructed IC field is unsmooth around the independent points [18]. Therefore, a more reasonable interpolation method needs to be found to combine with the adjoint method.

The surface spline interpolation, with a special type of piecewise polynomial called spline, is widely used as one popular technique for data interpolation. The surface spline is a powerful tool for interpolating irregular, continuous geological or other surfaces, and is often better than polynomial interpolation because the interpolation error can be made very small [19]. Many real applications of the surface spline method indicate that the results are usually appropriate for oceanographic and meteorological contexts and it is particularly good for inferring smooth structure from scattered data. As stated in the work of Harder et al. [20], the surface spline was proposed to interpolate wing deflections and computing slopes for aeroelastic calculations. Based on the surface spline interpolation, a new mathematical model for tropical cyclone wind speeds is proposed in [21]. Compared with the earlier wind model with linear interpolation, the surface spline model could produce a more accurate wind estimate. In [22], Yaghoobi et al. described a scheme based on a cubic spline interpolation which is applied to approximating the variable-order fractional integrals and is extended to solving a class of nonlinear variable-order fractional equations with time delay. Guo and Pan [18] validated this new IP scheme with twin experiments, and the results showed that the prescribed nonlinear distribution of bottom friction coefficients are better inverted with the surface spline interpolation. Due to its proved superior performance, the surface spline interpolation (SSI) is applied to inversion of ICs with a PM<sub>2.5</sub> transport adjoint model in this study.

The paper is organized as follows. Section 2 provides the detailed descriptions of the numerical model and implementation of SSI. Twin experiments and practical experiments are carried out to evaluate the performance of SSI in inversion of ICs in Sections 3 and 4, respectively. Finally, some key conclusions drawn from the work are presented in Section 5.

## 2. Numerical Model and Settings

*2.1. Forward Model.* The governing equations of the two-dimensional PM<sub>2.5</sub> transport model are as follows:

$$\frac{\partial C}{\partial t} + u \frac{\partial C}{\partial x} + v \frac{\partial C}{\partial y} = \frac{\partial}{\partial x} \left( A_H \frac{\partial C}{\partial x} \right) + \frac{\partial}{\partial y} \left( A_H \frac{\partial C}{\partial y} \right) + S \quad (1)$$

$$C(t^0, x, y) = C^0(x, y) \quad (2)$$

where  $C$  denotes the ground-level PM<sub>2.5</sub> concentration,  $u$  and  $v$  are the horizontal wind velocity in  $x$ -coordinate and  $y$ -coordinate, respectively,  $A_H$  is the horizontal diffusivity coefficient,  $S$  is the value of the source and sink, and  $C^0$  is the initial condition (IC) to be estimated in this study.

The boundary conditions are set as constant at the inflow boundary  $\Gamma^{\text{IN}}$  and no gradient boundary conditions at the outflow boundary  $\Gamma^{\text{OUT}}$ .

$$\frac{\partial C}{\partial t} = 0 \quad \text{on } \Gamma^{\text{IN}} \quad (3)$$

$$\frac{\partial C}{\partial \vec{n}} = 0 \quad \text{on } \Gamma^{\text{OUT}} \quad (4)$$

*2.2. Adjoint Model.* The adjoint model is defined to calculate the gradients of the cost function with respect to various input parameters, which incorporate all physical processes included in the governing model, to obtain the minimization of the distance between the model output and observations. Based on the governing equations (1)–(4), its adjoint model can be constructed as follows.

First, the distance is expressed by the cost function which is defined as

$$J = \frac{1}{2} \int_{\Sigma} K (C - C_{\text{obs}})^2 d\sigma \quad (5)$$

where  $\Sigma$  denotes the set of the observations in time and space domain and  $C$  and  $C_{\text{obs}}$  are the simulated and observed PM<sub>2.5</sub> concentrations, respectively. And  $K$  is the weighting matrix and should be the inverse of observation error covariance matrix theoretically.  $K$  can be fixed simply, assuming that the errors in the data are uncorrelated and equally weighted. In the present model,  $K$  is 1 when the observations are available and 0 otherwise.

Then the Lagrangian function is constructed based on the theory of Lagrangian multiplier method and can be expressed as

$$L = J + \int \left\{ p \times \left[ \frac{\partial C}{\partial t} + u \frac{\partial C}{\partial x} + v \frac{\partial C}{\partial y} - \frac{\partial}{\partial x} \left( A_H \frac{\partial C}{\partial x} \right) - \frac{\partial}{\partial y} \left( A_H \frac{\partial C}{\partial y} \right) - S \right] \right\} d\sigma \quad (6)$$

where  $p$  is the adjoint variable of  $C$ .

According to the typical theory of Lagrangian multiplier method, we have the following first-order derivatives of Lagrangian function with respect to all the variables and parameters:

$$\frac{\partial L}{\partial p} = 0 \quad (7)$$

$$\frac{\partial L}{\partial A_H} = 0, \quad (8)$$

$$\frac{\partial L}{\partial S} = 0$$

$$\frac{\partial L}{\partial C} = 0 \quad (9)$$

Equation (7) gives the governing equation (1) of the forward model. The adjoint equation can be developed from equation (9), which is given as follows:

$$\frac{\partial p}{\partial t} + u \frac{\partial p}{\partial x} + v \frac{\partial p}{\partial y} + \frac{\partial}{\partial x} \left( A_H \frac{\partial p}{\partial x} \right) + \frac{\partial}{\partial y} \left( A_H \frac{\partial p}{\partial y} \right) - K(C - C_{\text{obs}}) = 0 \quad (10)$$

Equations of the adjoint model and the numerical scheme of forward and adjoint equations are similar to Wang et al. [13].

**2.3. Optimization of Independent ICs.** In this adjoint model, the optimal parameters should be explored to minimize the cost function  $J$ . Minimization of the cost function is implemented through parameter optimization. This optimization routine is performed through iterative integrations of the governing and adjoint equations.

According to the steepest decent (SD) method, optimization of the control variable is conducted as follows:

$$k_l^{i+1} = k_l^i - \alpha^i \cdot p_l^i \quad (11)$$

In the above-mentioned equations,  $i$  denotes the iteration step,  $k_l$  is the  $l$ -th parameter,  $\alpha$  is the step factor, and  $N$  is the number of independent parameters. It should be noted that  $p$  is the normalized gradient of  $J$  in respect to  $C^0_l$ ,

$$p_l = \frac{\partial J / \partial C^0_l}{\sqrt{\sum_{l=1}^N (\partial J / \partial C^0_l)^2}} \quad (12)$$

The optimized gradients of the IC can be obtained by solving the equation  $\partial L / \partial C^0 = 0$ . We arrive at

$$\frac{\partial J}{\partial C^0} = \left( \frac{\partial p}{\partial t} \right)^0 + (\nabla \cdot \vec{V} p)^0 + (A_H \nabla^2 p)^0 \quad (13)$$

If the ICs at some grid points are selected as independent ICs, we can interpolate these independent ICs to obtain the whole IC by the following equation:

$$k_{i,j} = \sum_{l=1}^N W_{i,j}^l k_l \quad (14)$$

where  $k_{i,j}$  is the parameter at the grid point  $(i,j)$ ,  $k_l$  is the  $l$ -th independent parameter, and  $W_{i,j}^l$  is the coefficient of interpolation. Then the optimized gradients of IC with respect to the  $l$ -th independent IC are

$$\frac{\partial \hat{J}}{\partial C^0_l} = \frac{\partial J}{\partial C^0_l} + \sum_{i,j} W_{i,j}^l \frac{\partial J}{\partial C^0_{i,j}} \quad (15)$$

where  $(i,j)$  denotes grid points within the influence radius of the  $l$ -th independent IC.

Referring to previous studies, the parameters can be obtained by Cressman interpolation (hereafter abbreviated as CI), and the coefficient is traditionally calculated by Zhang et al. [24]:

$$W_{i,j}^l = \frac{w_{i,j}^l}{\sum_{l=1}^N w_{i,j}^l} \quad (16)$$

where  $w_{i,j}^l = (R^2 - (r_{i,j}^l)^2) / (R^2 + (r_{i,j}^l)^2)$  is the Cressman weight,  $r_{i,j}^l$  is the distance between the grid point  $(i,j)$  and the  $l$ -th

independent point, and  $R$  is the influence radius set based on experience.

In this study, the surface spline interpolation is adopted, and the SSI coefficients are shown as follows.

Assuming that ICs are known at  $N$  points, the whole IC filed can be constructed with a variation of the surface spline. The IC at grid points  $(i,j)$  is expressed as [25]

$$C^0_{i,j} = \sum_{l=1}^N A_l \left( \frac{r_{ij,l}^2}{R^2} \ln \frac{r_{ij,l}^2}{R^2} + 1 - \frac{r_{ij,l}^2}{R^2} \right) \quad (17)$$

where  $r_{ij,k}$  is the distance between the  $k$ -th independent point and grid  $(i,j)$ ,  $R$  is a prescribed radius, and  $A_k$  is the coefficient to be determined. Actually, the relationship between the known IC and the others can be expressed in matrix form as

$$WX = Y \quad (18)$$

The detailed forms of the three matrixes are given as

$$\begin{aligned} X &= (A_l)_{N \times 1} \\ Y &= (C^0_l)_{N \times 1} \\ W &= (w_{ij})_{N \times N} \end{aligned} \quad (19)$$

where  $w_{ij} = \begin{cases} 1, & i=j \\ (r_{ij}^2/R^2) \ln(r_{ij}^2/R^2) + 1 - r_{ij}^2/R^2, & i \neq j \end{cases}$  and  $r_{ij}$  is the distance between the  $i$ -th and  $j$ -th independent points. After calculation, we get

$$A_k = \sum_{l=1}^N M_{kl} C^0_l \quad (20)$$

where  $W^{-1} = (M_{kl})_{N \times N}$ . By Plugging (17) into (20), we arrive at

$$C^0_{i,j} = \sum_{l=1}^N W_{i,j}^l C^0_l \quad (21)$$

where  $W_{i,j}^l = \sum_{k=1}^N M_{kl} ((r_{ij,k}^2/R^2) \ln(r_{ij,k}^2/R^2) + 1 - r_{ij,k}^2/R^2)$  is the coefficient corresponding to the  $l$ -th independent IC at the grid  $(i,j)$ .

**2.4. Independent Point Scheme.** Uniform selection of the independent point over the survey region is quite commonly used in the adjoint model (e.g., [14–17]). Although this selecting strategy can be realized easily, but it is not a good choice due to little consideration about the physical characteristics of the research object [18]. As we know, the spatial distribution of  $PM_{2.5}$  presents geographic features. If the independent ICs are selected according to the spatial distribution of  $PM_{2.5}$ , the selection will be more reasonable. At the area where  $PM_{2.5}$  concentration is high, more independent points will be needed. Moreover, fewer independent points will be enough at the area with low  $PM_{2.5}$  concentration.

High concentration of  $PM_{2.5}$  was found in three areas of China: (1) the North China Plain including two of

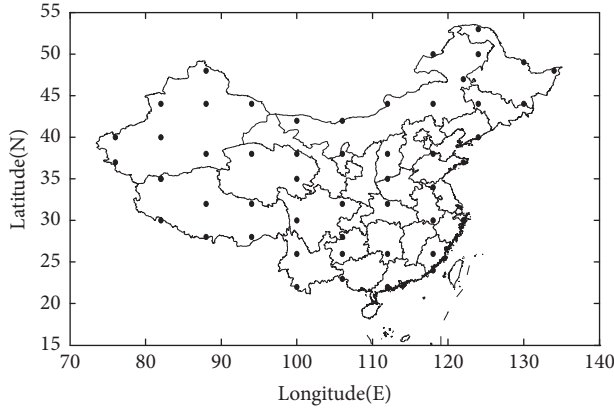


FIGURE 1: Map of computing area and distribution of independent points (dots).

China's four municipalities, Beijing and Tianjin, southern Hebei Province, western Shandong Province, and northern Henan province; (2) the Northeast China Plain; and (3) the Taklimakan desert (e.g., [3, 4]). Therefore, grid points in the above-mentioned high concentration area are selected as independent points from each  $5^\circ \times 5^\circ$  area. Grid points in other areas are selected as independent points from each  $6^\circ \times 6^\circ$  area. In this study, 67 independent points are selected and shown in Figure 1.

**2.5. Settings.** The area of modeling computation is China, covering  $70^\circ$ - $140^\circ$ E and  $15^\circ$ - $55^\circ$ N, with a space resolution of  $0.5^\circ \times 0.5^\circ$ . There are  $141 \times 71$  grids totally in the area. The simulation period is 168 hours and the inverse integral time step is 10 minutes. The wind datasets used in our experiments are the NCEP Final Analysis (GFS-FNL) with spatial resolution of 2.5 degrees and temporal resolution every 24 hours. We get the 0.5-degree data by using bilinear interpolation for space and linear interpolation for time and keep mass conservation of air. The background value is fixed as  $15.0 \mu\text{g}/\text{m}^3$ . Inflow boundary values are fixed equal to the background values. The horizontal diffusion coefficient  $A_H$  is fixed as  $100.0 \text{ m}^2/\text{s}$ .

Seventy-four major Chinese cities are treated as the observation positions. Labeled as "assimilated cities", the observations at these cities are assimilated in the optimization procedure. Meanwhile, Jinan (JNa), Zhengzhou (ZhZ), Shenyang (SY), Quanzhou (QZ), Hangzhou (HaZ), Kunming (KM), Chengdu (CD), and Beijing (BeJ) are selected as "checked cities" to independently evaluate the ability of the model's simulation and inversion. All of the 82 selected cities are shown in Figure 2.  $\text{PM}_{2.5}$  concentrations at the 82 major Chinese cities are taken as the observations every two hours in the present study.

### 3. Numerical Experiments

Results obtained in previous studies indicated that the SSI produced high efficiency to interpolate a smooth and exactly fitting surface based on either scattered data or rectangular-grid data. According to Guo et al. [18], the inverted nonlinear

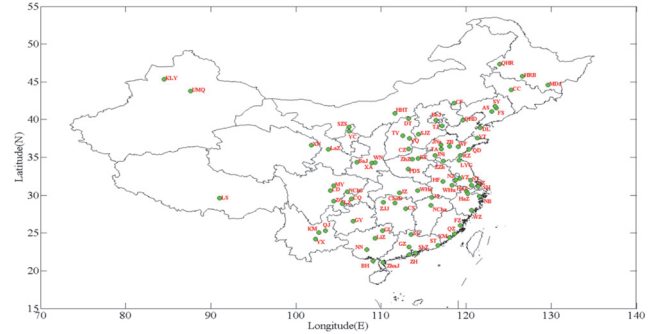


FIGURE 2: Map of computing area and the observation locations of 82 cities. The green dots denote the 82 cities used in the experiments. Full names of these cities can be found in [23].

parameter distribution was smoother than the surface constructed by the traditionally used linear interpolation in a two-dimensional tidal adjoint model. To evaluate the performance of the SSI, totally 12 twin experiments (TEs) are carried out and classified in two groups for the comparison with the CI results in the  $\text{PM}_{2.5}$  adjoint model

For each experiment, we run the forward model with a prescribed IC field. The model-generated  $\text{PM}_{2.5}$  concentrations at grid points of the observing positions shown in Figure 2 are regarded as the "observations". Considering the influence of the noises of in situ observations, we add an estimated maximum error of 5% to the "observations". The forward model is launched with an initial guess of ICs to obtain the simulations. Thereafter, the adjoint model is driven by the discrepancy between simulations and "observations". With variables obtained from the forward and adjoint models, gradients with respect to ICs are calculated. ICs at the independent points can be optimized according to (14). The ICs at other grids are determined by interpolation of the values at the independent points. Repeat the procedure with ICs being optimized until certain criteria are met. The optimization algorithm used in this work is the steepest decent method. And the criterion is that the number of iteration steps is equal to 300 at which the cost function can reach the minimum without large fluctuation. The flowchart of the process is shown in Figure 3.

Performance of the SSI or CI in combination of the adjoint model is evaluated by the mean absolute gross error (MAGE) [26] calculated as follows:

$$\text{MAGE} = \frac{1}{N} \sum_{i=1}^N |M_i - O_i| \quad (22)$$

where  $N$  is the number of observations and  $M$  and  $O$  are the modeled and observed results, respectively.

**3.1. Results and Discussions of Group One.** In Group one, two IC fields are prescribed (see Figure 6): a paraboloid opening downward (TE1) and a folding line distribution (TE2). The TEs focus on evaluating feasibility of the SSI in inversion of the ICs.

TABLE 1: Error statistics of the TEs in Group one before and after assimilation.

Experiment	$J_{300}/J_1^a$	K1 <sup>a</sup> ( $\mu\text{g}/\text{m}^3$ )		K2 <sup>a</sup> ( $\mu\text{g}/\text{m}^3$ )		K3 <sup>a</sup> ( $\mu\text{g}/\text{m}^3$ )		K4 <sup>a</sup>	
		Before	After	Before	After	Before	After	Before	After
SSI (TE1)	9.50e-4	32.81	0.97	29.03	0.89	6.33	1.14	13.34%	6.09%
CI (TE1)	1.96e-3	32.81	1.34	29.03	1.13	6.33	1.43	13.34%	6.66%
SSI (TE2)	1.73e-4	52.57	0.49	49.22	0.36	23.91	7.73	39.25%	14.64%
CI (TE2)	7.60e-4	52.57	1.04	49.22	1.12	23.91	7.87	39.25%	15.17%

<sup>a</sup> $J_{300}$  is the final value of cost function and  $J_1$  is the initial value of cost function. K1 is the MAGEs between simulated values and “observations” in “assimilated cities”. K2 is the MAGEs between simulated values and “observations” in “checked cities. K3 and K4 are the MAGEs and MNGEs between prescribed and inverted IC, respectively.

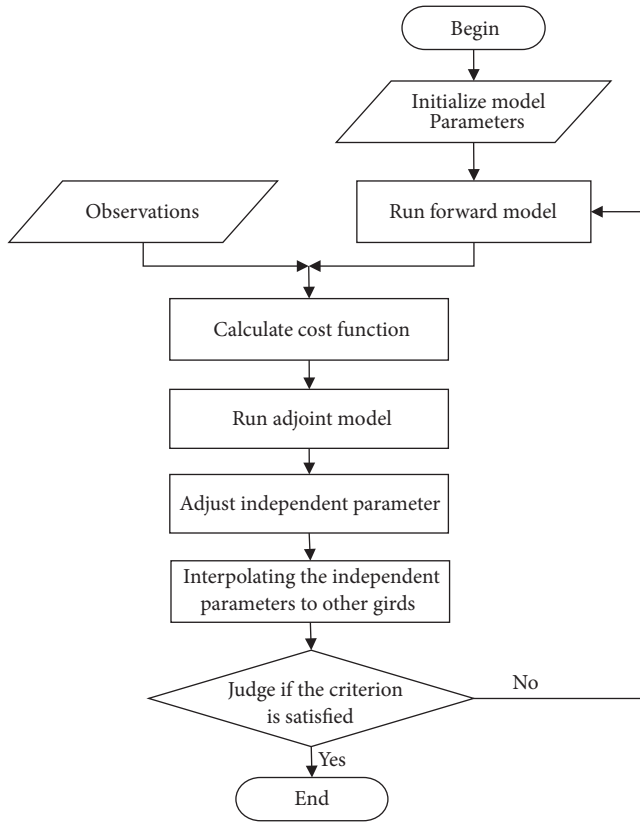


FIGURE 3: Flowchart of the experiments.

Figure 4 presents the iteration histories of the normalized cost function and MAGEs between the prescribed and inverted IC fields. As can be seen, the declining normalized cost function indicates that the misfit between the observations and model results is decreased and the observation data has been assimilated efficiently. Meanwhile, the decreased MAGEs suggest that the ICs are indeed optimized and getting close to the exact solution.

Results of the four TEs are summarized in Table 1. In TE1, it is apparent that the SSI shows an advantage over the CI in the model results. This is demonstrated by the normalized cost function values and the MAGEs between simulated values and “observations” in “assimilated cities” and “checked cities”. In addition, the SSI enables the MAGEs between the prescribed and inverted IC reduced by 81.99%, which is 4.58% better than the results obtained from the CI.

To further quantify the discrepancy between the prescribed and inverted ICs, the mean normalized gross error (MNGE) [26] is used and calculated as follows:

$$\text{MNGE} = \frac{1}{N} \sum_{i=1}^N \left[ \frac{|M_i - O_i|}{O_i} \right] \quad (23)$$

The calculated results are listed in Figure 5. The MNGEs between the prescribed and inverted paraboloid opening downward at the initial iteration step are 13.34%, which are introduced by the difference between the initial guess values and the true values of the adjusted model ICs. After the assimilation, the CI gets the MNGEs reduced to 6.66%, while the SSI gets the MNGEs reduced to 6.09%.

In fact, it is a statement that the SSI provides better interpolation quality. Further evidence to support the conclusion can be seen through the inversion IC showed in Figure 6. As can be seen, the IC fields inverted by the adjoint model combined with both methods are consistent with the prescribed field. The SSI results display smoother pattern, confirming that the SSI shows superiority in reconstructing IC fields in the  $\text{PM}_{2.5}$  adjoint model.

The same conclusions can be drawn from analysis of the TE2 results. The SSI results are superior to the CI results, manifested by the normalized cost function, MAGEs between simulated values and “observations”, and MAGEs between prescribed and inverted IC shown in Table 1. For the SSI simulations, the MAGEs between simulated values and “observations” in the “checked cities” before and after the assimilation are about two percent less than the CI simulations. The MNGEs between the prescribed and inverted folding line distribution at the initial iteration step are 39.25%. After the assimilation, the CI gets the MNGEs reduced to 15.17%, while the SSI gets the MNGEs reduced to 14.63%. Although the SSI gets the MAGEs and MNGEs between prescribed and inverted ICs slightly better than the CI, a smoother IC inversion also highlights the advantages of the SSI (Figure 6).

3.2. Results and Discussions of Group Two. The ill-posedness caused by incomplete number of the observation data is the key part needed to be solved in inversion problem. Feasibility of the SSI in inversion of the ICs is investigated by another group of twin experiments (Group two) under this assumption. According to the geographic distribution of the original 74 observation stations, the number of assimilated stations is

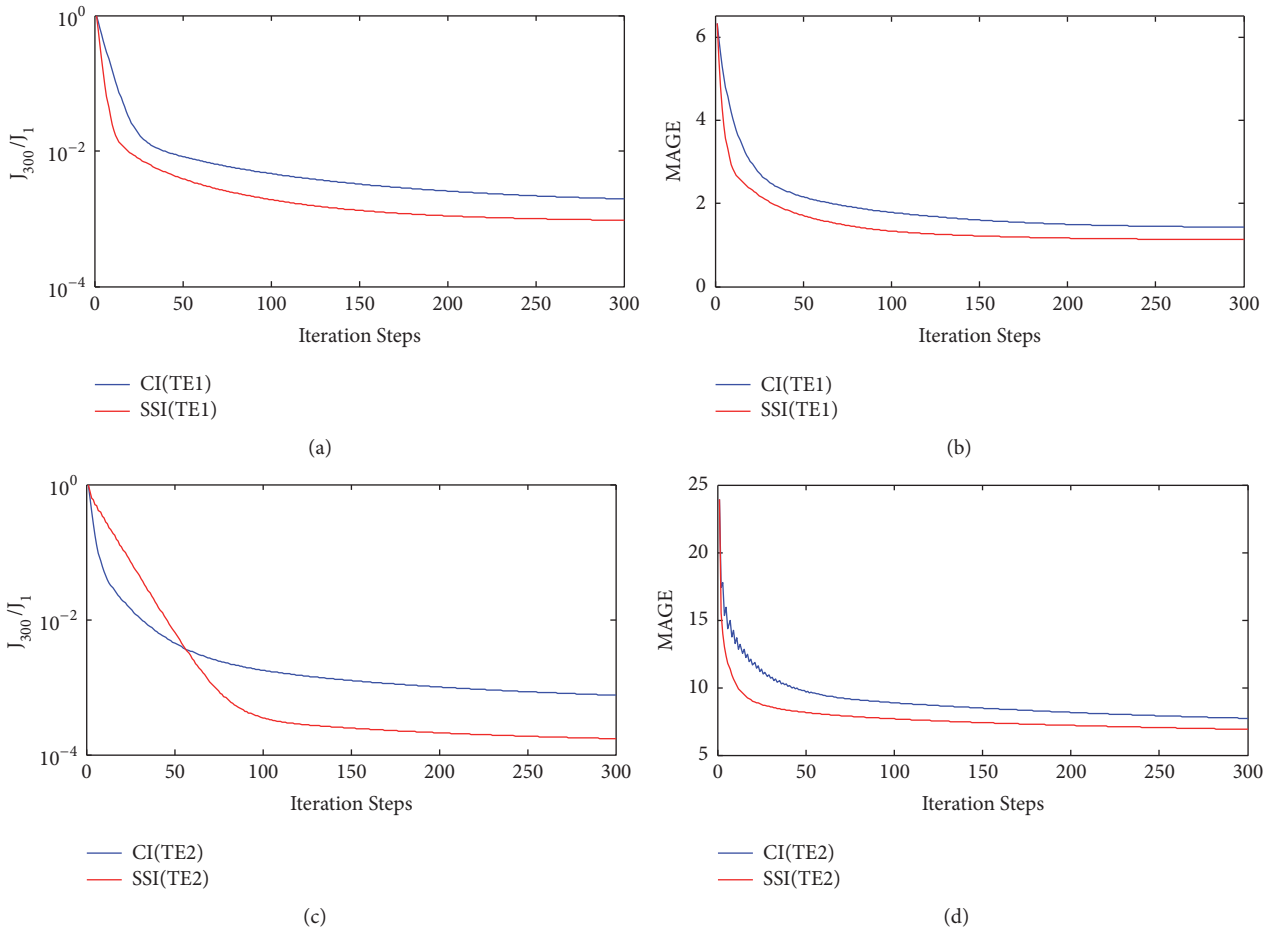


FIGURE 4: Iteration histories of the normalized cost function and the MAGEs between the prescribed and inverted ICs for Group 1.

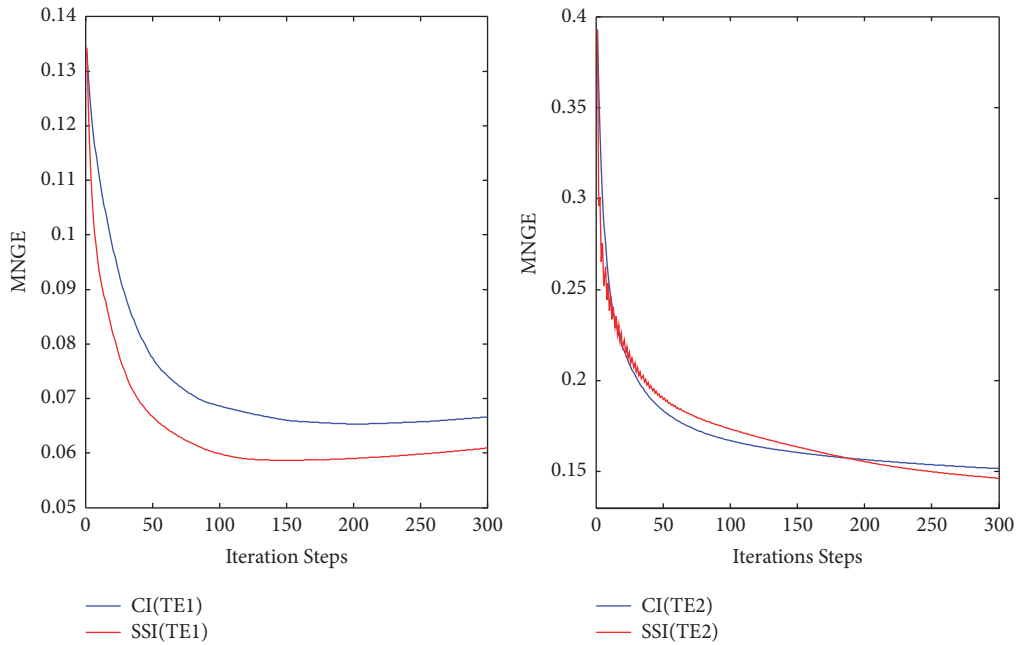


FIGURE 5: Iteration histories of the mean normalized gross errors (MNGEs) between the prescribed and inverted ICs for Group 1.

TABLE 2: Error statistics of TE3 and 4 and observations at 49 sites are assimilated in the TEs.

Experiment	$J_{300}/J_1^a$	K1 <sup>a</sup> ( $\mu\text{g}/\text{m}^3$ )		K2 <sup>a</sup> ( $\mu\text{g}/\text{m}^3$ )		K3 <sup>a</sup> ( $\mu\text{g}/\text{m}^3$ )		K4 <sup>a</sup>	
		Before	After	Before	After	Before	After	Before	After
SSI (TE3)	1.30e-3	30.49	1.06	29.01	0.98	6.33	1.18	13.34%	6.14%
CI (TE3)	2.75e-3	30.49	1.61	29.01	1.35	6.33	1.48	13.34%	6.74%
SSI (TE4)	9.56e-3	53.53	4.37	49.22	4.83	23.91	10.90	39.25%	23.48%
CI (TE4)	1.12e-2	53.53	4.88	49.22	5.35	23.91	11.21	39.25%	29.12%

<sup>a</sup> $J_{300}$  is the final value of cost function and  $J_1$  is the initial value of cost function. K1 is the MAGEs between simulated values and “observations” in “assimilated cities”. K2 is the MAGEs between simulated values and “observations” in “checked cities. K3 and K4 are the MAGEs and MNGEs between prescribed and inverted IC, respectively.

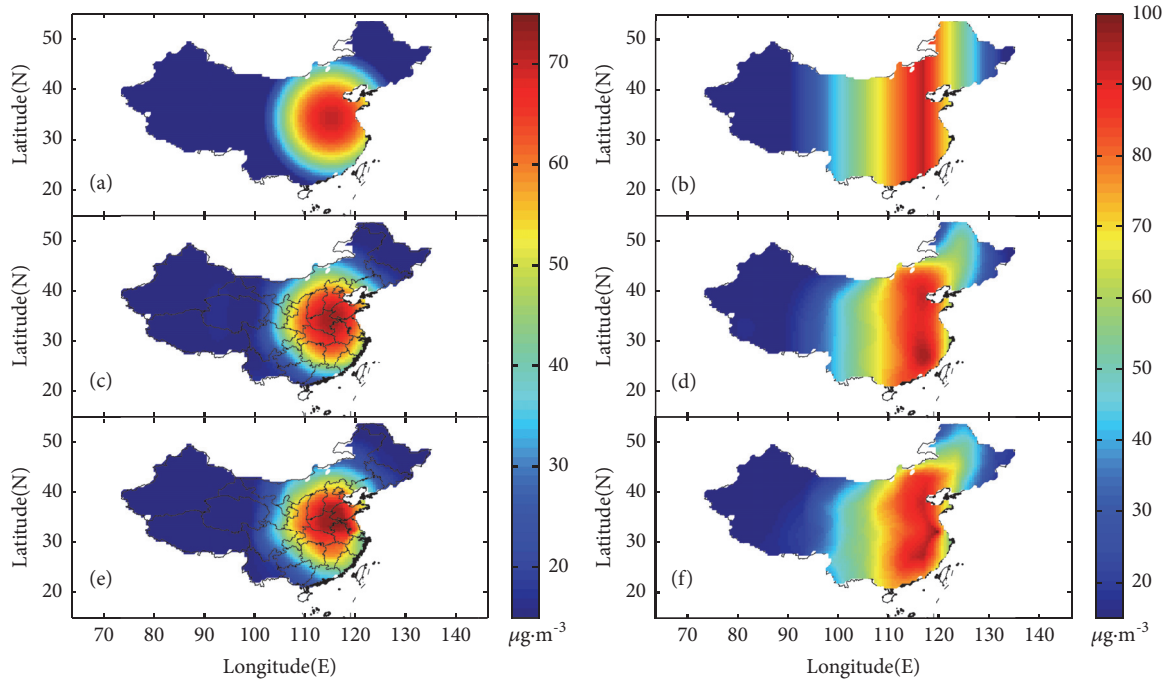


FIGURE 6: Two prescribed IC fields in twin experiments: (a) a paraboloid opening downward (TE1) and (b) a folding line distribution (TE2). The IC fields inverted combined with (c) the SSI and (e) the CI in TE1, (d) the SSI, and (f) the CI in TE2.

artificially reduced by a third and a half, respectively. The two kinds of prescribed IC fields in Group one are inverted in TE3 and TE4 by assimilating the observations at 49 observation sites. Meanwhile, data at 37 sites are taken as the observations in TE5 and TE6. Error statistics of the TEs in Group two are summarized in Tables 2 and 3. The assimilation procedures of the MAGEs and MNGEs between the prescribed and inverted ICs are shown in Figure 7.

As shown in Tables 2 and 3, the cost function can at least reach  $10^{-2}$  of their initial value, indicating the successful ICs inversion in all the TEs. Our direct comparison of the error statics shown in Tables 1–3 indicates that the SSI results remain more accurate than the CI results in all the TEs of this group. Therefore, the following analyses are carried out based on the SSI results.

When the observations at 49 observation sites are assimilated in the adjoint model, the MAGEs between the prescribed and inverted folding line distribution in TE4 are at least 3.43% better than that obtained when 37 observation

sites are adopted in TE6. Meanwhile, the MNGEs in TE4 get a 0.64% advantage than that in TE6. Compared with the inversion of the folding line distribution, the inversion of the paraboloid opening downward is obviously affected by inadequate observations. The MAGEs between the prescribed and inverted paraboloid opening downward are 27.33% worse than that obtained when more observations are used. And the MNGE in TE3 is 1.48% worse than that in TE5. This is consistent with the conclusion obtained by Chertok and Lardner in [27] that the ICs inversions can be more efficient if the provided observations from sufficient number of sites can be used.

Further comparison of the ICs inversion errors demonstrate that the SSI results get less MAGEs and MNGEs than the CI results, when fewer observations are assimilated in the model. All the experiments indicate that the adjoint model combined with the SSI can much effectively overcome the ill-posedness caused by inadequate observations.

TABLE 3: Error statistics of TE5 and 6, observations at 37 sites are assimilated in the TEs.

Experiment	$J_{300}/J_1^a$	K1 <sup>a</sup> ( $\mu\text{g}/\text{m}^3$ )		K2 <sup>a</sup> ( $\mu\text{g}/\text{m}^3$ )		K3 <sup>a</sup> ( $\mu\text{g}/\text{m}^3$ )		K4 <sup>a</sup>	
		Before	After	Before	After	Before	After	Before	After
SSI (TE5)	1.32e-2	32.14	3.49	31.98	5.68	6.33	1.45	13.34%	7.62%
CI (TE5)	2.22e-2	32.14	4.56	31.98	6.02	6.33	1.48	13.34%	7.69%
SSI (TE6)	7.91e-3	52.64	4.04	49.36	5.97	23.91	11.77	39.25%	24.12%
CI (TE6)	9.81e-3	52.64	4.61	49.36	6.00	23.91	11.86	39.25%	25.95%

<sup>a</sup> $J_{300}$  is the final value of cost function and  $J_1$  is the initial value of cost function. K1 is the MAGEs between simulated values and “observations” in “assimilated cities”. K2 is the MAGEs between simulated values and “observations” in “checked cities. K3 and K4 are the MAGEs and MNGEs between prescribed and inverted IC, respectively.

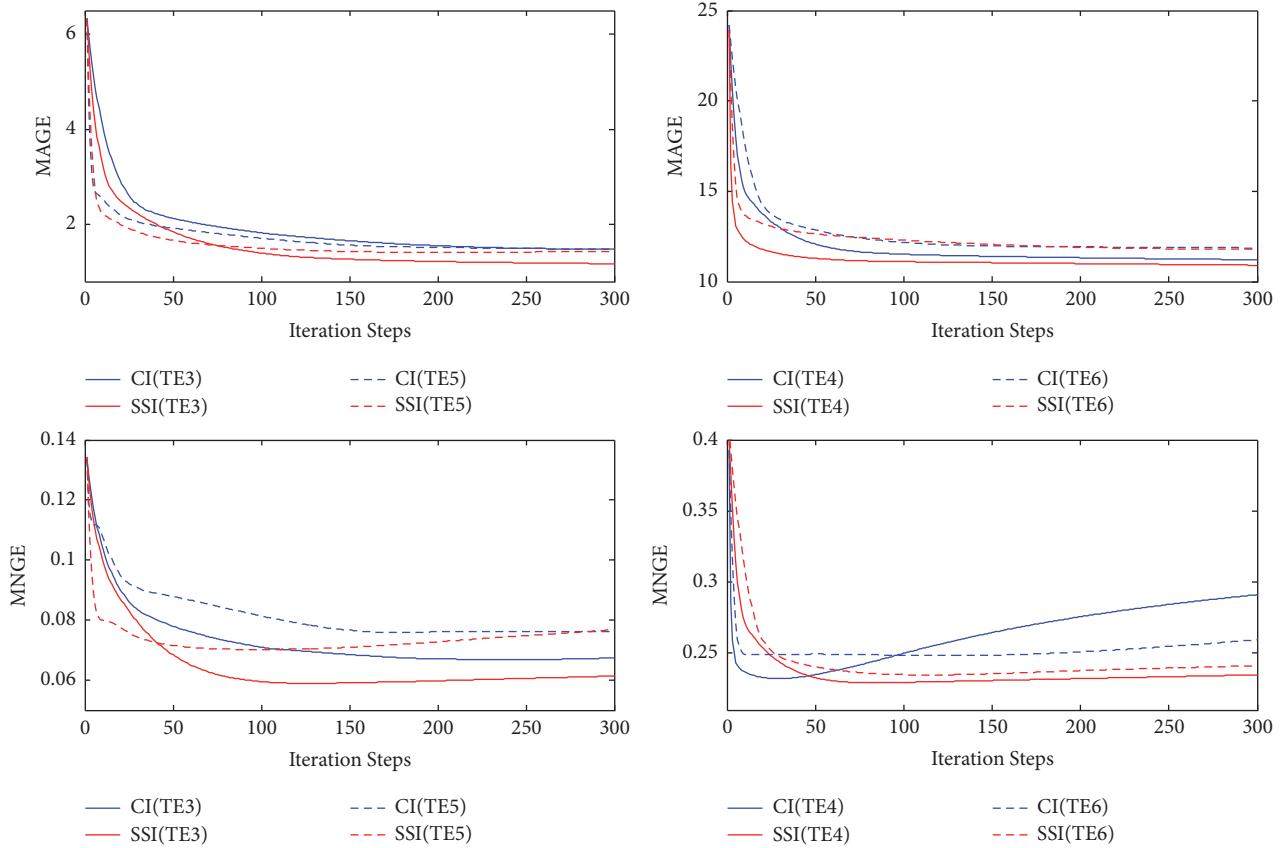


FIGURE 7: Iteration histories of the mean normalized gross errors (MNGEs) between the prescribed and inverted IC for Group 2.

#### 4. Practical Experiments and Discussion

Performance of the adjoint model combined with the two methods is evaluated in a practical context. Hourly ground-level  $\text{PM}_{2.5}$  observations (from 5 November to 11 November 2014) obtained from the Data Center of Ministry of Environmental Protection of the People’s Republic of China (<http://datacenter.mep.gov.cn/>) are assimilated into the model. These observations were measured based on the tapered element oscillating microbalance (TEOM) method (e.g., [10, 28]). Model-produced  $\text{PM}_{2.5}$  concentrations are used for evaluation of the simulated results.

The inverted ICs are shown in Figure 9. On the whole, they show similar patterns that ICs including the northeastern, eastern, central, and northwestern regions are exposed to

hazardous levels of  $\text{PM}_{2.5}$ , which reflects the observations at 5 November 0:00 shown in Figure 8. However, according to the MAGEs between the observations and simulations in all the observation cities at the initial time shown in Table 4, the adjoint model with SSI gets a 2.06% advantage over that with CI. Meanwhile, with a closer inspection, it can be found that the IC surface obtained with SSI is much smoother while that with CI has bumps and depressions around several grids.

Statistical errors are shown in Table 4, which demonstrates that the  $\text{PM}_{2.5}$  simulation is successful with both interpolation methods. The normalized cost function of the SSI and CI is 0.280 and 0.304, respectively. The SSI gets the MAGEs between simulated values and observations at the initial time to be 2.06% better than the CI results. Meanwhile, the MNGEs between simulated values and observations at the

TABLE 4: Error statistics of the practical experiment before and after assimilation.

Experiment	$J_{300}/J_1^a$	K1 <sup>a</sup> ( $\mu\text{g}/\text{m}^3$ )		K2 <sup>a</sup> ( $\mu\text{g}/\text{m}^3$ )		K3 <sup>a</sup> ( $\mu\text{g}/\text{m}^3$ )		K4 <sup>a</sup>	
		Before	After	Before	After	Before	After	Before	After
SSI	2.80e-1	37.87	20.82	42.93	22.15	40.23	24.27	48.88%	37.27%
CI	3.04e-1	37.87	21.65	42.93	23.40	40.23	25.10	48.88%	36.29%

<sup>a</sup> $J_{300}$  is the final value of cost function and  $J_1$  is the initial value of cost function. K1 and K2 are the MAGEs between simulated values and observations in assimilated cities and checked cities, respectively. K3 and K4 are the MAGEs and MNGEs between the observations and simulated results in all the observation cities at the initial time.

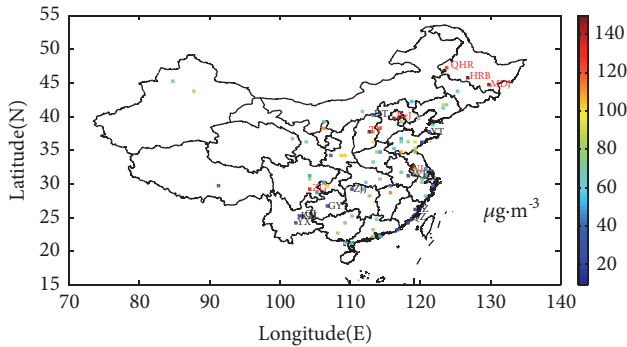


FIGURE 8: Observations at 5 November 0:00.

initial time have a 0.98% advantage, indicating superiority of the SSI. This statement is further validated by the MAGEs between observations and simulations in “assimilation cities” and “checked cities”. Simulations obtained with the SSI are used for further analysis of the model performance.

The values of mean simulations, normalized mean bias (NMB), normalized mean error (NME), and correlation coefficients are calculated as the statistical measures (e.g., [26, 28]) (domain wide averages) and plotted as an hourly time series in Figure 9. A closer inspection of the results indicates that the domain mean simulations show good agreement with the domain mean observations of the assimilation windows. As can be seen from Figure 10, the correlation coefficients, NMB, and NME values at initial time are 0.6289, -54.86%, and 55.36%, respectively, indicating the underestimations of  $\text{PM}_{2.5}$ . Since tapered element oscillating microbalance analyzers (TEOMs, which are commonly used in the EPA-China’s air quality monitoring network) measurements for  $\text{PM}_{2.5}$  should be considered as lower limits because of volatilization of soluble organic carbon species in the drying stages of the measurement [26], the undersimulation is likely to be more severe than this evaluation suggests. This may be caused by the lack of the observations in the first few hours. In addition, the NMB ranges from -27.91% (2:00 Beijing time, 5 November) to 11.93% (16:00 Beijing time, 5 November), most of which is between -10% and 10%. The NME values are approximate to 25.18% which is the NME value of all the observations, indicating the stability of the adjoint model during the selected time. Meanwhile, the correlation coefficients between the domain mean simulations and mean observations are most between 0.80 and 0.95. These results show that the scheme can effectively assimilate the  $\text{PM}_{2.5}$  observations.

The spatial distribution of simulated averaged  $\text{PM}_{2.5}$  concentrations during assimilation window across China is shown in Figure 11. Coal combustion leads to seasonal high level of  $\text{PM}_{2.5}$  concentrations in Northeast China in winter, which rose to 120-160  $\text{mg}/\text{m}^3$  during the assimilation window. Meanwhile, the concentrations are slightly large in middle and east coast of China, which is in conformity with industrial development. Mean  $\text{PM}_{2.5}$  concentrations of Beijing are about 60  $\text{mg}/\text{m}^3$ , half values in the same period of previous years [29]. Air quality in Beijing and nearby provinces are better in the assimilation window, a period which coincided with the introduction of an emergency emissions-reduction strategy during the Asia-Pacific Economic Cooperation (APEC) summit in November. Above spatial distribution were consistent with findings from previous studies [30].

### 5. Summary

The independent point strategy serves as a satisfactory solution to overcome the ill-posedness of the inverse problem caused by excessive control variables. Spatially varying parameter is constructed by interpolating values at a group of independent points under this scenario. In this paper, the independent point strategy is described using the SSI as an alternative to the traditionally used linear interpolation. The adjoint model combined with the SSI is evaluated in simulation of  $\text{PM}_{2.5}$  pollution in China by optimizing the ICs.

In twin experiments, the SSI results outperform the CI in the model simulations and inversion of nonlinear distribution of ICs. The IC fields reconstructed by the SSI are smoother than that by the CI. In addition, the SSI is verified to be more effective in solving the ill-posedness of the inversion problem than the CI. In practical experiments, ICs are optimized and the  $\text{PM}_{2.5}$  concentrations in China are simulated by assimilating the ground-level observations during the 22th APEC. The comparatively accurate  $\text{PM}_{2.5}$  distribution features demonstrate that the SSI plays a positive role in ICs inversion and simulations in practical application.

In conclusion, the SSI inversion strategy is feasible and better than the CI and can improve numerical results to some extent. We can obtain much smoother initial conditions which inverted with the SSI method and therefore are more in line with reality. And the improved IP scheme combined with the SSI is showing promise in the numerical model parameter inversions.

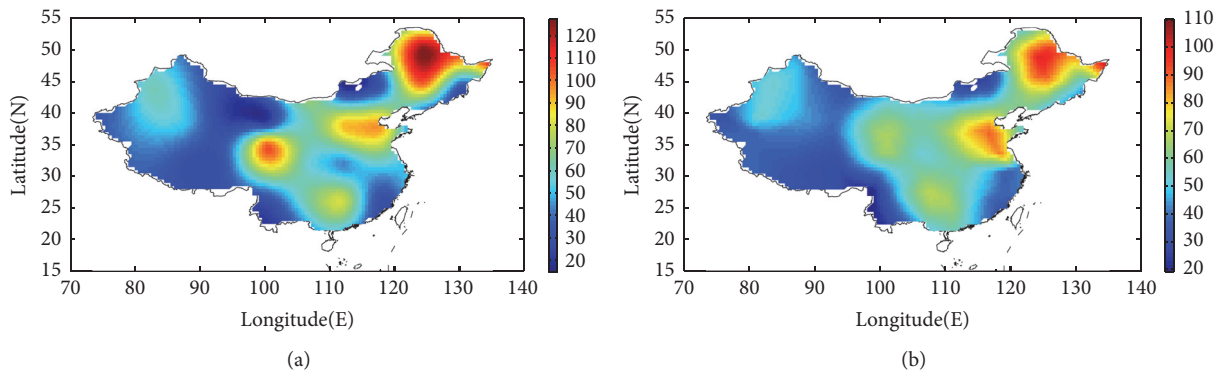


FIGURE 9: Inverted ICs obtained with the adjoint model combined with (a) SSI and (b) CI.

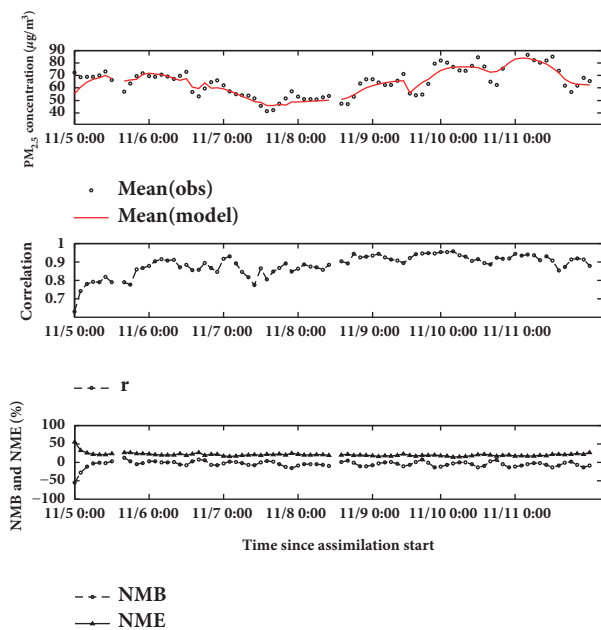


FIGURE 10: Comparison of the modeled and observed  $PM_{2.5}$  concentrations based on the results from the SSI: temporal variation of domain mean, NMB, NME, and correlation.

**Data Availability**

All relevant data are available within the paper. The wind datasets are available from the NCEP Final Analysis (GFS-FNL) with spatial resolution of 2.5 degrees and temporal resolution every 24 hours. Hourly ground-level  $PM_{2.5}$  observations are available from the Data Center of Ministry of Environmental Protection of the People’s Republic of China (<http://datacenter.mep.gov.cn/>).

**Conflicts of Interest**

The authors declare that there are no conflicts of interest regarding the publication of this paper.

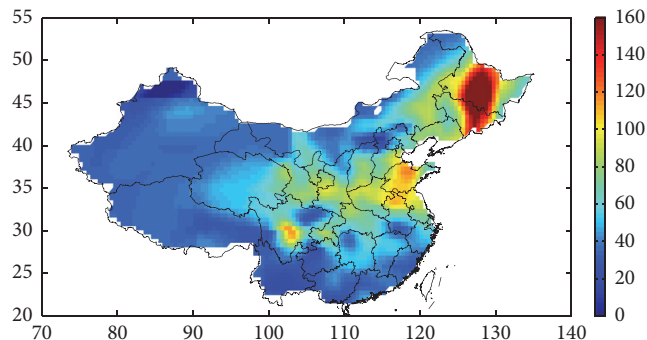


FIGURE 11: Spatial pattern of the average  $PM_{2.5}$  concentrations ( $\mu g/m^3$ ).

**Acknowledgments**

The authors highly appreciate the help and suggestions of the manuscript given by Daosheng Wang. And thanks are due to the surface spline numerical program provided by Haidong Pan. This work was partly supported by the National Key Research and Development Plan through Grants 2017YFC1404000 and 2017YFA0604100, the Natural Science Foundation of Zhejiang Province through Grant LY15D060001, and the Education Department Science Foundation of Liaoning Province of China (no. JDL2017019).

**References**

- [1] L. Han, W. Zhou, and W. Li, “City as a major source area of fine particulate ( $PM_{2.5}$ ) in China,” *Environmental Pollution*, vol. 206, pp. 183–187, 2015.
- [2] Y.-R. Ma, Q. Ji, and Y. Fan, “Spatial linkage analysis of the impact of regional economic activities on  $PM_{2.5}$  pollution in China,” *Journal of Cleaner Production*, vol. 2139, pp. 1157–1167, 2016.
- [3] H. Zhang, Z. Wang, and W. Zhang, “Exploring spatiotemporal patterns of  $PM_{2.5}$  in China based on ground-level observations for 190 cities,” *Environmental Pollution*, vol. 216, pp. 559–567, 2016.
- [4] L. Han, W. Zhou, and W. Li, “City as a major source area of fine particulate ( $PM_{2.5}$ ) in China,” *Environmental Pollution*, vol. 2139, pp. 1157–1167, 2016.

- [5] B. K. Pun and C. Seigneur, "Sensitivity of particulate matter nitrate formation to precursor emissions in the California San Joaquin Valley," *Environmental Science & Technology*, vol. 35, no. 14, pp. 2979–2987, 2001.
- [6] S. Yu, R. Mathur, K. Schere et al., "Evaluation of real-time  $PM_{2.5}$  forecasts and process analysis for  $PM_{2.5}$  formation over the eastern United States using the Eta-CMAQ forecast model during the 2004 ICARTT study," *Journal of Geophysical Research: Atmospheres*, vol. 113, no. 6, Article ID D06204, pp. 304–312, 2008.
- [7] C. Seigneur, "Current status of air quality models for particulate matter," *Journal of the Air & Waste Management Association*, vol. 51, no. 11, pp. 1508–1521, 2001.
- [8] D. K. Henze, J. H. Seinfeld, and D. T. Shindell, "Inverse modeling and mapping US air quality influences of inorganic  $PM_{2.5}$  precursor emissions using the adjoint of GEOS-Chem," *Atmospheric Chemistry and Physics*, vol. 9, no. 16, pp. 5877–5903, 2009.
- [9] L. Zhang, L. Liu, and Y. Zhao, "Source attribution of  $PM_{2.5}$  pollution over North China using the adjoint method," *AGU Fall Meeting Abstracts*, vol. 1, 2014.
- [10] S. Capps, D. K. Henze, and A. G. Russell, "Quantifying relative contributions of global emissions to  $PM_{2.5}$  air quality attainment in the US," *AGU Fall Meeting Abstracts*, vol. 1, 2011.
- [11] S. C. Liu, S. A. McKeen, E.-Y. Hsie et al., "Model study of tropospheric trace species distributions during PEM-West A," *Journal of Geophysical Research: Atmospheres*, vol. 101, no. 1, pp. 2073–2085, 1996.
- [12] K. Fu and D. Liang, "The conservative characteristic FD methods for atmospheric aerosol transport problems," *Journal of Computational Physics*, vol. 305, pp. 494–520, 2016.
- [13] D. Wang, N. Li, Y. Shen, and X. Lv, "The parameters estimation for a  $PM_{2.5}$  transport model with the Adjoint method," *Advances in Meteorology*, vol. 9, Article ID 9873815, pp. 1–13, 2016.
- [14] D. Wang, A. Cao, J. Zhang, D. Fan, Y. Liu, and Y. Zhang, "A three-dimensional cohesive sediment transport model with data assimilation: Model development, sensitivity analysis and parameter estimation," *Estuarine, Coastal and Shelf Science*, 2017.
- [15] D. Wang, J. Zhang, Y. P. Wang et al., "A methodology for estimating the parameters in three-dimensional cohesive sediment transport models by assimilating in situ observations with the adjoint method," *Journal of Atmospheric and Oceanic Technology*, vol. 34, no. 7, pp. 1469–1482, 2017.
- [16] D. Wang, J. Zhang, X. He et al., "Parameter estimation for a cohesive sediment transport model by assimilating satellite observations in the Hangzhou Bay: Temporal variations and spatial distributions," *Ocean Modelling*, vol. 121, pp. 34–48, 2018.
- [17] N. Li, Y. Liu, X. Lv, J. Zhang, and K. Fu, "The High Order Conservative Method for the Parameters Estimation in a  $PM_{2.5}$  transport adjoint model," *Advances in Meteorology*, vol. 2017, pp. 1–13, 2017.
- [18] Z. Guo, H. Pan, W. Fan, and X. Lv, "Application of surface spline interpolation in inversion of bottom friction coefficients," *Journal of Atmospheric and Oceanic Technology*, vol. 34, no. 9, pp. 2021–2028, 2017.
- [19] G. D. Knott, "Interpolating cubic splines," *Progress in Computer Science and Applied*, vol. 11, pp. 319–321, 1999.
- [20] R. L. Harder and R. N. Desmarais, "Interpolation using surface splines," *Journal of Aircraft*, vol. 9, no. 2, pp. 189–191, 1972.
- [21] J. S. Wijnands, G. Qian, and Y. Kuleshov, "Spline-based modelling of near-surface wind speeds in tropical cyclones," *Applied Mathematical Modelling: Simulation and Computation for Engineering and Environmental Systems*, vol. 40, no. 19–20, pp. 8685–8707, 2016.
- [22] S. Yaghoobi, B. P. Moghaddam, and K. Ivaz, "An efficient cubic spline approximation for variable-order fractional differential equations with time delay," *Nonlinear Dynamics*, vol. 87, no. 2, pp. 815–826, 2017.
- [23] W. J. Qu, R. Arimoto, X. Y. Zhang et al., "Spatial distribution and interannual variation of surface  $PM_{10}$  concentrations over eighty-six Chinese cities," *Atmospheric Chemistry and Physics*, vol. 10, no. 12, pp. 5641–5662, 2010.
- [24] J. Zhang and Y. P. Wang, "A method for inversion of periodic open boundary conditions in two-dimensional tidal models," *Computer Methods Applied Mechanics and Engineering*, vol. 275, pp. 20–38, 2014.
- [25] D. Liu, J. Zhang, and S. Wang, "Constrained fitting of faulted bedding planes for three-dimensional geological modeling," *Advances in Engineering Software*, vol. 33, no. 11–12, pp. 817–824, 2003.
- [26] Y. Zhang, M. Bocquet, V. Mallet, C. Seigneur, and A. Baklanov, "Real-time air quality forecasting, part I: history, techniques, and current status," *Atmospheric Environment*, vol. 60, pp. 632–655, 2012.
- [27] D. L. Chertok and R. W. Lardner, "Variational data assimilation for a nonlinear hydraulic model," *Applied Mathematical Modelling*, vol. 20, no. 9, pp. 675–682, 1996.
- [28] Y. Zhang, M. Bocquet, V. Mallet, C. Seigneur, and A. Baklanov, "Real-time air quality forecasting, part II: state of the science, current research needs, and future prospects," *Atmospheric Environment*, vol. 60, pp. 656–676, 2012.
- [29] K. B. He, F. Yang, Y. Ma et al., "The characteristics of  $PM_{2.5}$  in Beijing, China," *Atmospheric Environment*, vol. 35, no. 29, pp. 4959–4970, 2001.
- [30] J. L. Hu, Y. Wang, Q. Ying, and H. Zhang, "Spatial and temporal variability of  $PM_{2.5}$  and  $PM_{10}$  over the North China Plain and the Yangtze River Delta, China," *Atmospheric Environment*, vol. 95, pp. 598–609, 2014.

## Research Article

# Economic and Environmental Effects of Public Transport Subsidy Policies: a Spatial CGE Model of Beijing

Ping Xu <sup>1</sup>, Weiyu Wang,<sup>2</sup> and Chunxia Wei <sup>1</sup>

<sup>1</sup>*School of Economics, Beijing Technology and Business University, Beijing 100048, China*

<sup>2</sup>*Tax Institute of State Administration of Taxation, Yangzhou 225007, China*

Correspondence should be addressed to Ping Xu; xuping@th.btbu.edu.cn

Received 12 April 2018; Accepted 27 May 2018; Published 14 June 2018

Academic Editor: Xander Wang

Copyright © 2018 Ping Xu et al. This is an open access article distributed under the Creative Commons Attribution License, which permits unrestricted use, distribution, and reproduction in any medium, provided the original work is properly cited.

Public transport plays an important role in the environment. This study established a Spatial Computable General Equilibrium (SCGE) model to examine the economic and environmental effects of public transport subsidy policies. The model includes firms, consumers, and traffic modules in one framework. Statistical data from Beijing were used in calibration to obtain benchmark equilibrium. Based on the equilibrium, simulations compared citywide social welfare, jobs-housing spatial population distribution, and environmental outputs under four subsidy policies: fare subsidy, cash grants, road expansion, and public transport speedup. Based on the results regarding the effects of public transport policies, conclusions can be drawn about which policies will have greater overall social influence and should therefore be used.

## 1. Introduction

Public transport has acquired increasing significance in urban residential life, and governments all over the world provide different forms of transport-related subsidies. In 2005, for example, transport subsidies in the EU reached 270 billion euros, of which about 50% was utilized for road infrastructure construction. In 20 public transport systems in the United States, subway fare subsidies accounted for 29%–89% of operating costs, while bus fare subsidies accounted for as much as 57%–89% [1]. The case is similar in Beijing, China, where cumulative bus subsidies reached 122.5 billion in 2015, following the low-fare policy initiated in 2007. The economic and environmental effects of public transport subsidies are controversial topics among sociologists and policymakers.

The main purpose of public transport subsidy policies is to provide transit services to citizens. As such, studies have focused on the transit quality issue from various dimensions. Hensher, Stopher, and Bullock [2] investigated ways to quantify service quality and compare levels within and between bus operators. Eboli and Mazzulla [3] proposed a methodology for measuring transit service quality based on the use of both passenger perceptions and transit agency

performance measures. Hassan, Hawas, and Ahmed [4] combined subjective and objective measures to assess service quality. These studies have laid a solid theoretical foundation for the evaluation and development of public transport systems. Although measuring efficiency and effectiveness of transit services is very important, those studies did not consider the social effects of subsidy policies or reveal the subsidies' mechanisms of action.

Given the influence of subsidies on transport costs and travel times, some studies have investigated those effects from the perspective of social welfare. There are two noteworthy yet contrasting theories that either support subsidy policies or suggest canceling them.

Based on the Mohring effect [5], Jara-díaz and Gschwendter [6] acknowledged that government subsidies can guarantee adequate public transport services at fair prices. Santos, Behrendt, and Maconi et al. [7] suggested that if the use of private cars could not be charged at calculated full social costs, the suboptimal option would be to reduce public transport prices to enhance its substitutability for private cars. In a general model-based study, Parry and Small [1] found that related social welfare will still improve, even if a subsidy exceeds two-thirds of the total operating costs.

Other scholars, however, believe the effects of subsidies are limited and negligible. Hensher [8] argued that lowering service fares with subsidy support provided no significant improvement in the public transport split rate. Proost and Dender [9] argued that even if rush hour fares were fully subsidized, the rise in social welfare would be limited. Savage [10], moreover, suggested that subsidies could create inefficiencies in public transport companies since their management costs would increase faster with government subsidies. All of the abovementioned research has focused mainly on traffic, travel costs, and resident welfare. However, it has overlooked the effects of subsidies on residents' work-leisure choices and on population distribution.

Some studies have focused on the effects of subsidies on labor supply. Richter [11], for example, argued that subsidizing commuter traffic would be equivalent to taxing leisure and would thus stimulate labor supply. Borger and Wuyts [12] suggested that public transport subsidies could reduce the car travel demand, parking cost, and congestion issues as an embodiment of positive externalities. Dender [13] argued that subsidizing commuter trips would bring about significant efficiency improvements. Basso et al. [14, 15] compared the efficiency and substitutability of three different policies. These researches, however, only considered effects on the labor market without considering the effect of subsidies on consumers' choices for job-housing locations.

By introducing the concept of "space" into the research framework, the function of subsidies can be studied based on their action mechanisms in the spatial distribution of populations. The classical monocentric urban model assumes that transport subsidies will decrease the bid-rent curve slope, resulting in a larger urban area, lower population density, and a reduced suburban-urban rent differentiation, though they will cause urban expansion and road congestion [16, 17]. In light of such negative effects, Borck and Wrede [18], adopting the perspective of political economy, considered the political ramifications of government decisions to subsidize public transport as a form of income redistribution. In contrast, the multicenter urban model argues that transport subsidies can optimize the allocation of labor if there are wage differences, agglomerative economies, or job-housing spatial imbalances between zones. Martin [19] suggested that subsidies could gradually reduce the job-housing imbalance among low-income groups. Accordingly, Zenou [20] noted that different subsidies had varied effects on alleviating the job-housing imbalance among low-income groups. Borck and Wrede [21] argued that transport subsidies could reduce the distortions of residents' employment decisions caused by payroll taxes and internalize the externality of the employment area, resulting in more efficient labor allocation. The abovementioned studies considered both the labor market and job-housing location choices. Despite taking into account the spatial effects of subsidies, labor supply was usually considered as an exogenous variable for the convenience of calculation, regardless of the interactions between subsidies and "work-leisure" policies, consumption, or other factors.

Recently, a growing body of literature has assessed the environmental effects or external costs of transit. Ayyildiz et al. [22] compared fuel consumption and carbon emissions in

terms of driving styles before and after eco-driving training. Tong et al. [23] estimated the life-cycle ownership costs for buses and infrastructure as well as the environmental externalities of greenhouse gases and air pollutants emitted during the life cycle of buses powered by alternative fuels. These studies have shown that environmental effects are significant and should not be ignored when considering transport effects.

Subsidies have been shown to have prominent effects on social welfare, labor markets, and population distribution in diversified mechanisms. However, most previous studies have focused on such effects in terms of individual aspects as opposed to combining several different outputs into one analysis framework. Excising subsidies-involved variables from the resulting effects and neglecting the mechanisms of interactions can give rise to unilateralism in research results. Although computable general equilibrium (CGE) has been widely used in many studies, gradually becoming a mainstream approach for policy analysis models, only Tschaaktschiew and Hirte [24] have investigated transport subsidies using a CGE framework model—specifically, a spatial CGE model that considered "spatial" decisions. In addition, there have not been sufficient comparative studies of different levels and forms of subsidies, especially in terms of quantitative effects, all of which have practical significance for policymakers. Therefore, it is necessary to incorporate the effects of public transport subsidies on social welfare, labor markets, and the environment, as well as the mechanisms of various subsidies, into a framework system for further survey and discussion.

To investigate these practical problems, taking Anas and Xu [25] and Tschaaktschiew and Hirte [24] as the basis, this study constructed a SCGE model integrating traffic, social welfare, job-housing spatial choice, CO<sub>2</sub> emissions, and other factors into a framework based on the rudimentary theory of traffic and spatial economics. The goal of this discussion is to explain and analyze the comprehensive effects of public transport subsidies on city development, provide guidelines for improving subsidy policies, and deliver more efficient services to communities. The rest of this paper is organized as follows. Section 2 builds the public transport subsidy SCGE model. Section 3 describes the parameter calibration using data of Beijing and benchmark equilibrium. Section 4 explains the scenario design of the policies and presents simulation results and analysis. Section 5 concludes the paper and gives suggestions.

## 2. SCGE Model of Public Transport Subsidy

Assume that, in a typical circular city, a wedge-shaped city area with incision angle  $\varphi$  is studied, and the entire area is divided into  $I=9$  distinct zones, as shown in Figure 1. Among these nine zones, the central zone, where  $i=5$  is assigned as downtown, has a diameter of  $d_i$ , and the rest of the zones share a width of  $d_i$  as well.

As shown in Figure 1, zones 3–7 are urban areas, while zones 1, 2, 8, and 9 are suburban areas. Therefore, the downtown area is  $1/2d_i^2\pi\varphi$ , and the area of the remaining

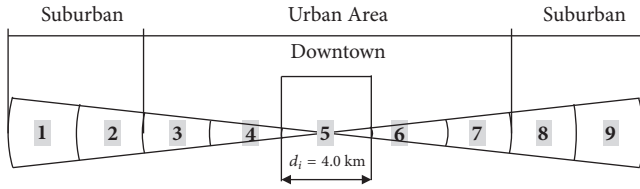


FIGURE 1: Structure of a wedge-shaped city.

zones  $i$  can be represented as  $A_i = \varphi\pi(R_i^2 - R_{i-1}^2)$ , where  $R_{i-1}$  and  $R_i$  are the inner and outer radiuses, respectively, for a certain zone. This assumption complies with the fact that the larger the distance between a zone and downtown, the more adequate the land supplies, which facilitates the model computation of travel distances.

**2.1. Firms Module.** It is assumed that firm production activities are distributed in all zones and that each zone produces only one kind of composite product exclusively. Land and labor markets are perfectly competitive markets. For zone  $i$ , the land market, labor market, and product market will clear in the zone, resulting in equilibrium rent  $r_i$ , wage  $w_i$ , and product price  $p_i$ . The Cobb-Douglas function is used as the production function. Further, only two types of inputs are discussed here—land and labor—without considering the number of firms. The aggregate output of zone  $i$  is  $X_i$ ;  $M_i$  and  $Q_i$  stand for the amount of labor input and land input in the zone, respectively. Then, the production equation of firms is

$$X_i = BM_i^\delta Q_i^\mu \quad \delta + \mu = 1, \quad (1)$$

where  $B$  is the efficiency coefficient and  $\delta$  and  $\mu$  are the output elasticities of labor and land. To obtain the maximal profit for firms, the conditional input demand functions are

$$\begin{aligned} M_i^* &= \delta p_i X_i w_i^{-1} \text{ and} \\ Q_i^* &= \mu p_i X_i r_i^{-1}, \end{aligned} \quad (2)$$

and the cost function is

$$C(w_i, r_i, X_i) = (B\delta^\delta \mu^\mu)^{-1} w_i^\delta r_i^\mu X_i \quad (3)$$

Free entry in each zone for all firms leads to equivalence in product equilibrium price and its marginal cost, which gives

$$p_i = [B\delta^\delta (1 - \delta)^{1-\delta}]^{-1} w_i^\delta r_i^{1-\delta}. \quad (4)$$

**2.2. Consumer Module.** Assume there are  $N$  consumers in the city. A consumer resides in some zone  $i$ , works in some zone  $j$ , and shops in some zone  $k$ . Thus, the consumer's work-home one-way commute distance is  $d_{ij}$ , and the one-way shopping travel distance is  $d_{ik}$ . Zone determination  $(i, j)$  stands for the residence-job location choice for the customer, which is an endogenous variable. In reality, customers can purchase products from any zone. However, to simplify calculations, residents are limited to purchasing one unit of a single kind of good without considering "trip chain." Therefore, as for

characteristic parameters under this limitation, the number of trips the consumer takes to zone  $k$ , represented by  $Z_{ijk}$ , is equal to the quantity of bought goods. Further, the lot size is  $q_{ij}$ , and leisure time is  $L_{ij}$ .

Under the income constraint, a consumer achieves utility maximization through buying composite products, making full use of the living space, and enjoying leisure time. Stochastic utility function  $U_{ij}$  is introduced to describe the consumer's choice:

$$U_{ij} = a \ln \left( \sum_{k=1}^I Z_{ijk}^\eta \right)^{1/\eta} + \beta \ln q_{ij} + \gamma \ln L_{ij} + u_{ij} \quad (5)$$

$$\alpha, \beta, \gamma > 0, \quad \alpha + \beta + \gamma = 1, \quad 0 < \eta < 1.$$

In this equation, the constant elasticity of substitution (CES) utility function is adopted as the subutility of purchase product  $Z_{ijk}$ , and the constant elasticity of substitution  $1/(1 - \eta)$  reflects the consumer's preference for shopping zones. When  $\eta$  approaches 1, the utility function develops into a linear elasticity of substitution function where the consumer chooses to make purchases in zones with minimum full economic shopping cost. When  $\eta$  approaches negative infinity, the utility function evolves into a complete complementary function where the consumer makes purchases based only on his or her demands, regardless of the full economic shopping costs.

In addition, the idiosyncratic taste constant  $u_{ij}$  is a heterogeneous preference variable that depicts the features of varied consumers and their preference differences in residence-job spatial choices. As in many other studies [24, 25], it is hypothesized here that idiosyncratic tastes are independently and identically distributed for each location choice  $(i, j)$ —namely, without spatial correlation. After considering his or her own heterogeneous preference, the consumer will make decisions about the optimal residence-job location. Assuming  $(i, j)$  pairs display a discrete distribution, the probability that a consumer chooses a specific  $(i, j)$  pair to achieve maximum utility  $U_{ij}^*$  is

$$\begin{aligned} \Psi_{ij} &= \text{Prob} [U_{ij}^* > U_{sm}, \forall (s, m) \neq (i, j)] \\ &= \text{Prob} [V_{ij} + u_{ij} > V_{sm} + u_{sm}, \forall (s, m) \neq (i, j)], \end{aligned} \quad (6)$$

where  $V_{ij}$  is the fixed utility partition. As discussed above, the i.i.d.  $u_{ij}$ 's are Gumbel distributed with expected value  $E[u_{ij}] = 0$ , standard variance  $\sigma^2$ , and dispersion parameter  $\lambda = \pi/(\sigma\sqrt{6})$ . Therefore, the probability of the consumer choosing residence-job location  $(i, j)$  can be described with a multinomial logit model:

$$\Psi_{ij} = \frac{\exp(\lambda V_{ij})}{\sum_{s=1}^I \sum_{m=1}^I \exp(\lambda V_{sm})} \quad (7)$$

$$\sum_{i=1}^I \sum_{j=1}^I \Psi_{ij} = 1.$$

Dispersion parameter  $\lambda$  mirrors the preference heterogeneity of all consumers in the zones. When  $\lambda \rightarrow \infty$ ,

consumer preferences demonstrate high-level homogeneity, and they tend to make identical decisions. In this case, the probability  $\Psi_{ij}$ , which corresponds to maximum utility  $V_{ij}$ , approaches 1, while other possibilities diminish. Meanwhile, when  $\lambda \rightarrow 0$ ,  $V_{ij}$ , the systematic part of utility is masked with heterogeneity, meaning that consumers choose working and living zones randomly, and each  $(i, j)$  pair's probability of being chosen is  $\Psi_{ij} = 1 / I^2$ .

Changes in social welfare are measured by the Hicksian equivalent variation (EV>0 for a welfare-improving policy)—that is, the equivalent income transfer necessary to compensate a household in the prepolicy benchmark case in order to reach equality with the postpolicy utility level. Overall utility, in turn, is calculated as the expected value of maximized utilities. Based on the probability hypothesis mentioned above, the maximum utility is also in compliance with Gumbel distribution, which derives the expected value of the maximized utilities as

$$E \left[ \max_{ij} (V_{ij} + u_{ij}) \right] = \frac{1}{\lambda} \ln \sum_{s=1}^I \sum_{m=1}^I \exp(\lambda V_{sm}). \quad (8)$$

To maintain model conciseness and research focus, it is assumed that the city economy is closed. The number of work days in a year for a consumer is  $D$ , and  $p_k$  stands for composite product price in zone  $k$ .  $c_{ij}(tm, \Gamma_i)$  is the one-way commuting travel cost from residential zone  $i$  to working zone  $j$ ;  $c_{ik}(tm, \Gamma_i)$  is the one-way shopping travel cost from zone  $i$  to shopping zone  $k$ ;  $t_{ij}(tm, \Gamma_i)$  is the one-way commuting time from residential zone  $i$  to working zone  $j$ ; and  $t_{ik}(tm, \Gamma_i)$  represents the one-way shopping travel time from zone  $i$  shopping zone  $k$ . Travel cost  $c_{i\xi}(tm, \Gamma_i)$  and travel time  $t_{i\xi}(tm, \Gamma_i)$  are both determined by travel modes  $tm$  and traffic condition  $\Gamma_i$ , where  $\xi \in [j, k]$ .

Excluding the bicycle, as it is a travel mode of less proportion, walking, private cars, and public transport are included as travel modes in the discussion—specifically,  $tm \equiv \{\text{walking, car, public transport}\}$ .  $\Gamma_i$  represents the traffic congestion condition and is defined as the ratio of road traffic flow and road capacity:  $\Gamma_i \equiv F_i / K_i$ , in which  $F_i$  is the double-sided traffic flow through zone  $i$  every day, including commuting and shopping trips, and  $K_i$  is the road area of zone  $i$  (road capacity).  $s^{tm}$  is the government subsidy ratio for travel mode  $tm$ , and  $S$  represents the cash grant by the government.  $M_{ij}$  is the labor hours supplied annually by the consumer. Then, the budget constraint of a consumer facing location choice  $(i, j)$  is

$$\sum_{k=1}^I Z_{ijk} [p_k + 2c_{ik}(tm, \Gamma_i)(1 - s^{tm})] + r_i q_{ij} + 2Dc_{ij}(tm, \Gamma_i)(1 - s^{tm}) = w_j M_{ij} + S. \quad (9)$$

The left side of (9) represents the consumer's total annual cost, including full shopping costs, housing expenses, and commuting costs. The full shopping cost comprises product price and travel cost after government subsidies. The right side of (9) is the disposable income of the consumer. In addition to budget constraints, the consumer is also subject

to time constraints.  $E$  represents the total annual time endowment, and  $T_{ij}$  represents commuting and shopping travel time. Then, we have

$$M_{ij} + T_{ij} + L_{ij} = E, \text{ and} \quad (10)$$

$$T_{ij} = 2Dt_{ij}(tm, \Gamma_i) + \sum_{k=1}^I 2t_{ik}(tm, \Gamma_i) Z_{ijk}. \quad (11)$$

### 2.3. Transport Module

**2.3.1. Travel Cost.** The consumer's travel cost includes two parts: variable cost and fixed cost.  $c^{1,tm}$  is the variable cost with travel mode  $tm$ , —namely, travel cost per km except for gasoline cost. Compared to walking and public transport, the variable travel cost of a private car includes gasoline cost, and  $c^{2,car}$  is gasoline price per liter, while  $g_{i\xi}^{car}$  is gas consumption for traveling from zone  $i$  to zone  $\xi$ .  $c^{3,tm}$  is the fixed cost with travel mode  $tm$ . Thus, one-way travel cost from zone  $i$  to zone  $\xi$  is

$$c_{i\xi}^{tm} = c^{1,tm} d_{i\xi} + c^{2,car} \times g_{i\xi}^{car} + c^{3,tm}. \quad (12)$$

In general, there is no congestion in walking and public transport (public transport in Beijing includes rail traffic and road traffic. Normally, there is no congestion in rail traffic. As a result of using dedicated bus lanes, there is only slight congestion in road traffic during the morning and evening rush hours). Under these two travel modes,  $v^{tm}$  is the average speed with travel mode  $tm$ , which gives one-way travel time from zone  $i$  to zone  $\xi$  as  $t_{i\xi}^{tm} = d_{i\xi} / v^{tm}$  in which  $tm = \{\text{walking, public transport}\}$ .

As for private car travel, travel speed and time depend on road congestion conditions. Adopting the commonly used BPR congestion function, a traveler spends an amount of time driving 1 km in zone  $i$  by private car as follows:

$$t_i^{car}(F_i, K_i) = d_{i0} \left[ 1 + b \left( \frac{F_i}{K_i} \right)^c \right] \quad d_{i0}, b > 0, c \geq 1, \quad (13)$$

where  $d_{i0} = 1/v_0$  is travel time by private car moving smoothly for 1 km in zone  $i$  and  $v_0$  is average speed without congestion. Larger values of  $b$  and  $c$  would result in exponential increments in estimated travel time.

Taking into consideration these three travel modes, and using  $Pro_{i\xi}^{tm}$  to denote the probability of choosing a specific travel mode, travel cost and time from zone  $i$  to  $\xi$  will be

$$c_{i\xi}(tm, \Gamma_i) = \sum_{tm} Pro_{i\xi}^{tm} c_{i\xi}^{tm}, \text{ and} \quad (14)$$

$$t_{i\xi}(tm, \Gamma_i) = \sum_{tm} Pro_{i\xi}^{tm} t_{i\xi}^{tm}. \quad (15)$$

Travel mode choice probability  $Pro_{i\xi}^{tm}$  is characterized using a multinomial logit model.  $V_{i\xi}^{tm}$  is the fixed utility with travel mode  $tm$ .  $l_1$  and  $l_2$  outline the effect of travel cost and

time, respectively.  $b^{tm}$  is a constant measuring other factors aside from travel time and cost.

$$Pro_{i\xi}^{tm} = \frac{\exp(V_{i\xi}^{tm})}{\sum_{tm} \exp(V_{i\xi}^{tm})}, \text{ and} \quad (16)$$

$$V_{i\xi}^{tm} = b^{tm} + l_1 c_{i\xi} + l_2 t_{i\xi}. \quad (17)$$

**2.3.2. Gas Consumption and CO<sub>2</sub> Emissions.** Traveling by private car engenders gasoline consumption and CO<sub>2</sub> emissions. Travel time, amount of gas consumption, and CO<sub>2</sub> emission are endogenous variables and are determined by travel speed. Thus, the amount of gas consumption when traveling 1 km in zone  $i$  by private car is

$$g_i^{car}(F_i, K_i) = \frac{1}{740} e \left[ e_0 + e_1 \left( \frac{1}{t_i^{car}(F_i, K_i)} \right)^2 + e_2 t_i^{car}(F_i, K_i) \right], \quad (18)$$

where  $1/740$  is used to convert gasoline consumption in grams into liters, and  $e_0 = 17.7766$ ,  $e_1 = 0.0023606$ , and  $e_2 = 1461.87$  are constant parameters in the expression.  $e$  is the efficiency coefficient for gas consumption calibration. Gas consumption leads to CO<sub>2</sub> emissions, and emissions in grams discharged by traveling 1 km by private car in zone  $i$  are

$$em_i^{car}(F_i, K_i) = \frac{ef}{740} e \left[ e_0 + e_1 \left( \frac{1}{t_i^{car}(F_i, K_i)} \right)^2 + e_2 t_i^{car}(F_i, K_i) \right]. \quad (19)$$

In (19),  $ef$  includes direct and indirect CO<sub>2</sub> emissions. The direct CO<sub>2</sub> emission and indirect emission for 1 liter of gasoline are 2340 g and 585 g CO<sub>2</sub>, respectively. Therefore, both gasoline consumption and CO<sub>2</sub> emission depend on the travel speed of the private car  $1/t_i^{car}(F_i, K_i)$ , which is determined by traffic flow  $F_i$  and road capacity  $K_i$ .

In addition, public transport inevitably generates CO<sub>2</sub> emissions, which can be represented by the average social CO<sub>2</sub> emission,  $em^{public} = ASCE$ . Hypothetically, public transport experiences no traffic congestion, and thus there is no difference in CO<sub>2</sub> emission levels among zones. Otherwise, for traffic flow  $F_i$ , the predicted commuting traffic flow from zone  $i$  to zone  $j$  is  $F_{ij}^w \equiv N\Psi_{ij}$ . Considering that no congestion occurs on weekends, for convenience, only shopping travel on working days is considered. Thus, the expected shopping travel per day from zone  $i$  to zone  $j$  is  $F_{ij}^s \equiv (N/D) \sum_{\xi=1}^I \Psi_{i\xi} Z_{\xi j}$ , where  $i$  is the residence zone,  $\xi$  is the working zone, and  $j$  is the shopping zone. Then, the total traveling traffic flow is

$$F_{ij} = F_{ij}^w + F_{ij}^s. \quad (20)$$

The travel time, gas consumption, and CO<sub>2</sub> emissions discussed above represent values corresponding to 1 km of travel in a specific zone. If travel crosses the boundaries of two or more zones, it is assumed that the travel distance in

starting zone  $i$ , as well as in destination zone  $j$ , is equivalent to half the zone width. Setting the travel set in zone  $i$  as  $\Omega_i \equiv \{t_i^{car}, g_i^{car}, em_i^{car}\}$ , travel set crossing from zone  $i$  to zone  $j$  is expressed as

$$\Omega_{ij} = \frac{1}{2} (d_i \Omega_i + d_j \Omega_j) + \sum_{\xi=i+1}^{j-1} d_\xi \Omega_\xi. \quad (21)$$

**2.4. Model Closure.** Combining all equations in the firm, consumer, and traffic modules, supply-demand equilibria are achieved for land, labor, and product markets. All land, labor, and product markets then result in clearing, characterized by the following equations:

Land market equilibrium:

$$N \sum_{j=1}^I \Psi_{ij}^* q_{ij}^* + Q_i^* + K_i = A_i; \quad (22)$$

Labor market equilibrium:

$$N \sum_{s=1}^I \Psi_{si}^* (E - T_{si}^* - L_{si}^*) = M_i^*; \text{ and} \quad (23)$$

Product market equilibrium:

$$N \sum_{n=1}^I \sum_{s=1}^I \Psi_{nsi}^* Z_{nsi}^* = X_i^*. \quad (24)$$

### 3. Parameters Calibration and Benchmark Equilibrium

Beijing is a representative city in China where public transport is subsidized. Here, its economics, population, and traffic-related statistics are used in calibration. The calibration commonly used to determine parameter values in CGE modeling ensures that the benchmark city found as a result of the basic simulation exhibits the economic figures, travel characteristics, and spatial patterns of a representative Beijing area. Data were mainly derived from the *Beijing Statistical Yearbook 2016* and *Beijing Traffic Development Annual Report 2016*. Certain parameters were derived from relevant domestic and international studies. Table 1 lists the calibrated values of the parameters in the SCGE model.

The fully circular city population is assumed to be 10.8 million, of which one-third is employed. That implies a population of 3.6 million commuters. Therefore, the total employed population is 100,000 in the 5° wedge-shaped city area. In the firm Cobb-Douglas production function, determinations of the function parameters  $B$ ,  $\delta$ , and  $\mu$  are attributed to Zhang et al. [26] and Wang and Ge [27] with slight adjustments. The utility function parameters  $\alpha$ ,  $\beta$ , and  $\gamma$  reflect the consumer's preference for shopping, housing, and leisure, respectively, and the values are set as 0.40, 0.17, and 0.43 to equilibrate the benchmark equilibrium values with the per capita consumption structure of Beijing data. The subutility function parameter of product purchasing is set as  $\eta=0.6$ , demonstrating that the substitutional elasticity

TABLE 1: Calibrated values of the parameters in SCGE.

City					
Incision angle	$\varphi=5^\circ$				
Zone width	$d_i=4\text{ km}$				
Firms					
Production function	$B=1.05$	$\delta=0.65$	$\mu=0.35$		
Consumers					
Population	$N=100\ 000$				
Labor	$D=250\text{ d}$	$E=4000\text{ h/a}$	$M_{ij}=2000\text{ h/a}$		
Utility function	$\alpha=0.40$	$\beta=0.17$	$\gamma=0.43$	$\eta=0.6$	
Dispersion parameter	$\lambda=0.8$				
Travel					
Travel modes ( $tm$ )	$v^{tm}$	$b^{tm}$	$c^{1,tm}$	$c^{2,car}$	$c^{3,tm}$
Walking	4 km/h	6.20	0	-	0
Private car	-	7.41	0.3	6.2	0
Public transport	15 km/h	7.16	0.2	-	1.5
Fixed utility function	$l_1=-0.1$	$l_2=-0.3$			
Transportation					
	Zone 1(9)	Zone 2 (8)	Zone 3 (7)	Zone 4 (6)	Zone 5
Road-land proportion	0.05	0.075	0.09	0.12	0.40
Travel time of private car $d_{i0}$	1/44	1/42	1/40	1/38	1/36
BPR function parameters	$b=6$	$c=4$			
Gasoline consumption	$e=1.26$				
CO <sub>2</sub> emissions	ASCE=11.9 g/pkm				

for interzone products is  $1/(1 - \eta) = 2.5$ . Assuming  $D=250$  for a consumer's annual working days, the available time endowment is  $E=250*16=4000$  hours, and the annual labor supply is  $M_{ij}=250*8=2000$  hours according to an 8-hour work day.

The dispersion parameter  $\lambda=8.0$  makes the employed population density in the benchmark equilibrium approximate to reality. Average walking speed is 4 km/h, and public transport speed is 15 km/h. In the travel mode choice function, parameters  $b^{tm}$ ,  $l_1$ , and  $l_2$ , reflecting the traveler's preference, were chosen according to the empirical literature on Beijing and real modal splits in Beijing (see Table 3). The travel cost for walking is set as 0. The variable travel cost of a private car  $c^{1,car}$  is 0.3 CNY per km, and gasoline price  $c^{2,car}$  is 6.2 CNY per liter. The variable cost of public transport  $c^{1,public}$  is 0.2 CNY per km, while its fixed cost  $c^{3,public}=1.5$  CNY.

When distance from downtown increases, the road-land proportion declines gradually with an average predetermined value according to real traffic conditions in Beijing. Speed limits vary among different zones; for example, the free flow travel speed in zone 1 (9) is set at 44 km/h. Owing to the increasing density of traffic lights closer to downtown, free travel speeds are set up as decreasing evenly along the zones inward. The values of BPR function parameters  $b$  and  $c$  refer to data from the US Bureau of Public Roads. The average CO<sub>2</sub> emission of public transport is specified as ASCE = 11.9 g/pkm, and the efficiency coefficient in gasoline consumption and CO<sub>2</sub> emission is  $e = 1.26$ , following the average CO<sub>2</sub> emission of public transport and the gasoline

consumption in benchmark equilibrium with the results of related studies [32].

Based on the established SCGE model and the parameters in Table 1, benchmark equilibrium can be obtained using GAMS; some of the results are listed in Table 2. Rent declines steeply with distance from the city center, and the rent downtown is much higher than in suburban areas. This is mainly due to the notion that land is immobile, and land supply increases with distance from downtown, while land near the city center is in much greater demand for residences, production, and road planning. Traffic flow reaches a summit downtown, giving rise to an especially obvious supply-demand conflict, explaining the high rent downtown compared to other zones. By contrast, labor supply and output are elastic in different zones. With increasing rent, firms are inclined to substitute labor for land, resulting in augmented labor demands. Labor is in greater demand downtown, but the supply increases relatively more, causing wages to reduce gradually in a smooth manner. Influenced by both rent and salaries, product prices are higher in zones near downtown; downtown prices are 1.7 times higher than in suburban areas. Moreover, the total output downtown is actually limited by the total land area, which is the lowest amongst all zones and accounts for 38% of production in the most distant suburban areas.

Furthermore, residence land ratio and average housing area are higher in zones further away from downtown. The housing area per capita in distant suburban areas is more than six times that of downtown. As for residence population, downtown has the lowest residence population,

TABLE 2: Partial results of benchmark equilibrium.

	Zone 1 (9)	Zone 2 (8)	Zone 3 (7)	Zone 4 (6)	Zone 5
Rent $r_i$ (¥/m <sup>2</sup> /a)	200	250	320	400	1200
Product price $p_i$ (¥/unit)	96.624	101.843	108.127	113.720	162.286
Output $X_i$ (million/a)	3.1720	3.1955	2.8373	2.4420	1.2089
Housing area per capita $q_i$ (m <sup>2</sup> )	77.834	61.964	47.309	36.869	12.127
Housing population	14242	14644	11686	8507	1842
Employment population	13394	13152	11200	8786	6939
Job–housing balance ratio	0.940	0.898	0.958	1.033	3.767
Housing population density (p/km <sup>2</sup> )	2550	3496	4185	6093	5276
Gasoline consumption of private cars (l/km)	0.095	0.098	0.107	0.138	0.169
CO <sub>2</sub> emissions of private car (g/km)	277.24	288.08	311.98	404.78	495.63

TABLE 3: Comparison of benchmark equilibrium results with empirical evidence.

Parameter	SCGE value	Empirical value	Empirical source and explanation
Average hourly wage (¥/h)	24.48	24.23	<i>Beijing Statistical Yearbook 2016</i> , annual disposable income/2000 hrs
Average job–housing distance (km)	6.77	6.4	Reference [28]
Average commuting time (h)	0.545	0.583	Reference [28]
Public transport split rate	50.1%	50%	<i>Beijing Traffic Development Annual Report 2016</i>
Cross-price elasticity of demand for public transport with respect to gasoline price	0.2	0.1–0.8	Reference [29]
Own-price elasticity of demand for private car with respect to gasoline price	-0.5	-0.1– -0.5	Reference [30]
Own-price elasticity of demand for public transport with respect to fare	-0.035	-0.0171 (bus) -0.1538 (subway)	Reference [31]
Ratio of commuting travel to total travel	50.50%	51.96%	<i>Beijing Traffic Development Annual Report 2016</i> , including school commuting
Ratio of transport expense to total disposable income	6.5%	6.8%	<i>Beijing Traffic Development Annual Report 2016</i> , commuting expense/ disposable income

and the urban zones have more while the suburban zones have the most. There are no distinct differences in residence population numbers among suburban zones. As for the working population, downtown has the least—almost half that of suburban areas.

In terms of job–housing balance, downtown is a job-rich area, while the suburban zones are housing-rich areas; urban zones are relatively balanced. Therefore, housing density tends to decrease from downtown outward to the suburban areas; thus, suburban housing density is far less than downtown housing density. It has been shown that the gasoline consumption and CO<sub>2</sub> emission of private cars in 1 km of travel diminish with diminishing traffic congestion. Although the differences between zones are relatively small, gasoline consumption and CO<sub>2</sub> emission escalate downtown and near downtown due to the serious traffic congestion.

To further investigate the model’s authenticity—especially the accuracy of the traffic condition description—we

compare some of the key results in the benchmark equilibrium with the corresponding empirical values (Table 3). The simulation results are shown to be approximate to the empirical values, including average salary per hour, average job–housing distance, average commute time, public transport split rate, ratio of commuting travel to total travel, and ratio of transport expense to total disposable income, among others. The transport-related elasticity coefficients comply with the empirical value ranges given in the references. Thus, the constructed SCGE model is reliable and applicable to the simulation analysis of public transport subsidies in Beijing.

#### 4. Simulation Results and Discussion

4.1. Scenario Design. Here, we present four different simulation policies.

*Scenario 1* (change the public transport fare subsidy rate). From 2007 to 2014, the local government of Beijing had implemented a policy where passengers with a bus IC card could travel on buses at a 60% discount. With the new fare policy in 2015, the subsidy rate was decreased to 50%. Thus, the public transport fare subsidy rate in the benchmark equilibrium is  $s^{public} = 0.5$ , set based on the current policy. In Scenario 1, the fare subsidy rate will be changed to varied levels, and the effects caused by the changes are discussed.

*Scenario 2* (substitute cash grant for fare subsidy). Here, the public transport subsidy rate  $s^{public}$  decreases to 0, and a fund is granted to increase cash subsidy  $S$ . In China, most of the employed population is not covered by cash transport grants, except for minority groups such as civil servants, so the one-time cash grant is determined as  $S=0$  in the benchmark equilibrium. Scenario 2 simulates the implementation of a cash grant policy and compares the outputs with other scenarios under the same total subsidy budget level.

*Scenario 3*. The subsidy fund is invested in the road capacity expansion of urban areas (zones 3–7). This means  $s^{public}$  decreases to 0, and the fund is allocated to increase the proportion of road land. The simulation under this condition considers whether subsidizing passengers or improving road infrastructure is more efficient using the same amount of money. The cost of road expansion is calculated by the rental opportunity cost of the additional urban land allocated to roads (in Beijing, public-private partnerships between government agencies and private-sector companies are used to finance, build, and operate many projects, including public transport networks. For simplicity, it is assumed that the private-sector company affords the labor, machine, and raw materials costs of road construction. For the local government, the main cost is land input. Because this study aimed to investigate government subsidy, it is assumed that road expansion costs for the government consist only of the rental opportunity cost of the additional urban land allocated for roads).

*Scenario 4*. The subsidy fund is invested in public transport speedup. When  $s^{public}$  decreases to 0, the fund is spent on improving average public transport travel speed. Public transport speedup may result from updating bus vehicles, rescheduling routes, and adding bus lanes. After the speedup, the average travel time by public transport will be reduced. Thus, the subsidy cost of public transport speedup is calculated by the time opportunity cost of reduced travel time for public transport travelers (speedup policy is considered to subsidize time cost, which equals the benefit the policy brings to travelers).

All simulations mentioned above are based on the benchmark equilibrium level where the fare subsidy rate is 0.5 and the fluctuating step is 0.1 for the rate. By increasing and decreasing the corresponding subsidy amount, the effects on social welfare, population, and CO<sub>2</sub> emissions are examined.

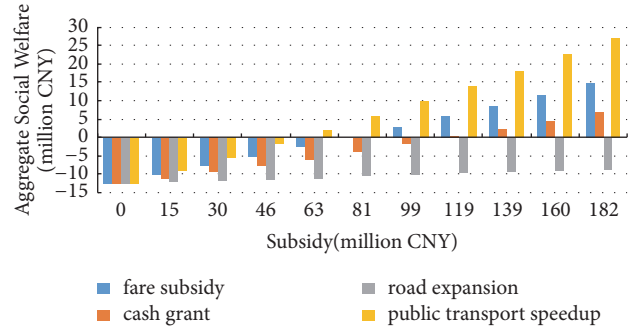


FIGURE 2: Social welfare effects of four transport subsidy policies.

*4.2. Social Welfare Effects.* When the public transport fare is completely subsidized, the subsidy fund amount is 182.36 million CNY, where the subsidy level ranges from 0.00 to 182.36 million CNY under Scenarios 1–4. Figure 2 shows the social welfare effects tendency under four policies when the fare subsidy rate changes from 0 to 1, while the total subsidy amount increases from 0.00 to 182.36 million CNY.

The horizontal axis represents the total subsidy amount with different fare subsidy rates from 0 to 1. For example, the total subsidization amount of ¥99.12 million corresponds to public transport fare subsidy rate  $s^{public} = 0.6$ , cash grant  $S = ¥991$ , 10.95% improvement in road land use rate, or public transport speedup to 21.4 km/h. The vertical axis depicts social welfare effects under four policies, which are calculated as the expected value of the maximized utilities, as in (8).

As shown in Figure 2, if the fare subsidy rate decreases from the current value of 0.5 to 0, overall social welfare will decline by 12.6293 million CNY, implying that average social welfare decreases by 2.526 million when the subsidy rate drops by 0.1. However, if the government gradually raises the fare subsidy rate to 1, overall social welfare will increase by 14.4774 million. Specifically, social welfare increases on average by 2.896 million with 0.1 increments in the subsidy rate. If the current fare subsidy is canceled and the same subsidy fund amount is distributed in the form of cash, overall social welfare will be lower than in the benchmark equilibrium by 3.9751 million. Only when total subsidization increases to 118.56 million, corresponding to a fare subsidy rate of 0.7, will the social welfare in the benchmark equilibrium be achieved.

Otherwise, as the total amount of subsidization increases, the aggregate social welfare under all four scenarios shows an uptrend. However, the ascending rate varies for each policy. Among them, Scenario 4 has the fastest increase rate, followed by Scenarios 1 and 2, while Scenario 3 increases the slowest. If public transport speedup policy is implemented, the benchmark equilibrium social welfare level can be obtained by investing less than 70 million, equivalent to a fare subsidy rate of 0.35. Meanwhile, when the subsidy fund is used to expand road capacity, even if all 182.36 million is invested, overall social welfare will remain substantially below the benchmark equilibrium level. This indicates that subsidizing public transport speedup has the most significant influence on social welfare, followed by fare subsidy and

TABLE 4: Spatial effects of four public transport subsidy policies.

Subsidy(millions)	Scenario											
	Scenario 1			Scenario 2			Scenario 3			Scenario 4		
	14.55	80.55	182.36	14.55	80.55	182.36	14.55	80.55	182.36	14.55	80.55	182.36
Urban residents	+402	0	-554	+499	+519	+547	+548	+756	+995	+335	-509	-2115
Urban residents ratio (%)	+0.95	0.0	-0.07	+1.18	+1.23	+1.29	+1.30	+1.79	+2.36	+0.79	-1.21	-5.01
Urban employed population	-34	0	+61	-9	+137	+359	+1	+170	+361	-82	-361	-1054
Urban employed population ratio (%)	-1.31	0.0	+0.13	-0.02	+0.29	+0.77	0.00	+0.36	+0.77	-0.17	+0.77	-2.25
Interzone commuting ratio (%)	-27.13	0.0	+41.85	-32.67	-31.32	-29.20	-32.70	-31.52	-30.10	-23.11	+33.73	+159.83
Interzone shopping ratio (%)	-9.22	0.0	+12.63	-11.40	-11.49	-11.62	-11.40	-11.46	-11.49	-7.78	+10.54	+45.05
Innerzone commuting ratio (%)	+2.51	0.0	-3.61	+2.99	+2.57	+1.93	+2.94	+2.34	+1.64	+2.14	-2.04	-8.10
Innerzone shopping ratio (%)	+1.64	0.0	-2.30	+2.20	+2.05	+2.09	+1.90	+1.44	+0.90	+1.31	-1.77	-6.10

cash grant, while road capacity expansion has relatively little effect. This is because public transport speedup significantly shortens travel time for consumers, leading directly to more working time and output, and indirectly to more product consumption. For instance, when public transport speed increases to 29.67 km/h, total output grows by 2.04% compared to the benchmark speed of 15 km/h. Yet, road expansion policy is hampered by the high land rent in urban areas. Although it can contribute to curtailing travel time and the cost of private cars, the population benefit from road expansion is less than in other scenarios, and the influence is less critical; thus, road expansion policy has no apparent role in boosting overall social welfare.

*4.3. Job-Housing Spatial Effects.* Various public transport subsidy policies have effects on citizen job-housing location, which can be measured by changes in the population distribution of residences and employment in different zones, as well as changes in short- and long-distance travel ratios. Table 4 shows variations in residence and employment distributions in urban areas compared to the benchmark equilibrium under the four subsidy policies when the total subsidizations are 14.55, 80.55, and 182.36 million, as well as the changes in inter- and innerzone commuting and shopping travel.

As shown in Table 4, under Scenario 1, as the subsidy fund increases, residents in urban areas are reduced, and resident distribution is mildly prone to suburbanization, with the residential ratio decreasing by 0.07% if the fare rate changes from 0.5 to 1. However, the employed population does not display an outward trend, and even a slight population aggregation to urban areas occurs. The main reason for this is that fare subsidy policy lowers travel costs and therefore encourages consumers to choose areas with cheaper living costs. However, the choices for working places mainly depend on average hourly wages, so the employed population tends to assemble in urban areas. This produces a significant increase in interzone commuting and shopping and a decrease in innerzone commuting and shopping. The results indicate that fare subsidy policy is not helpful for employed population suburbanization; it can only assist in encouraging residents to move outward to suburban areas and to travel longer distances.

Under Scenarios 2 and 3, public transport subsidies have similar effects on population distribution. When subsidization increases, both residential and employed populations converge on urban areas and downtown, and the convergence of the residential population is greater than that of the employed population. For example, when the total subsidization is 182.36 million, urban residential populations under two policies increase by 547 and 995, respectively, compared to the benchmark equilibrium, while the employed populations increase by 359 and 361, respectively. Interzone commuting and shopping travel reduce remarkably, while innerzone commuting and shopping travel gain modest growth. This is because, in general, cash grants can enlarge consumers' disposable incomes. Meanwhile, road expansion can reduce both the travel time of urban private cars and travel costs. In short, subsidizing public transport, either through cash distribution or road infrastructure construction, intensifies urban agglomeration.

Contrary to Scenarios 2 and 3, residential and employed populations show suburbanization to some extent under Scenario 4, and the suburbanization degree for the employed population is lower than that of the residential population. For example, when the total subsidization is 182.36 million, residential and employed population ratios in urban areas decrease by 5.01% and 2.25%, respectively, compared to the benchmark equilibrium level. Meanwhile, interzone commuting and shopping travel ratios increase by 159.83% and 45.05%, respectively, while innerzone commuting and shopping ratios decrease somewhat. Clearly, public transport speedup can stimulate long-distance commuting and shopping travel by decreasing travel time, thus strengthening urban sprawl. Therefore, public transport speedup can help relieve the urban agglomeration of residential and employed populations.

*4.4. Environmental Effects.* The effects of subsidy policies on the environment are embodied in changing consumers' travel modes and reducing pollution. Therefore, environmental effects are measured by changes in the public transport split rate and travel-related CO<sub>2</sub> emissions (for more details on the environmental consequences of CO<sub>2</sub> emissions, see cost analyses of carbon emissions, such as Tong et al. (2017)).

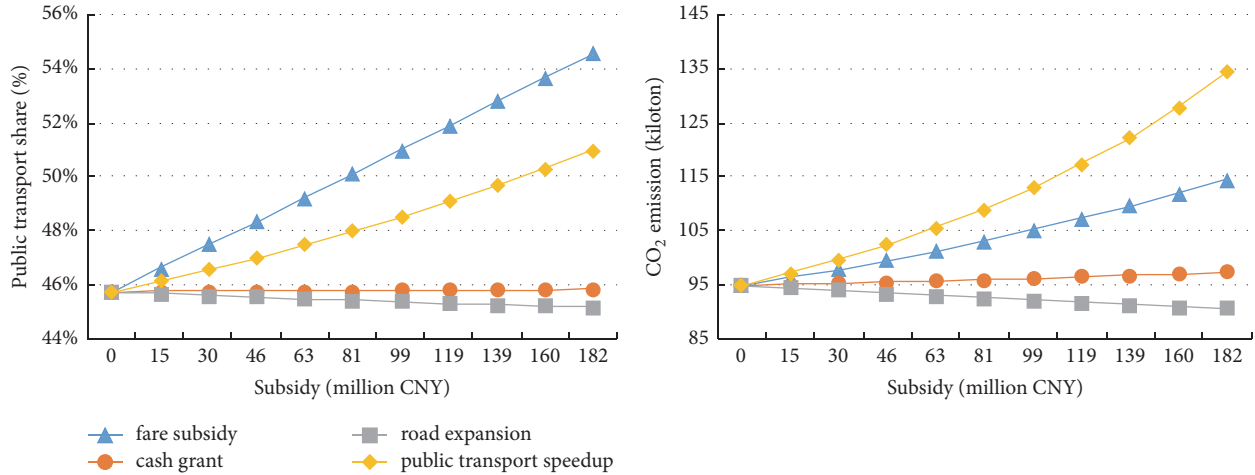


FIGURE 3: Environmental effects of four transport subsidy scenarios.

Figure 3 compares public transport split rates under different subsidy scenarios. Scenarios 1, 2, and 4 are shown to improve the public transport split rate to some degree. In general, however, the improvement effects are not remarkable. Among the scenarios, the effect of fare subsidy is relatively outstanding. When the fare subsidy rate increases from 0 to 1, the public transport split rate rises to 54.54% from 45.77%. If the same amount of subsidization is invested in public transport speedup, the effect is less significant, and the split rate improves to 50.99% with a total subsidization of 182.36 million. Otherwise, if the subsidy fund is granted by cash, which exerts the smallest influence, the split rate stays at almost the original level of 45.8%. However, with subsidization used for road expansion, the split rate decreases inconsiderably to 45.19%. This is because expanding road capacity can lower congestion and thus reduce both travel time and travel cost for urban private cars. When congestion decreases, traveling by private car becomes more attractive.

Figure 3 also shows the CO<sub>2</sub> emissions generated by transport with varying subsidization levels under different policies. In reality, governments usually consider transport subsidy as a tool for reducing CO<sub>2</sub> emissions. However, the simulation results show that whether CO<sub>2</sub> emissions are reduced depends on the type of subsidy policy. As shown in Figure 3, Scenarios 1, 2, and 4 increase travel-related CO<sub>2</sub> emissions, while Scenario 3 reduces emissions. This is mainly because road expansion has two effects on CO<sub>2</sub> emissions. First, the CO<sub>2</sub> emissions of 1km of travel by private car are reduced because of the faster speed. Second, as mentioned above, both residential and employed populations are converging on urban areas and downtown. Interzone commuting and shopping travel are remarkably reduced, while innerzone commuting and shopping travel gain modest growth. This means less total travel distance. Both effects lower CO<sub>2</sub> emissions. Thus, even though the public transport split rate declines mildly, an apparent decline in travel-related CO<sub>2</sub> emissions occurs. The other three policies trigger more consumer traveling by lowering shopping costs, increasing income, or amplifying production. As for public transport

speedup, it can reduce travel time to produce more aggregate output, which will trigger more consumer trips. It can also stimulate long-distance commuting and shopping travel by decreasing travel time. The other two policies, fare subsidy and cash grant, trigger more consumer traveling by lowering shopping cost and increasing income. Thus, traffic-related CO<sub>2</sub> emissions still increase, even though the public transport split rate increases or stays the same. This tells us that traffic-related CO<sub>2</sub> emissions are determined by travel mode preferences and travel frequency. CO<sub>2</sub> emissions are definitely augmented when the negative effects of more frequent travel outweigh the positive effects of higher public transport shares.

## 5. Conclusion

With job-housing spatial choice predetermined as the endogenous variable, this study constructed a SCGE model containing firms, consumers, and transport modules in one framework to investigate the effects of public transport subsidies. Using a benchmark equilibrium calibrated for Beijing, the model simulated social welfare, population distribution, and travel-related CO<sub>2</sub> emission effects under different subsidization levels with four forms of subsidy policies: fare subsidy, cash grant, road expansion, and public transport speedup. The conclusions from the simulation studies are summarized below.

First, public transport subsidies can enhance overall social welfare, regardless of what form the policy takes. Moreover, public transport speedup has the strongest effect on social welfare, followed by fare subsidy, cash grant, and road expansion, respectively.

Second, different forms of public transport subsidies can exert varied influences on city job-housing population distribution. Cash grant policy and road expansion construction encourage urban agglomeration, and residential populations aggregate more densely than employed populations. Fare subsidy policy affects employed population distribution only slightly but stimulates residential population diffusion

to suburban areas. In addition, public transport speedup suburbanizes both residential and employed populations, and residential populations show a stronger suburbanization, which can alter population convergence on the downtown area.

Third, most public transport subsidy policies give rise to modestly higher public transport split rates. Comparatively, fare subsidies have the most apparent effect, followed by public transport speedup, while cash grants have no influence on public transport share. Road expansion, however, acts in the opposite way, slightly reducing public transport share.

Fourth, except for road capacity expansion, public transport subsidy policies do not reduce travel-related CO<sub>2</sub> emissions. In fact, fare subsidy, cash grant, and public transport speedup policies all stimulate higher travel frequency among consumers and therefore aggravate total travel-related CO<sub>2</sub> emissions. CO<sub>2</sub> emissions can only be reduced by investing subsidies in road expansion construction.

In conclusion, the social welfare, spatial, and environmental effects of the four subsidy policies are quite different. Therefore, when governments decide on the level and form of public transport subsidization, the strategic goal of the subsidy policy should be ascertained by combining local conditions. By matching the goal with the subsidy form and considering the fiscal budget, an appropriate public transport subsidy plan can be established and recommended. For example, if the subsidy policy aims to improve social welfare, then a public transport speedup policy (e.g., setting up more bus lanes or renewing vehicles) is recommended. If the subsidy policy aims to control CO<sub>2</sub> emissions, road expansion construction should be prioritized. Finally, if the subsidy policy aims to encourage people to use public transport, a fare subsidy policy would be the most appropriate approach.

## Data Availability

The data used for model calibration were mainly derived from the Beijing Statistical Yearbook 2016 and the Beijing Traffic Development Annual Report 2016, which can be found at <http://www.bjstats.gov.cn/tjsj/ndtjzl/2018ndtjzl/index.html> and <http://www.bjtrc.org.cn/JGJS.aspx?id=5.2&Menu=GZCG>, respectively. The simulation results exported from our GAMS program are available from the corresponding author upon request.

## Conflicts of Interest

The authors declare that there are no conflicts of interest.

## Acknowledgments

This work was supported by Project 15JGC160, funded by the Social Science Foundation of Beijing.

## References

- [1] I. W. H. Parry and K. A. Small, "Should urban transit subsidies be reduced?" *American Economic Review*, vol. 99, no. 3, pp. 700–724, 2009.
- [2] D. A. Hensher, P. Stopher, and P. Bullock, "Service quality—developing a service quality index in the provision of commercial bus contracts," *Transportation Research Part A: Policy and Practice*, vol. 37, no. 6, pp. 499–517, 2003.
- [3] L. Eboli and G. Mazzulla, "A methodology for evaluating transit service quality based on subjective and objective measures from the passenger's point of view," *Transport Policy*, vol. 18, no. 1, pp. 172–181, 2011.
- [4] M. N. Hassan, Y. E. Hawas, and K. Ahmed, "A multi-dimensional framework for evaluating the transit service performance," *Transportation Research Part A: Policy and Practice*, vol. 50, no. 2, pp. 47–61, 2013.
- [5] H. Mohring, "Optimization and scale economies in urban bus transportation," *American Economic Review*, vol. 62, no. 4, pp. 591–604, 1972.
- [6] S. R. Jara-Diaz and A. Gschwender, "The effect of financial constraints on the optimal design of public transport services," *Transportation*, vol. 36, no. 1, pp. 65–75, 2009.
- [7] G. Santos, H. Behrendt, L. Maconi, T. Shirvani, and A. Teytelboym, "Part I: externalities and economic policies in road transport," *Research in Transportation Economics*, vol. 28, no. 1, pp. 2–45, 2010.
- [8] D. A. Hensher, "Establishing a fare elasticity regime for urban passenger transport," *Journal of Transport Economics and Policy*, vol. 32, no. 2, pp. 221–246, 1998.
- [9] S. Proost and K. V. Dender, "Optimal urban transport pricing in the presence of congestion, economies of density and costly public funds," *Transportation Research Part A: Policy and Practice*, vol. 42, no. 9, pp. 1220–1230, 2008.
- [10] I. Savage, "Management objectives and the causes of mass transit deficits," *Transportation Research Part A: Policy and Practice*, vol. 38, no. 3, pp. 181–199, 2004.
- [11] W. F. Richter, "Efficiency effects of tax deductions for work-related expenses," *International Tax and Public Finance*, vol. 13, no. 6, pp. 685–699, 2006.
- [12] B. De Borger and B. Wuyts, "Commuting, transport tax reform and the labour market: Employer-paid parking and the relative efficiency of revenue recycling instruments," *Urban Studies*, vol. 46, no. 1, pp. 213–233, 2009.
- [13] K. Van Dender, "Transport taxes with multiple trip purposes," *The Scandinavian Journal of Economics*, vol. 105, no. 2, pp. 295–310, 2003.
- [14] L. J. Basso, C. A. Guevara, A. Gschwender, and M. Fuster, "Congestion pricing, transit subsidies and dedicated bus lanes: efficient and practical solutions to congestion," *Transport Policy*, vol. 18, no. 5, pp. 676–684, 2011.
- [15] L. J. Basso and H. E. Silva, "Efficiency and substitutability of transit subsidies and other urban transport policies," *American Economic Journal: Economic Policy*, vol. 6, no. 4, pp. 1–33, 2014.
- [16] J. K. Brueckner, "Transport subsidies, system choice, and urban sprawl," *Regional Science & Urban Economics*, vol. 35, no. 6, pp. 715–733, 2005.
- [17] Q. Su and J. S. Desalvo, "The effect of transportation subsidies on urban sprawl," *Journal of Regional Science*, vol. 48, no. 3, pp. 567–594, 2008.
- [18] R. Borck and M. Wrede, "Political economy of commuting subsidies," *Journal of Urban Economics*, vol. 57, no. 3, pp. 478–499, 2005.
- [19] R. W. Martin, "Spatial mismatch and costly suburban commuters: can commuting subsidies help?" *Urban Studies*, vol. 38, no. 8, pp. 1305–1318, 2001.

- [20] Y. Zenou, "Urban unemployment, agglomeration and transportation policies," *Journal of Public Economics*, vol. 77, no. 1, pp. 97–133, 2000.
- [21] R. Borck and M. Wrede, "Subsidies for intracity and intercity commuting," *Journal of Urban Economics*, vol. 66, no. 1, pp. 25–32, 2009.
- [22] K. Ayyildiz, F. Cavallaro, S. Nocera, and R. Willenbrock, "Reducing fuel consumption and carbon emissions through eco-drive training," *Transportation Research Part F: Traffic Psychology and Behaviour*, vol. 46, pp. 96–110, 2017.
- [23] F. Tong, C. Hendrickson, A. Biehler, P. Jaramillo, and S. Seki, "Life cycle ownership cost and environmental externality of alternative fuel options for transit buses," *Transportation Research Part D: Transport and Environment*, vol. 57, pp. 287–302, 2017.
- [24] S. Tscharkschiew and G. Hirte, "Should subsidies to urban passenger transport be increased? A spatial CGE analysis for a German metropolitan area," *Transportation Research Part A: Policy and Practice*, vol. 46, no. 2, pp. 285–309, 2012.
- [25] A. Anas and R. Xu, "Congestion, land use, and job dispersion: a general equilibrium model," *Journal of Urban Economics*, vol. 45, no. 3, pp. 451–473, 1999.
- [26] J. Zhang, S. H. Shi, and S. Y. Chen, "The industry reform and efficiency change in China: Methodology, data, literatures and conclusions," *China Economic Quarterly*, vol. 3, no. 1, pp. 1–38, 2003.
- [27] J. Y. Wang and Y. X. Ge, "A study on aggregate production function of China based on time-varying parameter," *Journal of Quantitative & Technical Economics*, no. 8, pp. 150–161, 2012.
- [28] Z. L. Liu, Y. Zhang, and Y. W. Chai, "Home-work separation in the context of institutional and spatial transformation in urban China: evidence from beijing household survey data," *Urban Studies*, vol. 16, no. 9, pp. 110–117, 2009.
- [29] P. B. Goodwin, "A review of new demand elasticities with special reference to short and long run effects of price changes," *Journal of Transport Economics and Policy*, vol. 26, no. 2, pp. 155–169, 1992.
- [30] T. H. Oum, W. G. Waters, J. S. Yong, and W. G. Waters II, "Concepts of price elasticities of transport demand and recent empirical estimates: an interpretative survey," *Journal of Transport Economics and Policy*, vol. 26, no. 2, pp. 139–154, 1992.
- [31] P. Qin, Y. A. Chen, J. T. Xu et al., "Travel behavior analysis for the residents in Beijing: value of time and travel dem and elasticity estimates," *Economic Geography*, vol. 34, no. 11, pp. 17–22, 2014.
- [32] X. Y. Zhang, X. M. Yang, and Y. Yan, "Statistical estimation method for energy consumption and CO<sub>2</sub> emissions by urban transport," *China Soft Science*, no. 6, pp. 142–150, 2014.

## Research Article

# Study on Viscoelastic Deformation Monitoring Index of an RCC Gravity Dam in an Alpine Region Using Orthogonal Test Design

Yaoying Huang <sup>1</sup> and Zhiyong Wan <sup>2</sup>

<sup>1</sup>College of Hydraulic & Environmental Engineering, China Three Gorges University, Yichang 443002, China

<sup>2</sup>State Key Laboratory of Water Resources and Hydropower Engineering Science, Wuhan University, Wuhan 430072, China

Correspondence should be addressed to Zhiyong Wan; zhiyongwan@whu.edu.cn

Received 15 January 2018; Accepted 26 March 2018; Published 9 May 2018

Academic Editor: Xander Wang

Copyright © 2018 Yaoying Huang and Zhiyong Wan. This is an open access article distributed under the Creative Commons Attribution License, which permits unrestricted use, distribution, and reproduction in any medium, provided the original work is properly cited.

The main objective of this study is to present a method of determining viscoelastic deformation monitoring index of a Roller-compacted concrete (RCC) gravity dam in an alpine region. By focusing on a modified deformation monitoring model considering frost heave and back analyzed mechanical parameters of the dam, the working state of viscoelasticity for the dam is illustrated followed by an investigation and designation of adverse load cases using orthogonal test method. Water pressure component is then calculated by finite element method, while temperature, time effect, and frost heave components are obtained through deformation statistical model considering frost heave. The viscoelastic deformation monitoring index is eventually determined by small probability and maximum entropy methods. The results show that (a) with the abnormal probability 1% the dam deformation monitoring index for small probability and maximum entropy methods is 23.703 mm and 22.981 mm, respectively; thus the maximum measured displacement of the dam is less than deformation monitoring index, which indicates that the dam is currently in a state of safety operation and (b) the obtained deformation monitoring index using orthogonal test method is more accurate due to the full consideration of more random factors; the method gained from this study will likely be of use to diagnose the working state for those RCC dams in alpine regions.

## 1. Introduction

A Roller-compacted concrete (RCC) dam is constructed with the Roller-compacted placement method in thin layers of dry lean concrete, composed of mixed sand aggregate and cement [1]. In recent years, RCC dams have been commonly applied in dam domains because of its low cost, rapid construction, and a better control of heat generation of concrete. However, the safety of RCC dams during operation period is extremely crucial, especially in alpine regions. In order to ensure the safety operation of dams over the long-term service period, it is necessary to monitor the dam working performance by carrying out real-time analysis of monitoring data [2, 3]. As the deformation monitoring index is a crucial index to evaluate and monitor dam safety, it is of high engineering significance for the safety operation of dams. Generally, the

deformation monitoring index is an alarm or extreme value of deformation under possible loads according to the *Technical Specification for Concrete Dams Safety Monitoring* [4].

The deformation monitoring index of dams may be primarily determined using two approaches. Initially, the deformation monitoring index is obtained through the mining of dam deformation information using mathematical model on the basis of the existing monitoring effect quantity. Prior studies on monitoring index determined by mathematical model have focused on the methods of confidence interval, small probability, and statistical model [5, 6] which have been commonly used in numerous projects. However, due to the lack of consideration about spaciousness and fuzziness as well as randomness for multipoint monitoring in these methodologies, in recent years, Lei et al. [7] proposed the early warning index of spatial deformation of high concrete

dams based on deformation entropy; G. Yang and M. Yang [8] proposed the determination method of multistage warning indicators for the overall deformation of concrete dam regarding fuzziness and randomness; Qin et al. [9] combined comprehensive block displacement with multidimensional confidence region method to diagnose the safety of concrete double-curvature arch dam in Sichuan Province, China. Although it is convenient for engineers to determine deformation monitoring index by these mathematical models, the calculated displacement is the only alarm value or extreme value when the dam has experienced the extreme load case combinations in the long-term monitoring data.

On the other side, the deformation extreme value can also be determined on the basis of the structural numerical techniques of the dam body and its foundation. Numerous scholars have attempted, in terms of finite element numerical techniques, to assemble the adverse loads of dams that may occur during operation period, which makes up for the shortage of the adverse load combination cases of monitoring data series observed by precise instruments. For instance, Wu et al. [10] proposed that the structural characteristics of RCC dams should be divided into three stages: elasticity, elastic-plasticity, and unstable failure. The deformation monitoring index of dams was determined through the introduction of the statistical model [11–14], and the method was successfully applied to Shapai RCC arch dam in Sichuan province, China. Considering the complexity characteristics of RCC structure [15], such as the complex anisotropy, Gu [16] defined the diagnostic index of three-stage safety deformation from the perspective of yield ratio mutation feature of layer surface and foundation plane, and then the theory was successfully applied to Longtan dam project in Guangxi province, China.

Prior studies on monitoring index have focused on adverse load combinations that offer a simple combination by the accumulation of adverse loads rather than forming a full consideration on the actual situations (e.g., loads, boundary conditions, and uncertain parameters). For instance, the Canadian Turkstra combination rule is customarily used in the engineering field, which holds that the maximum effect value of the load combination manifests when a variable load reaches the maximum value in the design benchmark period and the other variable loads are in the form of instantaneous value [10]. The form of load combination is pretty rough with the characteristics of subjective factor; in particular, the running state of dams presents the characteristics of fuzziness and randomness; thus the load combination cases selected are not always representative. Moreover, with the presentation of the complex behavior of dams in alpine regions, only few scientific publications have been published concerning deformation monitoring index of dams in alpine regions. Therefore, a typical combination of adverse case sample is selected using orthogonal test design method [17] so as to determine deformation monitoring index of dams in alpine regions.

In this study, a typical RCC gravity dam in an alpine region is taken as a case, and the typical water retaining dam block is selected as an analysis object. A combination sample of adverse cases is designed using orthogonal test method; the total effect quantity (i.e., deformation) sample is obtained

through statistical model and finite element method, and then the viscoelastic deformation monitoring index for the dam in an alpine region is eventually determined based on the small probability and maximum entropy methods.

## 2. A Method of Determining Viscoelastic Deformation Monitoring Index for RCC Gravity Dams

**2.1. Orthogonal Test Design.** Orthogonal test design, as a highly efficient way capable of dealing with multifactor tests, is commonly adopted to arrange and analyze datasets by means of selecting a reasonable orthogonal table based on levels and factors [17]. In considerable combinations, it is convenient to conduct a test with the method employed to select a representative combination with the characteristics of “uniform dispersion” and “neatly comparable.” Simultaneously, it may make the test cases with approaches of different combinations analyzed comprehensively available, which is characterized by less times, high execution efficiency, and convenient operation.

### 2.2. Effect Quantities of Adverse Load Combination

**2.2.1. Deformation Statistical Model Considering Frost Heave.** In the case of an RCC dam in an alpine region, the dam crest displacement is affected by water pressure, temperature, time effect, and frost heave [6, 18, 19] when the dam crest has no thermal insulation measures. For this purpose, the modified deformation statistical model for the concrete dams considering frost heave in alpine regions is expressed as follows:

$$\delta = \delta_H + \delta_T + \delta_\theta + H(\lambda_0 - \lambda)\delta_D, \quad (1)$$

where  $\delta_H$  represents the displacement caused by dam body and its foundation deformation under the action of a water load;  $\delta_T$  represents the displacement caused by the temperature change of dam body concrete and dam foundation rock;  $\delta_\theta$  denotes the time effect (time-dependent) displacement which is employed to represent the creep of dam concrete and bedrock, as well as the plastic joint deformation;  $\delta_D$  (i.e.,  $\delta_D = \delta_{D1} + \delta_{D2}$ ) denotes the frost heave deformation of dams in alpine regions, including a periodic term  $\delta_{D1}$  and a hysteresis term  $\delta_{D2}$ . The water pressure, temperature, and frost heave are assumed to be elastic components, while the plastic components caused by water pressure, temperature, and frost heave are all included in the time effect component. These components [6, 18] can be written as follows:

$$\delta_H = \sum_{i=0}^m a_i (H^i - H_0^i), \quad (2)$$

$$\delta_T = \sum_{i=1}^{m_1} \left[ b_{1i} \left( \sin \frac{2\pi it}{365} - \sin \frac{2\pi it_0}{365} \right) + b_{2i} \left( \cos \frac{2\pi it}{365} - \cos \frac{2\pi it_0}{365} \right) \right], \quad (3)$$

$$\delta_\theta = c_1 (\ln \theta - \ln \theta_0) + c_2 (e^{-0.1\theta} - e^{-0.1\theta_0}) + c_3 (e^{-0.01\theta} - e^{-0.01\theta_0}), \quad (4)$$

$$\delta_{D1} = \sum_{i=2,4,8,\dots}^m \left[ d_{i1} I \sin \left( \frac{2\pi i (x - x_0)}{365} \right) + d_{i2} I \cos \left( \frac{2\pi i (x - x_0)}{365} \right) \right], \quad (5)$$

$$\delta_{D2} = d_1 I_{20-10} + d_2 I_{20-20} + d_3 I_{20-30} + d_4 I_{30-10} + d_5 I_{30-20} + d_6 I_{30-30}, \quad (6)$$

where  $a_i$  is the water pressure component regression coefficient;  $m = 3$  for a gravity dam and  $m = 4$  for an arch dam;  $H$  is the water depth on the monitoring day and  $H_0$  is the water depth of the beginning day; and  $b_{1i}$  and  $b_{2i}$  are temperature component regression coefficients.  $m_1 = 1$  or 2 corresponds to a year and half-year cycle, respectively, and  $c_1$ ,  $c_2$ , and  $c_3$  are time effect component regression coefficients.  $t$  denotes the cumulative days from the beginning day to the monitoring day,  $t_0$  denotes the days from the beginning day to the calculated day;  $\theta$  denotes the number of days from the beginning day to the monitoring day divided by 100;  $\theta_0$  denotes the number of days from the beginning day to the calculated day divided by 100.

$I$  represents the frost heave factor to distinguish the periodic function in the same model;  $x$  represents the number of days from the beginning day to the monitoring day;  $x_0$  represents the number of days from the beginning day of the analyzed monitoring series to the beginning day of the negative temperature in the same year;  $d_{i1}$  and  $d_{i2}$  are the frost heave component periodic regression coefficients;  $d_1, d_2, \dots$ , and  $d_i$  ( $i = 1-6$ ) are the frost heave component hysteresis regression coefficients; and  $I_{i,j}$  represents temperature hysteresis factor,  $i$  denotes the effect of time on temperature hysteresis, and  $j$  denotes the number of days at the average temperature before the hysteresis time is affected. Generally, as a unit of weeks, days, or months, the hysteresis days are determined by the measured temperature and hysteresis temperature of dams.

Additionally,  $H(\lambda_0 - \lambda)$  in (1), with respect to a definite step function, is defined by

$$H(\lambda_0 - \lambda) = \begin{cases} 0 & \lambda > \lambda_0 \text{ (without considering frost heave)} \\ 1 & \lambda < \lambda_0 \text{ (considering frost heave)} \end{cases} \quad (7)$$

in which  $\lambda_0 = 0^\circ\text{C}$  is the reference temperature of the concrete,  $\lambda$  denotes the concrete temperature, and the function "differential" is a Dirac  $\delta$  function due to a jump when  $\lambda = \lambda_0$ ; thus,  $H(\lambda_0 - \lambda)$  is referred to as the unit step function.

**2.2.2. Effect Quantities.** The basic loads consist of water pressure, uplift pressure, sediment pressure, and other loads regarding the permanent cases during the operation period of dams. Some analysis is conducted by selecting and combining

these loads which have a strong influence on structure deformation. Due to the complexity of load combination under adverse cases, in this study, the water pressure and uplift pressure are recognized as the investigated loads, and then the orthogonal test method, according to the range of loads and levels as well as factors, is introduced to assemble loads under adverse cases. Combined with (1), together with finite element numerical techniques, it is feasible to obtain total effect quantity samples.

To be specific, effect quantities consist of water pressure component, temperature component, time effect component, and frost heave component in this study. Water pressure component is calculated using the finite element method, and the transversely isotropic mechanical parameters in the finite element model are obtained from inversion; while the temperature component is calculated through statistical model expression form, as shown in (3), time effect and frost heave components are also calculated by statistical model expressions, as shown in (4) and (5)-(6), respectively.

### 2.3. Deformation Monitoring Index of Dams

**(1) Small Probability Method.** Effect quantities under each adverse load combination are obtained through the 3D finite element method and deformation statistical model of an RCC dam; thus the sample space is developed; moreover, the Kolmogorov-Smirnov (K-S) distribution test method is utilized to diagnose the probability density function  $f(E')$  on the basis of the eigenvalues (i.e., mean and standard deviation) of samples. Here  $E'_m$  is considered as the deformation monitoring index value; the running state of a dam will be abnormal provided that  $E'$  (measured data) is greater than  $E'_m$  (monitoring index); the abnormal probability of dam deformation can be given by

$$P(E' > E'_m) = P_\alpha = \int_{E'_m}^{\infty} f(E') dE'. \quad (8)$$

As the abnormality of a dam is regarded as a small probability event, the abnormal probability ( $P_\alpha$ ) is conventionally determined by the project grade or rank; thus the deformation monitoring index is written as  $E'_m = F^{-1}(\bar{E}', \sigma_E, P_\alpha, \dots)$ , where  $\bar{E}'$ ,  $\sigma_E$  are mean and standard deviation of samples, respectively.

**(2) Maximum Entropy Method.** The maximum entropy method is able to be adopted when the distribution function for the actual monitoring effect quantities can not fully conform to the classical distribution function. There is no need to assume the distribution function type of samples in advance; the probability density function with higher precision can be obtained directly based on the numerical eigenvalues of samples [20]. The calculation steps are as follows.

*Step 1.* According to the principle of maximum entropy, when the probability distribution reaches the minimum deviation under the given constraint condition of sample information,

the entropy  $H(x)$  will reach the maximum. The objective function and constraints are written as

$$\max H(x) = - \int_R f(x) \ln f(x) dx \quad (9)$$

$$\text{s.t } \int_R f(x) dx = 1 \quad (10a)$$

$$\int_R x^i f(x) dx = \mu_i \quad (i = 0, 1, 2, \dots, n). \quad (10b)$$

Additionally,

$$\mu_i = \sum_{k=1}^N \frac{x_k^i}{N}, \quad (11)$$

where  $x_k$  denotes the  $k$ -th sample value;  $N$  represents sample size;  $R$  is the domain of integration and generally it can be approximated as  $[E - 5\sigma, E + 5\sigma]$ ;  $E$  and  $\sigma$  are sample mean value and standard deviation, respectively;  $\mu_0 = 1$ ;  $\mu_i$  ( $i = 1, 2, \dots, n$ ) is  $i$ -th origin moment;  $n$  is the order of origin moment.

*Step 2.* According to a set of sample information  $x = \{x_1, x_2, \dots, x_N\}$ , the origin moment of displacement sample is calculated, and the Lagrange multiplier method is employed to solve the maximum value of the entropy  $H(x)$ . The maximum entropy probability density function is, therefore, expressed as

$$f(x) = \exp\left(\lambda_0 + \sum_{i=1}^n \lambda_i x^i\right), \quad (12)$$

where  $\lambda_0$  and  $\lambda_i$  ( $i = 1, 2, \dots, n$ ) represent Lagrange multiplier coefficients.

Hence, according to (10a) and (10b) and (12), the following equation can be obtained.

$$\begin{aligned} \int_R x^i f(x) dx &= \int_R x^i \exp\left(\lambda_0 + \sum_{j=1}^n \lambda_j x^j\right) dx \\ &= \frac{\int_R x^i \exp\left(\sum_{j=1}^n \lambda_j x^j\right) dx}{\int_R \exp\left(\sum_{j=1}^n \lambda_j x^j\right) dx} = \mu_i \end{aligned} \quad (13)$$

$$(i = 1, 2, \dots, n).$$

The Lagrange multiplier coefficients of the aforementioned formula are estimated by optimization algorithm.

*Step 3.*  $x_m$  is assumed as the deformation monitoring index; the abnormal or dangerous possibility for dams can be described by

$$P_\alpha = \int_{x_m}^{+\infty} f(x) dx \quad (x > x_m). \quad (14)$$

The probability of abnormal behavior for dams is rather low, the abnormal probability ( $P_\alpha$ ) is commonly regarded as 1% or 5% considering structural importance (rank or grade), and then the deformation monitoring index value can be obtained based on the property of the inverse cumulative distribution function.

The flow diagram of implementation for viscoelastic deformation monitoring index of dams is shown as Figure 1.

*2.4. Deformation Alarm of RCC Dams.* Compared with the measured data  $E_m$  of the monitoring series, the deformation monitoring index  $E'_m$  can be exploited to diagnose the existing working condition of a dam and offer an early alarm for dam safety; some details are as follows:

(1) The running state of a dam is within normal range provided that the measured data  $E_m$  is less than  $E'_m$ .

(2) The measured data exceeds the normal range provided that the measured data  $E_m$  is greater than  $E'_m$ , and the running state of a dam is abnormal. Thus, it is essential to analyze the reasons and take timely effective engineering measures to control dam deformation until the dam is in normal operation.

### 3. Case Study

#### 3.1. Description of an RCC Gravity Dam

*(1) General of the Project.* A large-scale water conservancy project is situated in the Northwest alpine region of China. Based on many years of data, the annual average temperature is 2.8°C at the dam site, with an extreme minimum temperature of -49.8°C and an extreme maximum temperature of 40.1°C which have been observed in history. Hence, the environment of region is so harsh that it can be considered as an alpine region. The project has a total reservoir capacity of  $2.419 \times 10^9 \text{ m}^3$ , and reservoir's normal storage water level and dead water level are 739.00 m and 680.00 m, respectively. The power station has a total installed capacity of 140 MW, and the annual generating capacity reaches  $5.19 \times 10^8 \text{ KWh}$ .

The project is mainly composed of dam, water diversion system, power plant, and other hydraulic structures. The main dam is composed of a full section Roller-compacted concrete (RCC) gravity dam with a length of 1489 m, a maximum height of 121.50 m, and a dam crest elevation of 745.50 m. Seen from the scale of water conservancy, the safety grade of the project is grade I or larger (1). Layout of the project is shown as Figure 2.

*(2) Dam Safety Monitoring Layout.* The typical water retaining dam block is selected as the analyzed dam block, as shown in Figure 2. There are three plumb lines and one inverted plumb line. Namely, the monitoring points of PL5-1, PL5-2, and PL5-3 measured by the plumb line are arranged at the elevation of 675.10 m, 706.50 m, and 742.70 m, respectively, whereas IP5 is measured by an inverted plumb line in the dam foundation anchored at the elevation of 586.30 m, as shown in Figure 3.

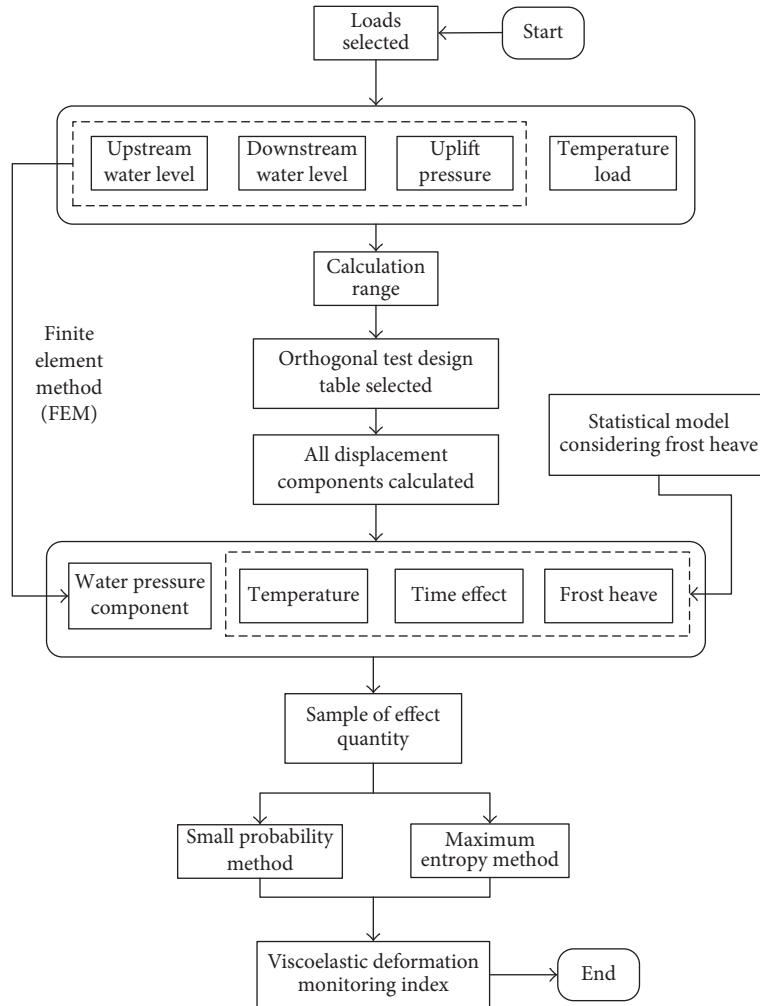


FIGURE 1: Flow diagram of implementation for viscoelastic deformation monitoring index.

### 3.2. Analysis and Demonstration of Viscoelastic Deformation

(1) *Quantitative Analysis of Dam Deformation.* In view of the typical representation of dam crest monitoring point, the PL5-3 monitoring point of the dam crest is selected as a research object. It can be seen from the measured temperature and the simulation results of dam crest temperature field that large range of negative temperature area appears in the vicinity of dam crest during the period from December 10th to April 25th of the following year. Therefore, it is essential to consider the frost heave deformation of dam crest. The deformation statistical model considering frost heave is established by (1). The fitted data calculated by stepwise regression analysis method is compared with the measured data, as shown in Figure 4. The results show that the measured displacement is in good agreement with the fitted ones, and the complex correlation coefficient is around 0.974. The separated water pressure component, temperature component, time effect component, and frost heave component (for the initial measured value) are shown in Figure 5. It can be seen from the figure that the frost heave component presents fluctuation, the water pressure component is highly

correlated with the change trend of the reservoir water level, and the time effect component tends to be stable in the later stages.

(2) *Transversely Isotropic Mechanical Parameters.* According to the laboratory test data of the roller compacted concrete (RCC) gravity dam in an alpine region, the elastic modulus of the dam is 31.5–38.0 GPa, and the average value of elastic modulus is 34.8 GPa. Since the RCC dam is vibrated and compacted with layering by the vibrating grindstone, the RCC is commonly perceived as the transversely isotropic material.

On the basis of the water pressure component separated by the deformation statistical model considering frost heave, the physical and mechanical parameters of the dam and its foundation are back analyzed by uniform design method, BP neural network, and finite element method [21]. Namely, the horizontal equivalent elastic modulus of dam is 39.00 GPa; the vertical equivalent elastic modulus of dam is 26.85 GPa; the vertical equivalent shear modulus of dam is 16.21 GPa; the equivalent deformation modulus of dam foundation is 36.16 GPa.



FIGURE 2: Layout of an RCC gravity dam project.

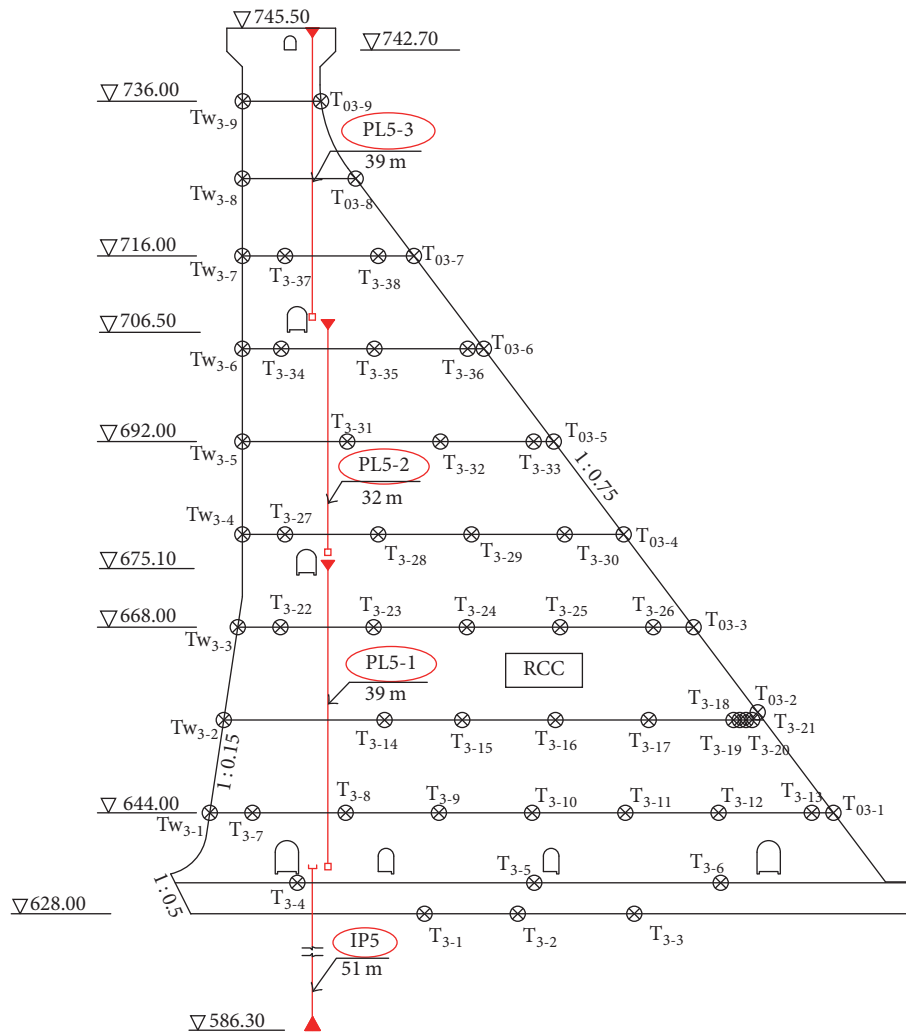


FIGURE 3: Cross-sectional monitoring layout of the typical water retaining dam block (elevation: m).

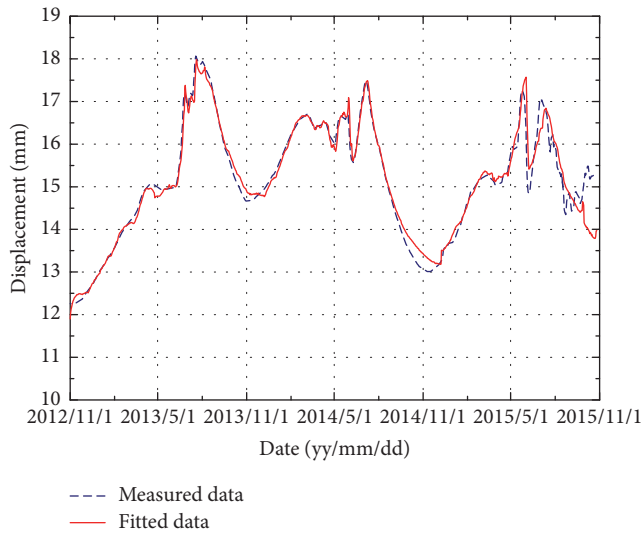


FIGURE 4: Comparison between the measured and the fitted displacement of monitoring point for dam crest.

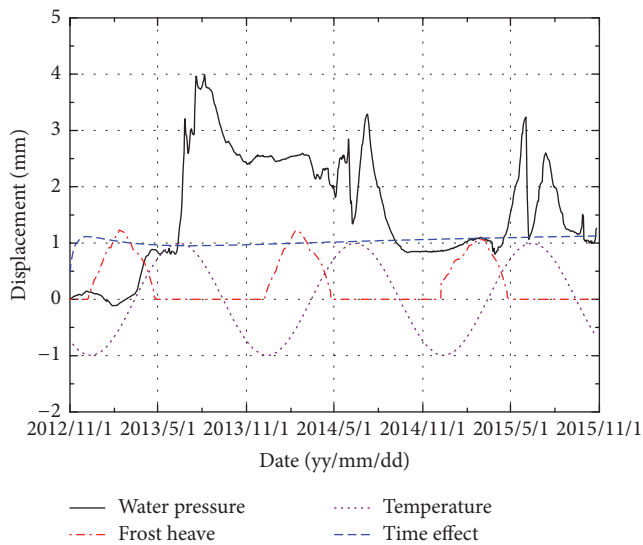


FIGURE 5: The separated displacement components of monitoring point for dam crest.

There are several discrepancies between the parameters obtained by the inversion and the design parameters. The maximum difference is the horizontal equivalent elastic modulus, and the inversion value is 1.12 times of the designed value; the ratio of horizontal equivalent elastic modulus to vertical equivalent elastic modulus is 1.45, which is in accordance with the general variation law of RCC (i.e., 1-2).

(3) *Demonstration on Working Performance of This RCC Gravity Dam.* The viscoelastic deformation of concrete dams not only can embody time-dependent factor but also can present elastic and viscous deformation, which has a crucial scientific significance in the engineering field. From the aforementioned analysis of the established deformation statistical model, we can see that the time effect component of the dam tends to be stable in the later stages; meanwhile, the

transversely isotropic parameters of the RCC obtained by the inversion are greater than the design values. To sum up, it can be concluded that the RCC gravity dam is currently in a state of viscoelasticity. Therefore, the viscoelastic deformation monitoring index of the dam is mainly determined during operation period in the following paper.

3.3. *Selection of Adverse Load Combination.* Prior to selecting adverse cases, the factor having a strong influence or greater variability on a dam is considered as a random variable. According to actual engineering, with the potential impact of the temperature on RCC in alpine regions, the running state of a dam is affected by hydrostatic pressure along upstream and downstream of dams. Furthermore, stability and strength of the dam will be unfavorable if the uplift pressure is too large. Thus the upstream and downstream water level, temperature load, and uplift pressure are perceived as the main influencing factors. The water pressure component is calculated by the inversion results of parameters; the temperature component is calculated by the quasi-stable temperature field and statistical model. In addition, there is no available measured data about the uplift pressure; thus the reduction coefficient of uplift pressure is only analyzed herein.

(1) *Determining the Scope of Influencing Factors*

(i) *Reservoir Water Level.* For the analysis of the dam measured data, it can be seen that the reservoir water level is above normal reservoir water level (739.00 m) from July 19, 2013, to August 22, 2013, the maximum water level has reached 739.50 m during operation period, and the high water level in other periods is below 739.00 m. The extreme values of adverse deformation may not occur in history since the monitoring series is rather short; thus in order to reflect the impact of water load upon dam deformation at different high water levels, the range of reservoir water level is selected as 737.50–743.50 m, whereas the range of downstream water level is selected as 641.02–646.18 m.

(ii) *Temperature Load.* In the absence of load design data of the dam, the maximum rise and drop in temperature are determined by the simulation results of quasi-stable temperature field. The range of temperature load for the monitoring point of dam crest is  $-10.1-18.4^{\circ}\text{C}$ .

(iii) *Uplift Pressure Load.* Due to lack of measured data, the effect of uplift pressure reduction coefficient upon dam deformation is analyzed herein. The range of reduction coefficient is 0.19–0.31.

(2) *Orthogonal Design Table.* Till now, the maximum water level of the dam during operation period is basically close to normal storage water level (739.00 m), the sample data of the monitoring is insufficient, and the extreme value of monitoring series may not contain the adverse cases that occurred in history. Therefore, in order to ensure the accuracy of the deformation monitoring index, a combination of adverse cases is obtained comprehensively using orthogonal test design method.

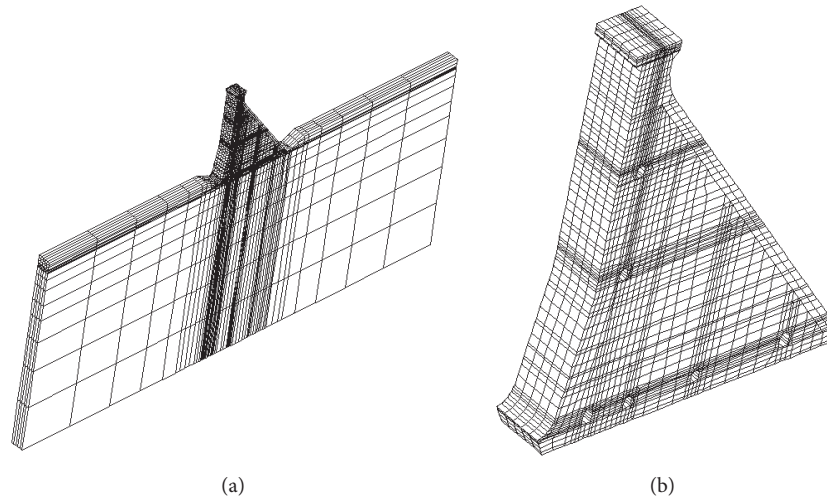


FIGURE 6: 3D finite element model of the typical water retaining dam block. (a) Dam-foundation model and (b) Dam body model.

It is seen from the analysis that the upstream reservoir water level, the downstream water level, the temperature load, and the uplift pressure are considered as the main loads that affect dam deformation. Therefore, according to the orthogonal test design table, four influential factors of upstream water level, downstream level, temperature load, and reduction coefficient of uplift pressure are selected, and four levels are set for each factor, as shown in Table 1.

The orthogonal table  $L_{16}(4^5)$  is selected to constitute 16 sets of load combinations including 4 factors and 4 levels, as shown in Table 2.

As presented in Table 2, the columns of A, B, C, and D in the orthogonal table are used because of four factors, and A, B, C, and D represent upstream water level, downstream water level, temperature load, and uplift pressure reduction coefficient, respectively. Taking number 5 as an example, the calculated cases primarily include A-2, B-1, C-2, and D-3, where A-2 represents the reservoir water level 739.50 m, B-1 represents the downstream water level 641.02 m, C-2 represents the temperature load  $-0.6^\circ\text{C}$ , D-3 represents the uplift pressure reduction coefficient 0.27, and other similar cases can be obtained by analogy.

### 3.4. Calculation and Analysis of Adverse Load Combination Samples

(1) *Computation Model.* A 3D finite element model is established to calculate the water pressure component using the mechanical parameters of RCC dam body and its foundation. The other components (e.g., temperature, time effect, and frost heave) are calculated by the expressions of statistical model, as shown in (3)–(7). Remarkably, the finite element model information of dam and its foundation is as follows.

The calculation range of the model is twice the height of dam along the upstream and downstream as well as the depth of dam foundation. The positive direction of  $x$ -axis is towards downstream, and  $z$ -axis is directed from left bank to right bank which is perpendicular to the direction of

water flow. The positive direction of  $y$ -axis is upward. The upstream and downstream surfaces have their horizontal displacements constrained to zero, respectively; the left and right banks have their horizontal displacements constrained to zero, respectively; the bottom of the dam foundation has its horizontal and vertical displacements constrained to zero.

The mesh division of dam and its foundation is conducted using hexahedral eight-node isoparametric element and a small amount of degraded tetrahedron or pentahedral elements. The monitoring points are arranged on the nodes as soon as possible when the mesh is divided. Simultaneously, the mesh generation in the vicinity of gallery is conducted using the local mesh refinement method. The total number of element in the finite element model is 13620, with the dam body containing 10540 elements, and the number of nodes is 17274. The finite element model of the typical water retaining dam block is shown in Figure 6.

(2) *Further Analysis.* As shown in Figure 5, the change of each month is basically identical due to the periodic variation of the temperature component and frost heave component, so the selected displacements depend on temperature load. Namely, the occurrence time of temperature load is determined by the quasi-stable temperature field, and then the corresponding value (i.e., temperature component and frost heave component) of deformation monitoring statistical model is determined. Moreover, all components are determined from the relative values between the calculated water level and the initial water level (initial value measured on November 1, 2012); the convergence value is considered as the time effect value since the time effect component tends to be stable. The adverse load combination and all components are shown in Table 3. The calculated total displacement of dam crest is shown in Table 4.

The following conclusions can be obtained from Table 4.

(i) When the high water level is at elevation of 737.50 m, 739.50 m, 741.50 m, and 743.50 m, with the changes of temperature load and uplift pressure, the deformation monitoring

TABLE 1: Factors and levels diagram of adverse loads.

Levels	Factors			
	Upstream water level (m)	Downstream water level (m)	Temperature load (°C)	Reduction coefficient of uplift pressure
1	737.50	641.02	-10.1	0.19
2	739.50	642.74	-0.6	0.23
3	741.50	644.46	8.9	0.27
4	743.50	646.18	18.4	0.31

TABLE 2: The orthogonal design table  $L_{16}(4^5)$ .

Number	A	B	C	D	E
1	1	1	1	1	1
2	1	2	2	2	2
3	1	3	3	3	3
4	1	4	4	4	4
5	2	1	2	3	4
6	2	2	1	4	3
7	2	3	4	1	2
8	2	4	3	2	1
9	3	1	3	4	2
10	3	2	4	3	1
11	3	3	1	2	4
12	3	4	2	1	3
13	4	1	4	2	3
14	4	2	3	1	4
15	4	3	2	4	1
16	4	4	1	3	2

index of dam crest is also unidentical. The mean values of the four cases are 19.39 mm, 20.08 mm, 21.42 mm, and 22.21 mm, respectively. From the analysis of the measured data, such as water level of 737.58 m that appeared on July 7, 2013 when it was in hot season, the monitoring displacement value of 17.20 mm which is less than the deformation monitoring index of 19.39 mm, and the actual operation of the project shows that the dam is in a state of safety operation. Also high water level of 739.5 m appeared on August 6, 2013; the actual monitoring value of 17.89 mm is less than deformation monitoring index of 20.08 mm; thus it is demonstrated that the dam does not present adverse situation. To summarize, the dam is currently in a safe condition.

(ii) As presented in Table 4, the water level of 737.50 m and 739.50 m is subordinate to high water level of the prototype monitoring series, and the deformation monitoring index based on the monitoring series of PL5-3 monitoring point of dam crest is around 19.00 mm [21], while the deformation monitoring index based on statistical model and finite element method is around 18.60–20.64 mm. It is shown that the deformation monitoring index calculated by statistical model and finite element method is close to the deformation monitoring index based on the monitoring series. In addition, the determined monitoring index based on the orthogonal test design method has been taken thoroughly into account the adverse load combination cases of the dam during operation

period, which is considered to be more representative and accurate.

**3.5. Deformation Monitoring Index.** Based on the total displacement sample of 16 sets of adverse load combination cases (Table 4), according to the principles described in Section 2.3, the small probability method and the maximum entropy method are employed to determine the deformation monitoring index of an RCC dam in this alpine region.

*(1) Small Probability Method.* The K-S test method shows that the relationship between the maximum theoretical empirical difference ( $D_n$ ) and critical value ( $D_{n1\%}$  or  $D_{n5\%}$ ) corresponding to the assumed abnormal probability is  $\max D_n = 0.1058 < D_{n1\%} = 0.2500$  and  $\max D_n = 0.1058 < D_{n5\%} = 0.2130$ , respectively, indicating that the displacement distribution of the monitoring point at dam crest satisfies normal distribution, namely,  $\delta \sim N(\delta_1, \sigma_1)$ ; thus the characteristic parameters (i.e., mean  $\delta_1$  and standard deviation  $\sigma_1$ ) of this distribution are  $\delta_1 = 20.7744$  and  $\sigma_1 = 1.2589$ , respectively.

When the measured value  $\delta$  is greater than  $x_m$  (i.e., deformation monitoring index), the abnormal probability ( $P_\alpha$ ) of dam deformation is presented as follows:

$$F(\delta > x_m) = P_\alpha = \int_{x_m}^{+\infty} \frac{\exp[-(\delta - \delta_1)^2 / 2\sigma_1^2]}{\sqrt{2\pi}\sigma_1} d\delta. \quad (15)$$

It is seen from the statistical principle and structural importance (rank or grade) that empirical analysis shows that the event is impossible to occur when the abnormal probability ( $P_\alpha$ ) is assumed to be small. Resuming the abnormal probability 1% or 5%, the deformation monitoring index of dam crest is 23.703 mm and 22.845 mm, respectively.

*(2) Maximum Entropy Method.* According to the total displacement sample series in Table 4, the probability density function of the sample can be obtained using the maximum entropy method. To begin with, the origin moment  $\mu_i$  ( $i = 1, 2, 3, 4$ ) of sample is calculated, and then (13) is transformed into a system of nonlinear equations; thus  $\lambda_i$  ( $i = 1, 2, 3, 4$ ) is obtained by the optimization of Newton iterative method, and  $\lambda_0$  is determined by (10a) and (12). In the course of calculation, as the order of origin moment of sample is larger in Table 4, the sample data  $x$  of monitoring series is transformed into the form of  $(x - \mu)/\sigma$  considering the calculation efficiency and precision and  $\mu$  and  $\sigma$  are the mean and standard deviation of sample, respectively. The coefficients and eigenvalues of maximum entropy probability function are shown in Table 5.

TABLE 3: The adverse load combinations and components.

Number	A (m)	B (m)	C (°C)	D	Water pressure component (mm)	Temperature component (mm)	Time effect component (mm)	Frost heave component (mm)
1	737.50	641.02	-10.1	0.19	5.34	0.26	0.61	1.21
2	737.50	642.74	-0.6	0.23	5.37	0.14	0.61	0.22
3	737.50	644.46	8.9	0.27	5.40	1.73	0.61	0.00
4	737.50	646.18	18.4	0.31	5.43	0.99	0.61	0.00
5	739.50	641.02	-0.6	0.27	6.15	0.14	0.57	0.22
6	739.50	642.74	-10.1	0.31	6.18	0.26	0.57	1.21
7	739.50	644.46	18.4	0.19	6.05	0.99	0.57	0.00
8	739.50	646.18	8.9	0.23	6.08	1.73	0.57	0.00
9	741.50	641.02	8.9	0.31	6.97	1.73	1.13	0.00
10	741.50	642.74	18.4	0.27	6.92	0.99	1.13	0.00
11	741.50	644.46	-10.1	0.23	6.86	0.26	1.13	1.21
12	741.50	646.18	-0.6	0.19	6.81	0.14	1.13	0.22
13	743.50	641.02	18.4	0.23	7.67	0.99	1.13	0.00
14	743.50	642.74	8.9	0.19	7.61	1.73	1.13	0.00
15	743.50	644.46	-0.6	0.31	7.74	0.14	1.13	0.22
16	743.50	646.18	-10.1	0.27	7.69	0.26	1.13	1.21

Note. A, B, C, and D represent the upstream water level, downstream water level, temperature load, and uplift pressure reduction coefficient, respectively, which is the same as the symbols of Table 4. The values of all components are relative to the value of November 1, 2012. The initial water level is 714.46 m, the downstream water level is 642.10 m, and the initial total displacement is 12.26 mm.

TABLE 4: The total displacement of dam crest under different cases.

Number	A (m)	B (m)	C (°C)	D	Total displacement (mm)
1	737.50	641.02	-10.1	0.19	19.68
2	737.50	642.74	-0.6	0.23	18.60
3	737.50	644.46	8.9	0.27	20.00
4	737.50	646.18	18.4	0.31	19.29
5	739.50	641.02	-0.6	0.27	19.34
6	739.50	642.74	-10.1	0.31	20.48
7	739.50	644.46	18.4	0.19	19.87
8	739.50	646.18	8.9	0.23	20.64
9	741.50	641.02	8.9	0.31	22.09
10	741.50	642.74	18.4	0.27	21.30
11	741.50	644.46	-10.1	0.23	21.72
12	741.50	646.18	-0.6	0.19	20.56
13	743.50	641.02	18.4	0.23	22.05
14	743.50	642.74	8.9	0.19	22.73
15	743.50	644.46	-0.6	0.31	21.49
16	743.50	646.18	-10.1	0.27	22.55

TABLE 5: List of numerical eigenvalues and function coefficients.

Observation point number	Eigenvalues	Results	Coefficients	Results
PL5-3	$\mu_0$	1.0000	$\lambda_0$	-1.5726538
	$\mu_1$	-6.25e - 04	$\lambda_1$	0.0182553
	$\mu_2$	0.9385	$\lambda_2$	1.1987995
	$\mu_3$	-0.0122	$\lambda_3$	-0.0109235
	$\mu_4$	1.6258	$\lambda_4$	-0.4863553

TABLE 6: List of deformation monitoring indexes (Unit: mm).

Observation point number	Eigenvalues		Small probability method		Maximum entropy method	
	$\delta_1(\mu)$	$\sigma_1(\sigma)$	$P_\alpha = 1\%$	$P_\alpha = 5\%$	$P_\alpha = 1\%$	$P_\alpha = 5\%$
PL5-3	20.7744	1.2589	23.703	22.845	22.981	22.671

The maximum entropy probability density function of displacement for dam crest is written as follows:

$$f(x) = \exp \left[ -1.5726538 + \frac{0.0182553(x - \mu)}{\sigma} + 1.1987995 \left( \frac{x - \mu}{\sigma} \right)^2 - 0.0109235 \left( \frac{x - \mu}{\sigma} \right)^3 - 0.4863553 \left( \frac{x - \mu}{\sigma} \right)^4 \right]. \quad (16)$$

It can be assumed that the abnormal probability is 1% or 5% by focusing on the importance of engineering (rank or grade). Considering (14), the deformation monitoring index of dam crest is 22.981 mm and 22.671 mm, respectively.

(3) *Comparison Results of Two Methods.* As shown in Table 6, the deformation monitoring index of dam crest determined by small probability method is larger, whereas the dam crest deformation monitoring index calculated by maximum entropy method is smaller. For instance, with the abnormal probability of 1%, the dam crest deformation monitoring index based on small probability method is 23.703 mm, while the dam crest deformation monitoring index for maximum entropy method is 22.981 mm.

**3.6. Deformation Alarm of an RCC Gravity Dam.** The diagnosis of running state for an RCC gravity dam in an alpine region is conducted via the comparison between the deformation monitoring index determined by small probability and maximum entropy method (Table 6) and the measured data (Figure 4). Results show that the current maximum measured displacement of the dam crest is around 18.0 mm which is less than the deformation monitoring index. Thereby, the dam is currently in a state of safety operation; on the contrary, it is essential to take the countermeasures to control dam deformation until the deformation is less than the security alarm value provided that the actual monitoring value is greater than the deformation monitoring index in Table 6.

## 4. Conclusions

In this study, an RCC gravity dam project is taken as a case; the method of determining viscoelastic deformation monitoring index of RCC dams in alpine regions is proposed. The following conclusions can be drawn from this study:

(1) The modified monitoring model considering frost heave is proposed; an RCC gravity dam in an alpine region during operation period is taken as a case study; it is demonstrated that the dam is in the viscoelastic working state

based on the analysis of the time effect component and the inversed mechanical parameters.

(2) The method of determining viscoelastic deformation monitoring index of RCC dams in alpine regions is proposed. Initially, the combination sample of adverse cases is designed using orthogonal test method, and then each displacement component is calculated using the statistical model and the finite element method. Namely, water pressure component is calculated based on finite element method, and the temperature component is calculated through the quasi-stable temperature field and the statistical model expression; time effect component and frost heave component are both calculated using statistical model expression; thus the total displacement is obtained under different cases; on the basis of this, the viscoelastic deformation monitoring index is determined by small probability and the maximum entropy methods. The results show that, according to the abnormal probability 1%, the dam crest deformation monitoring index is 23.703 mm for small probability method, whereas the dam crest deformation monitoring index based on maximum entropy method is 22.981 mm.

(3) On the whole, it is pretty reasonable to determine the deformation monitoring index of the RCC dams in alpine regions based on statistical model and finite element method because of a full consideration of adverse load combination during operation period. Furthermore, it is noteworthy that the maximum measured value is less than the deformation monitoring index, indicating that the dam is currently in a state of safety operation.

## Conflicts of Interest

The authors declare that there are no conflicts of interest regarding the publication of this article.

## Acknowledgments

This research is supported by National Natural Science Foundation of China (nos. 51779130 and 51209124).

## References

- [1] U. S. Army Corps of Engineers (USACE), *Roller-compacted Concrete, Engineering Manual, No. 1110-2-2006*, U.S. Army Corps of Engineers, Washington, DC, USA, 1992.
- [2] H. Yu, Z. R. Wu, T. F. Bao, and L. Zhang, "Multivariate analysis in dam monitoring data with PCA," *Science China Technological Sciences*, vol. 53, no. 4, pp. 1088–1097, 2010.
- [3] J. Eichenberger, A. Ferrari, and L. Laloui, "Early warning thresholds for partially saturated slopes in volcanic ashes," *Computers & Geosciences*, vol. 49, pp. 79–89, 2013.

- [4] Ministry of Water Resources, *Technical Specification for Concrete Dams Safety Monitoring*, China Water & Power Press, Beijing, China, 2013.
- [5] M. Fanelli, "Automatic observation for dam safety," *International Water Power & Dam Construction*, pp. 10–15, 1979.
- [6] Z. R. Wu, *Safety monitoring theories & applications of hydraulic structure*, Higher Education Press, Beijing, China, 2003.
- [7] P. Lei, X. L. Chang, F. Xiao, G. J. Zhang, and H. Z. Su, "Study on early warning index of spatial deformation for high concrete dam," *Science China Technological Sciences*, vol. 54, no. 6, pp. 1607–1614, 2011.
- [8] G. Yang and M. Yang, "Multistage Warning Indicators of Concrete Dam under Influences of Random Factors," *Mathematical Problems in Engineering*, vol. 2016, Article ID 6581204, 12 pages, 2016.
- [9] X. Qin, C. Gu, B. Chen, C. Liu, B. Dai, and Y. Yu, "Multi-block combined diagnosis indexes based on dam block comprehensive displacement of concrete dams," *Optik - International Journal for Light and Electron Optics*, vol. 129, pp. 172–182, 2017.
- [10] Z. R. Wu, C. S. Gu, and X. H. Wu, *RCCD safety monitoring theory and its applications*, Science Press, Beijing, China, 2001.
- [11] D. Tonini, "Observed behavior of several leakier arch dams," *New York: Journal of the Power Division*, vol. 82, pp. 115–123, 1956.
- [12] P. Bonaldi, M. Fanelli, and G. Giuseppetti, "Displacement forecasting for concrete dams via deterministic mathematic models," *Water Power & Dam Construction*, vol. 29, pp. 74–78, 1977.
- [13] E. G. Gaziev, "Safety provision and an expert system for diagnosing and predicting dam behavior," *Hydrotechnical Construction*, vol. 34, no. 6, pp. 285–289, 2000.
- [14] J. Mata, A. Tavares de Castro, and J. Sá da Costa, "Constructing statistical models for arch dam deformation," *Structural Control and Health Monitoring*, vol. 21, no. 3, pp. 423–427, 2014.
- [15] C. Gu, Y. Wu, H. Su, and L. Tang, "A new method of estimating the equivalent elastic modulus of RCCD," *Science China Technological Sciences*, vol. 50, no. 1, pp. 136–143, 2007.
- [16] C. S. Gu, *Theories and methods of safety diagnosis and early-warning for roller compacted concrete dams*, Hohai University Press, Nanjing, China, 2013.
- [17] K. T. Fang and C. X. Ma, *Orthogonal and uniform test design*, Science Press, Beijing, 2001.
- [18] J. P. Zhang, Z. C. Lu, L. B. Li, C. Zhao, and S. M. Li, "Study on statistics model for analysis of frost heaving deformation of concrete dams," *Dam Safety*, vol. 4, pp. 28–32, 2007.
- [19] H. Su, Z. Wen, X. Sun, and M. Yang, "Time-varying identification model for dam behavior considering structural reinforcement," *Structural Safety*, vol. 57, pp. 1–7, 2015.
- [20] E. T. Jaynes, "Information theory and statistical mechanics," *Physical Review A: Atomic, Molecular and Optical Physics*, vol. 106, no. 4, pp. 620–630, 1957.
- [21] Z. Y. Wan, *Investigation on deformation monitoring index of a roller compacted concrete gravity dam in an alpine region during operation period [M.S. thesis]*, China Three Gorges University, 2017.

## Research Article

# A Complete MCDM Model for NPD Performance Assessment in an LED-Based Lighting Plant Factory

Wen-Chin Chen <sup>1</sup>, Yen-Fu Lin,<sup>2</sup> Kai-Ping Liu,<sup>3</sup> Hui-Pin Chang,<sup>4</sup>  
Li-Yi Wang <sup>1</sup>, and Pei-Hao Tai <sup>1</sup>

<sup>1</sup>Department of Industrial Management, Chung Hua University, No. 707, Sec. 2, Wufu Rd., Hsinchu 30012, Taiwan

<sup>2</sup>Ph.D. Program of Technology Management, Chung Hua University, No. 707, Sec. 2, Wufu Rd., Hsinchu 30012, Taiwan

<sup>3</sup>Department of Marketing and Logistics Management, Ling Tung University, No. 1, Ling Tung Rd., Taichung 40852, Taiwan

<sup>4</sup>General Education Center, Hsing Wu University, No. 101, Sec. 1, Fenliao Rd., Linkou District, New Taipei City 24452, Taiwan

Correspondence should be addressed to Pei-Hao Tai; [d09403015@chu.edu.tw](mailto:d09403015@chu.edu.tw)

Received 4 December 2017; Revised 30 January 2018; Accepted 27 February 2018; Published 15 April 2018

Academic Editor: Zoe Li

Copyright © 2018 Wen-Chin Chen et al. This is an open access article distributed under the Creative Commons Attribution License, which permits unrestricted use, distribution, and reproduction in any medium, provided the original work is properly cited.

Globally, industries and economies have undergone rapid development and expansion over the last several decades. As a result, global warming and environmental contaminations have resulted in climate change and jeopardized food security. In many developing countries, already decreasing crop yields are threatened by extreme weather and soil damaged by genetically modified food, making environmental problems worse and increasing food and organic product prices. For these reasons, this study proposes a hybrid multicriteria decision-making (MCDM) model for new product development (NPD) in the light-emitting diode- (LED-) based lighting plant factory. First, literature reviews and expert interviews are employed in constructing a list of decision-making objectives and criteria for new product development. Then, a fuzzy Delphi method (FDM) is used to screen the elements of the objectives and criteria, while a fuzzy decision-making trial and evaluation laboratory (FDEMATEL) is used to determine the relationships among the objectives and criteria. Finally, a fuzzy analytic network process (FANP) and a composite priority vector (CPV) are manipulated to determine the relative importance weights of the critical objectives and criteria. Results show that the proposed method can create a useful and assessable MCDM model for decision-making applications in new product development, and a case study is herein performed to validate the feasibility of the proposed model in a Taiwanese LED-based lighting plant factory, which not only provides the decision-makers with a feasible hierarchical data structure for decision-making guidance but also increases the competitive advantages of trade-offs on developing novel products.

## 1. Introduction

Global resource demands are constantly on the rise as a result of global population growth and the development and expansion of economies worldwide. People now face the danger of depleting fossil fuel reserves. Since the industrial revolution, industrial and economic prosperity came at the cost of severe environmental problems like global warming, ozone depletion, air and water pollution, and more. The effects of the weather warming include the melting of the ice sheet in the Arctic and climate change. In addition to dwindling resources and global warming, reduced food security resulting from overuse of land and chemicals is a very serious problem. A 2007 Intergovernmental Panel on

Climate Change (IPCC) climate report predicted that the global surface temperature is likely to rise a further 1.1 to 6.4°C between 2007 and 2100. It is also predicted that 15.0% to 40.0% of the Earth's species will become extinct if the average temperature of Earth's atmosphere rises by about 2°C. If Earth's mean surface temperature increases by 4°C, around 3 billion people will lose access to safe drinking water. The Kyoto Protocol or Kyoto Treaty hoped to coordinate a response to global warming, including mitigation by emission reduction, in an international convention attended by more than 50 countries in Kyoto, Japan, on December 11, 1997. The treaty was validated in 2002 and the resolution was passed on February 2005, with countries committing to endeavor to reduce emissions of CO<sub>2</sub>, CH<sub>4</sub>, N<sub>2</sub>O, HFC, PFC,

and SF<sub>6</sub> to 5.2% of the amount in 1990. The Copenhagen Accord was created by the COP 15 on December 7 and 8, 2009, to further strengthen the commitment of countries party to the Kyoto Agreement's goals. Afterwards, IPCC's Working Group II (WGII) did the literature survey on the wide range of impacts and risks of climate change and identified impediments and opportunities and warned that failure to make "substantial and sustained" reductions in greenhouse gas (GHG) emissions will increase the likelihood of severe and irreversible impacts [1]. In February 2015, they further assessed submissions related to the frequency and scheduling of reports in light of structure and operations [2]. However, three actions are to be suggested for the IPCC's decision-makers: (1) incorporating more practitioners to enhance the awareness and understanding in terms of climate change; (2) allowing a practitioner-led IPCC Special Report representing good-practice responses to climate change; (3) reporting good practices on timely climate response strategies [3]. Above all, understanding anthropogenic factors to assist decision-makers in implementing policies and actions on a weather event or climatic process and abiding by the Paris Agreement, enhanced understanding, action, and support, are needed in several areas related to addressing loss and damage, including comprehensive risk assessment and building the resilience of communities, livelihoods, and ecosystems, which can reduce the likelihood of extreme events happening [4].

In recent years, the environmental problems described above have prompted countries to develop green-related products and enterprises and to adopt strategies of renewable energy for new product development. Climate change and food security are among those threats considered to have the most significant impact on people, especially in the Afro-Asian regions, and so any new product able to overcome or alleviate these problems will be distinguished in the mainstream market. Since new product development in the 21st century needs to meet emission reduction and energy saving requirements, light-emitting diodes (LEDs), a semiconductor light source, are a typical choice and are being increasingly used for most forms of artificial lighting. For example, LEDs are used in traffic lights at intersections, outdoor billboards, landscape design, mobile phones, laptops, vehicles, televisions, and vegetative growth controlled by considerable parameters variability under different LED spectrum supplementation [5]. In other words, it seems that LEDs have become the new light sources for modern ecoenergy. The Fukushima Daiichi nuclear disaster served as a dire warning that high pollution and nonrenewable energy pose a lasting threat to the environment and must be replaced. Even though Taiwan has been deficient in many kinds of energy resources and highly dependent on imported energy, it has mature optic engineering and agriculture technology. Efforts to integrate these advantages that meet green-related product criteria have thus received significant attention recently.

Enterprises have to seek beneficial investments such as international cooperation, new product development, and equipment maintenance in order to survive in this highly competitive global economy. New product development

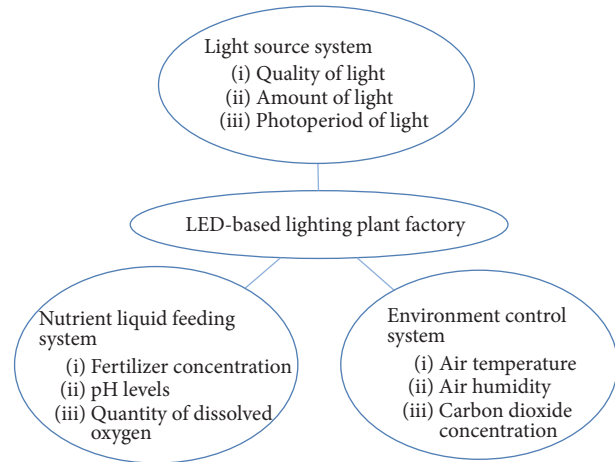


FIGURE 1: The schematic structure of an LED-based lighting plant factory.

(NPD) is deemed the most difficult of such investments. In general, the cost of new product development, the number of development team members, and the duration of a project are in direct proportion. In addition, enterprises need to pay for equipment and tools for manufacturing. It is not easy for enterprises to develop an unflawed product, and it actually takes a great deal of time and money to successfully develop a new product. New product development challenges include decision-making, regulation change, manufacturing details, time stress, market economy, producing schedule, customer needs, member diversity, and team work. As a result, performance assessment for new product development is very important in any industry.

The proposed LED-based lighting plant factory can be composed of a light source system, an environmental control system, and a nutrient liquid feeding system, as shown in Figure 1. The light source system includes variations for the light quality, amount, and photoperiod. The environment control system controls the air temperature, humidity, and carbon dioxide concentration. The nutrient liquid feeding system controls fertilizer concentration, pH levels, and the quantity of dissolved oxygen.

Team members working on the new product development usually work in a specific project group. Bad decisions by the group will result in significant financial losses for the enterprise. Thus, the financial risks involved in decision-making must be reduced as far as possible, and this can be achieved with an assessment system. LEDs are likely to be in the spotlight in the 21st century since illumination products are becoming popular, lighting technologies are improving, and costs are decreasing. LEDs offer many advantages over other forms of lighting, including their flexible emitted light color design and low energy consumption. Of significant value are their potential use in agriculture and versatility and robustness in terms of weather and geography. This study conducts a performance assessment of new product development in the LED-based lighting plant factory whose contributions are described below:

- (i) Discovering the exact objectives and criteria which meet environmental requirements
- (ii) Indicating the relationships between objectives and criteria in view of new product development in the LED-based lighting plant factory
- (iii) Evaluating the weights of potential critical factors and top priority factors to help enterprises' selection of trade-offs in new product development
- (iv) Constructing a novel performance assessment system for new product development in the LED-based lighting plant factory.

The remainder of this study is arranged as follows. Section 2 examines the literature on the subjects and methodologies adopted in this study. Section 3 establishes a hybrid MCDM performance evaluation model for NPD in an LED-based lighting plant factory. A case study of an LED-based lighting plant factory in Taiwan is carried out to verify the practicality of the proposed model in the next section. The final section sums up this research and offers conclusions.

## 2. Literature Review

As noted above, in order to eliminate as much financial risk as possible in new product development, this study aims to develop an integrated MCDM evaluation model for new product development in LED-based lighting plant factories. This section will discuss previous studies in new product development (NPD), plant factory and related light-emitting diode (LED) lighting system, fuzzy Delphi method (FDM), fuzzy decision-making trial and evaluation laboratory (FDEMATEL), fuzzy analytic network process (FANP), and composite priority vector (CPV).

New product development (NPD) is a specific process which has a lifecycle with a high level of diversity from creativity in the concept stage to logistics actions in the commercialization stage. NPD is not a single act of invention but often described interchangeably with innovation or creativity, and NPD has a distinct purpose, characteristics, and applications. In addition, NPD encompasses the entire process with numerous critical success factors bringing a new product or service to the marketplace [6] where this process identifies consumers' wants and needs and transforms them into a commercialized product. In other words, new product development (NPD) is considered the most powerful weapon against competitors and also one of the most important MCDM issues for evaluating the sustainable development of enterprises [7]. NPD is one of the core operational management processes in enterprises and requires the capabilities of creation, innovation, enforcement, technology, teamwork, and integration. Each step during the development procedure has a significant impact on NPD, including customers' needs, competitors' intimidation, technical risk, cross-department cooperation, and resource allocation. Some environmental factors of NPD process can be noted in four aspects: firstly, the effect of the market context on business performance generally has been neglected; secondly, most of the NPD projects only focused on "main effects" relationships without

concerning their environments, especially the external environment; thirdly, further research on the interaction between product design and market uncertainty is required at last, numerous unanswered questions with respect to the effects of environmental uncertainty on NPD still exist [8]. As new product development (NPD) is also a high-risk and costly process with significant failure rate, NPD success factors normally can be classified into firm internal environment, organizational capability, NPD process, level of new product's competitive advantage, and market environment; and among company-related factors, management commitment to NPD projects and managerial capabilities can be deemed two crucial factors [9]. Successful NPD is important in the survival and competitive advantage of enterprises [10]; it not only means sustainable development for a business, but also helps as a buffer in times of recession. NPD involves two highly related criteria, technology feasibility and market profitability, whereas effectiveness and efficiency are the main criteria for NPD performance. Enterprises may employ different methods to assess performance in light of their features, strategies, and designs. These methods include performance measurement balance matrix, performance measurement questionnaires, the Cambridge performance measurement design process, performance criteria systems, or performance measurement integration models. This study integrates FDM, FDEMATEL, and FANP with composite priority vector (CPV) to create a performance assessment model for NPD utilized in a Taiwanese LED lighting plant factory.

Plant factories are so-called artificially controlled environment systems which control the environmental factors such as lighting, temperature, humidity, water, and the concentration of carbon dioxide and can stably produce high-quality crops in an indoor space. In Asia, plant factory systems are able to cultivate high-profit fruits, vegetables, seedlings, and herbs with outstanding merits of high output, being pollution-free, safety, no pesticides, chemicals, and eco-friendliness [11, 12]. Normally, the configuration of plant factories is a closed plant production system which consists of six principal structural elements: thermally well-insulated and nearly airtight warehouse, multitier system equipped with lighting devices, air conditioners, and fans, a CO<sub>2</sub> delivery unit, a nutrient solution delivery unit, and an environmental control unit including EC (electric conductivity) and pH controllers for the nutrient solution [13]. Previously, the conventional light sources such as fluorescent lamp, metal halide lamp, and high pressured sodium (HPS) lamp were generally used to promote plant growth, in which some unnecessary light that mismatches with photosynthesis action spectrum (PAS) is included. To enhance the photosynthetic efficiency of the plants, it is vital to generate artificial lighting sources with coincided spectra with PAS. It is worth mentioning that the light qualities including peak position and intensity are able to be adjusted using wavelength tunable LEDs.

LEDs, typical energy saving, high efficiency, long-life-time, and environmental-friendly illuminating sources, have come to play a significant role in plant lighting. LED lighting systems have many advantages over lamps currently used in plant growth. LEDs can control the spectral output of

a lighting system for specific crops and even be modified over the course in view of a photoperiod or growth cycle. Special lighting modes can also be used to solve plant disease or injury problems [14]. Additionally, LED lighting systems can be configured to produce very high light levels, have a very long operating life, and can be turned on and turned off instantly without warm-up time. Moreover, LEDs have the potential for significant cost savings, do not contain mercury, which needs to be safely disposed of, do not have glass envelopes or high surface temperatures that can cause injury, and do not produce damaging ultraviolet wavelengths. As LEDs replace existing lamp technologies in lighting applications, significant cost decreases will be driven by economies of scale. These advantages mean that LEDs meet the standards of environmentally friendly energy. LEDs present a different technology from lamps currently used in plant lighting. LED technology is considered one of the most valuable advances in plant lighting because of the capabilities mentioned above. Many previous studies have shown the development and benefits of LED lighting systems for plant production. In the late 1980s and early 1990s, testing of LEDs for plant growth was conducted with lettuce, potato, spinach, and wheat. LEDs began to be explored for tissue culture systems in Japan [15]. LEDs were discovered to be particularly effective in germinating seeds and rooting cuttings in the Netherlands [16] and later in other researches [17, 18]. These early developments quickly led to the development of LED-based systems for plant physiology experimentation, since blue LED technology did not offer sufficient levels of blue irradiance. Researchers worked with NASA at the Kennedy Space Center (KSC) on plant-based regenerative life-support systems for future Moon and Mars bases and investigated the effect of LED-based light systems on several crop plants such as wheat, radish, spinach, lettuce, and peppers [19–21].

The Delphi method was developed in 1960 to combat some shortcomings of traditional prediction methods such as theoretical or quantitative models or trend extrapolation. However, ambiguity and uncertainty problems persisted in survey questions and responses [22]. In order to address these problems, fuzzy set theory was first incorporated with the Delphi method in 1985. The Delphi method was originally proposed by Dalkey and Helmer in 1963 and has been used in a wide range of research applications. The Delphi method systematically shows that group judgments are more valid than individual ones. In general, the standard procedure requires experts in the relevant field to answer questionnaires in two or more rounds. The researcher then provides an anonymous comment on the experts' forecasts from the previous round after each round of the survey. The experts are encouraged to revise their earlier answers according to the responses of other members of their panel. It is believed that the group will converge towards the correct answer, since the range of the answers will decrease during this process. Eventually, the process is repeated several times until a consensus emerges and the mean scores of the final round determine the result. Although the conventional Delphi method offers much scaffolding, the method still includes ambiguity and uncertainty problems in survey questions and responses

[22–24]. The incorporation of fuzzy set theory with the traditional Delphi method is one of the approaches to solving these problems [25–27]. Murray et al. [28] first applied fuzzy theory to the traditional Delphi method in 1985. Ishikawa et al. [29] utilized the cumulative frequency distribution function and fuzzy integration to convert the expert judgments into fuzzy numbers and employed the “gray zone,” the overlap section of the triangular fuzzy numbers, to develop the maximum membership degree and the FDM. FDM has been applied in many different fields of study. Chang et al. [24] established the key successful factors (KSFs) of knowledge management for university students using e-portfolio by using FDM and FAHP. Mohammad [30] developed educational system strategies in university student applications by using a hybrid fuzzy Delphi AHP. The research identifies elements which affect the admission and application of students in an Iranian University.

The decision-making trial and evaluation laboratory (DEMATEL) was proposed by Fontela and Gabus [31] for the application of solving complex problems. DEMATEL aims to yield casual dimensions and intensity of impact by using matrix computation through direct comparison of the interrelation between criteria. These structure and casualty matrices are used to express the relationship between properties in order to find the core issues of an evaluation system [32]. These methods thus benefit the decision-maker in terms of execution. DEMATEL is frequently applied to multiple criteria decision-making (MCDM) to understand the core problems and construct evaluation performance models using the mutual impact between factors and the cause-and-effect diagram drawn based on their significance. J.-K. Chen and I.-S. Chen [33] discussed the innovative performance of Taiwan's advanced education institutes in academic research and used DEMATEL, FANP, and TOPSIS to determine the relative weight of each measurement criterion and were thereby able to evaluate how to form the ideal solution and technology that will support the system through development innovation. Büyüközkan and Çifçi [34] noted that enterprises responded to increased public awareness following environmental impacts, while at the same time environmental (green) criteria and strategies became more important. The environmental performance of enterprises is not only related to the internal efforts of enterprises, but also subject to impact from the environmental performance and image of suppliers. Nonetheless, the choice of suppliers is a complex and multiple criteria decision-making problem. Therefore, green supply chain management and the capacity for green supply chain management should be employed as a basis to combine MCDM with DEMATEL in order to find the core factors to building a green supplier evaluation model for automobile companies using ANP and TOPSIS.

The Analytic Hierarchy Process (AHP), proposed by Saaty in 1971, assumes that criteria (effecting factors) in the same level are mutually independent. However, because this assumption does not reflect reality, Saaty and Takizawa [35] indicated dependence and independence from linear hierarchies to nonlinear networks using the composite vector of priorities (or composite priority vector, CPV),

which illustrated how to generate priorities for decisions in view of the dependence of criteria on criteria, criteria on alternatives, and alternatives on alternatives, based on the hierarchical feedback system framework. They distinguish two types of dependence: either functional, semantic, or qualitative dependence or structural or quantitative dependence. Moreover, they represented two kinds of dependence (outer dependence: dependence between components; inner dependence: interdependence within a component combined with feedback between components) in a nonlinear network diagram. Saaty [36] proposed the analytic network process (ANP) to extend AHP by gathering dependency and feedback with AHP. The purpose of the ANP method is to improve the traditional AHP structure in which the criteria in the same level are not interactive and dependent. In the real world, the factors influencing decision-making are no longer limited by a linear top-down structure. In other words, factors interact more like a network than a linear relationship, as one hierarchy may dominate or be dominated by other hierarchies, namely, the feedback effects. ANP tolerates criteria with feedback in the same cluster (inner dependence) and allows criteria feedback in different clusters (outer dependence). Researchers can identify the relationship among criteria in a cluster and the relationship among the clusters and then infer the priority of the alternatives.

Many previous studies have used FANP to solve complex problems in decision-making models, choosing the best alternative or strategy by fuzzy weights. Mikhailov and Singh [37] published an extended ANP approach that includes personal preference, transfers fuzzy evaluation values to range values by  $\alpha$ -cut method, and obtains the weights in light of the range value to design a decision-making system. Promentilla et al. [38] applied the ANP technique to analyze polluted yards and assess improvement strategies. The procedure of their methodology is to apply the  $\alpha$ -cut method, interval arithmetic, and fuzzy optimism index to the definite matrix and then find the priority weights by calculating the eigenvalues. Each value in the pairwise comparison matrix represents the subjective opinions of a decision-maker. Associating ANP with fuzzy theory can demonstrate the fuzzy consensus from the group evaluators' point of view on the importance between any two criteria. Büyükoçkan et al. [39] introduced a fuzzy number to the supermatrix using linguistic assessment and a fuzzy algorithm to solve the fuzzy problems arising from the criteria selection and judgment process. Mohanty et al. [40] employed the FANP method to analyze the risks and uncertainty for investments, calculating the weights based on scope analysis and selecting the best R&D project by fuzzy cost analysis. An FANP method provided enriched insights into strategic management in the Turkish airline industry [41]. Chen and Chang [42] employed ISM (Interpretative Structural Modeling) to obtain the dimension-dimension and criterion-criterion dependence relationship and used the fuzzy analytic network process (Fuzzy ANP) to determine the top priority weight for assessment improvement in new product development solutions. Song et al. [43] depended on an integrated AHP and ISM method to make an exploration of the vulnerability factors.

### 3. Proposed Methodologies and Procedures

This study employs the fuzzy Delphi method (FDM), fuzzy decision-making trial and evaluation laboratory (FDEMATEL), fuzzy analytic network process (FANP), and composite priority vector (CPV) to make better decisions in new product investments in LED plant lighting industries. The procedure consists of two stages. In the first stage, major perspectives and all performance criteria affecting new product design will be collected from previous studies and analyzed. Experts from different LED plant lighting industry areas are then selected and invited to take part in the study, according to problems identified in the analysis. The experts are also asked to complete a questionnaire. After determining the indicators for the hierarchical structure by literature review and expert interviews, an FDM is applied to screening those perspectives and criteria for the performance assessment model. In the second stage, FDEMATEL is used to obtain the relationships among the perspectives (outer dependence) and among the performance criteria (inner dependence). A supermatrix is created by using an FANP, and the weights of perspectives and all criteria are computed. A determination of the ranking weights shows the importance of investments in a new product project. The complete MCDM research flowchart is presented in Figure 2.

*Step 1* (explore and define research questions). The first thing to be done is to collect data pertaining to the LED plant lighting industry through literature reviews in order to identify the problems encountered during new product development. Other LED applications including product development, manufacturing, marketing, and recycling will also be discussed.

*Step 2* (establish an expert committee). Since the field of this study is the LED plant lighting industry, the challenges in designing renewable energy-related new products will be addressed through related data collection, expert interviews, and questionnaires.

*Step 3* (analyze the responses of the surveys). A fuzzy Delphi method (FDM) is used to obtain a reasoned consensus and consolidate individual judgments systematically. First, the questionnaire is completed by the selected experts for their suggestions and then reframed by those experts until a consensus is reached. This study uses the FDM proposed by Ishikawa et al. [29] and Lee et al. [44], and the process of the FDM is briefly explained as follows.

*Step 4* (collect the possible evaluation criteria).  $U = \{u_i \mid i = 1, 2, 3, \dots, n\}$ , where  $u_i$  is criterion  $i$ . Once the initial perspectives and criteria are established through literature review, this study obtains critical criteria for new product development. A 0–10 point evaluation scale is designed in the questionnaires and sent to the experts. Each expert is asked to give a value  $S^i = \{(C_k^i, O_k^i)\}$ , where  $S^i$  should be an integer;  $C_k^i$  and  $O_k^i$  are the lowest value and the highest value for the criterion  $u_i$  scored by the expert  $k$ . These two values also, respectively, indicate the quantitative scores of

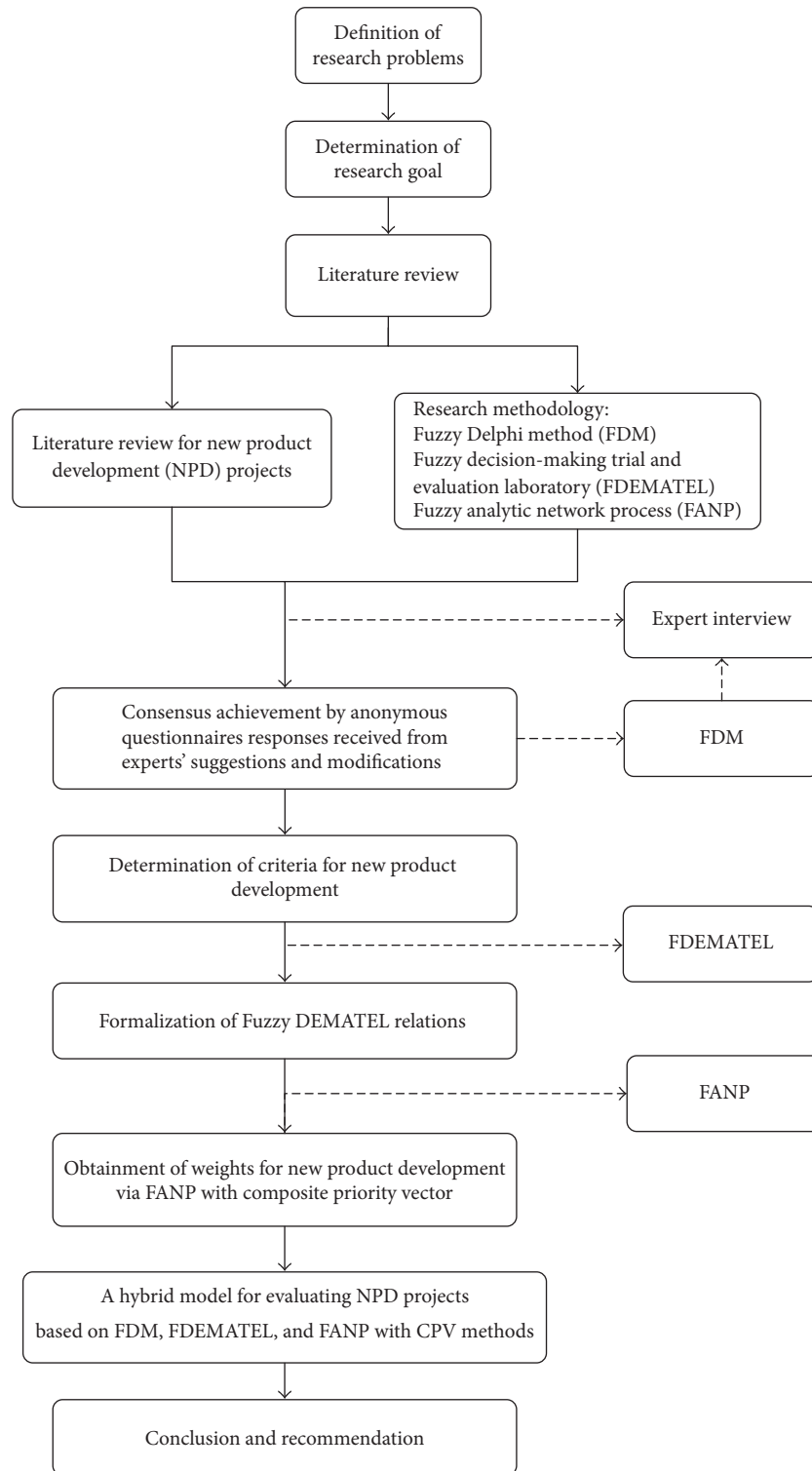


FIGURE 2: The proposed complete MCDM research flowchart.

the criteria for each expert's most conservative value and most optimistic value. The lowest level  $C_k^i$  and the highest level  $O_k^i$  of all expert judgments for each criterion  $u_i$  are then statistically calculated, and any extreme values greater than twice the standard deviation will be removed from

the criteria  $U$  [22]. The triangular values (the minimum  $C_L^i$ , the geometric mean  $C_M^i$ , and the maximum  $C_U^i$ ) of the remaining most conservative value  $C_k^i$  and the triangular values (the minimum  $O_L^i$ , the geometric mean  $O_M^i$ , and the maximum  $O_U^i$ ) of the qualified most optimistic

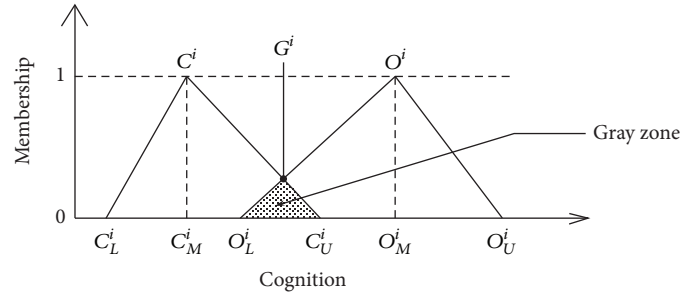


FIGURE 3: Gray zone in two triangular fuzzy numbers.

value  $O_k^i$  are then processed, resulting in a triangular fuzzy number.

As indicated above, this study creates two triangular fuzzy numbers,  $C^i = (C_L^i, C_M^i, C_U^i)$  and  $O^i = (O_L^i, O_M^i, O_U^i)$ , for each criterion  $u_i$  with triangular values of the remaining most conservative value  $C_k^i$  and the qualified most optimistic value  $O_k^i$ . If they overlap, the area of the overlap is the “gray zone” [22, 45] shown in Figure 3.

According to the gray zone of each criterion  $u_i$ , operate the importance of consensus value  $G^i$ , and examine the expert opinions to see if they arrive at a valid consensus. The consensus value  $G^i$  expresses how important a criterion  $u_i$  is. The higher the  $G^i$  value, the more important the criterion  $u_i$ . Once  $C_U^i$  and  $O_L^i$  are obtained from Step 4, the consensus value  $G^i$  can be met as the following formula.

(1) If the two triangles do not overlap ( $C_U^i \leq O_L^i$ ), the criterion  $u_i$  achieves consensus among the experts. The consensus importance value  $G^i$  will be the average of  $C_M^i$  and  $O_M^i$ .

(2) If the two triangles overlap ( $C_U^i > O_L^i$ ), there is a gray zone  $Z^i$  in the criterion  $u_i$  and  $Z^i = C_U^i - O_L^i$ . The value ranging between the geometric mean of the most optimistic value and the geometric mean of the most conservative value can be shown as  $M^i = O_M^i - C_M^i$ . The relationship between  $M^i = O_M^i - C_M^i$  and  $Z^i = C_U^i - O_L^i$ , meanwhile, ought to be identified as follows:

(a) If  $Z^i < M^i$ , it seems that there is no consensus among the experts, but the extreme opinions attributed by the experts are considered not far from other opinions given by the rest. For this reason, let the consensus on the importance  $G^i$  of the criterion  $u_i$  be the fuzzy relationship in order to find the fuzzy sets, and then obtain the maximum membership degree [44].  $\mu_F(x_j)$  represented below is the membership function of the fuzzy triangular numbers  $C^i$  and  $O^i$ :

$$F^i(x_j) = \left\{ \int_x \{\min[C^i(x_j), O^i(x_j)]\} dx \right\}, \quad j \in U, \quad (1)$$

$$G^i = \{x_j \mid \max \mu_{F^i}(x_j)\}, \quad j \in U.$$

(b) If  $Z^i > M^i$ , it is certain that there is no consensus among the experts, and the extreme opinions

attributed by the experts are considered far from other opinions given by the rest. Thus, the criterion  $u_i$  which is not converged will provide the experts with the ranging value  $M^i$  for the next questionnaire. All criteria are expected to reach a convergence until the consensus value  $G^i$  is generated.

As  $G^i$  above indicates, a threshold  $S$  is set to estimate whether a criterion  $u_i$  is qualified or not. That is, compare a consensus value  $G^i$  with  $S$ ; a criterion  $u_i$  will be selected if  $G^i > S$ ; otherwise, it will be eliminated [46]. In general, a threshold  $S$  is suggested from 6.0 to 7.0, according to literature review; however, this is subject to change in order to make a better choice [46, 47].

To sum up, the FDM procedure described above can be organized into three main phases as follows.

*Phase 1.* Calculate twice the standard deviation ( $2 * SD$ ).

*Phase 2.* Identify the gray zone (yes or no).

*Phase 3.* Set the threshold.

*Step 5.* Identify the relationships among the perspectives and among the criteria by utilizing a fuzzy decision-making trial and evaluation laboratory (FDEMATEL) method, and build a network relationship map.

*Step 6.* Derive the weights of the perspectives and criteria in new product design by using a fuzzy analytic network process (FANP). This study employs a 9-point scale of relative importance, proposed by Saaty, to design the FANP questionnaire. Experts are then asked to represent decision-makers in LED plant lighting industries for the purposes of the survey. The FANP is processed as follows.

(1) Form the network structure in which the goal, the perspectives and criteria are well defined, and the exterior relationship among the perspectives and the interior relationship among criteria are determined.

(2) Form pairwise comparison matrices with the 1 to 9 scores received from the expert responses in the questionnaires. Analyze consistency. The priority of the elements can be compared by the computation of eigenvalues and eigenvectors:

$$A \times w = \lambda_{\max} \times w, \quad (2)$$

where  $w$  is the eigenvector, the weight vector, of matrix  $A$ , and  $\lambda_{\max}$  is the largest eigenvalue of matrix  $A$ .

(3) Check the consistency of pairwise matrices with consistency index (CI) and consistency ratio (CR). The consistency property of the matrix is then checked to ensure the consistency of judgments in the pairwise comparison.

As suggested by Saaty [48], the upper threshold CR values are 0.05 for a  $3 \times 3$  matrix, 0.08 for a  $4 \times 4$  matrix, and 0.10 for larger matrices. If the consistency test is not passed, the original values in the pairwise comparison matrix must be revised by the decision-maker.

(4) Construct fuzzy positive matrices. The pairwise comparison scores are transformed into linguistic variables, which are represented by positive triangular fuzzy numbers. According to Buckley [49], the fuzzy positive reciprocal matrix can be defined as

$$\tilde{R}^k = [\tilde{r}_{ij}]^k, \quad (3)$$

where  $\tilde{R}^k$  is a positive reciprocal matrix;  $k$  is the number of decision-makers;  $\tilde{r}_{ij}$  is relative importance between elements  $i$  and  $j$ ;

$$\begin{aligned} \tilde{r}_{ij} &= 1, \quad \forall i = j, \\ \tilde{r}_{ij} &= \frac{1}{\tilde{r}_{ji}}, \quad \forall i, j = 1, 2, \dots, n. \end{aligned} \quad (4)$$

(5) Calculate fuzzy weights. Based on the Lambda-Max method proposed by Csutora and Buckley in 2001, calculate the fuzzy weights of decision elements. The procedures are as follows.

Apply  $\alpha$ -cut. Let  $\alpha = 1$  to obtain the positive matrix of decision-maker  $k$ ,  $\tilde{R}_b^k = [\tilde{r}_{ij}]_b^k$ ,  $\tilde{R}_a^k = [\tilde{r}_{ij}]_a^k$ , and let  $\alpha = 0$  to obtain the lower and upper bound positive matrices of decision-maker  $k$ , and  $\tilde{R}_c^k = [\tilde{r}_{ij}]_c^k$ . Based on the weight calculation procedure proposed in ANP, calculate weight matrices  $W_b^k = [w_i]_b^k$ ,  $W_a^k = [w_i]_a^k$ , and  $W_c^k = [w_i]_c^k$ ,  $i = 1, 2, \dots, n$ .

In order to minimize the fuzziness of the weight, two constants,  $M_a^k$  and  $M_c^k$ , are chosen as follows:

$$\begin{aligned} M_a^k &= \min \left\{ \frac{W_{ib}^k}{W_{ia}^k}, 1 \leq i \leq n \right\}, \\ M_c^k &= \max \left\{ \frac{W_{ib}^k}{W_{ic}^k}, 1 \leq i \leq n \right\}. \end{aligned} \quad (5)$$

The upper and lower bounds of the weight are defined as

$$\begin{aligned} W_{ia}^{*k} &= M_a^k W_{ia}^k, \\ W_{ic}^{*k} &= M_c^k W_{ic}^k. \end{aligned} \quad (6)$$

The upper and lower bound weight matrices are

$$\begin{aligned} W_a^{*k} &= [W_{ia}^{*k}]_a, \\ W_c^{*k} &= [W_{ic}^{*k}]_c, \end{aligned} \quad (7)$$

$$i = 1, 2, \dots, n.$$

By combining  $W_a^{*k}$ ,  $W_b^k$ , and  $W_c^{*k}$ , the fuzzy weight matrix for decision-maker  $k$  can be obtained and is defined as  $\tilde{W}_i^k = (W_{ia}^{*k}, W_{ib}^k, W_{ic}^{*k})$ ,  $i = 1, 2, \dots, n$ .

(6) Integrate the opinions of decision-makers. Geometric average is applied to combine the fuzzy weights of decision-maker opinions:

$$\overline{\tilde{W}}_i = \left[ \prod_{k=1}^K \tilde{W}_i^k \right]^{1/K}, \quad \forall k = 1, 2, \dots, K, \quad (8)$$

where  $\overline{\tilde{W}}_i$  is the combined fuzzy weight of decision element  $i$  of  $K$  decision-makers,  $\tilde{W}_i^k$  is the fuzzy weight of decision element  $i$  of decision-maker  $k$ , and  $K$  is the number of decision-makers.

(7) Defuzzify the synthetic triangular fuzzy numbers into crisp numbers by centroid method.

Form pairwise comparison matrices using the defuzzification values, and combine each submatrix with priority vectors to be an initial supermatrix. As they may not fit the column stochastic rule, normalize each column matrix to make a weighted supermatrix. Calculate a limited supermatrix by taking the weighted supermatrix to  $2k + 1$  powers so that the supermatrix converges into a stable supermatrix.

*Step 7.* The weight values acquired from FANP with CPV are ranked, and the best alternative is selected. Moreover, the significant elements (factors) that LED-based lighting plant factories try to use in developing a new product will be indicated and will provide decision-makers with important guidance.

*Step 8.* Conclusions and recommendations will be summarized.

## 4. Case Study

This study aims to construct an investment decision-making model using the fuzzy Delphi method (FDM), Fuzzy DEMATEL (FDEMATEL), and the fuzzy analytic network process (FANP) for new product development (NPD). An empirical case study from the LED-based lighting plant industry is presented as follows: (1) integrating crucial objectives and criteria of new product development obtained by literature review and expert interviews; (2) exploiting the FDM to screen the elements of objectives and criteria and identifying the cause-and-effect relationships among them; (3) determining the weights of priority vectors of objectives and criteria using FANP, which can facilitate the decision-making quality and enhance the NPD investment benefits in the LED-based lighting plant factory.

As this study is primarily concerned with decision-making in new product development in the LED-based lighting plant factory, it invites industrial and academic experts experienced in electromechanics, agriculture, and venture capital. Relevant literature surveys and repeated discussions between experts and scholars allow the study to identify crucial elements of potential objectives and criteria of new product development in an LED-based lighting plant factory,

TABLE 1: FDM participants' backgrounds and qualifications.

Expertise areas	The number of people
Academia	7
Plant industry	7 (including photoelectric 3 & agriculture 4)
Machinery industry	2
Investment consultancy	1

TABLE 2: The definition of objectives in the FDM process.

Objectives	Definitions
O1: management team	NPD team members of LED lighting plant project
O2: financial fund	Required investment and cost for LED lighting plant project
O3: product & technology	Required technical support and R&D capabilities
O4: marketing	Market successfully accepted by consumers
O5: external environment	Natural environment or man-made force majeure

and the proposed evaluation model can be further utilized in the future development of new products.

In the first phase, the expert questionnaires for the fuzzy Delphi method (FDM) are implemented to select the critically affected elements of objectives and criteria in new product development. The expert questionnaire for the fuzzy decision-making trial and evaluation laboratory (FDEMATEL) is next employed to determine the degree and direction of impact from each performance index and to draw the network structure of each index via causality relationships in the second phase. In addition, a fuzzy analytic network process (FANP) is applied to analyze the objective and criteria weights and to determine the priorities of critical impact factors in the third phase. Through the above process, the critical priority factors are identified in this research, which will affect investment in new product development in an LED-based lighting plant factory.

In addition to the literature survey and expert interviews, this study arranges five objectives and twenty-two criteria as FDM factor-screened samples. This is sufficient to obtain the cumulative frequency distribution function and the fuzzy integration to turn the experts' judgments into fuzzy numbers using 10 to 15 participants. Using more than 10 participants in the FDM process effectively reduces the error among them [50]. A total of 17 experts from different professional and academic fields take part in this study, including the photovoltaic industry, agricultural industry, machinery industry, and academia. The various FDM participants' backgrounds and qualifications are listed in Table 1.

In recent years, a plant factory-related research has received significant attention as an emerging industry. This study focuses on an LED-based lighting plant factory in view of the current market situation and limited human resources, with the aim of meeting potential consumers' NPD demands. Based on the research methodology of the previous section, the study allows experts and scholars to proceed to the related FDM questionnaires and identify the objectives and criteria using brainstorming discussions, which are described in Tables 2 and 3.

By integrating the results of comparing extreme values with their threshold values, the trimmed new product development decision-making model for an LED-based lighting plant factory can be generated by using the Fuzzy Delphi method (FDM) and represents 4 objectives and 11 criteria, as shown in Table 4. Moreover, the decision-making hierarchy schematic model for an LED-based lighting plant factory is depicted in Figure 4.

The impact interactions of the above 11 key indicators (i.e., A to K) can be identified through the Fuzzy DEMATEL survey, which invited six domestic industrial experts and scholars in the plant factory field to take part in the questionnaires. They were asked to identify, based on their expertise, the direct effects exerted by each element on other elements, using a scale ranging from 0 to 4, where "0," "1," "2," "3," and "4," respectively, mean "no influence," "low influence," "medium influence," "high influence," and "very high influence." The larger the value of impact indicators, the greater the influence of the factor on another factor! After completing the above questionnaires, each expert evaluates the direct impact effects and places them in direct-relation matrices, and the corresponding triangle fuzzy number can be seen in Table 5.

The direct-relation matrix is developed by summing all vectors and taking the sum of maximum vectors as the benchmark of form. The initial direct-relation matrix  $D$  is shown in (9). The normalized direct-relation matrix ( $X$ ) can be obtained by calculating (10) and (11).

$$D = \begin{bmatrix} 0 & D_{12} & \cdots & D_{1j} \\ D_{21} & 0 & \cdots & D_{2j} \\ \vdots & \vdots & \ddots & \vdots \\ D_{i1} & D_{ij} & \cdots & 0 \end{bmatrix}, \quad (9)$$

$$\lambda = \frac{1}{\max_{1 \leq i \leq n} (\sum_{j=1}^n D_{ij})}, \quad (10)$$

$$X = \lambda \times D. \quad (11)$$

TABLE 3: The definition of criteria in the FDM process.

Criteria	Definitions
C1-1: expertise and management skills	The background of the team members should allow them to communicate and coordinate
C1-2: business management philosophy	Whether the management concept of board members is consistent
C1-3: top management approval	Department heads are actively involved in product development plan
C2-1: investment preparation in funding	Required project (customer satisfaction) investment funds
C2-2: cost of investment opportunities for government grants	The government provides the relevant laws and regulations, subsidies or tax cuts, and other measures
C2-3: return on investment	The economy scale of the investment is the percentage ratio between the income and the cost
C3-1: technical personnel and R&D capability	R&D efficiency and technical support capability
C3-2: effective manufacturing processes	The manufacturing process of the product must be comprehensive and flexible and effectively enhance the production capacity
C3-3: technical resources management	Promoting the maintenance and management capabilities of optoelectronics, agriculture, and machinery fields
C3-4: product added value	Not only food but also architectural design and ornament can be further developed
C3-5: patents and intellectual property rights	Intellectual property rights and patents for the LED plant growth box portfolio
C4-1: potential market demands	Total demands for LED plant growth boxes in target markets
C4-2: product differentiation of the market competitive advantage	Differences in the products and services provided by the company and its competitors
C4-3: new product marketing strategy	Hybrid innovative marketing model for LED plant growth box
C4-4: market status survey	Current LED plant growth box in the target market vendor survey
C4-5: consumer acceptance	The perception of target consumers, which benefits from the LED plant growth box
C4-6: channel profit	The profits from assisting before LED plant growth box products given to the consumers
C4-7: integrity of after-sales service	Providing after-sales service and support after the product enters the market
C5-1: imitation by competitors	Product portfolio can be copied by existing competitors or potential competitors
C5-2: government decrees and patents	Changes in government regulations or patent factors leading to product supply chain or promotion affected
C5-3: research report unfavorable to this industry	Research report will affect the promotion of products in the market
C5-4: geography, climate, and other extreme environmental constraints	Force majeure of natural and environmental factors for LED plant growth box products

TABLE 4: The trimmed NPD decision-making model.

Objectives	Definitions	Criteria
O1: management team	NPD team members of LED lighting plant project	A: expertise and management skills B: business management philosophy
O2: financial funding	Required investment and cost for LED lighting plant project	C: investment preparation in funding D: return on investment E: technical personnel and R&D capability
O3: product & technology	Required technical support and R&D capabilities	F: effective manufacturing processes G: technical resources management H: potential market demands
O4: marketing	Market successfully accepted by consumers	I: new product marketing strategy J: market status survey K: consumer acceptance

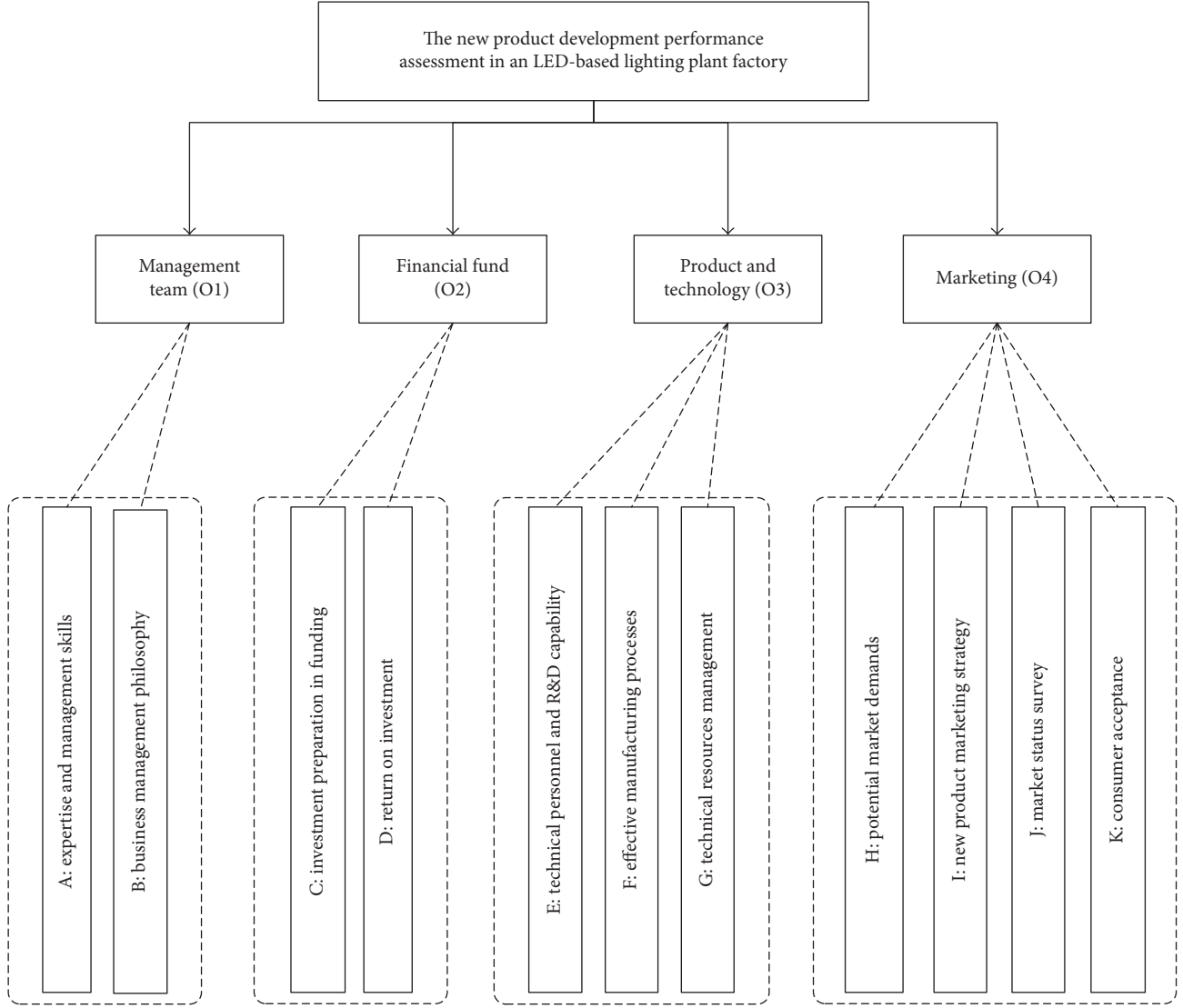


FIGURE 4: The decision-making hierarchy schematic diagram of an NPD project.

TABLE 5: Triangle fuzzy number of identified direct effect and scale range.

Direct effect	Scale	Triangle fuzzy number
No influence	0	(0, 0, 0)
Low influence	1	(0, 0.25, 0.5)
Medium influence	2	(0.25, 0.5, 0.75)
High influence	3	(0.5, 0.75, 1)
Very high influence	4	(0.75, 1, 1)

Substitute the direct-relation matrix  $X$  into (12) to calculate the total-relation matrix ( $T$ ), while the direct-relation matrix can also be addressed as the total-relation matrix. Particularly, the unit matrix  $I$  is defined in (13), and all criteria

direct-relation matrices are combined to become the total-relation matrix:

$$T = \lim_{k \rightarrow \infty} (X^1 + X^2 + \dots + X^k) = X(I - X)^{-1}, \quad (12)$$

$$I = \begin{bmatrix} 1 & 0 & 0 & \dots & 0 \\ 0 & 1 & 0 & \dots & \vdots \\ 0 & 0 & 1 & \dots & 0 \\ \vdots & \vdots & \vdots & \ddots & \vdots \\ 0 & 0 & 0 & \dots & 1 \end{bmatrix}. \quad (13)$$

At the outset of constructing the experts' questionnaires, the elements of objectives such as management team, financial funding, product and technology, and marketing are used

TABLE 6: Relevance and level of impact among objectives after integration.

Objectives	$D_i$	$R_j$	$D_i + R_j$	$D_i - R_j$
O1: management team	92.1266	92.1266	183.2259	-1.027280765
O2: financial fund	89.8125	89.8125	179.6254	0.000492328
O3: product & technology	93.0257	93.0257	183.9982	-2.053063573
O4: marketing	87.8109	87.8109	178.7017	3.07985201
Average			181.3878	(0.00)

to obtain the relevance and level of impact through direct-relation analyses, as shown in Table 6. The sum of  $D_i$  on each column and the sum of  $R_j$  on each row, respectively, are then calculated, as shown in (14), where  $D_i$  denotes the level of impact directly and affects other criteria;  $R_j$  denotes the level; and criterion  $j$  is directly affected by other criteria.  $D_i + R_j$  denotes relevance, signifying the intensity of the relationship between criteria.  $D_i - R_j$  denotes level of impact, also known as the intensity with which criteria have effect or are affected.

$$D_i = \sum_{j=1}^n x_{ij}, \quad i = 1, 2, 3, \dots, n, \tag{14}$$

$$R_j = \sum_{i=1}^n x_{ij}, \quad j = 1, 2, 3, \dots, n.$$

Using two-dimensional coordinates as the base of a causal diagram and taking  $D_i + R_j$  as the  $x$ -axis and  $D_i - R_j$  as the  $y$ -axis, the relevance and level of impact of each criterion are marked on the coordinates. The causality between criteria is drawn according to the threshold, in addition to analysis. In particular, if  $D_i - R_j$  is a positive value, it suggests that  $i$  affects criterion  $j$ ; conversely, if  $D_i - R_j$  is a negative value, it suggests that  $j$  affects criterion  $i$ . In order to obtain the relevance and level of impact among objectives, the matrix values are substituted into (14) to yield  $D_i$  and  $R_j$ , which, in addition to a summary, are found in Table 16. In particular,  $D_i + R_j$  represents the relevance value between objectives, whereas  $D_i - R_j$  denotes the level of impact or impact value.

The relevance value and impact value are set up in two-dimensional coordinates, where relevance value ( $D_i + R_j$ ) is filled in the  $x$ -axis, and impact value ( $D_i - R_j$ ) is filled in the  $y$ -axis. This study configures a threshold to highlight the causality. In particular, the threshold value is 1.073, which is the maximum value of diagonal elements within the total-relation matrix ( $T$ ). Through the configuration of the threshold, a number smaller than the threshold will be deleted, while a number greater than or equal to the threshold will be drawn on the coordinates to form the direct-relation causal diagram for objectives. The causal diagram for objectives is shown in Figure 5.

The relevance and level of impact of management team, financial funding, product and technology, and marketing are shown in Tables 7–10, and causal diagrams for management team, financial funding, product and technology, and marketing are shown in Figures 6–9.

In addition to the above, a fuzzy analytic network process (FANP) is used to calculate the relative weights of relationships between objectives and criteria, so that enterprises or

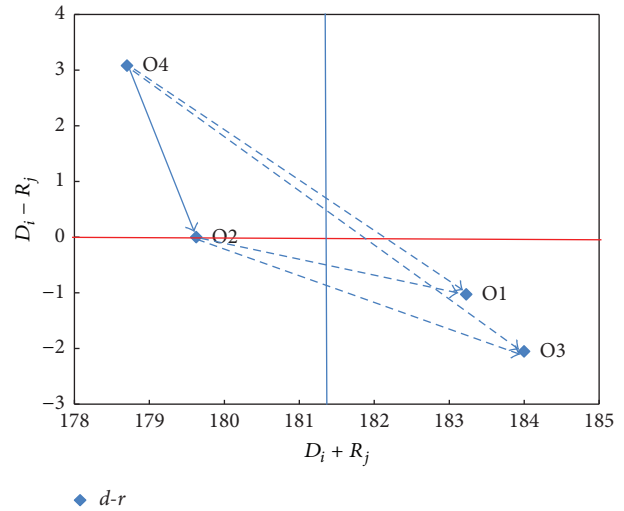


FIGURE 5: Causal diagram for objectives.

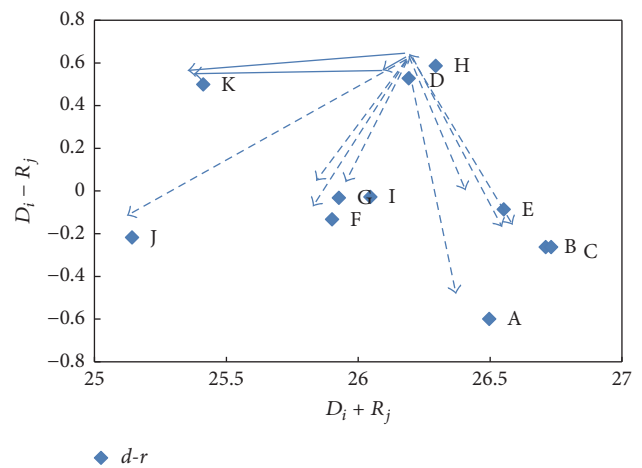


FIGURE 6: Causal diagram for management team.

R&D departments can select the most important elements in the new product development decision-making scheme. This study constructed dependency relationships between hierarchical relationships of the key elements of objectives and criteria in new product development of an LED-based lighting plant factory using Fuzzy DEMATEL. Moreover, the study composes pairwise relative weights of the FANP architecture, while the questionnaire responses of 10 experts are assessed with the fuzzy semantic variables integrated by

TABLE 7: The relevance and level of impact (6 experts) for management team.

Items	Elements	$D_i$	$R_j$	$D_i + R_j$ (relevance)	$D_i - R_j$ (level of impact)
A	Expertise and management skills	12.95	13.55	26.50	-0.60
B	Business management philosophy	13.23	13.49	26.71	-0.26
C	Investment preparation in funding	13.23	13.50	26.73	-0.26
D	Return on investment	13.36	12.83	26.19	0.53
E	Technical personnel and R&D capability	13.23	13.32	26.55	-0.09
F	Effective manufacturing processes	12.88	13.02	25.90	-0.13
G	Technical resources management	12.95	12.98	25.93	-0.03
H	Potential market demands	13.44	12.85	26.29	0.59
I	New product marketing strategy	13.01	13.04	26.05	-0.03
J	Market status survey	12.46	12.68	25.14	-0.22
K	Consumer acceptance	12.96	12.46	25.41	0.50
	Average			26.13	(0.00)

TABLE 8: The relevance and level of impact (6 experts) for financial fund.

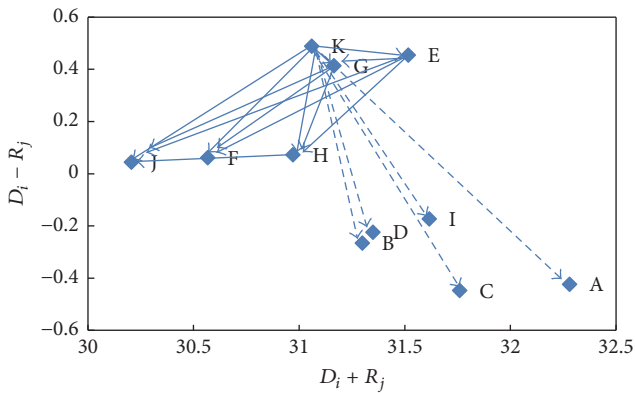
Items	Elements	$D_i$	$R_j$	$D_i + R_j$ (relevance)	$D_i - R_j$ (level of impact)
A	Expertise and management skills	15.93	16.35	32.28	-0.42
B	Business management philosophy	15.52	15.78	31.30	-0.27
C	Investment preparation in funding	15.66	16.10	31.76	-0.45
D	Return on investment	15.56	15.79	31.35	-0.22
E	Technical personnel and R&D capability	15.99	15.53	31.52	0.45
F	Effective manufacturing processes	15.31	15.25	30.57	0.06
G	Technical resources management	15.79	15.38	31.16	0.41
H	Potential market demands	15.52	15.45	30.97	0.07
I	New product marketing strategy	15.72	15.90	31.62	-0.17
J	Market status survey	15.12	15.08	30.21	0.04
K	Consumer acceptance	15.77	15.29	31.06	0.49
	Average			31.25	(0.00)

TABLE 9: The relevance and level of impact (6 experts) for product and technology.

Items	Elements	$D_i$	$R_j$	$D_i + R_j$ (relevance)	$D_i - R_j$ (level of impact)
A	Expertise and management skills	18.56	18.28	36.83	0.28
B	Business management philosophy	18.38	18.58	36.96	-0.21
C	Investment preparation in funding	18.68	18.50	37.19	0.18
D	Return on investment	18.50	18.03	36.53	0.47
E	Technical personnel and R&D capability	18.42	18.21	36.62	0.21
F	Effective manufacturing processes	17.96	17.88	35.85	0.08
G	Technical resources management	18.42	18.84	37.26	-0.42
H	Potential market demands	17.97	18.27	36.23	-0.30
I	New product marketing strategy	18.23	18.40	36.63	-0.18
J	Market status survey	17.87	17.98	35.85	-0.11
K	Consumer acceptance	18.31	18.32	36.63	-0.01
	Average			36.60	0.00

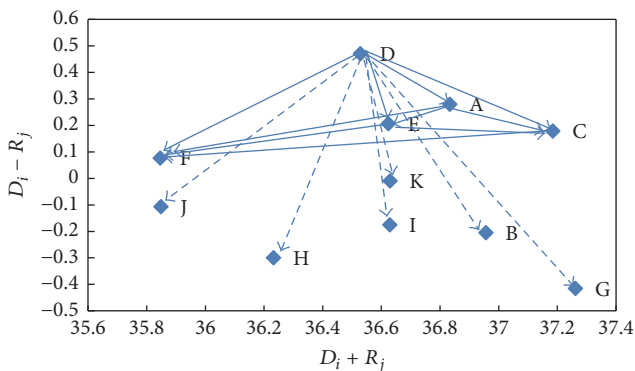
TABLE 10: The relevance and level of impact (6 experts) for marketing.

Items	Elements	$D_i$	$R_j$	$D_i + R_j$ (relevance)	$D_i - R_j$ (level of impact)
A	Expertise and management skills	16.29	16.40	32.70	-0.11
B	Business management philosophy	16.17	15.81	31.98	0.36
C	Investment preparation in funding	16.07	16.15	32.22	-0.08
D	Return on investment	15.86	16.04	31.91	-0.18
E	Technical personnel and R&D capability	16.19	15.82	32.01	0.36
F	Effective manufacturing processes	15.47	15.86	31.33	-0.40
G	Technical resources management	16.22	15.71	31.93	0.52
H	Potential market demands	15.95	15.77	31.72	0.18
I	New product marketing strategy	16.27	16.47	32.73	-0.20
J	Market status survey	14.97	15.63	30.60	-0.66
K	Consumer acceptance	15.59	15.39	30.98	0.20
	Average			31.83	0.00



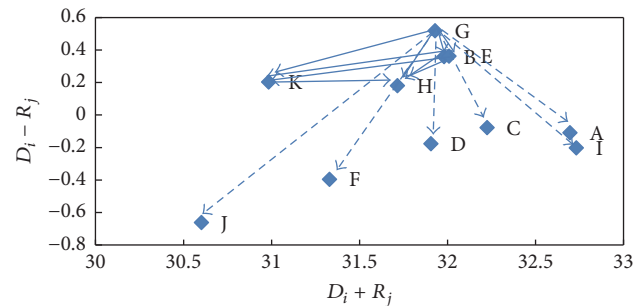
◆  $d-r$

FIGURE 7: Causal diagram for financial funding.



◆  $d-r$

FIGURE 8: Causal diagram for product and technology.



◆  $d-r$

FIGURE 9: Causal diagram for marketing.

geometric mean, and the holistic process of the FANP is illustrated as follows.

*Step 1* (establish the network structure). An analytics network process structure consisting of the business goal and objectives and criteria well defined in the first step of this case study is established. This structure includes the exterior relationship among criteria and the interior relationship among criteria under each objective, as shown in Figure 10.

*Step 2* (form pairwise comparison matrices). Based on the (1–9) scores from the expert responses to the FANP questionnaires, the pairwise comparison matrices for the objective and criteria are formed. Meanwhile, the entries in each column are normalized and the eigenvectors are obtained. The fuzzy and defuzzy pairwise comparison matrices from 10 experts’ answers to the four objectives are shown in Tables 11 and 12.

*Step 3* (examine the consistency). Once the eigenvectors are obtained, the largest eigenvalue for each matrix can be computed. Then, the consistency index (CI), random index (RI), and the consistency ratio (CR) are calculated. According to Saaty’s suggestion, the consistency is satisfied if the CR is smaller than 0.1. Thus, the expert responses are

TABLE II: The fuzzy pairwise comparison matrix (10 experts) for objectives.

Objectives	Management team		Financial fund		Product & technology		Marketing		
O1: management team	1.000	1.000	0.480	0.567	0.687	0.344	0.457	0.394	0.459
O2: financial fund	1.455	1.764	1.000	1.000	1.000	0.443	0.521	0.404	0.492
O3: product & technology	1.446	2.187	1.560	1.918	2.259	1.000	1.000	0.497	0.575
O4: marketing	1.823	2.178	1.578	2.032	2.472	1.473	1.740	1.000	1.000

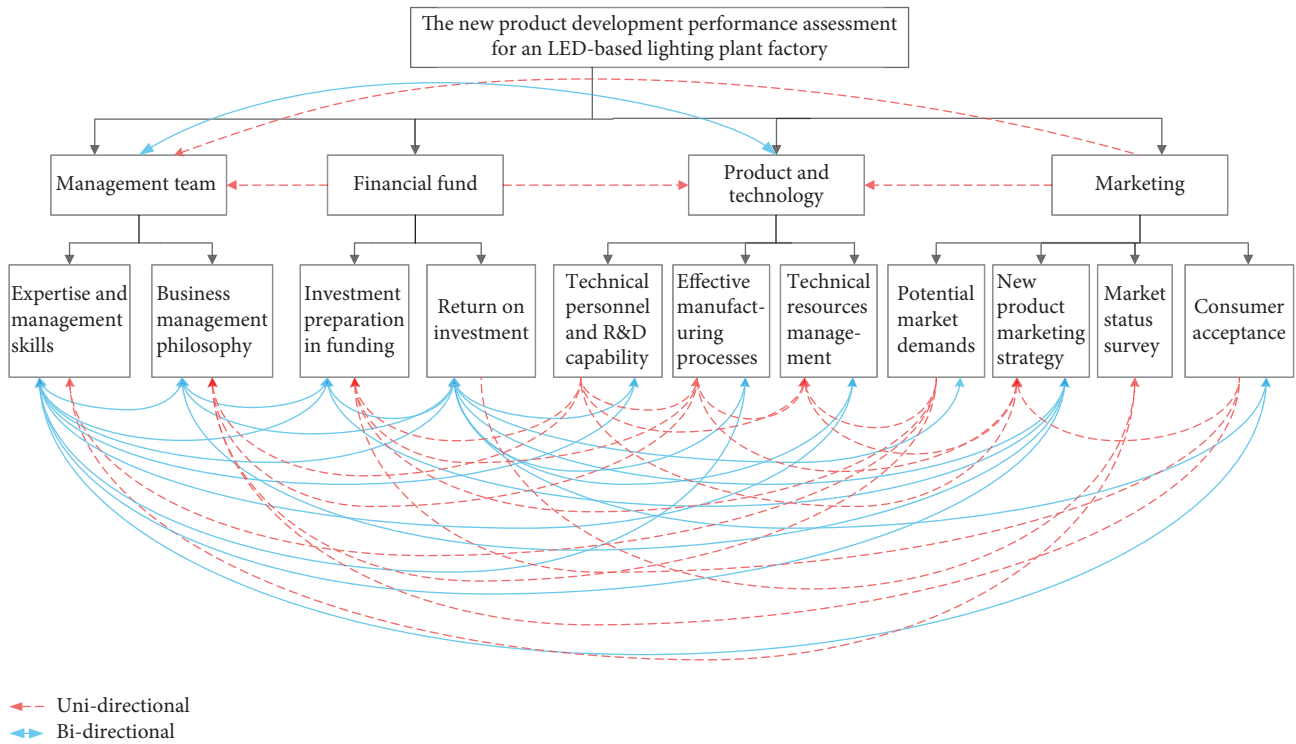


FIGURE 10: An analytics network process structure of the proposed MCDM model.

TABLE 12: The defuzzy pairwise comparison matrix (10 experts) for objectives.

Objectives	Management team	Financial fund	Product & technology	Marketing
O1: management team	1.0000	0.5780	0.4976	0.4671
O2: financial fund	1.7674	1.0000	0.5350	0.5100
O3: product & technology	2.1797	1.9123	1.0000	0.5836
O4: marketing	2.1804	2.0276	1.7413	1.0000

TABLE 13: The consistency assessment of fuzzy pairwise comparison matrix.

Objectives	Management team	Financial fund	Product & technology	Marketing	Weight
O1: management team	0.1403	0.1048	0.1319	0.1824	0.1398
O2: financial fund	0.2480	0.1812	0.1418	0.1992	0.1925
O3: product & technology	0.3058	0.3466	0.2650	0.2279	0.2863
O4: marketing	0.3059	0.3675	0.4614	0.3905	0.3813

$\lambda_{max} = 4.1092$ ;  $CI = 0.0364$ ;  $RI = 0.9$ ;  $CR = 0.040$ .

analyzed using the above process. The results show that all CR values are less than 0.1. This means that the questionnaires are validated. As an example, a consistency examination including CI, RI, and CR from the same experts' answers to the four objectives is shown in Table 13.

*Step 4 (construct the supermatrix).* Each matrix is defuzzified to obtain the weights of the matrix, and then the weights are brought into the supermatrix, and an iterative computing model is used to generate the limited matrix from

the supermatrix. Table 14 is an unweighted supermatrix, and a weighted supermatrix is shown in Table 15; after iterative computing, the limited supermatrix is generated, as shown in Table 16.

In addition, this study uses the expert questionnaire responses to obtain the positive reciprocal matrix required for AHP and FANP research and to obtain the priority weight of each objective and each criterion through the structure of composite priority vector of Figure 11.

TABLE 14: The unweighted supermatrix.

Assessed Items	Objectives														
	O1	O2	O3	O4	C1	C2	C3	C4	C5	C6	C7	C8	C9	C10	C11
O1: management team	0.3615	0.2203	0.5546	0.2245	0.0000	0.0000	0.0000	0.0000	0.0000	0.0000	0.0000	0.0000	0.0000	0.0000	0.0000
O2: financial fund	0.1925	0.5150	0.1925	0.1925	0.0000	0.0000	0.0000	0.0000	0.0000	0.0000	0.0000	0.0000	0.0000	0.0000	0.0000
O3: product & technology	0.6385	0.2647	0.4454	0.2948	0.0000	0.0000	0.0000	0.0000	0.0000	0.0000	0.0000	0.0000	0.0000	0.0000	0.0000
O4: marketing	0.3813	0.3813	0.3813	0.4807	0.0000	0.0000	0.0000	0.0000	0.0000	0.0000	0.0000	0.0000	0.0000	0.0000	0.0000
C1: expertise and management skills	0.0000	0.0000	0.0000	0.0000	0.0688	0.1252	0.1222	0.0630	0.0818	0.0790	0.1194	0.0994	0.1099	0.0909	0.1363
C2: business management philosophy	0.0000	0.0000	0.0000	0.0000	0.0581	0.1147	0.0970	0.0548	0.0683	0.0674	0.0609	0.0968	0.1099	0.0909	0.0833
C3: investment preparation in funding	0.0000	0.0000	0.0000	0.0000	0.1408	0.2443	0.3575	0.1565	0.2591	0.2765	0.2714	0.3448	0.3283	0.0909	0.2813
C4: return on investment	0.0000	0.0000	0.0000	0.0000	0.0604	0.1876	0.1806	0.0770	0.1068	0.1110	0.1240	0.1421	0.1432	0.0909	0.1209
C5: technical personnel and R&D capability	0.0000	0.0000	0.0000	0.0000	0.1222	0.0000	0.0000	0.0821	0.0994	0.0000	0.0000	0.0000	0.0000	0.0909	0.0000
C6: effective manufacturing processes	0.0000	0.0000	0.0000	0.0000	0.0883	0.0000	0.0000	0.0694	0.0815	0.1022	0.0000	0.0000	0.0000	0.0909	0.0000
C7: technical resources management	0.0000	0.0000	0.0000	0.0000	0.0913	0.0000	0.0000	0.0748	0.0793	0.0971	0.1539	0.1498	0.0000	0.0909	0.2229
C8: potential market demands	0.0000	0.0000	0.0000	0.0000	0.0000	0.0000	0.0000	0.0950	0.0000	0.0000	0.0000	0.1671	0.0000	0.0909	0.1553
C9: new product marketing strategy	0.0000	0.0000	0.0000	0.0000	0.1926	0.3281	0.2426	0.1528	0.2237	0.2668	0.2704	0.0000	0.2888	0.0909	0.0000
C10: market status survey	0.0000	0.0000	0.0000	0.0000	0.0797	0.0000	0.0000	0.0918	0.0000	0.0000	0.0000	0.0000	0.0000	0.0909	0.0000
C11: consumer acceptance	0.0000	0.0000	0.0000	0.0000	0.0979	0.0000	0.0000	0.0828	0.0000	0.0000	0.0000	0.0000	0.0000	0.0909	0.0000

TABLE 15: The weighted supermatrix.

Assessed items	Objectives															
	O1	O2	O3	O4	O1	C1	C2	C3	C4	C5	C6	C7	C8	C9	C10	C11
O1: management team	0.2297	0.1595	0.3524	0.1883	0.0000	0.0000	0.0000	0.0000	0.0000	0.0000	0.0000	0.0000	0.0000	0.0000	0.0000	0.0000
O2: financial fund	0.1223	0.3728	0.1223	0.1614	0.0000	0.0000	0.0000	0.0000	0.0000	0.0000	0.0000	0.0000	0.0000	0.0000	0.0000	0.0000
O3: product & technology	0.4057	0.1916	0.2830	0.2472	0.0000	0.0000	0.0000	0.0000	0.0000	0.0000	0.0000	0.0000	0.0000	0.0000	0.0000	0.0000
O4: marketing	0.2423	0.2761	0.2423	0.4031	0.0000	0.0000	0.0000	0.0000	0.0000	0.0000	0.0000	0.0000	0.0000	0.0000	0.0000	0.0000
C1: expertise and management skills	0.0000	0.0000	0.0000	0.0000	0.0688	0.1252	0.1222	0.0630	0.0818	0.0790	0.1194	0.0994	0.1297	0.0909	0.1363	0.0833
C2: business management philosophy	0.0000	0.0000	0.0000	0.0000	0.0581	0.1147	0.0970	0.0548	0.0683	0.0674	0.0609	0.0968	0.1099	0.1099	0.0909	0.0833
C3: investment preparation in funding	0.0000	0.0000	0.0000	0.0000	0.1408	0.2443	0.3575	0.1565	0.2591	0.2765	0.2714	0.3448	0.3283	0.0909	0.2813	0.2813
C4: return on investment	0.0000	0.0000	0.0000	0.0000	0.0604	0.1876	0.1806	0.0770	0.1068	0.1110	0.1240	0.1421	0.1432	0.0909	0.1209	0.1209
C5: technical personnel and R&D capability	0.0000	0.0000	0.0000	0.0000	0.1222	0.0000	0.0000	0.0821	0.0994	0.0000	0.0000	0.0000	0.0000	0.0909	0.0000	0.0000
C6: effective manufacturing processes	0.0000	0.0000	0.0000	0.0000	0.0883	0.0000	0.0000	0.0694	0.0815	0.1022	0.0000	0.0000	0.0000	0.0909	0.0000	0.0000
C7: technical resources management	0.0000	0.0000	0.0000	0.0000	0.0913	0.0000	0.0000	0.0748	0.0793	0.0971	0.1539	0.1498	0.0000	0.0909	0.2229	0.2229
C8: potential market demands	0.0000	0.0000	0.0000	0.0000	0.0000	0.0000	0.0000	0.0950	0.0000	0.0000	0.0000	0.1671	0.0000	0.0909	0.1553	0.1553
C9: new product marketing strategy	0.0000	0.0000	0.0000	0.0000	0.1926	0.3281	0.2426	0.1528	0.2237	0.2668	0.2704	0.0000	0.2888	0.0909	0.0000	0.0000
C10: market status survey	0.0000	0.0000	0.0000	0.0000	0.0797	0.0000	0.0000	0.0918	0.0000	0.0000	0.0000	0.0000	0.0000	0.0909	0.0000	0.0000
C11: consumer acceptance	0.0000	0.0000	0.0000	0.0000	0.0979	0.0000	0.0000	0.0828	0.0000	0.0000	0.0000	0.0000	0.0000	0.0909	0.0000	0.0000



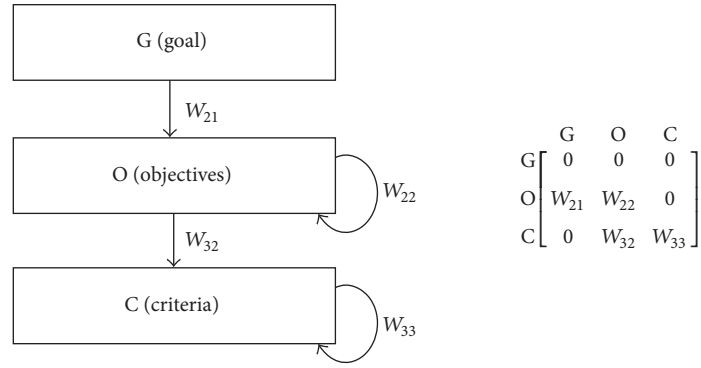


FIGURE 11: The structure of composite priority vector.

(1) The independent weights matrix under selected objectives is shown below:

$$W_{21} = \begin{matrix} O_1 \\ O_2 \\ O_3 \\ O_4 \end{matrix} \begin{bmatrix} 0.1398 \\ 0.1925 \\ 0.2863 \\ 0.3813 \end{bmatrix}. \quad (15)$$

(2) The relational weight matrix between dependencies of objectives is then calculated, as shown below:

$$W_{22} = \begin{bmatrix} 0.2297 & 0.1595 & 0.3524 & 0.1883 \\ 0.1223 & 0.3728 & 0.1223 & 0.1614 \\ 0.4057 & 0.1916 & 0.2830 & 0.2472 \\ 0.2423 & 0.2761 & 0.2423 & 0.4031 \end{bmatrix}. \quad (16)$$

(3) The independent weight matrix of the elements (criteria) under each objective is generated:

$$W_{32} = \begin{bmatrix} 0.0630 \\ 0.0548 \\ 0.1565 \\ 0.0770 \\ 0.0821 \\ 0.0694 \\ 0.0748 \\ 0.0950 \\ 0.1528 \\ 0.0918 \\ 0.0828 \end{bmatrix}. \quad (17)$$

(4) The relative weights between the dependency matrices of criteria are calculated:

$$W_{33} = \begin{bmatrix} 0.0688 & 0.1252 & 0.1222 & 0.0630 & 0.0818 & 0.0790 & 0.1194 & 0.0994 & 0.1297 & 0.0909 & 0.0909 \\ 0.0581 & 0.1147 & 0.0970 & 0.0548 & 0.0683 & 0.0674 & 0.0609 & 0.0968 & 0.1099 & 0.0909 & 0.0833 \\ 0.1408 & 0.2443 & 0.3575 & 0.1565 & 0.2591 & 0.2765 & 0.2714 & 0.3448 & 0.3283 & 0.0909 & 0.2813 \\ 0.0604 & 0.1876 & 0.1806 & 0.0770 & 0.1068 & 0.1110 & 0.1240 & 0.1421 & 0.1432 & 0.0909 & 0.1209 \\ 0.1222 & 0.0000 & 0.0000 & 0.0821 & 0.0994 & 0.0000 & 0.0000 & 0.0000 & 0.0000 & 0.0909 & 0.0000 \\ 0.0883 & 0.0000 & 0.0000 & 0.0694 & 0.0815 & 0.1022 & 0.0000 & 0.0000 & 0.0000 & 0.0909 & 0.0000 \\ 0.0913 & 0.0000 & 0.0000 & 0.0748 & 0.0793 & 0.0971 & 0.1539 & 0.1498 & 0.0000 & 0.0909 & 0.2229 \\ 0.0000 & 0.0000 & 0.0000 & 0.0950 & 0.0000 & 0.0000 & 0.0000 & 0.1671 & 0.0000 & 0.0909 & 0.1553 \\ 0.1926 & 0.3281 & 0.2426 & 0.1528 & 0.2237 & 0.2668 & 0.2704 & 0.0000 & 0.2888 & 0.0909 & 0.0000 \\ 0.0797 & 0.0000 & 0.0000 & 0.0918 & 0.0000 & 0.0000 & 0.0000 & 0.0000 & 0.0000 & 0.0909 & 0.0000 \\ 0.0979 & 0.0000 & 0.0000 & 0.0828 & 0.0000 & 0.0000 & 0.0000 & 0.0000 & 0.0000 & 0.0909 & 0.0000 \end{bmatrix}. \quad (18)$$

(5) The actual weights among objectives are calculated:

$$W_{\text{goal-objectives}} = W_{22} \times W_{21} = \begin{bmatrix} 0.2355 \\ 0.1855 \\ 0.2689 \\ 0.3101 \end{bmatrix}. \quad (19)$$

$$W_{\text{objectives-criteria}} = W_{33} \times W_{32} = \begin{bmatrix} 0.1052 \\ 0.0854 \\ 0.2656 \\ 0.1278 \\ 0.0305 \\ 0.0330 \\ 0.0773 \\ 0.0444 \\ 0.1894 \\ 0.0204 \\ 0.0209 \end{bmatrix}. \quad (20)$$

(6) The actual weight of the criteria under each objective is calculated:

(7) The overall weight of each criterion for the goal is calculated:

$$W_{\text{goal-criteria}} = W_{32} \times W_{\text{goal-objectives}} = \begin{bmatrix} 0.0148 & 0.0129 & 0.0368 & 0.0181 & 0.0193 & 0.0163 & 0.0176 & 0.0224 & 0.0360 & 0.0216 & 0.0195 \\ 0.0117 & 0.0102 & 0.0290 & 0.0143 & 0.0152 & 0.0129 & 0.0139 & 0.0176 & 0.0283 & 0.0170 & 0.0154 \\ 0.0170 & 0.0147 & 0.0421 & 0.0207 & 0.0221 & 0.0187 & 0.0201 & 0.0255 & 0.0411 & 0.0247 & 0.0223 \\ 0.0195 & 0.0170 & 0.0485 & 0.0239 & 0.0255 & 0.0215 & 0.0232 & 0.0295 & 0.0474 & 0.0285 & 0.0257 \end{bmatrix}. \quad (21)$$

Normally, a decision-making model for NPD performance assessment includes a hierarchical structure with a variety of objectives and criteria, which is directly related to the processes of technology and management of different types of information (technological, economic, social, and environmental). Traditional single objective decision-making which is basically concerned with either maximization or minimization of a particular element or variable remains beneficial only in a study of small system. With the increase in the complexity and multiplicity in the problem, the single objective optimization/decision-making analysis is no longer a prevalent approach. Current multiple criteria decision-making (MCDM), considered as an evaluation structure to solve technical, socioeconomic, environmental, and institutional barriers, is a branch of operational research dealing with finding optimal weights of elements (factors) in complex scenarios including various indicators, conflicting objectives, and criteria [51]. The traditional evaluation methods, such as the macroeconomic and cost-benefit analysis indicators, are not sufficient to integrate all the elements (i.e., objectives or criteria) included in an LED-based light plant factory. On the contrary the MCDM methods provide more appropriate processes to evaluate a wide range of elements in different ways and thus offer valid decision support. This study provides evidence on the multicriteria decision-making approaches using FANP and CPV. The results of the data analytics and comparisons of FANP and the composite priority vector method for objectives and criteria are shown

in Table 17 and Figure 12. As the represented trend chart between FANP and CPV methods in Figure 12, the weight priority of both approaches reflects a consistent tendency. On the other hand, in light of the weights of objectives and criteria listed in Table 17, the most important objective is O4, marketing (FANP: 29.59%, CPV: 31.01%), followed by O3, product and technology (FANP: 28.55%, CPV: 26.89%), indicating the marketing for NPD priority of trade-offs is greater than product and technology in an LED-based light plant factories. Furthermore, the top three criteria are as follows: C3: investment preparation in funding (FANP: 27.36%, CPV: 26.56%); C9: new product marketing strategy (FANP: 22.98%, CPV: 18.94%); C4: return on investment (FANP: 13.519%, CPV: 12.78%).

### 5. Conclusion

This study first described objectives and performance criteria affecting new product design, collected and analyzed from previous studies and expert interviews and questionnaires. Experts were selected for their expertise and experience in various fields relating to LED plant lighting. Moreover, a reasoned consensus and consolidated individual judgments were systematically obtained by analyzing the responses of the surveys of a fuzzy Delphi method (FDM), and a fuzzy decision-making trial and evaluation laboratory (FDEMATEL) was managed to determine the relationships among the objectives and performance criteria. Secondly,

TABLE 17: Comparison of FANP and composite priority vector.

Assessed items	Weight for FANP	FANP rank	Weight for CPV	CPV rank
O1: management team	0.2399	3	0.2355	3
O2: financial fund	0.1787	4	0.1855	4
O3: product & technology	0.2855	2	0.2689	2
O4: marketing	0.2959	1	0.3101	1
C1: expertise and management skills	0.1072	4	0.1052	4
C2: business management philosophy	0.0881	5	0.0854	5
C3: investment preparation in funding	0.2736	1	0.2656	1
C4: return on investment	0.1351	3	0.1278	3
C5: technical personnel and R&D capability	0.0292	7	0.0305	9
C6: effective manufacturing processes	0.0260	8	0.0330	8
C7: technical resources management	0.0419	6	0.0773	6
C8: potential market demands	0.0224	11	0.0444	7
C9: new product marketing strategy	0.2298	2	0.1894	2
C10: market status survey	0.0230	10	0.0204	11
C11: consumer acceptance	0.0238	9	0.0209	10

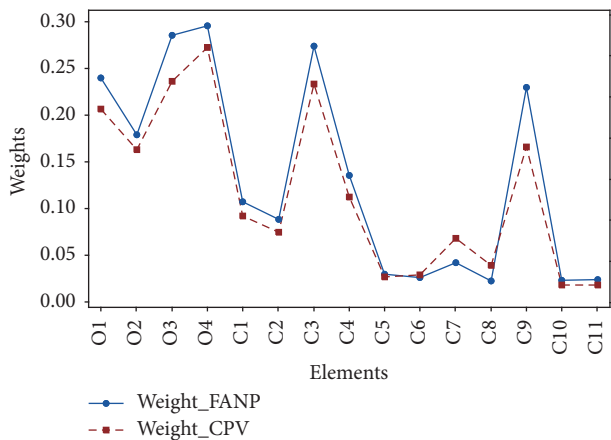


FIGURE 12: Comparisons of weights of objectives and criteria between FANP and CPV.

environmental green standards can be met using the objectives and criteria obtained, which indicate the relationships among new product development objectives and criteria in the LED plant lighting industry. As a result, the weights of potential risk factors and top priority factors with FANP and the composite priority vector (CPV) can be generated to help enterprises establish an efficient decision-making assessment system, able to determine the most suitable alternatives for new product development in the LED-based lighting plant factories.

### Conflicts of Interest

The authors declare that there are no conflicts of interest regarding the publication of this paper.

### References

- [1] IPCC, "Climate change 2014: Synthesis report. Contribution of Working Group II to the Fifth Assessment Report of the Intergovernmental Panel on Climate Change," 2014.
- [2] IPCC Secretariat, "IPCC takes decisions on future work," Press Release 27 February 2015. Accessed 2 March, 2015.
- [3] C. Howarth, D. Viner, S. Dessai, C. Rapley, and A. Jones, "Enhancing the contribution and role of practitioner knowledge in the Intergovernmental Panel on Climate Change (IPCC) Working Group (WG) II process: Insights from UK workshops," *Climate Services*, vol. 5, pp. 3–10, 2017.
- [4] E. Roberts and M. Pelling, "Climate change-related loss and damage: translating the global policy agenda for national policy processes," *Climate and Development*, vol. 10, no. 1, pp. 4–17, 2018.
- [5] C. Burattini, B. Mattoni, and F. Bisegna, "The impact of spectral composition of white LEDs on spinach (*Spinacia oleracea*) growth and development," *Energies*, vol. 10, no. 12, p. 1383, 2017.
- [6] K. B. Kahn, *The PDMA Handbook of New Product Development*, John Wiley & Sons, 2012.
- [7] W.-C. Chen, L.-Y. Wang, and M.-C. Lin, "A hybrid MCDM model for new product development: applied on the Taiwanese LifePO<sub>4</sub> Industry," *Mathematical Problems in Engineering*, vol. 2015, Article ID 462929, 15 pages, 2015.
- [8] L. Bstielier, "The moderating effect of environmental uncertainty on new product development and time efficiency," *Journal of Product Innovation Management*, vol. 22, no. 3, pp. 267–284, 2005.
- [9] N. Yousefi, G. Mehralian, H. R. Rasekh, and M. Yousefi, "New product development in the pharmaceutical industry: Evidence from a generic market," *Iranian Journal of Pharmaceutical Research*, vol. 16, no. 2, pp. 831–843, 2017.
- [10] A. H. I. Lee, H. H. Chen, and H.-Y. Kang, "A model to analyze strategic products for photovoltaic silicon thin-film solar cell power industry," *Renewable & Sustainable Energy Reviews*, vol. 15, no. 2, pp. 1271–1283, 2011.

- [11] C. Dong, L. Shao, Y. Fu et al., "Evaluation of wheat growth, morphological characteristics, biomass yield and quality in Lunar Palace-1, plant factory, green house and field systems," *Acta Astronautica*, vol. 111, article no. 5359, pp. 102–109, 2015.
- [12] J. Chen, C. Guo, Z. Yang, T. Li, and J. Zhao, "Li<sub>2</sub>SrSiO<sub>4</sub>:Ce<sup>3+</sup>, Pr<sup>3+</sup> phosphor with blue, red, and near-infrared emissions used for plant growth LED," *Journal of the American Ceramic Society*, vol. 99, no. 1, pp. 218–225, 2016.
- [13] T. Kozai, "Resource use efficiency of closed plant production system with artificial light: Concept, estimation and application to plant factory," *Proceedings of the Japan Academy Series B: Physical and Biological Sciences*, vol. 89, no. 10, pp. 447–461, 2013.
- [14] A. C. Schuerger and J. T. Richards, "Effects of artificial lighting on the detection of plant stress with spectral reflectance remote sensing in bioregenerative life support systems," *International Journal of Astrobiology*, vol. 5, no. 2, pp. 151–169, 2006.
- [15] Y. Miyashita, Y. Kitaya, T. Kozai, and T. Kimura, "Effects of red and far-red light on the growth and morphology of potato plantlets in vitro: using light emitting diode as a light source for micropropagation," *Acta Horticulturae*, vol. 393, pp. 189–194, 1995.
- [16] C. T. Nijssen, O. A. Kuhn, and W. Verbeek, *U.S. Patent No. 4,914,858*, U.S. Patent and Trademark Office, Washington, DC, USA, 1990.
- [17] M. Johkan, K. Shoji, F. Goto, S.-N. Hashida, and T. Yoshihara, "Blue light-emitting diode light irradiation of seedlings improves seedling quality and growth after transplanting in red leaf lettuce," *HortScience*, vol. 45, no. 12, pp. 1809–1814, 2010.
- [18] H.-C. Wu and C.-C. Lin, "Red light-emitting diode light irradiation improves root and leaf formation in difficult-to-propagate protea cynaroides L. Plantlets in vitro," *HortScience*, vol. 47, no. 10, pp. 1490–1494, 2012.
- [19] C. S. Brown, A. C. Schuerger, and J. C. Sager, "Growth and photomorphogenesis of pepper plants under red light-emitting diodes with supplemental blue or far-red lighting," *Journal of the American Society for Horticultural Science*, vol. 120, no. 5, pp. 808–813, 1995.
- [20] G. D. Goins, L. M. Ruffe, N. A. Cranston, N. C. Yorio, R. M. Wheeler, and J. C. Sager, "Salad crop production under different wavelengths of red light-emitting diodes (LEDs)," *SAE Technical Papers*, 2001.
- [21] N. C. Yorio, G. D. Goins, H. R. Kagie, R. M. Wheeler, and J. C. Sager, "Improving spinach, radish, and lettuce growth under red light-emitting diodes (LEDs) with blue light supplementation," *HortScience*, vol. 36, no. 2, pp. 380–383, 2001.
- [22] W.-M. Wey and K.-Y. Wu, "Using ANP priorities with goal programming in resource allocation in transportation," *Mathematical and Computer Modelling*, vol. 46, no. 7-8, pp. 985–1000, 2007.
- [23] Y. Shen, G. T. R. Lin, and G. Tzeng, "Combined DEMATEL techniques with novel MCDM for the organic light emitting diode technology selection," *Expert Systems with Applications*, vol. 38, no. 3, pp. 1468–1481, 2011.
- [24] C.-C. Chang, C. Liang, K.-M. Shu, and C.-W. Tsai, "Key successful factors of knowledge management for university students using e-portfolios: approach of fuzzy delphi and fuzzy AHP," *Computer Applications in Engineering Education*, vol. 23, no. 5, pp. 673–681, 2015.
- [25] Y.-H. Chang, W.-M. Wey, and H.-Y. Tseng, "Using ANP priorities with goal programming for revitalization strategies in historic transport: a case study of the alishan forest railway," *Expert Systems with Applications*, vol. 36, no. 4, pp. 8682–8690, 2009.
- [26] A. H. I. Lee and C.-Y. Lin, "An integrated fuzzy QFD framework for new product development," *Flexible Services and Manufacturing Journal*, vol. 23, no. 1, pp. 26–47, 2011.
- [27] W.-M. Wang, A. H. I. Lee, L.-P. Peng, and Z.-L. Wu, "An integrated decision making model for district revitalization and regeneration project selection," *Decision Support Systems*, vol. 54, no. 2, pp. 1092–1103, 2013.
- [28] T. J. Murray, L. L. Pipino, and J. P. Van Gigch, "A pilot study of fuzzy set modification of delphi," *Human Systems Management*, vol. 5, no. 1, pp. 76–80, 1985.
- [29] A. Ishikawa, M. Amagasa, T. Shiga, G. Tomizawa, R. Tatsuta, and H. Mieno, "The max-min Delphi method and fuzzy Delphi method via fuzzy integration," *Fuzzy Sets and Systems*, vol. 55, no. 3, pp. 241–253, 1993.
- [30] M. Mohammad, "The use of a hybrid fuzzy-Delphi-AHP approach to develop educational system's strategies in the university students' application," *Asian Journal of Research in Social Sciences and Humanities*, vol. 5, no. 1, pp. 180–187, 2015.
- [31] E. Fontela and A. Gabus, "Perceptions of the World Problematic: Communication Procedure. Communicating with Those Bearing Collective Responsibility," Tech. Rep., Battelle Memorial Institute Geneva Research Centre, Geneva, Switzerland, 1973.
- [32] W.-C. Chen, H.-P. Chang, K.-M. Lin, and N.-H. Kan, "An efficient model for NPD performance evaluation using DEMATEL and fuzzy ANP-applied to the TFT-LCD touch panel industry in Taiwan," *Energies*, vol. 8, no. 10, pp. 11973–12003, 2015.
- [33] J.-K. Chen and I.-S. Chen, "Using a novel conjunctive MCDM approach based on DEMATEL, fuzzy ANP, and TOPSIS as an innovation support system for Taiwanese higher education," *Expert Systems with Applications*, vol. 37, no. 3, pp. 1981–1990, 2010.
- [34] G. Büyüközkan and G. Çifçi, "A novel hybrid MCDM approach based on fuzzy DEMATEL, fuzzy ANP and fuzzy TOPSIS to evaluate green suppliers," *Expert Systems with Applications*, vol. 39, no. 3, pp. 3000–3011, 2012.
- [35] T. L. Saaty and M. Takizawa, "Dependence and independence: from linear hierarchies to nonlinear networks," *European Journal of Operational Research*, vol. 26, no. 2, pp. 229–237, 1986.
- [36] T. L. Saaty, *The Analytic Network Process: Decision Making with Dependence and Feedback; The Organization and Prioritization of Complexity*, Rws Publications, 1996.
- [37] L. Mikhailov and M. G. Singh, "Fuzzy analytic network process and its application to the development of decision support systems," *IEEE Transactions on Systems, Man, and Cybernetics, Part C: Applications and Reviews*, vol. 33, no. 1, pp. 33–41, 2003.
- [38] M. A. B. Promentilla, T. Furuichi, K. Ishii, and N. Tanikawa, "A fuzzy analytic network process for multi-criteria evaluation of contaminated site remedial countermeasures," *Journal of Environmental Management*, vol. 88, no. 3, pp. 479–495, 2008.
- [39] G. Büyüközkan, T. Ertay, C. Kahraman, and D. Ruan, "Determining the importance weights for the design requirements in the house of quality using the fuzzy analytic network approach," *International Journal of Intelligent Systems*, vol. 19, no. 5, pp. 443–461, 2004.
- [40] R. P. Mohanty, R. Agarwal, A. K. Choudhury, and M. K. Tiwari, "A fuzzy ANP-based approach to R&D project selection: a case study," *International Journal of Production Research*, vol. 43, no. 24, pp. 5199–5216, 2005.

- [41] M. Sevкли, A. Oztekin, O. Uysal, G. Torlak, A. Turkyilmaz, and D. Delen, "Development of a fuzzy ANP based SWOT analysis for the airline industry in Turkey," *Expert Systems with Applications*, vol. 39, no. 1, pp. 14–24, 2012.
- [42] W.-C. Chen and H.-P. Chang, "The application of fuzzy ANP in the development of new product decision-making—a case study of the solar module industry," *Advanced Materials Research*, vol. 472–475, pp. 1333–1338, 2012.
- [43] L. Song, Q. Li, G. F. List, Y. Deng, and P. Lu, "Using an AHP-ISM based method to study the vulnerability factors of urban rail transit system," *Sustainability*, vol. 9, no. 6, article 1065, 2017.
- [44] A. H. I. Lee, W.-M. Wang, and T.-Y. Lin, "An evaluation framework for technology transfer of new equipment in high technology industry," *Technological Forecasting & Social Change*, vol. 77, no. 1, pp. 135–150, 2010.
- [45] T.-Y. Hsiao, "Establish standards of standard costing with the application of convergent gray zone test," *European Journal of Operational Research*, vol. 168, no. 2, pp. 593–611, 2006.
- [46] R.-J. Dzung and K.-S. Wen, "Evaluating project teaming strategies for construction of Taipei 101 using resource-based theory," *International Journal of Project Management*, vol. 23, no. 6, pp. 483–491, 2005.
- [47] Y.-F. Kuo and P.-C. Chen, "Constructing performance appraisal indicators for mobility of the service industries using Fuzzy Delphi Method," *Expert Systems with Applications*, vol. 35, no. 4, pp. 1930–1939, 2008.
- [48] T. L. Saaty, "How to make a decision: the analytic hierarchy process," *Interfaces*, vol. 24, no. 6, pp. 19–43, 1994.
- [49] J. J. Buckley, "Fuzzy hierarchical analysis," *Fuzzy Sets and Systems*, vol. 17, no. 3, pp. 233–247, 1985.
- [50] R. Csutora and J. J. Buckley, "Fuzzy hierarchical analysis: the lambda-max method," *Fuzzy Sets and Systems*, vol. 120, no. 3, pp. 181–195, 2001.
- [51] A. Kumar, B. Sah, A. R. Singh et al., "A review of multi criteria decision making (MCDM) towards sustainable renewable energy development," *Renewable & Sustainable Energy Reviews*, vol. 69, pp. 596–609, 2017.

## Research Article

# Effect of Shaft Pillar Extraction on Stability of Main Shaft: A Case Study at Xincheng Gold Mine, China

Xige Liu, Wancheng Zhu , Kai Guan, and Hongxun Zhang

Key Laboratory of Ministry of Education on Safe Mining of Deep Metal Mines, Northeastern University, Shenyang 110819, China

Correspondence should be addressed to Wancheng Zhu; [zhuwancheng@mail.neu.edu.cn](mailto:zhuwancheng@mail.neu.edu.cn)

Received 6 November 2017; Accepted 20 February 2018; Published 5 April 2018

Academic Editor: Xander Wang

Copyright © 2018 Xige Liu et al. This is an open access article distributed under the Creative Commons Attribution License, which permits unrestricted use, distribution, and reproduction in any medium, provided the original work is properly cited.

Mining of ore body in the vicinity of a shaft has a significant influence on its stability. The in situ monitoring and numerical simulation are employed to analyze the effect of shaft pillar extraction at Xincheng Gold Mine. The XI# ore body is recently found around and beneath the shaft, and mining in this area may be detrimental to the shaft. Firstly, on the base of geological survey and in situ displacement monitoring, mechanical parameters of rock mass are obtained and the displacement around the shaft is measured. Secondly, the sensitivities of five main factors that may affect the shaft displacement are analyzed by means of orthogonal experiment according to the numerical simulation with FLAC<sup>3D</sup>. Finally, a numerical model is established according to the in situ condition; in order to forecast the shaft displacement induced by mining activities of XI# orebody, the Mining Priority Index (MPI) is put forward and used to select the optimal mining sequence. Based on the comparison between the numerical results with the monitoring data, it is determined that the ore within 100 m from the shaft is not suggested to be extracted until the last period of the shaft life.

## 1. Introduction

Shafts are vital access ways for many underground mines, providing passageways for personnel, materials, and ventilation air. The shaft must be designed as a long-term workable and operational structure. As we know, a series of adverse factors threaten the stability of the shaft, such as faults, high geological stress, and mining activities. The conventional method of protecting vertical shafts and their associated service excavations from the mining disturbance is to leave a sufficient large pillar in the vicinity of the shaft. However, with the mining operation going deeper, sometimes fresh ore bodies may be found near the shaft; this is the case that happened at Xincheng Gold Mine, China. In this regard, the stability of shaft will be mainly concerned during the mining operations when the ore body near the shaft is going to be mined out. Furthermore, delineating a shaft pillar in conformity to a certain limit angle is the most common approach to be adopted for this issue. As a result, the amount of mineral resources cannot be mined out around the shaft, and the unworkable mineral will increase with the depth of

the shaft. Therefore, this method is not applicable when the shaft depth is greater than 2.5 to 3.0 km in South Africa [1].

Recently, the downturn of the mining commodities price forces mining companies to extend the possible productivities, such as the ore body in the shaft pillar. As for the Xincheng Gold Mine in Shandong Gold Group, China, in recent years, the XI# ore body is found around the main production shaft that is currently used to hoist minerals from the V# ore body, Figure 1. In this regard, it is essential to keep the shaft workable and operational for a long time if the XI# ore body is intended to be mined out.

Many studies have been conducted on the mining operation of shaft pillars and a great number of experiences have been accumulated. Effects of the extraction of tabular deposits around vertical shafts in deep-level mines were numerically studied by Budavari and Croeser [1]; however, due to the limitation of the computing power and the difficulty in quantifying the rock mass parameters and specifying in situ stress conditions, the calculation results usually deviate from the in situ reality to some degree. When extracting the reef around the shaft at the start of mining operations, several

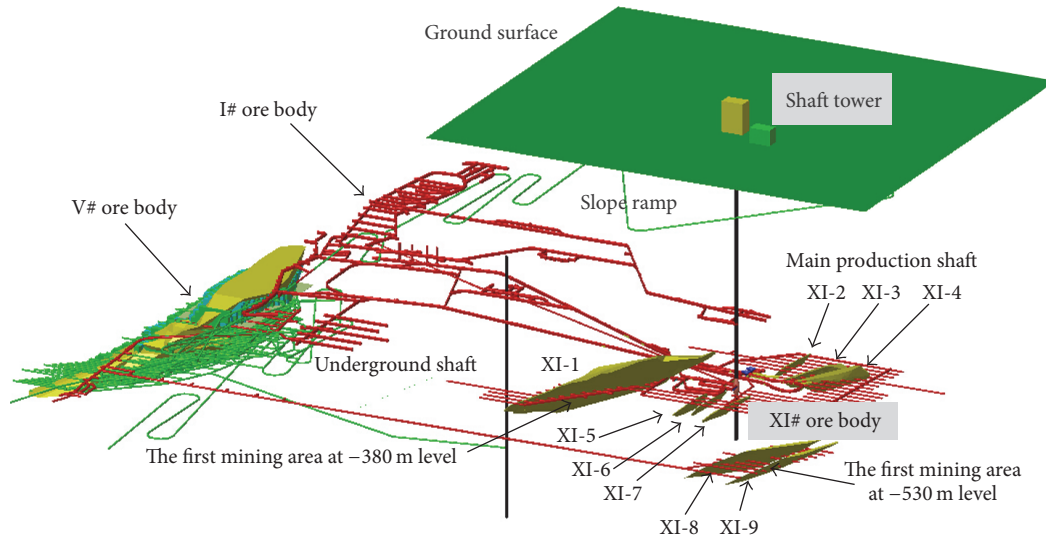


FIGURE 1: The overall layout of Xincheng Gold Mine.

alternatives to protect shaft pillars for deep vertical shaft systems were put forward [2], including the use of backfill, suitable mining layouts, and delaying shaft steelwork and lining installation until residual deformations are tolerable. A combination of strategically placed satellite pillars, yield pillars, and backfill method was chosen to protect the shaft from possible damaging stress changes and to minimize displacement in the shaft-reef area at Beatrix number 3 vertical shaft [3]. In Sumitomo Akabira Colliery, changing the displacement angle of the shaft pillar from  $60^\circ$  to  $80^\circ$ , the shaft damage was limited when the main fault crossing the shaft was considered as special attention [4]. Mining of the Ross pillar at Homestake Mine indicated that unexpected shaft wall movement could occur at a distance of 450 m from the current mining area [5]. A waste-cut across the shaft was proposed to extract the entire shaft pillar at the number 4 shaft of the African Rainbow Minerals (ARM) mine, which is located in highly stratified and poor-quality rock masses [6]. A shaft destressing slot is excavated to protect the main production shaft at Newmont Canada's Golden Giant Mine from potential damage from the high mining-induced stresses, and it allows the mine to extract a lot of high grade ore [7]. Degradation occurs to the X41 shaft at Copper Mine because of two major geological structures, the W41 and W42 faults, which intersect the shaft at two distinct locations [8, 9]. By virtue of the high geotechnic stress, serious deformation occurs during the sinking of a main shaft at Jinchuan Mine number 3; a tolerable deformation of 95 mm before lining is reasonable in order to maintain the shaft stability, as suggested by Zhao et al. [10]. In addition, it is noted that the dynamic interaction between the conveyances and the conveyance guiding system of aging mine shafts should be analyzed in order to examine the workability of shaft [11]. At Chengchao Iron Ore in China, the shaft exhibited evident degradation because of mining activities, Huang et al. [12] thought that the east shaft can continue to be used despite the surface subsidence rate of 0.314 mm/d

and 0.144 mm/d in horizontal and vertical directions, respectively. Besides, some researches presented that lengthening or shortening the shaft lining by no more than 3 mm/m or 1 mm/m, respectively, generally does not cause sufficient damage to threaten the safety of shaft operations [13], and the shaft vertical displacement of 35 mm can be used as a threshold for lining damage of the X41 shaft at Copper Mine [8].

All of the case studies and above conclusions indicate that the extraction of shaft pillar is feasible if the sufficient measures such as backfilling, suitable mining layouts, and displacement monitoring are taken to mitigate the effect of mining operation on shaft displacement, even though in some cases shaft degradation occurs because of geological structures that are not clearly understood.

The theoretical analysis, in situ monitoring, and numerical methods are generally employed to examine the mining-induced responses to the shaft. Specifically, the theoretical model is of poor generality to represent the in situ condition of underground mining. The in situ monitoring could provide a lot of data, but they are sometimes difficult to be interpreted because dozens of uncertainties exist. On the other hand, the numerical simulation could give the prediction by using sophisticated numerical models; however, the rock mass parameters and in situ stress data are difficult to ensure accuracy and reliability. Therefore, the issue of shaft displacement and damage is complex, which should be solved by combining the performance of different methods. The solution strategy in this paper includes geological survey, in situ monitoring, and numerical simulation, hoping to achieve a better prediction of shaft deformation and to provide a reasonable suggestion to the mining operations.

## 2. Description of the Mine Site

The Xincheng Gold Mine is operated by Shandong Gold Group Co., Ltd, located in Shandong Province, China,

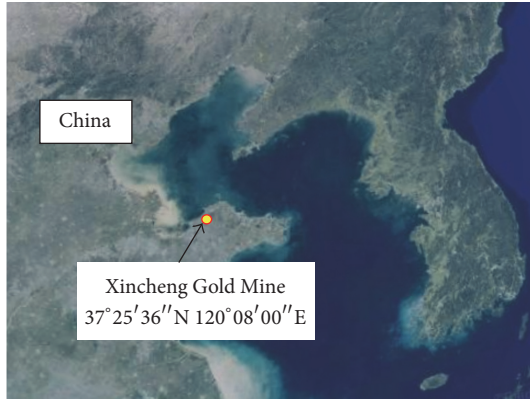


FIGURE 2: Location map of Xincheng Gold Mine in Shandong Province, China.

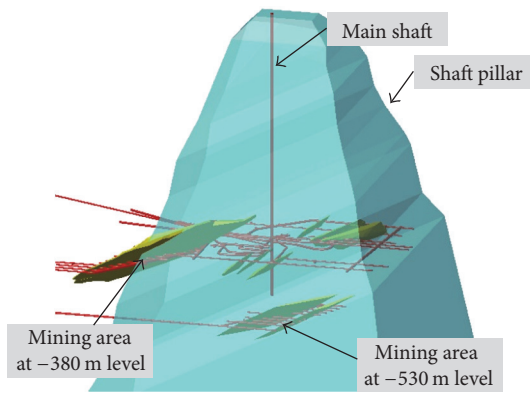


FIGURE 3: The XI# ore body and shaft pillar.

Figure 2. The construction of Xincheng Gold Mine started in 1975, and it was completed and put into production in 1980.

The shaft at Xincheng Gold Mine is 499 m deep, and the ground surface elevation is +33 m. According to the latest exploration near the main shaft, a new ore body numbered XI# that consists of 7 ore veins at  $-380$  m level and 2 ore veins at  $-530$  m level are found, Figure 1. Distribution of the XI# ore veins is scattered, the average strike is  $NE57^\circ$ , and the dip of the veins is in the  $25\text{--}30^\circ$  range, which is parallel to the stratigraphic dip, and detailed information of the ore veins is listed in Table 1. In the beginning, a shaft pillar (Figure 3) has been delineated according to the respective rock movement angle of different strata, Table 2. Under these circumstances, more than 1140 kt ore cannot be mined out, which accounts for 67.4% of the XI# ore body. The first mining areas are designed in the XI-1 ore vein at  $-380$  m level and in the XI-8 and XI-9 ore veins at  $-530$  m level, and 280 kt ores have been mined out up to March, 2017. In order to protect the shaft, the following stopping sequence needs to be optimized and the stopping boundary needs to be determined.

The upward horizontal cut and backfill stopping method has been adopted for many years at Xincheng Gold Mine, and a wealth of experience has been accumulated. Compared with the open stopping method and stope caving method, the stopping-and-filling method is better in terms of maintaining

TABLE 1: Information of the XI# ore veins.

Vein number	Tonnage of ore/kt	Percentage/%	Distance from the shaft/m
XI-1	1174.51	69.43%	210
XI-2	7.84	0.46%	129
XI-3	49.87	2.95%	133
XI-4	75.55	4.47%	157
XI-5	40.28	2.38%	78
XI-6	4.96	0.29%	65
XI-7	49.87	2.95%	59
XI-8	155.90	9.22%	103
XI-9	132.92	7.86%	103
In total	1691.71	100.00%	-

the surrounding rock mass stable and preventing the surface subsidence. Therefore, this method is also adopted to excavate the XI# ore body in field production.

### 3. Geological Survey

The detail rock mechanical parameters of the Xincheng Gold Mine were obtained during the shaft sinking which are listed in Table 2. The thickness of the quaternary surface soil is thin, while the bedrock is mainly magmatic rock and metamorphic rock with high mechanical strength, which are relatively intact, stable. Besides, the major geological structures in this area include the Jiaojia Fault, the Houjia Fault, and the Hexi Fault, as shown in the 155# vertical cross-section map, Figure 4. The Hexi Fault especially is close to the bottom of the shaft and overlapped with the ore veins XI-8 and XI-9 at  $-530$  m level; thus, it needs to be given special attention. In fact, the three faults in this area are crushed zones with thickness of dozens of meters, rather than the general faults with the main fracture surfaces.

Former studies have shown that the horizontal geotechnic stress is significant at Xincheng Gold Mine [14], the  $\sigma_{\max}$  and  $\sigma_{\min}$  are both horizontal at the  $-280$  m level and below, and the direction of  $\sigma_{\max}$  is perpendicular to the strike of the strata, while the direction of  $\sigma_{\min}$  is parallel to it contrastively. So, it can be further inferred that the faults in this area tend to be reverse faults, and this deduction provides a foundation for the follow-up analysis of the shaft stability. Thickness of the shaft liner is 0.3 m, and the net diameter is 5 m. Inside the shaft are a cage compartment, a ladder compartment, a skip compartment, and a pipe line compartment. Arrangement of the shaft section is depicted in Figure 5.

According to the Chinese relevant specification for protecting the mine shaft, when the rollers sliding along the steel shaft guides are used, the clearance of sliding guide groove on each side should be kept less than 10–15 mm in order to maintain the regular operation of the hoister in the shaft [15]. So the displacement of the main production shaft should not be larger than this threshold in order to guarantee the normal operation of the shaft. Currently, the hoister of the main production shaft runs well, indicating that the

TABLE 2: Main mechanical parameters of the rock samples retrieved around shaft.

Shaft depth/m	Lithology	Rock movement angle/°	Density/kg/m <sup>3</sup>	Young's modulus/GPa	Poisson's ratio	UCS/MPa	Internal friction angle/°	Cohesion/MPa
0-33.80	Quaternary overburden	45	-	-	-	-	-	-
	Cataclastic granite							
33.80-116.18	Sericitole lithified granite	70	2490	42.7	0.18	50.3	35.75	40
	Sericite & chlorite lithified granite							
116.18-168.00	Cataclastic granite	65	2570	96.8	0.36	46.4	36.5	32
	Potassium feldspar & biotite lithified granite							
168.00-225.00		80	2560	67.7	0.30	96.2	32.27	86
	Sericitole lithified mylonitic granite							
225.00-272.00		70	2540	39.4	0.16	56.2	36.87	30
	Sericitole lithified mylonitic granite							
272.00-341.53		65	2500	41.6	0.28	28.3	33.02	35
	Pyritic phyllic cataclastic							
	Pyritic phyllic granite							
341.53-366.89	Sericite & kaolin clay lithified granite	70	2530	46.4	0.16	41.6	33.02	38
	Biotite granite							
366.89-422.00	Pyritic silicified granite	80	2580	48.2	0.16	79.4	36.87	48
	Biotite granite							
422.00-465.50		80	2620	49.4	0.18	78.9	33.82	59
	Phyllic cataclastic granite							
465.50-529.74	Phyllic biotite granite	60	2630	78.8	0.24	63.5	33.22	41
	Pyritic phyllic cataclastic							
529.74-663.20	Porphyritic granodiorite	80	2620	133.1	0.34	123.8	33.22	51

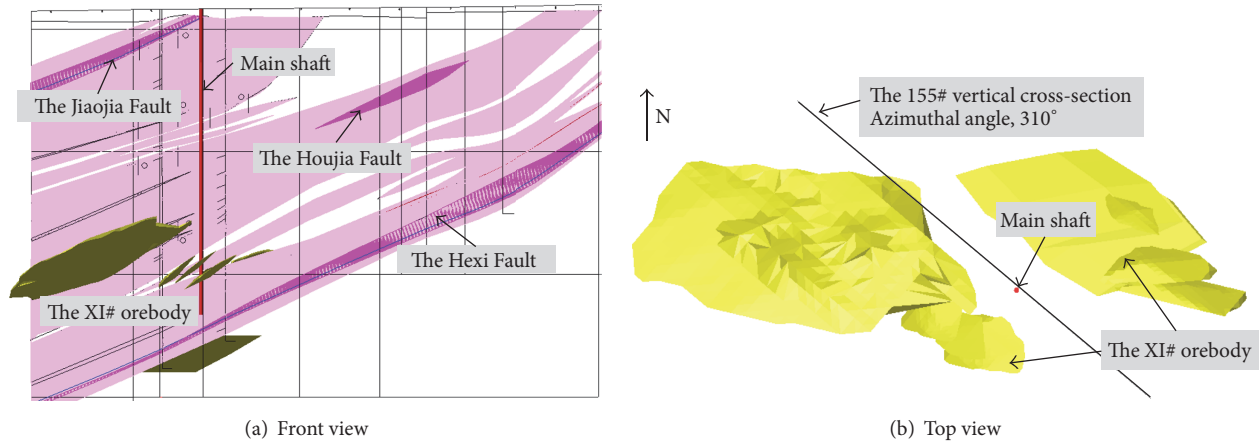


FIGURE 4: The 155# vertical cross-section.

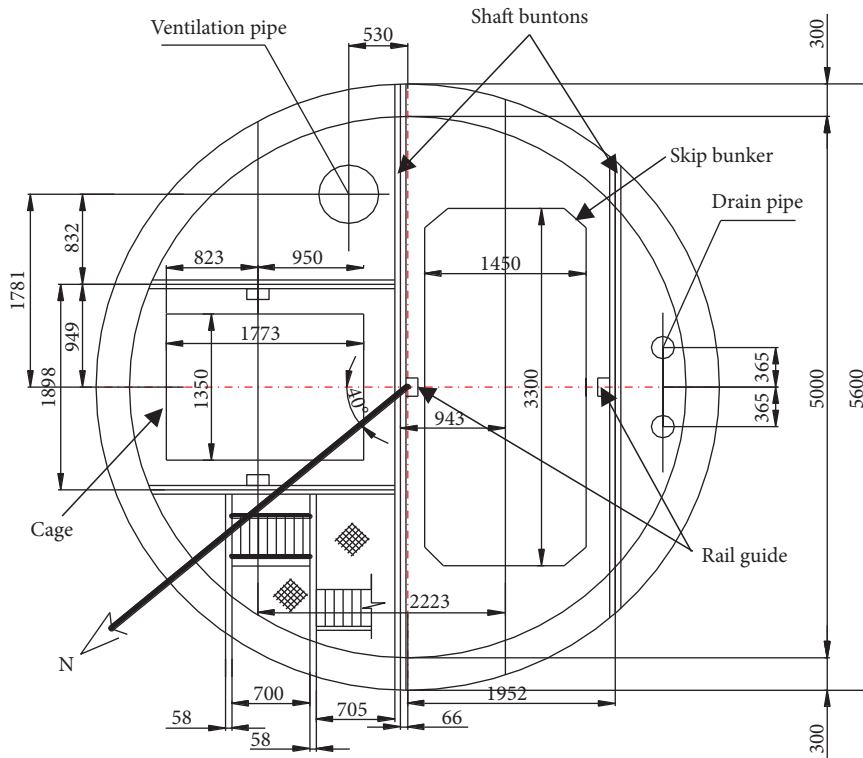


FIGURE 5: Cross-section diagram of the shaft.

clearance does not exceed the above-mentioned threshold. Most importantly, considering that the shaft will be used longer than 10 years, the 10 mm is selected as the upper limit for the shaft displacement, which is much less than the critical allowable displacement of the concrete liner.

#### 4. In Situ Displacement Monitoring

In order to trace the response of the main production shaft at Xincheng Gold Mine during mining of the XI# ore body, it is essential to monitor the shaft displacement. In situ displacement monitoring can also provide data for validating

the numerical simulation so as to improve the reliability of prediction. However, it is almost impossible to install monitoring equipment directly inside the shaft, because it may disturb the daily lifting operation. On the other hand, the shaft deformation is dependent on its adjacent rock stratum movement during underground excavation, and the method of monitoring the surrounding rock mass around the shaft is applied extensively to evaluate the displacement and stability of the shaft.

4.1. Installation of the Monitoring Equipment. The Sliding Micrometer, a high-precision strain meter ( $\pm 0.002$  mm/m),

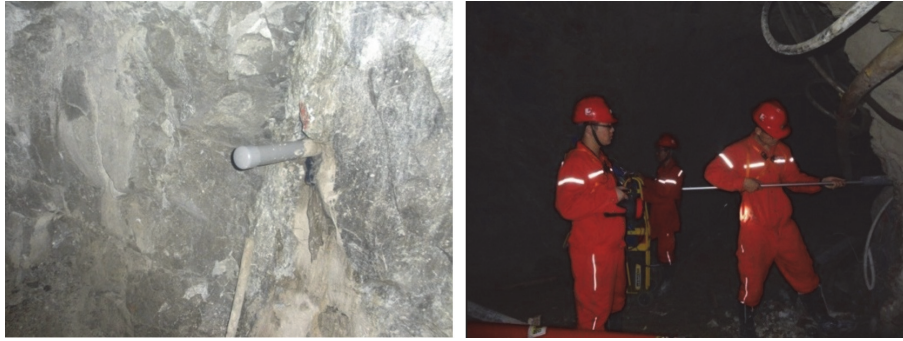


FIGURE 6: On-site measurement using the Sliding Micrometer system.

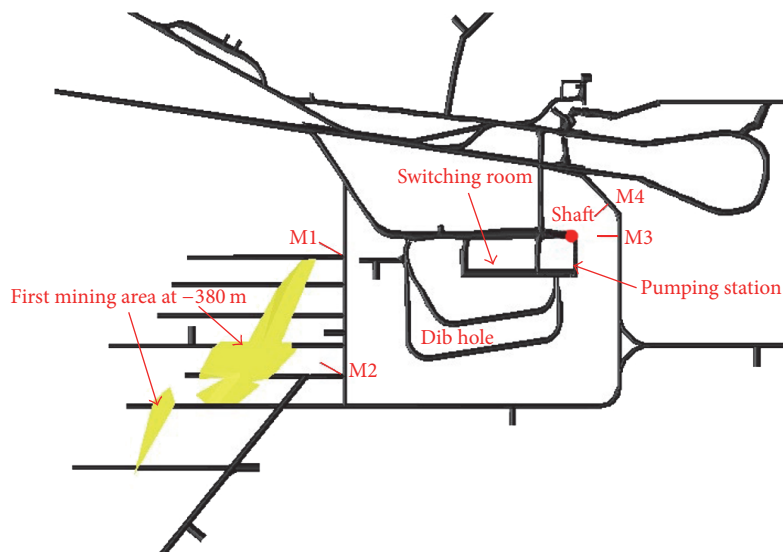


FIGURE 7: Arrangement of the 4 monitoring boreholes of Sliding Micrometer at  $-380$  m level.

is applied to monitor the rock mass at  $-380$  m level near the shaft. This monitoring system consists of the probe, cable, rod, readout unit, data-processing unit, and calibration device. It is noted that the probe uses the ball-and-cone positioning principle in the measuring marks of the measuring tube, and it needs regular calibration before and after each measurement.

4 Sliding Micrometer pipes, M1, M2, M3, and M4, were installed in the monitoring boreholes and then were grouted with cement mortar which should be cured for about 24 hours before measurement operate, in case the cement hardening may have detrimental influence on the monitoring displacement. On-site measurement diagram is shown in Figure 6. The 4 monitoring boreholes are horizontal and about 10–12 meters deep; boreholes M1 and M2 are near the XI# orebody and their borehole mouths are 110 m and 130 m far away from the shaft, respectively. Boreholes M3 and M4 are near the shaft and their bottoms are 7 m and 8 m from the shaft wall, Figure 7.

**4.2. Monitoring Results.** The initial monitoring values were collected on October 26, 2013, and the deformation of rock

mass was obtained by subtracting the initial data from the subsequent monitored values. Excavating of the XI# ore body at  $-380$  m level started on January 23, 2014. As of the latest collecting, March 27, 2017, more than 280 kt ores were mined out. The cumulative displacements of the 4 monitoring boreholes are shown in Figure 8. Positive value means tensile strain and the negative one stands for compressive strain.

Over more than the past three years, it is found that the max cumulative displacements at monitoring boreholes M1, M3, and M4 are 3.5 mm,  $-1.4$  mm, and  $-0.3$  mm, respectively, while M2 is up to 28.9 mm, because the borehole M2 was located in an isolated pillar after one slice of ore was mined out, Figure 7. However, as this mined-out area was backfilled, the displacement monitored at this borehole becomes stable, which indicates that the noticeable displacement monitored at M2 results from the mining activities. However, this mining-induced displacement in surrounding rock mass has little influence on the stability of shaft because the stope is far enough away from the protected shaft.

Correspondingly, the monitoring displacements of M3 and M4 ( $-1.4$  mm and  $-0.3$  mm) reflect the shaft displacement more directly; it indicates that the shaft displacement

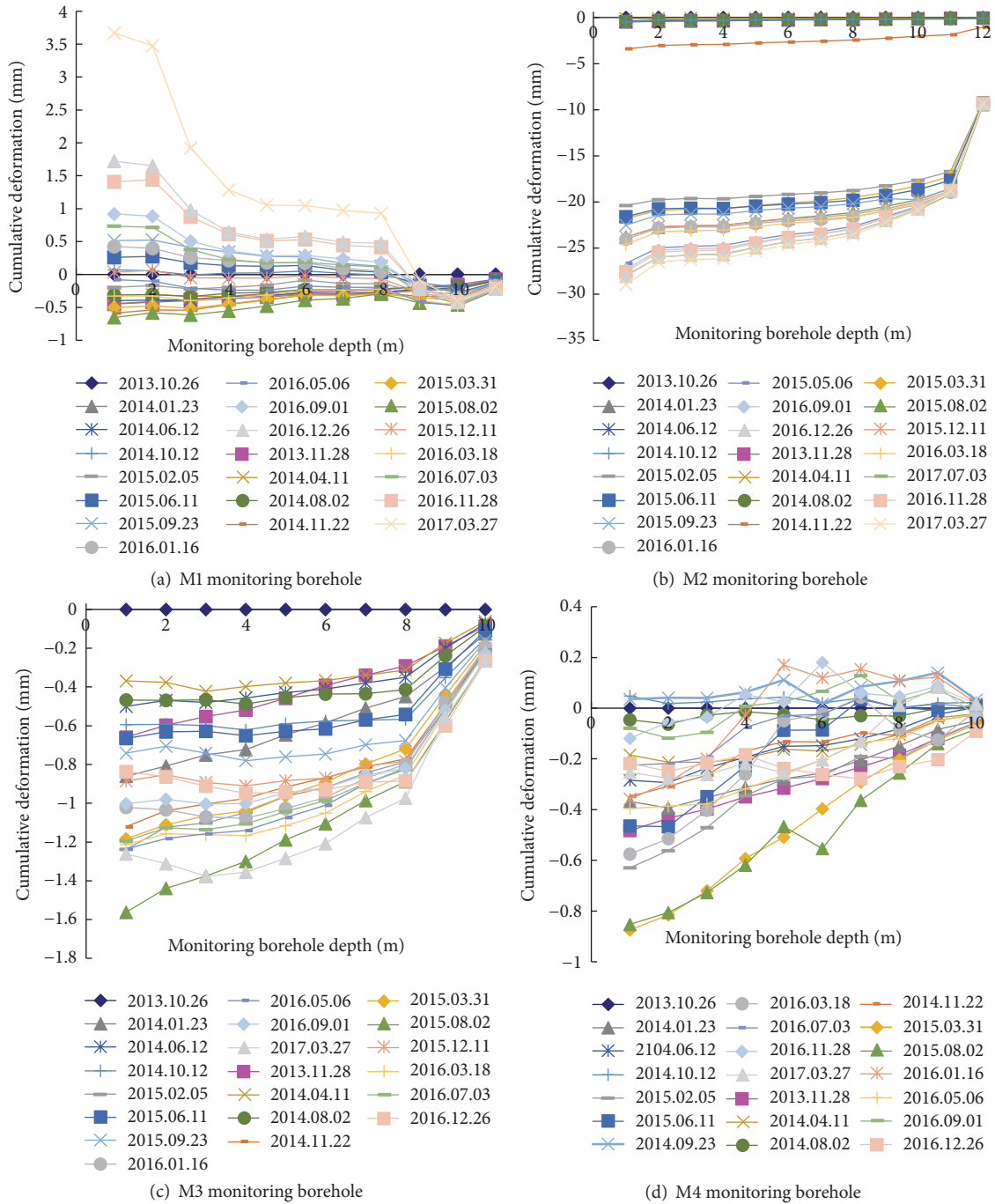


FIGURE 8: Cumulative displacement measured at 4 monitoring boreholes.

is much smaller than the threshold of 10 mm. Although a certain degree of fluctuation exists among the data during this monitoring period, according to the latest data, the max lateral displacement of shaft is 1.4 mm.

### 5. Sensitive Analysis of Factors Affecting the Shaft Displacement

The deformation mechanism of shaft can be very complicated; it is necessary to find the dominant factors affecting the

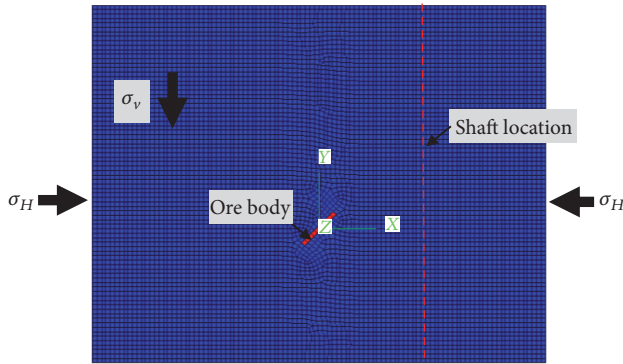
shaft displacement based on a concept model. The influential factors include lithology of the rock mass, in situ stress state, mined-out area shape in terms of the ore body shape, location of the shaft, mining method and mining intensity, dynamic disturbances such as blasting vibration, special geological structure such as faults, groundwater, characteristics of the lining, service life, and maintenance. The concept of orthogonality is important in design of experiments because it says something about independence. Experimental analysis of an orthogonal design is usually straightforward because you can

TABLE 3: Mechanical parameters of the numerical orthogonal experimental.

Young's modulus/GPa	Poisson's ratio	Tensile strength/MPa	Internal friction angle/°	Cohesion/MPa	Density/kg/m <sup>3</sup>
26	0.21	3.34	46.33	8.33	2650

TABLE 4: Design of factors and levels for the orthogonal experimental design.

Levels	Factors				
	Lateral pressure coefficient/ $\lambda$	Dip/°	Thickness/m	Distance/m	Location
1	1.0	20	10	50	Hanging wall
2	1.5	45	20	100	Footwall
3	2.0	70	30	150	

FIGURE 9: Numerical model of FLAC<sup>3D</sup> of the concept model.

estimate each main effect and interaction independently. In this section, orthogonal experimental design was used to find the dominant one that affects the shaft displacement remarkably.

**5.1. Orthogonal Experimental Design.** The orthogonal numerical experiment has been done in virtue of the calculation of different scenarios with FLAC<sup>3D</sup> software, as shown in Figure 9, and the numerical model is simplified to be a conceptual model in plain strain condition, whose size is 1000 m \* 800 m \* 20 m, and the 3rd dimension is just 20 m, in which direction the displacement is not concerned in this simplified model; in this respect, a 2D model may be also acceptable for this case. And the shaft is not considered in the grid of FLA3D in order to eliminate the error that may be induced because its diameter of 5 m is too small to be considered. In this respect, the displacement of the shaft is interpolated from the nodes nearby. The maximum and minimum principal stresses occur in the X and Y directions while the gravitational stress is applied along the Z direction, specifically,  $\sigma_v = \gamma H$ ,  $\sigma_H = \lambda \gamma H$  ( $\lambda = 1.0, 1.5,$  and  $2.0$ , as shown in Table 4), and  $\sigma_h = 0.5\gamma H$ . The stress boundary conditions are adopted for the two numerical models in this paper, and when the calculation reached an equilibrium status, the initial displacements are set to zero, and then, the new displacements are considered to be caused by mining activities, because this numerical model is only a simplified

concept model, primarily aimed at finding the dominant factors affecting the shaft displacement in general situations and providing useful references to the researchers. Referring to the rock mechanics parameters of Xincheng Gold Mine, the orebody and surrounding rock mass are of the similar lithology in this model, as listed in Table 3.

Selecting the lateral pressure coefficient of the in situ stress state, distance between the shaft and mined-out area, location of the shaft (at the footwall or hanging wall of ore body), dip of ore body, and thickness of ore body as controllable factors in the orthogonal experiments and the levels of these factors are designed and listed in Table 4.

**5.2. Orthogonal Experimental Results.** The orthogonal table  $L_{18} (2 \times 3^7)$  is applied and the result is shown in Table 5. Through the analysis of Fisher's  $F$  distribution, numerical results indicate that dip of the ore body, lateral pressure coefficient, and distance between the shaft and mined-out area are significant factors affecting the shaft displacement. In contrast, thickness of the ore body and the location of the shaft are indistinctive. On condition that the shaft is located at the hanging wall, the deformation region is more extensive than that at the footwall, as shown in Figure 10.

Based on this orthogonal experiment, the dip of the ore body, lateral pressure coefficient, and distance between the shaft and mined-out area are specially considered in the later numerical simulation. In particular, the mining activity is most closely relevant to the distance between the mining stope and the shaft.

## 6. Numerical Analyze of the Shaft Stability

**6.1. Modelling Strategy.** A bigger numerical model of the Xincheng Gold Mine was established subsequently, whose size is 1000 m \* 1200 m \* 1000 m, Figure 11; X is the strike direction, Y is the dip direction, and Z is the gravity direction. The Hexi Fault is adjacent to the bottom of the shaft and overlaps with the XI-8 and XI-9 ore veins at -530 m level, so it is meshed intensively. As a matter of fact, the Hexi Fault is a crushed zone with thickness of dozens of meters, rather than a general fault with the main fracture surfaces. Thus, the "interface" element is not adopted in this model; instead, it is embodied through a series of weaker mechanical parameters; as shown in Table 6, the buried depth from 465.50 to 529.74

TABLE 5: Variance analysis of the orthogonal experiment.

Source of the variance	Quadratic sum	Degrees of freedom	Mean sum of square	$F$	$F_\alpha$	Significance
Lateral pressure	0.002088	2	0.001044	12.626479	3.98	Very high
Distance	0.002317	2	0.001158	14.006953	3.98	Very high
Dip	0.003780	2	0.001890	22.855622	3.98	Very high
Thickness	0.000168	2	0.000084			Low
Location <sup>△</sup>	0.000047	1	0.000047			Low
$e^\Delta$	0.000694	8	0.000087			Low
$e'$	0.000910	11	0.000083			Low
In total	0.010005	17				Low

“△” indicate that the mean sum of square of this factor is smaller than that of error term, being incorporated into the error term.

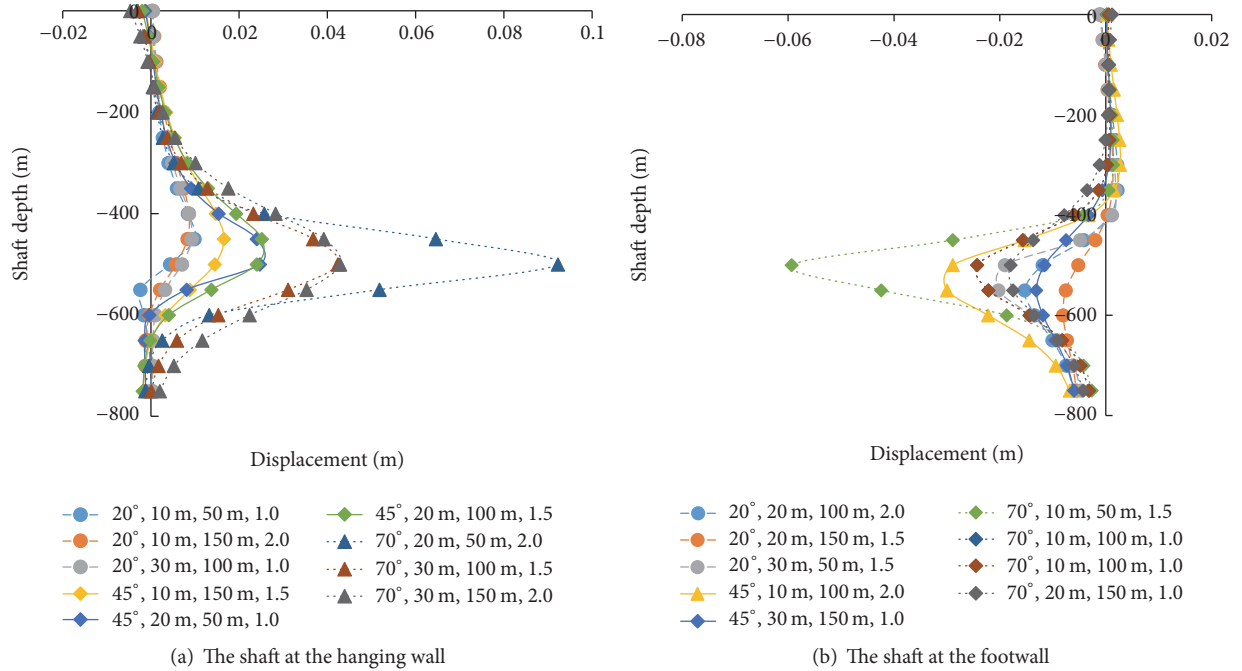


FIGURE 10: Shaft displacement for different depths, the legend “20°, 10 m, 50 m, 1.0” means the dip and thickness of orebody are 20° and 10 m, the distance between the ore and shaft is 50 m, and the lateral pressure coefficient is 1.0.

is the location of Hexi Fault. The same method is also applied to the other two faults.

The ideal elastic-plastic model with Mohr-Coulomb yield surface in the FLAC<sup>3D</sup> software is adopted, that is,

$$f = \sigma_1 - \sigma_3 \frac{1 + \sin \varphi}{1 - \sin \varphi} - 2c \sqrt{\frac{1 + \sin \varphi}{1 - \sin \varphi}}, \quad (1)$$

where  $\sigma_1$  and  $\sigma_3$  are the maximum and minimum principal stress, respectively,  $c$  is internal cohesive force, and  $\varphi$  is angle of internal friction. When  $f > 0$ , failure occurs.

6.2. Mechanical Parameters of Rock Mass. The modified Hoek-Brown criterion with the RocLab software [16] is applied to obtain the reasonable rock mass parameters, which is expressed as

$$\sigma_1 = \sigma_3 + \sigma_c \left( m_b \frac{\sigma_3}{\sigma_c} + s \right)^\alpha, \quad (2)$$

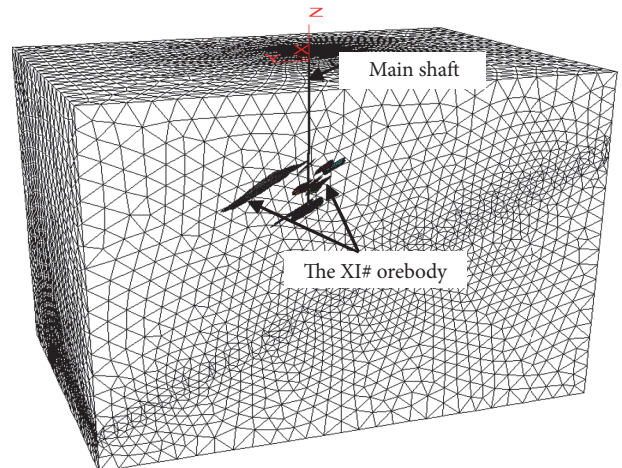


FIGURE 11: The overall numerical model of Xincheng Gold Mine.

TABLE 6: Mechanical parameters of rock mass calculated according to Hoek-Brown criterion.

Shaft depth/m	$m_i$	GSI	UCS/MPa	$D$	Young's modulus/GPa	Internal friction angle/ $^\circ$	Poisson's ratio	Cohesion/MPa	Tensile strength/MPa
0–33.80	-*	-	-	-	8.04	42	0.29	2.00	0.05
33.80–116.18	33	60	50.3	0	12.61	43.84	0.18	4.08	0.075
116.18–168.00	33	65	46.4	0	16.15	45.30	0.36	4.01	0.1
168.00–225.00	33	70	96.2	0	30.02	46.74	0.30	8.90	0.304
225.00–272.00	33	70	56.2	0	23.71	46.74	0.16	5.20	0.177
272.00–341.53	33	65	28.3	0	12.62	45.30	0.28	2.45	0.061
341.53–366.89	33	70	41.6	0	20.40	46.74	0.16	3.85	0.131
366.89–422.00	33	75	79.4	0	37.58	48.15	0.16	7.90	0.365
422.00–465.50	33	75	78.9	0	37.46	48.15	0.18	7.85	0.363
465.50–529.74	33	60	63.5	0	14.17	43.84	0.24	5.14	0.094
529.74–663.20	30	70	123.8	0	31.62	45.94	0.34	11.19	0.43

\* Intact rock core cannot be obtained in the stratum from 0 to 33.8 m beneath the surface.

where  $m_b$  is a reduced value of the material constant  $m_i$  as given by

$$m_b = m_i \exp\left(\frac{\text{GSI} - 100}{28 - 14D}\right), \quad (3)$$

and  $s$  and  $\alpha$  are constants for the rock mass given by

$$s = \exp\left(\frac{\text{GSI} - 100}{9 - 3D}\right), \quad (4)$$

$$\alpha = \frac{1}{2} + \frac{1}{6} \left[ \exp\left(\frac{-\text{GSI}}{15}\right) - \exp\left(\frac{-20}{3}\right) \right];$$

$D$  is a factor which depends upon the degree of disturbance, it varies from 0 for undisturbed in situ rock masses to 1 for much disturbed rock masses,  $m_i$  is a material constant according to the lithology, and geological strength index (GSI) was introduced to quantify the rock mass and surface conditions of the discontinuities.

In this study, rock masses are treated as undisturbed materials; namely,  $D = 0$  is set for all of the rock strata around the shaft,  $\sigma_c$  is the uniaxial compressive strength (UCS) of the intact rock, and  $m_i$  can be selected according to Table 2. The values of geological strength index GSI cannot be obtained directly; they must be obtained based on in situ investigation of the rock mass around the shaft. However, it is scarcely possible to scan the joints and fissures on the surface of the shaft. Therefore, the in situ survey work was conducted in the drifts near the shaft.

The rock joints and interfaces at the drifts surface of all of the strata are scanned by using the ShapeMetriX3D system (Austrian Startup Company, 2008), and then, a 3D digital image of the surface containing the joints information can be built, as shown in Figure 12. Based on this real 3D rock surface, some visible rock mass features, such as the orientations, traces, areas, lengths, and position of joints, are retrieved. In addition, according to the field investigation, the GSI values of the rock mass around the shaft are estimated based on the geological descriptions in [17]. The mechanical parameters of all the rock strata are listed in Table 6.

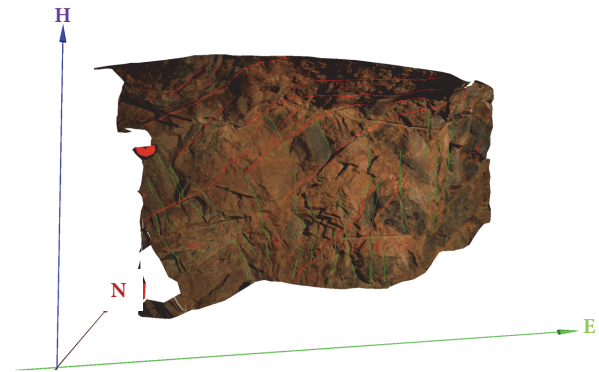


FIGURE 12: Joint sets (indicated in red and green colors) retrieved with ShapeMetriX3D.

Due to the difference of strata, the premining stress distribution depends on both depth and rock properties [18], as shown in Figure 13. Obviously, by using the stress boundary conditions, when the calculation reaches to an equilibrium status, the strata with higher Young's modulus hold higher stress than the rest of the geological formations.

**6.3. Simulated Mining Sequence.** Limited by the computing ability of computer, this big numerical model, Figure 11, is difficult to be established so meticulously. As a result, it aims to give advices on the mining sequence from a macroscopic view at present, and the simulative excavation scope of each step is large.

In the numerical simulation, scenario I is approaching to the shaft gradually, which is advantageous for stopping mining according to the shaft displacement, and it consists of 6 steps, Figure 14(a). Firstly, the XI-1, XI-2, XI-3, and XI-4 veins at  $-380$  m level are mined in 4 steps towards the main shaft until a distance of 100 m; and then, the XI-8 and XI-9 veins at  $-530$  m level are extracted; at last, the rest of the orebodies within 100 m distance from the shaft, including XI-5, XI-6, and XI-7 ore veins and a small part of the XI-1 vein,

TABLE 7: Details of scenario I.

Simulative excavating steps	Mineral output/kt	Ore proportion/%	Shaft displacement/m	displacement proportion/%	MPI
1	264.19	15.62%	0.001236	10.07%	1.55
2	363.85	21.51%	0.002031	16.55%	1.30
3	373.34	22.07%	0.003656	29.80%	0.74
4	295.83	17.49%	0.003887	31.68%	0.55
5	289.31	17.10%	-0.00022	-1.79%	-9.55
6	105.20	6.22%	0.00168	13.69%	0.45
In total	1691.71	100%	0.01227	100%	1.00

TABLE 8: Backfilling mechanical parameters in the numerical simulation.

Material	Density/kg/m <sup>3</sup>	Young's modulus/GPa	Poisson's ratio	UCS/MPa	Internal friction angle/°	Cohesion/MPa
Backfilling	2020	1.21	0.28	2	40	0.5

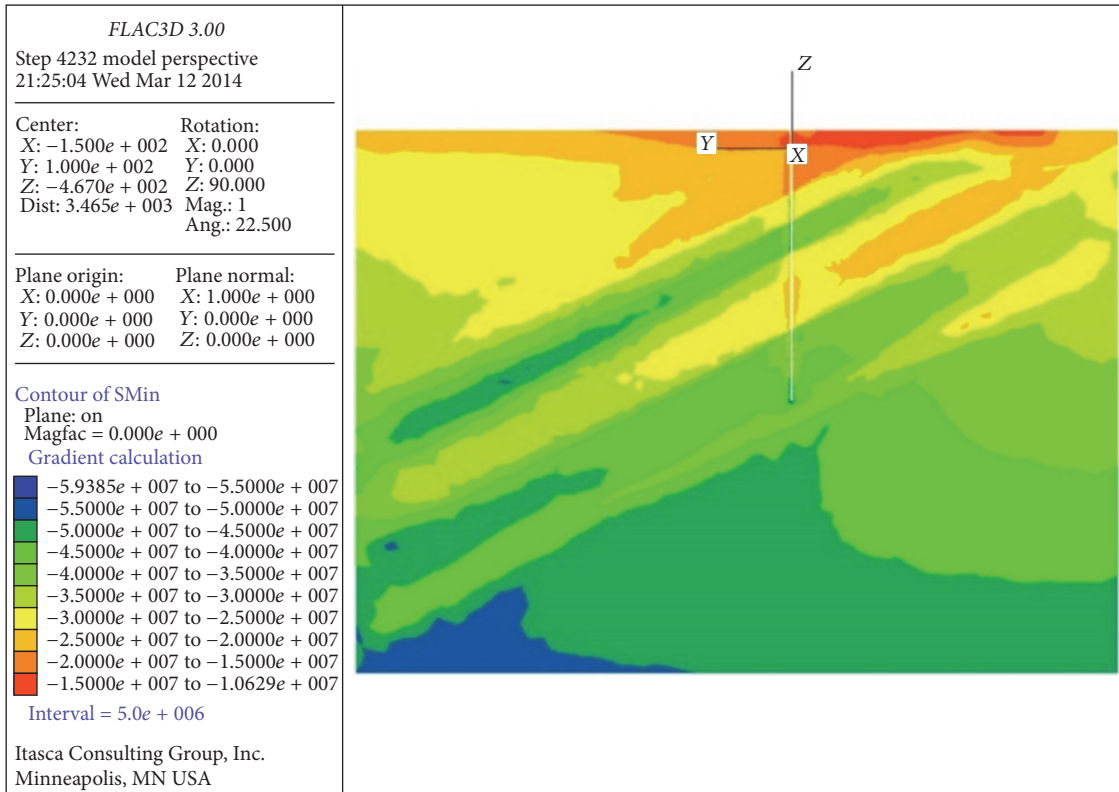


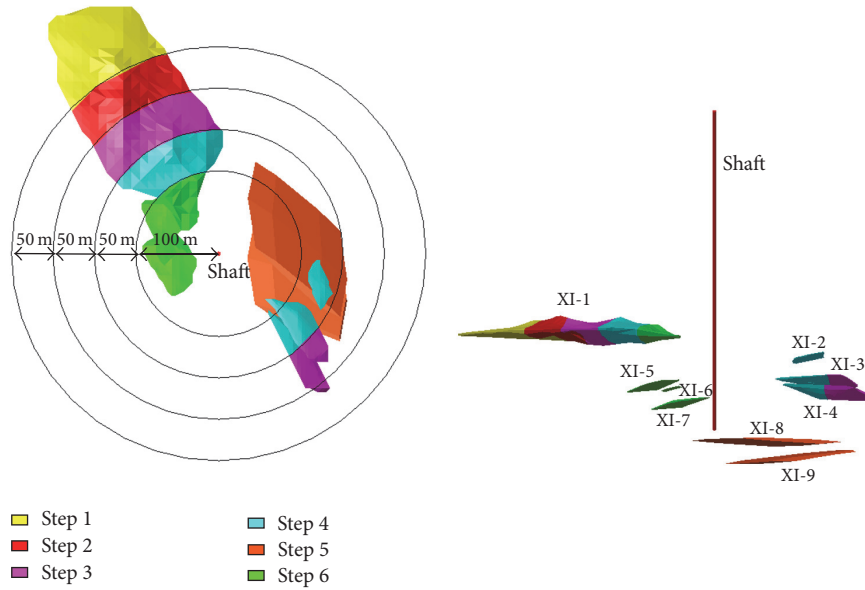
FIGURE 13: Contour of initial maximum principal stress.

are extracted. The output ore at each step is listed in Table 7. Besides, backfilling is simulated to be completed before the next step of extraction, whose mechanical parameters are listed in Table 8.

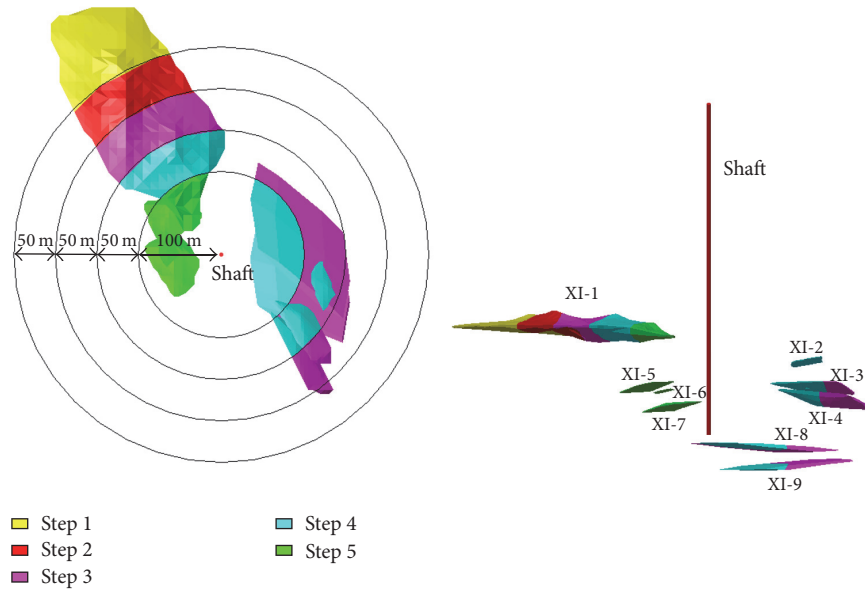
**6.4. Numerical Simulation Results.** When the ore is mined out completely, the contour of displacement field is illustrated in Figure 15. Rock mass tends to move towards the mined-out area, and the maximum displacement occurs in the hanging wall, reaching to 56.7 mm. Because the shaft locates at the footwall of the XI# ore body, the excavation leads to a limited

influence on it. However, due to high horizontal in situ stress and the mining activities, the Hexi Fault distorts seriously; as a result, the displacement of the shaft bottom is up to 12 mm.

Figure 16 shows the displacement along the lateral (strike, dip) and vertical direction, respectively. It is shown that the lateral displacement accounts for a significant proportion in the total displacement of the shaft. Lateral distortion along the strike direction is no more than 3 mm even when the XI# ore body is excavated completely. In contrast, the lateral distortion along the dip direction is much more serious, which exceeds 10 mm at the shaft bottom. In the vertical



(a) Scenario I



(b) Scenario II

FIGURE 14: Mining scenarios for the numerical simulation.

direction, subsidence occurs mainly at the upper part of the shaft and floor heaving occurs at the shaft bottom, which is consistent with the contour of displacement shown in Figure 15.

Besides, the displacements of the shaft are recorded during excavation at the foreshaft, -270 m level, -380 m level, and the bottom, respectively, Figure 17(a). It indicates that the shaft displacements at the foreshaft and -270 m level increase slowly until 3.5 mm, while the displacement at -380 m level and the shaft bottom increases rapidly. Particularly in the last few mining steps, the maximum displacement which occurs at the shaft bottom exceeds the safety threshold 10 mm

when the whole orebody is mined out. It is worth mentioning that spring-back displacement occurs after excavating the XI-8 and XI-9 veins (Step 5), which indicates that the mining sequence outlined in scenario I is required to be optimized, in order to control the shaft displacement under the threshold of 10 mm.

Since both the ore production and the corresponding displacement of shaft are different in each mining step, it is difficult to draw a conclusion directly. In order to quantify the relationship between ore production and shaft displacement, a Mining Priority Index (MPI) which is described as the ratio between percentage of ore production and the percentage of

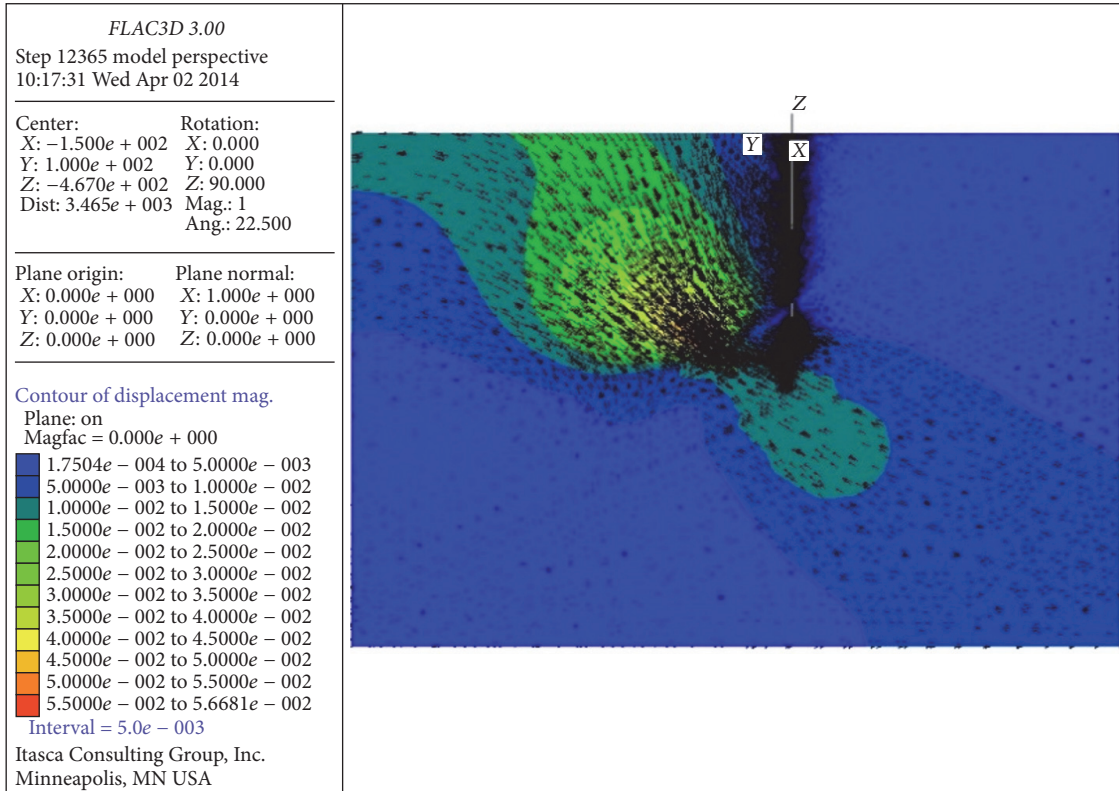


FIGURE 15: Contour of maximum displacement.

the induced maximum incremental displacement of shaft in each mining step, is defined.

$$\text{Mining Priority Index (MPI)} = \frac{\text{Ore production percentage}}{\text{Shaft deformation percentage}} \quad (5)$$

Just as the definition implies, the higher the MPI is, the smaller the incremental shaft displacement occurs when the ore production remains the same, or more ores will be mined out if the incremental shaft displacement remains constant. Substantially, the MPI value is a comprehensive evaluation index considering both the economic benefit and the safety of shaft. Obviously, the overall MPI value of the XI# ore body is 1 (100% to 100%). If the MPI is larger than 1, excavating this part of ore body is relatively better than the others. Otherwise, the mining conditions may be worse, especially, if the MPI value is negative, indicating that this mining step is not reasonable; namely, spring-back shaft displacement occurs.

Table 7 shows information of the scenario I that the MPI values declines gradually with mining operation, indicating that the overall mining sequence, excavating approaching to the shaft, is reasonable. However, the negative MPI value which appeared at step 5 indicates that the excavating of XI-8 and XI-9 veins should be coordinated in order to avoid this kind of excavation.

The modified mining sequence scenario II is to extract the XI-8 and XI-9 veins (Step 5) together with step 3 and step 4,

Figure 12(b), while other steps stay the same as the scenario I; thus, only 5 steps are left in the scenario II. As for the scenario II, the orebodies XI-1 and XI-2, XI-3, XI-4, XI-8, and XI-9 at two sides of the shaft are mined simultaneously, which may be better for balancing the possible tilt of shaft. The relevant displacement results are shown in Figures 17(b) and 18, and the maximum displacement (at the shaft bottom) does not exceed 10 mm if all the orebody is mined out for the scenario II.

For the scenario II, the deformation patterns along the shaft depth change a little but the maximum shaft displacement decreases evidently. The MPI values are listed in Table 9; negative values do not emerge; correspondingly, displacement of the shaft also increases steadily in a small scale, and there is no spring-back displacement of shaft.

By comparison, scenario II is better in controlling the shaft deformation than scenario I, and the maximum shaft displacement is 9.7 mm when the XI# ore body is excavated completely. Although the maximum displacement does not exceed the safety threshold 10 mm, the MPI value at step 5 is too low, which means that the ore production within the distance of 100 m from the shaft is small but the influence on the shaft displacement is significant; as a result, this part of ore is suggested to be left as the shaft pillar. Compared to the original shaft pillar delineated according to the rock movement angles, more than 1000 kt ore can be mined out.

TABLE 9: Details of scenario II.

Simulative excavating steps	Mineral output/kt	Ore proportion/%	Shaft displacement/m	Displacement proportion/%	MPI
1	264.19	15.62%	0.0012	12.71%	1.23
2	363.85	21.51%	0.002	20.88%	1.03
3	563.42	33.30%	0.0026	26.26%	1.27
4	395.06	23.35%	0.0025	25.36%	0.92
5	105.20	6.22%	0.0014	14.79%	0.42
In total	1691.71	100.00%	0.0097	100%	1.00

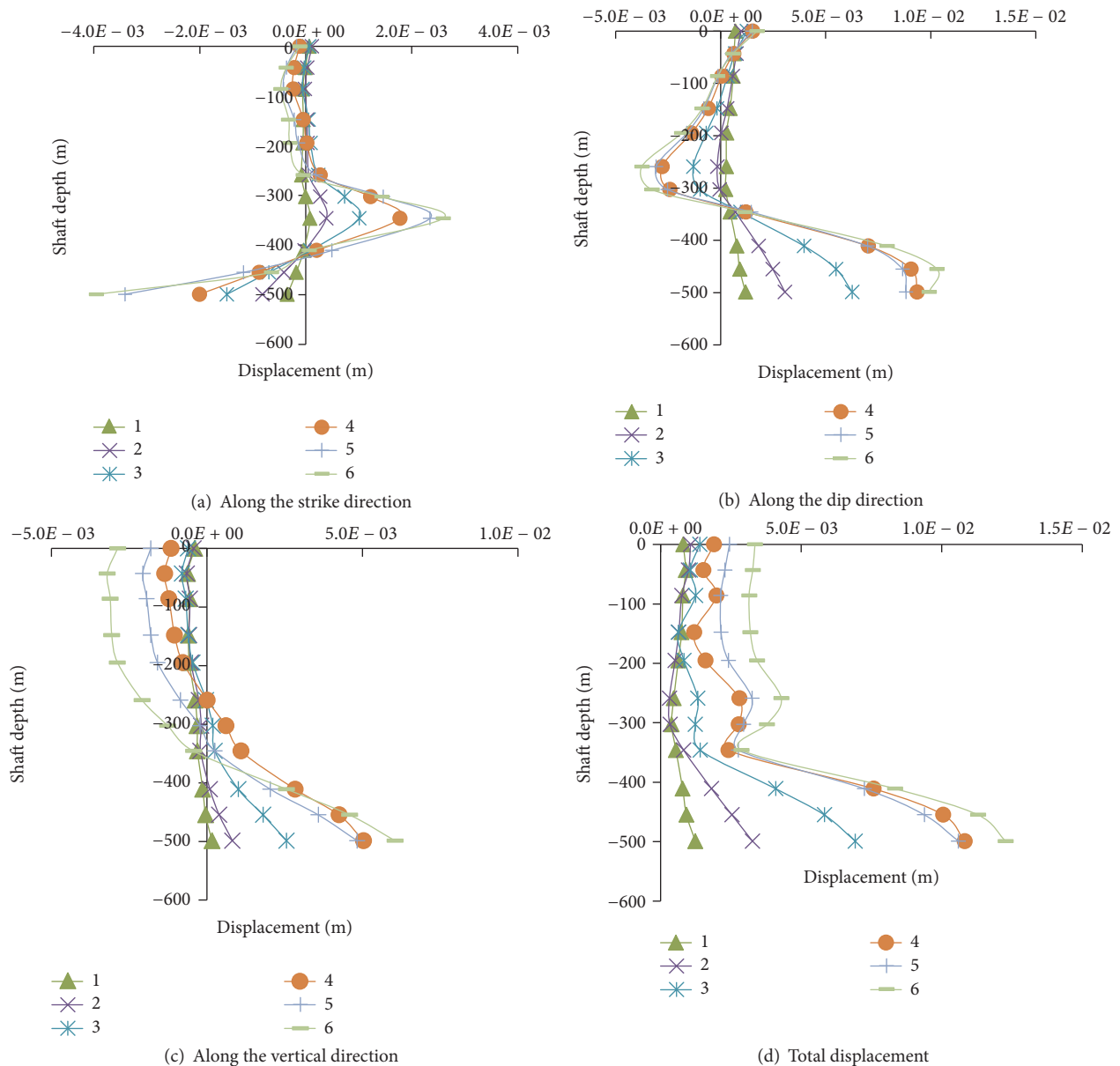


FIGURE 16: Shaft displacement during mining with scenario I.

According to the numerical simulation, the max shaft displacement at  $-380$  m level is  $1.6$  mm at this time, and the monitoring shaft lateral displacement is  $1.4$  mm. In this regard, we deem that the numerical simulation results are well in agreement with the monitoring data; of course, it

needs to be validated further against the in situ monitoring for a long time. Even so, the main value of this crude numerical model mainly comes from the comparison with itself; by this way, a better mining sequence and a proper mining boundary are obtained.

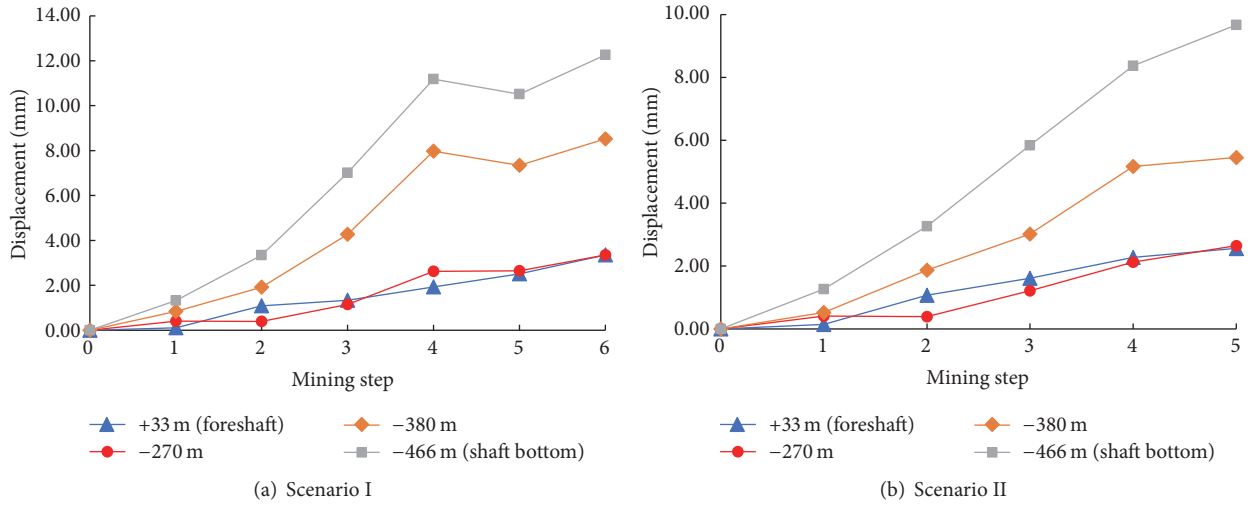


FIGURE 17: Shaft displacement at 4 positions during mining with scenarios I and II.

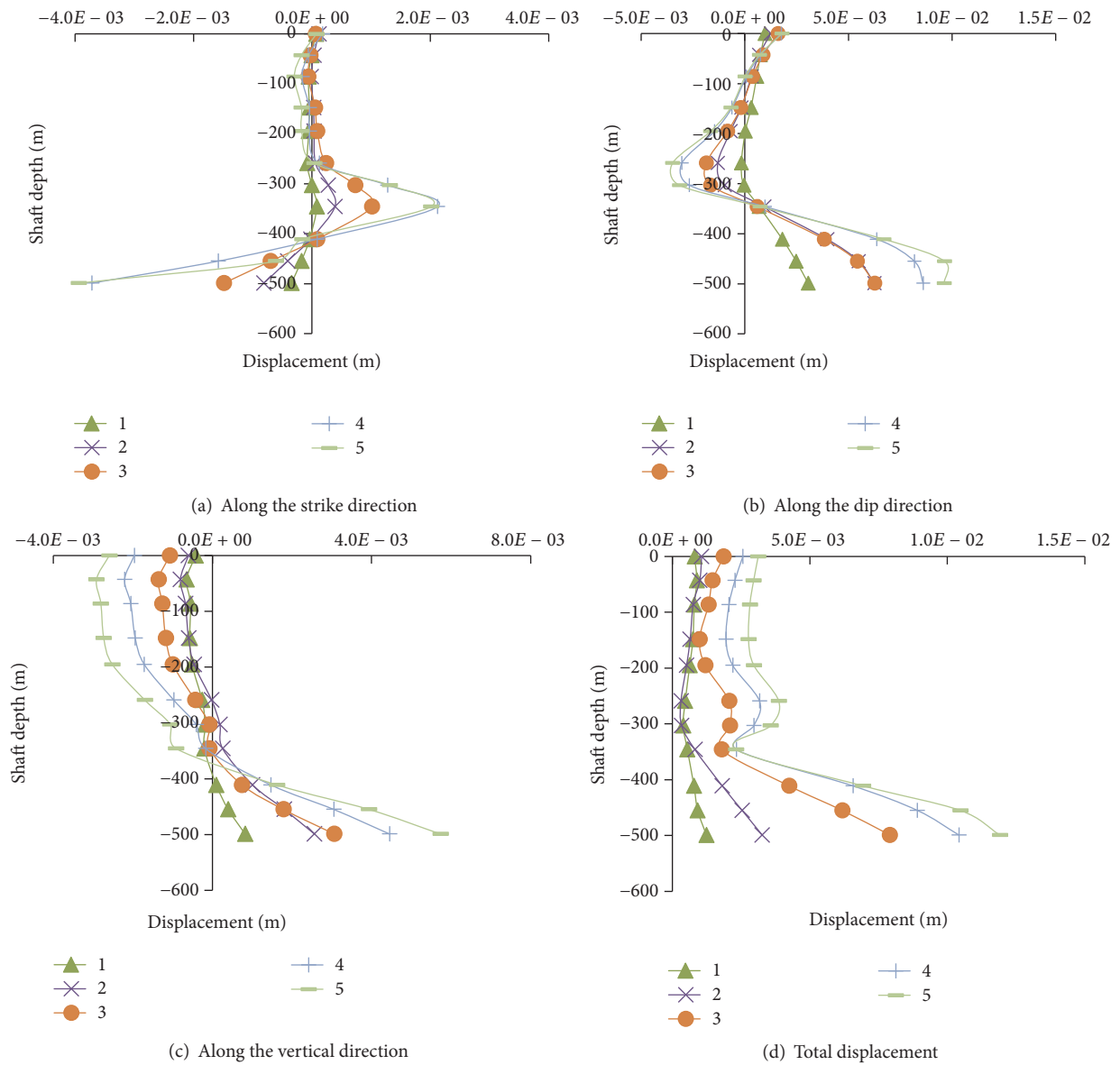


FIGURE 18: Shaft displacement during mining with scenario II.

## 7. Discussions and Conclusions

In this paper, the effects of mining activities on the stability of the main mine shaft at the Xincheng Gold Mine in China were investigated by means of in situ monitoring and numerical simulation; the following conclusions are drawn:

(1) By means of orthogonal design experiment and numerical simulation, sensitivities of the five main factors affecting the shaft displacement have been studied. Dip of the ore body, lateral pressure coefficient, and distance between the shaft and mined-out area are significant factors affecting the shaft displacement.

(2) The Mining Priority Index (MPI) has been defined in order to quantify the relationship between the mineral output and shaft displacement, and then, the optimal mining sequence is selected according to the ranking of MPI values. The MPI is simple but practical, which can be of reference to other similar mining projects.

(3) Based on in situ displacement monitoring and numerical simulation, we deem that the numerical simulation results are generally in agreement with the monitored ones. Thus the numerical simulation is validated against the in situ monitoring up to now. It indicates that excavation of the XI# orebody is tolerable if the ore within a distance of 100 m away from the shaft is kept as pillars, and the original shaft pillar delineated according to the rock movement angles is too conservative.

With the advancing of mining activities, both the in situ monitoring and numerical simulation should be conducted to trace and predict the mining-induced responses of shaft. Of course, the numerical model established at present is relatively rough; a more sophisticated numerical model with detailed stope design should be established in the future. Based on that, a more detailed mining sequence also can be optimized by means of ranking the MPI values.

## Conflicts of Interest

The authors declare that they have no conflicts of interest.

## Acknowledgments

The support provided by the National Key Research and Development Program of China (Grant no. 2016YFC0801607), the National Natural Science Foundation of China (Grant nos. 51525402, 51404067, 51374049, and 51534003), and Fundamental Research Funds for the Central Universities of China (Grant nos. N160104005 and N160103005) is gratefully acknowledged. Moreover, this work was accomplished with the assistance of Xincheng Gold Mine; the authors would like to acknowledge the contributions of mine personnel at Xincheng Gold Mine.

## References

- [1] S. Budavari and R. W. Croeser, "Effects of the extraction of tabular deposits around vertical shafts in deep-level mines," *Proc. 6th congress International Society for Rock Mechanics, Montreal, 1987. Vol. 2*, pp. 825–828, 1987.
- [2] S. D. McKinnon, "Alternatives to shaft pillars for the protection of deep vertical shaft systems," in *Proceeding of the 6th International Conference on Rock Mechanics*, vol. 2, pp. 1129–1134, Montreal, Canada, 1987.
- [3] J. W. Klokow and S. L. Mulder, "Early shaft reef removal at Beatrix No 3 Vertical Shaft," in *Proceeding of the 10th ISRM Congress*, pp. 249–254, Sandton, South Africa, 2003.
- [4] Y. Fujii, D. Ishijima, and M. Igarashi, "Shaft damages due to mining," in *Proceedings of the 7th ISRM Congress*, pp. 16–20, Aachen, Germany, 1991.
- [5] J. C. Johnson and S. A. Orr, "Rock mechanics applied to shaft pillar mining," *International Journal of Mining and Geological Engineering*, vol. 8, no. 4, pp. 385–392, 1990.
- [6] G. D. T. Judeel, "Study of the effects of shaft pillar extraction on a vertical shaft located in highly stratified and poor quality rock masses," in *Proceeding of the 10th ISRM Congress*, Sandton, South Africa, 2003.
- [7] J. McMullan, W. F. Bawden, and R. Mercer, "Excavation of a shaft distress slot at the Newmont Canada Golden Giant Mine," in *Proceedings of the Proceeding of the 6th North America Rock Mechanics Symposium (NARMS)*, p. 5, 2004.
- [8] G. Bruneau, D. B. Tyler, J. Hadjigeorgiou, and Y. Potvin, "Influence of faulting on a mine shaft—a case study: Part I—Background and instrumentation," *International Journal of Rock Mechanics and Mining Sciences*, vol. 40, no. 1, pp. 95–111, 2003.
- [9] G. Bruneau, M. R. Hudyma, J. Hadjigeorgiou, and Y. Potvin, "Influence of faulting on a mine shaft—a case study: Part II—Numerical modelling," *International Journal of Rock Mechanics and Mining Sciences*, vol. 40, no. 1, pp. 113–125, 2003.
- [10] Q.-L. Zhao, Q. Gao, Z.-P. Zhang, and W.-G. Xiao, "Deformation Analysis and Stability Evaluation of the Main Shaft at Jinchuan Mine," *Journal of China University of Mining and Technology*, vol. 17, no. 2, pp. 290–294, 2007.
- [11] M. M. Khan and G. J. Krige, "Evaluation of the structural integrity of aging mine shafts," *Engineering Structures*, vol. 24, no. 7, pp. 901–907, 2002.
- [12] P. Huang, C. Chen, and G. Xiao, "Feasibility analysis on using shaft in the region with large deformation," in *Proceedings of the 1st International Symposium on Mine Safety Science and Engineering, ISMSSE 2011*, pp. 1726–1730, China, October 2011.
- [13] H. Kratzsch, *Mining Subsidence Engineering*, Springer Berlin Heidelberg, Berlin, Heidelberg, 1983.
- [14] M. F. Cai, L. Qiao, and C. H. Li, "Measuring results and regularity of in situ stress in Xincheng gold mine," *Nonferrous Metals*, vol. 52, no. 3, pp. 1–6, 2000 (Chinese).
- [15] *The State Bureau of Safe Production Supervision and Administration, GB16423-2006 Safety Regulations for Metal and Nonmetal Mines*, vol. 62, GB16423-2006 Safety Regulations for Metal and Nonmetal Mines, 2005.
- [16] E. Hoke, C. Carranza-Torres, and B. Corkum, "Hoek-Brown failure criterion," in *Proceedings of NARMS-TAC2002, Mining Innovation and Technology*, Toronto, 2002, 2672ng I.
- [17] E. Hoek and E. T. Brown, "Practical estimates of rock mass strength," *International Journal of Rock Mechanics and Mining Sciences*, vol. 34, no. 8, pp. 1165–1186, 1997.
- [18] S. Shnorhokian, H. S. Mitri, and D. Thibodeau, "Numerical simulation of pre-mining stress field in a heterogeneous rockmass," *International Journal of Rock Mechanics and Mining Sciences*, vol. 66, pp. 13–18, 2014.

## Research Article

# Analytical Solution and Application for One-Dimensional Consolidation of Tailings Dam

Hai-ming Liu <sup>1,2</sup>, Gan Nan,<sup>1</sup> Wei Guo,<sup>1</sup> Chun-he Yang,<sup>2</sup> and Chao Zhang<sup>2</sup>

<sup>1</sup>Faculty of Civil Engineering and Mechanics, Kunming University of Science and Technology, Kunming, Yunnan 650224, China

<sup>2</sup>State Key Laboratory of Geomechanics and Geotechnical Engineering, Institute of Rock and Soil Mechanics, Chinese Academy of Sciences, Wuhan 430071, China

Correspondence should be addressed to Hai-ming Liu; [haiming0871@163.com](mailto:haiming0871@163.com)

Received 10 November 2017; Revised 16 January 2018; Accepted 12 February 2018; Published 19 March 2018

Academic Editor: Shuo Wang

Copyright © 2018 Hai-ming Liu et al. This is an open access article distributed under the Creative Commons Attribution License, which permits unrestricted use, distribution, and reproduction in any medium, provided the original work is properly cited.

The pore water pressure of tailings dam has a very great influence on the stability of tailings dam. Based on the assumption of one-dimensional consolidation and small strain, the partial differential equation of pore water pressure is deduced. The obtained differential equation can be simplified based on the parameters which are constants. According to the characteristics of the tailings dam, the pore water pressure of the tailings dam can be divided into the slope dam segment, dry beach segment, and artificial lake segment. The pore water pressure is obtained through solving the partial differential equation by separation variable method. On this basis, the dissipation and accumulation of pore water pressure of the upstream tailings dam are analyzed. The example of typical tailings is introduced to elaborate the applicability of the analytic solution. What is more, the application of pore water pressure in tailings dam is discussed. The research results have important scientific and engineering application value for the stability of tailings dam.

## 1. Introduction

Based on the assumption that the soil is isotropic and uniform, an external surface load is instantaneously applied and is held constant; a classical one-dimensional (1D) consolidation theory was proposed by Terzaghi [1]. In order to analyze time-dependent loading, an analytical solution to the layered consolidation problem for a general set of boundary conditions and an arbitrary load history was presented by Schiffman and Stein [2]. The 1D consolidation analytical solutions considering ramp loading were presented by Olson [3]. A simple semianalytical method to solve the problem of 1D consolidation by taking into account the varied compressibility of soil under cyclic loadings was brought up by Cai et al. [4]. A rigorous solution of the conventional Terzaghi 1D consolidation under haversine cyclic loading with any rest period was proposed by Müthing et al. [5], which is achieved using Fourier harmonic analysis for the periodic function representing the rate of imposition of excess pore water pressure. A semianalytical solution to 1D consolidation of viscoelastic unsaturated soils with a finite thickness under

oedometric conditions and subjected to a sudden loading was put forward by Qin et al. [6]. A semianalytical solution to 1D consolidation equation of fractional derivative Kelvin-Voigt viscoelastic saturated soils subjected to different time-dependent loadings was presented by Wang et al. [7]. Under the condition of the increasing weight of superincumbent material and the length of the drainage path varies, a solution for the 1D consolidation of a clay layer whose thickness increases with time was proposed by Gibson [8]. An exact analytical solution of the nonhomogeneous partial differential equation governing the conventional 1D consolidation under haversine repeated loading was derived and discussed by Razouki et al. [9, 10].

In order to analyze different boundary conditions, single drainage solutions for several specific variations of the permeability and shear modulus were given by Mahmoud and Deresiewicz [11]. Several analytical solutions for the consolidation analysis of a soil layer with fairly general laws of variation of permeability and compressibility for both a single-drained condition and a double-drained condition were proposed by Zhu and Yin [12]. Tang et al. [13] propose



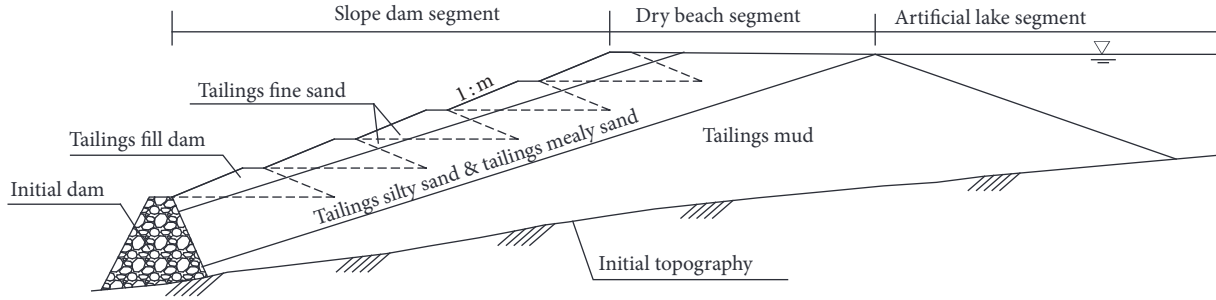


FIGURE 2: Schematic diagram of the upstream tailings dam.

Substituting (10) into (9) yields

$$\sigma' = (\sigma_0 + \Delta\sigma) + \gamma'z - u. \quad (11)$$

Take the derivative of (11) with respect to  $t$  and consider the relationship  $\partial z/\partial t$  equals  $\partial H/\partial t$

$$\frac{\partial \sigma'}{\partial t} = \frac{\partial}{\partial t} (\Delta\sigma) + \gamma' \frac{\partial H}{\partial t} - \frac{\partial u}{\partial t}. \quad (12)$$

According to the compression curve of 1D consolidation test, the volume compressibility factor  $m_v$  can be defined as follows:

$$m_v = \frac{1}{1+e} \frac{\partial e}{\partial \sigma'}, \quad (13)$$

$$\frac{\partial \varepsilon_z}{\partial t} = \frac{1}{1+e} \frac{\partial e}{\partial t}. \quad (14)$$

Substituting (13) into (14) gives

$$\frac{\partial \varepsilon_z}{\partial t} = m_v \frac{\partial \sigma'}{\partial t}. \quad (15)$$

Substituting (15) into (8), it is noted that the last term of (8) has the following relation:

$$m\gamma_w v_z \frac{1}{k^2} \frac{dk}{dz} = -F_z \frac{1}{k} \frac{dk}{dz} = -\left( \frac{\partial p_w}{\partial z} + \gamma_w \right) \frac{1}{k} \frac{dk}{dz}. \quad (16)$$

Equation (8) can be derived as

$$\frac{\partial^2 p_w}{\partial z^2} + \frac{m_v \gamma_w}{k} \frac{\partial \sigma'}{\partial t} + \left( \frac{\partial p_w}{\partial z} + \gamma_w \right) \frac{1}{k} \frac{dk}{dz} = 0. \quad (17)$$

Substituting (15) into (17), (17) can be expressed as pore water pressure. Equation (18) can be obtained

$$\frac{\partial^2 u}{\partial z^2} + \frac{m_v \gamma_w}{k} \left[ \frac{\partial \Delta\sigma}{\partial t} + \gamma' \frac{\partial H}{\partial t} - \frac{\partial u}{\partial t} \right] + \frac{1}{k} \frac{dk}{dz} \frac{\partial u}{\partial z} = 0. \quad (18)$$

Equation (18) is a general equation which reflects the 1D consolidation process. It takes into account the situation where the applied load changes with time, the soil thickness changes with time, the soil permeability changes with depth, and so on.

### 3. Accumulation and Dissipation of Pore Water Pressure in Tailings Dam

Tailings are mine wastes produced in the mining engineering, which are sent to tailings reservoir by pipe or flume. The tailings dam is an important part in mining engineering, which is consisted by the initial dam and fill dam. The initial dam is made by permeable rockfill generally, and the fill dam is formed by tailings. In general, the construction of a tailing dam takes many decades or even a century. According to construction method, the tailings dam can be divided into upstream tailings dam, downstream tailings dam, midline method tailings dam, and so on. The number of tailings ponds in China has reached more than 12,000 by statistics. Because the downstream of the tailings dam is residents living area or mining production area generally the social and people's property damage a huge impact if the tailings dam is failed.

Because the upstream tailings dam has advantages of simple operation, low construction costs, the less need for coarse particles, and so on, according to statistics, 95% of the tailings dams are adopting the construction of the upstream tailings dam in China. On the other hand, the construction process of the upstream tailings dam cannot precisely control the shape of the tailings dam. The deposition structure of the tailings dam is very complex. The upstream tailings have shortcoming of long infiltration distant and poor stability. In view of the tailings slurry discharge and tailings particle deposition following the sediment mechanics, the section profile of the tailings dam has obvious regularity. The coarser the particle size is, the shorter the average distance migrates and vice versa. Generally, the deposition order of the tailings dam along the dry beach face is tailings fine sand, tailings silt, tailings sand, and tailings mud.

If particle size distribution of the tailings and the length of the dry beach face are kept constant, the interface of the tailings material should be substantially parallel to the surface of the dam slope, which is shown in Figure 2. For most of the tailings dams, because the tailings water contains more heavy metals, the initial topography and the side of tailings dam are treated as an impermeable boundary. On the other hand, the tailings dam extends very long in the direction of the reservoir area. Therefore, the consolidation of the tailings dam is a 1D problem.

As can be seen from Figure 2, the closer to inside the reservoir area is, the thicker the tailings mud is and the worse

the average consolidation is. In other words, the closer to inside the reservoir area is, the greater pore water pressure of the tailings dam is and the lower shear strength of the tailings material is. Generally speaking, the construction of a tailings dam needs several decades to reach the design elevation. With the continuous production of mining, the height of the tailings dam is increasing. During this process, the accumulation and dissipation of the excess pore water pressure of the tailings material experience several different stages of development.

**3.1. Tailings Thickness Increases with Time.** In this stage, the thickness of the tailings increases with time. The tailings material produces great compressive deformation under self-weight effect. The pore water pressure produced by the self-weight pressure at the early stage is partially dissipated. Nevertheless, the pore water pressure caused by self-weight pressure is increased with the tailings thickness at the later stage, which leads to the increase of the pore water pressure with time. Therefore, the net pore water pressure is accumulated during this process.

**3.2. Load on the Tailings Layer Increases with Time.** The self-deposition of the tailings mud continues to extend to interior of the tailings reservoir area in this stage. The self-deposition of the tailings layer has ended where the end of the tailings reservoir is near. It overlapped with particles coarse tailings and tailings mud. The tailings mud has to bear a growing load with time. The tailings mud continues to consolidate under the combined action of self-weight and additional load. At this stage, the pore pressure produced by the self-weight pressure dissipates a little part, and the more pore water pressure produced by additional load accumulates. The net pore water pressure tends to accumulate in this process.

**3.3. The Additional Load of the Tailings Material Remains Constant.** For a specific part of the tailings dam, the upper boundary of the tailings dam has reached the designed elevation at a certain moment. Therefore, the additional load will remain unchanged from this moment. During this stage, the tailings mud will continue to consolidate under the combined action of self-weight and constant additional load. Thus, the pore water pressure will dissipate within the tailings dam. Obviously, the different parts of tailings mud have different consolidation stages. There is no additional load at the thickest tailings mud in the tailings reservoir until it is closed. Therefore, the tailings mud is always in the first stage and will never enter the second and third stages. From the above qualitative analysis, the pore water pressure, which is located at the slope dam segment, reaches the maximum value when the additional load just stops growing. The pore water pressure, which is located at dry beach segment and artificial lake segment, achieves the maximum value when the tailings dam reaches the maximum height. The numerical values of the pore water pressure at different locations and moments can be obtained by solving the partial differential equations of consolidation problems.

## 4. Analytical Solutions of the Pore Water Pressure

It is necessary to accurately calculate the accumulation and dissipation of the pore water pressure in tailings dam, of which a solution of 1D consolidation problem can be simplified. During the consolidation process, the soil parameters of tailings material (such as the change of bulk density, permeability coefficient, and consolidation coefficient) are changed with the consolidation process. The change law can be determined through many experiments. Under normal circumstances, it is difficult to obtain the analytical solution when the change law of soil parameters is considered. Therefore, the exact solution of the problem can only be depended on numerical calculation method.

As the horizontal length of the tailings reservoir is usually far greater than the vertical thickness (i.e., the horizontal length is 10 times more than the vertical thickness), the drainage consolidation effect of the horizontal direction can be ignored. Therefore, the vertical direction of drainage is needed to consider. Then, it is only a 1D consolidation problem. Based on the assumption of small-strain and constant of soil parameters, such as  $m_v$ ,  $k$ ,  $\partial\Delta\sigma/\partial t$ ,  $\gamma'$ , and  $\partial H/\partial t$  are constant, (18) is degenerated into a constant coefficient nonhomogeneous parabolic partial differential equation

$$\frac{\partial^2 u}{\partial z^2} + \frac{1}{c_v} \left( \alpha + \gamma' Q - \frac{\partial u}{\partial t} \right) = 0, \quad (19)$$

where

$$\begin{aligned} \alpha &= \frac{\partial\Delta\sigma}{\partial t}, \\ Q &= \frac{\partial H}{\partial t}, \\ c_v &= \frac{k}{m_v \gamma_w}. \end{aligned} \quad (20)$$

The above three different stages are specifically discussed as follows.

**4.1. The Thickness Mud of Tailings Mud Increases with Time.** The overburden load of the tailings mud at this stage is zero, that is,  $\alpha = 0$ . The consolidation equation yields

$$\frac{\partial^2 u}{\partial z^2} + \frac{1}{c_v} \left( \gamma' Q - \frac{\partial u}{\partial t} \right) = 0. \quad (21)$$

If the bottom of the tailings mud is impermeable, the coordinates origin is taken as the impermeable bottom. The boundary conditions of the problem can be given as follows:

$$\begin{aligned} z &= 0, \\ \frac{\partial u}{\partial z} &= 0, \end{aligned} \quad (22)$$

$$\begin{aligned} z &= H, \\ u &= 0. \end{aligned} \quad (23)$$

The initial condition of the problem is given by

$$\begin{aligned} t &= 0, \\ u &= 0. \end{aligned} \quad (24)$$

According to Gibson's [20] study, (25) is chosen as the solution of (21)

$$u = \gamma' h - t^{-1/2} \int_0^\infty g(\xi) \left( e^{-(x-\xi)^2/4c_v t} + e^{-(x+\xi)^2/4c_v t} \right) d\xi. \quad (25)$$

It can be verified that (25) satisfies the boundary condition (22). The choice of function  $g(\xi)$  needs to satisfy (23). Substituting (25) into (23) gives

$$\frac{1}{2} \gamma' h t^{1/2} e^{h^2/4c_v t} = \int_0^\infty g(\xi) e^{-(x+\xi)^2/4c_v t} \cosh \frac{h\xi}{2c_v t} d\xi. \quad (26)$$

For any function  $h(t)$ , the partial differential equation (26) has no numerical solution. With regard to  $h(t) = mt$ , the following parameters can be introduced to transform the equation

$$\begin{aligned} \xi^2 &= \tau, \\ p &= \frac{1}{4} c_v t, \\ F(\tau) &= g(\tau) \tau^{-1/2} \cosh \frac{k\tau^{1/2}}{2c_v}. \end{aligned} \quad (27)$$

Equation (26) can be transformed into

$$\frac{1}{8} m \gamma' c_v^{-3/2} p^{-3/2} e^{m^2/16c_v^2 p} = \int_0^\infty F(\tau) e^{-p\tau} d\tau. \quad (28)$$

Equation (28) can be obtained through the Laplace change:

$$F(\tau) = \frac{\gamma'}{2\pi^{1/2} c_v^{1/2}} \sinh \frac{m\tau^{1/2}}{c_v}. \quad (29)$$

Thence

$$g(\xi) = \frac{\gamma' \xi}{2\pi^{1/2} c_v^{1/2}} \tanh \frac{m\xi}{c_v}. \quad (30)$$

Combining the solutions of (25) and (30), the solution of (21) is obtained

$$\begin{aligned} u &= \gamma' Q t - \gamma' (\pi c_v t)^{-1/2} \exp\left(\frac{-z^2}{4c_v t}\right) \int_0^\infty \xi \tanh \frac{Q\xi}{2c_v} \\ &\quad \cdot \cosh \frac{z\xi}{2c_v t} \exp\left(\frac{-\xi^2}{2c_v t}\right) d\xi. \end{aligned} \quad (31)$$

It can be verified that (31) satisfies the initial condition of (24).

#### 4.2. The Additional Load of Tailings Mud Increases with Time.

During this stage, the thickness of tailings mud not only does not increase with time but also gradually decreases with the increase of effective stress. For the sake of simplicity, assuming that the thickness of tailings mud  $H$  is constant, the basic consolidation differential (19) can be simplified as

$$c_v \frac{\partial^2 u}{\partial z^2} = \frac{\partial u}{\partial t} - \frac{\partial \Delta \sigma}{\partial t}. \quad (32)$$

The initial condition of the problem is given by

$$\begin{aligned} t &= t_1, \\ u &= u_0(z). \end{aligned} \quad (33)$$

The boundary conditions of the problem can be given as

$$\begin{aligned} z &= 0, \\ u &= 0 \\ z &= H, \\ \frac{\partial u}{\partial z} &= 0. \end{aligned} \quad (34)$$

The following three questions are called problem A, problem B, and problem C, respectively:

A:

$$\begin{aligned} \frac{\partial u}{\partial t} &= c_v \frac{\partial^2 u}{\partial z^2} \\ \text{Initial conditions: } t &= t_1, \\ u &= u_0(z) \\ \text{Boundary conditions: } z &= 0, \\ u &= 0 \\ z &= H, \\ \frac{\partial u}{\partial z} &= 0. \end{aligned} \quad (35)$$

B:

$$\begin{aligned} \frac{\partial u}{\partial t} &= c_v \frac{\partial^2 u}{\partial z^2} + \frac{\partial \Delta \sigma}{\partial t} \\ \text{Initial conditions: } t &= t_1, \\ u &= 0 \\ \text{Boundary conditions: } z &= 0, \\ u &= 0 \\ z &= H, \\ \frac{\partial u}{\partial z} &= 0. \end{aligned} \quad (36)$$

C:

$$\frac{\partial u}{\partial t} = c_v \frac{\partial^2 u}{\partial z^2} + \frac{\partial \Delta \sigma}{\partial t}$$

Initial conditions:  $t = t_1,$   
 $u_0(z)$

Boundary conditions:  $z = 0,$  (37)  
 $u = 0$   
 $z = H,$   
 $\frac{\partial u}{\partial z} = 0.$

If the solution of problem A, problem B, and problem C is  $u_A, u_B,$  and  $u_C$  respectively, it can be directly proved through substitution method:

$$u_C = u_A + u_B. \quad (38)$$

The solution of  $u_A$  belongs to the Terzaghi classical 1D consolidation problem. The analytical solution can be obtained.

$$u_A = \sum_{j=1}^{\infty} A_n \sin \frac{j\pi z}{2H} \exp \left[ \frac{-j^2 \pi^2 c_v (t - t_1)}{4H^2} \right], \quad (39)$$

where

$$A_n = \frac{1}{H} \int_0^{2H} u_0(z) \sin \frac{j\pi z}{2H} dz. \quad (40)$$

$u_0(z)$  is the solution of (31). Substituting (31) into (40) by Matlab software,  $A_n$  can be obtained. Substituting it into (39), the numerical solution  $u_A$  can be given.

For solution to the problem  $u_B$ , Schiffman [21] acquires the following series solutions:

$$u_B = \frac{16\alpha H^2}{\pi^3 c_v} \sum_{1,3,5}^{\infty} \frac{1}{j^3} \sin \frac{j\pi z}{2H} \cdot \left\{ 1 - \exp \left[ \frac{-j^2 \pi^2 c_v (t - t_1)}{4H^2} \right] \right\}. \quad (41)$$

When the tailings mud is below the groundwater level, the total stress  $\sigma(z)$  of the tailings mud at the depth  $z$  can be expressed as follows:

$$\sigma(z) = \gamma' z + \frac{\partial \Delta \sigma}{\partial t} (t - t_1). \quad (42)$$

The ratio of pore water pressure to total stress can be easily determined as follows:

$$U_z = \frac{u_A + u_B}{\sigma(z)}. \quad (43)$$

4.3. *The Additional Load on the Tailings Mud Remains Constant.* In this stage, the basic differential equation and the definite condition are problem D:

D:

$$\frac{\partial u}{\partial t} = c_v \frac{\partial^2 u}{\partial z^2}$$

$t = t_2,$   
 $u = (u_A + u_B)|_{t=t_2}$   
 $z = 0,$  (44)  
 $u = 0$   
 $z = H,$   
 $\frac{\partial u}{\partial z} = 0.$

The following questions can be called problem E:

E:

$$\frac{\partial u}{\partial t} = c_v \frac{\partial^2 u}{\partial z^2}$$

$t = t_2,$   
 $u = u_B|_{t=t_2} = u_1(z)$   
 $z = 0,$  (45)  
 $u = 0$   
 $z = H,$   
 $\frac{\partial u}{\partial z} = 0.$

If the solution of problem A is  $u_A$  and the solution of problem E is  $u_E$ , the solution of problem D can be easily demonstrated is  $u_D$  as follows:

$$u_D = u_A + u_E. \quad (46)$$

The definite condition of problem E and problem A is exactly the same in form, except that the function  $u_1(z)$  is different from the function  $u_0(z)$ .

Suppose that

$$u_E = \sum_{j=1}^{\infty} B_n \sin \frac{j\pi z}{2H} \exp \left[ \frac{-j^2 \pi^2 c_v (t - t_2)}{4H^2} \right]. \quad (47)$$

Then

$$B_n = \frac{1}{H} \int_0^{2H} u_1(z) \sin \frac{j\pi z}{2H} dz, \quad (48)$$

where

$$u_1(z) = \frac{16\alpha H^2}{\pi^3 c_v} \cdot \sum_{1,2,3}^{\infty} \frac{1}{j^3} \sin \frac{j\pi z}{2H} \left\{ 1 - \exp \left[ \frac{-j^2 \pi^2 c_v (t_2 - t_1)}{4H^2} \right] \right\}. \quad (49)$$

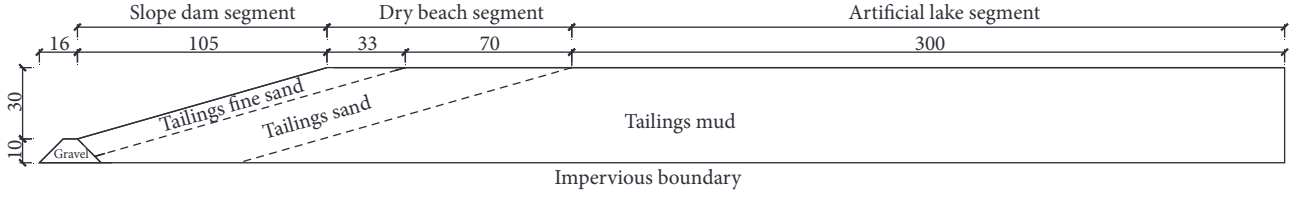


FIGURE 3: Simplified section for calculation of pore water pressure in a tailings dam.



FIGURE 4: Distribution of pore water pressure at the moment when the dam rises to its maximum height.

According to the orthogonal rule of the solution, the following relationship can be obtained:

$$\frac{1}{H} \int_0^{2H} \sin \frac{m\pi z}{2H} \sin \frac{j\pi z}{2H} dz = \begin{cases} 0, & m \neq j \\ 1, & m = j. \end{cases} \quad (50)$$

Equation (48) can be simplified through (50)

$$B_n = \begin{cases} \frac{16\alpha H^2}{\pi^3 c_v} \frac{1}{j^3} \left\{ 1 - \exp \left[ \frac{-j^2 \pi^2 c_v (t_2 - t_1)}{4H^2} \right] \right\} & j = 1, 3, 5 \\ 0 & j = 2, 4, 6. \end{cases} \quad (51)$$

Substituting (51) into (47) yields

$$u_E = \frac{16\alpha H^2}{\pi^3 c_v} \sum_{1,3,5} \frac{1}{j^3} \left\{ 1 - \exp \left[ \frac{-j^2 \pi^2 c_v (t_2 - t_1)}{4H^2} \right] \right\} \cdot \sin \frac{j\pi z}{2H} \exp \left[ \frac{-j^2 \pi^2 c_v (t - t_2)}{4H^2} \right]. \quad (52)$$

For the third stage, the analytical solution of pore water pressure is obtained.

Similar to (42), the ratio of pore water pressure to total stress at a certain depth of tailings mud at this stage is as follows:

$$U_z = \frac{u_A + u_E}{\sigma(z)}. \quad (53)$$

During this stage,  $\sigma(z)$  does not change with time, and it can take the following value:

$$\sigma(z) = \gamma' z + \alpha(t_2 - t_1). \quad (54)$$

## 5. Example

The simplified calculation section of the representative section of a tailings dam is shown in Figure 3. The length of the tailings dam is 368 m. Therefore, the problem can be simplified as 1D consolidation. The slime layer below the level is assumed for impervious boundary. The rising speed of the

dam height is 1.75 m/y. The saturation density of gravel is 22.0 kN/m<sup>3</sup>, the saturation density of the tailings fine sand is 19.6 kN/m<sup>3</sup>, the saturation density of the tailings sand is 19.1 kN/m<sup>3</sup>, and the saturation density of the tailings mud is 18.8 kN/m<sup>3</sup>. The permeability coefficient of gravel is 3 × 10<sup>-3</sup> m/s, the permeability coefficient of the tailings fine sand is 5 × 10<sup>-6</sup> m/s, the permeability coefficient of the tailings sand is 2 × 10<sup>-6</sup> m/s, and the permeability coefficient of the tailings mud is 1.5 × 10<sup>-8</sup> m/s. The consolidation coefficient of gravel is 3.8 × 10<sup>-1</sup> cm<sup>2</sup>/s, the consolidation coefficient of the tailings fine sand is 5.4 × 10<sup>-3</sup> cm<sup>2</sup>/s, the consolidation coefficient of the tailings sand is 2.8 × 10<sup>-3</sup> cm<sup>2</sup>/s, and the consolidation coefficient of the tailings mud is 1.2 × 10<sup>-5</sup> cm<sup>2</sup>/s. Please determine the distribution of pore water pressure when the tailings dam reaches maximum height.

The above problem can be solved through (31), (46), and (52). The calculation can be accomplished through the MATLAB software. Firstly, a coordinate system can be set up. Then, the corresponding coordinates are taken out of the interval 1 m. The region is determined according to the coordinates. Then, the pore water pressure can be calculated through the corresponding equation. Finally, the contour map can be drawn through a set of array. The results of the calculation are shown in Figure 4.

## 6. Discussion

Due to the similarity between the tailings dam and the reservoir dam in the geotechnical structure, many scholars directly introduce the calculation methods of the reservoir dam, whose theory is relatively mature, into the tailings dam. Considering the difference on construction cycle, construction materials between the tailings dam and reservoir dam, it makes the calculation results inconsistent with the actual.

Based on the Terzaghi consolidation theory of 1D, the tailings dam is divided into the slope dam segment, the dry beach segment, and the artificial lake segment. The solutions of the pore water pressure are derived, respectively. The analysis shows that the additional load of the slope dam segment is unchanged, which can be calculated using (46). The analysis indicates that tailings thickness of the artificial

lake segment increases with time during construction period, which can be calculated by (31). The situation of the dry beach section is slightly complicated. The additional load of the dry beach section which is under the slope dam segment is basically the same, which can be calculated by (52). The additional load on the other sections of the dry beach segment increases with time, which can be calculated using (31).

The theoretical derivation is based on 1D consolidation theory. It is only considering consolidation in the vertical direction. Since the horizontal scale of most tailings dams is much larger than the vertical direction, it has little influence to ignore the drainage of horizontal. From the point of engineering view, it is conservative to the stability of the tailings dam. Considering drainage of the horizontal, the pore water pressure will be lessened and the safety factor of the tailings dam will be greater.

It is assumed that the deformation of the tailings is small deformation during the consolidation process. If the actual tailings are loose relatively, the deformation of the tailings is large deformation. He et al. [22] studied the pore water pressure of saturated soils using the updated Lagrangian formulation of large strain method (ULM), total Lagrangian formulation of large strain method (TLM), and small strain method (SSM). The results point out that the pore water pressure of the above three methods is exactly the same when the strain is less than 2.4%. When the strain is greater than 2.4%, the pore water pressure of the ULM and SSM still keeps the same, and the pore water pressure of the TLM is obviously less than the ULM and SSM. When the strain reaches 7.5%, the pore water pressure of the ULM and SSM began to bifurcate. When the deformation of the tailings dam is examined for a relatively short time, the consolidation of prophase tailings dam has been completed under previous load. The consolidation deformation of the whole tailings dam is relatively small, and its deformation conforms to the small deformation assumption. On the other hand, it is difficult to calculate and solve partial differential equations using large deformation theory. The differences between large deformation and small deformation need to be further studied.

It is supposed that the mechanical parameters such as permeability coefficient and consolidation coefficient are constant during the consolidation process. Previous studies [23] have shown that the permeability coefficient of rock and soil decreases with the increase of deformation during the consolidation process. It is believed that the value of  $C_c/C_k$  decides whether it is necessary to take under consideration the effect of nonlinear property by Zhuang et al. [24]. The results show that pore water pressure calculated depends on the ratio of loading intensity to the initial effective vertical stress subjected to time-dependent loading by Conte and Troncone [25]. How the permeability coefficient of tailings material changes during the consolidation process is less studied by relevant scholars. How the permeability coefficient of tailings material changes during the consolidation process is less studied by relevant scholars. From the aspect of engineering view, the larger the pore water pressure of actual is, the smaller the safety factor of tailings dam is. Therefore,

it is dangerous for the tailings dam. The law of permeability coefficient of tailing material during consolidation process needs to be further studied.

## 7. Conclusion

Tailings dam is a very important geotechnical structure of mine engineering. The calculation of pore water pressure has a great impact on the safety factor of tailings dam slope. How to accurately estimate pore water pressure is very difficult. Based on the assumption of 1D consolidation and small strain of tailings material, a general equation of the pore water pressure is proposed. According to dissipation and accumulation characteristics of the pore water pressure in the tailings dam, the tailings dam can be divided into the slope dam segment, the dry beach segment, and the artificial lake segment. The analytic solutions of the corresponding segment are obtained through solving the partial differential equation, which has great significance to the stability of the tailings dam.

## Notations

$\tau$ :	Shear strength of the tailings material
$\sigma(z)$ :	Maximum increases in vertical total stress as a function of depth $z$
$\xi$ :	A parameter introduced to transform an equation
$\alpha$ :	The rate of the additional load on the tailings mud, $\alpha = \partial\Delta\sigma/\partial t$
$x$ :	Coordinate of $x$ direction
$p$ :	A parameter introduced to transform an equation
$n$ :	Porosity of the tailings material
$m, j$ :	Counters, 1, 2, 3, . . .
$g(\tau)$ :	A function of variable $\tau$
$g(\xi)$ :	A function introduced into solving partial differential equation
$Q$ :	The rate of the thickness of the tailings mud, $Q = \partial H/\partial t$
$F(\tau)$ :	A function introduced to transform an equation
$\sigma$ :	Stress of the tailings material
$z$ :	Coordinate of $z$ direction
$u$ :	The pore water pressure
$k$ :	Coefficient of coefficient
$h$ :	The height of static water level
$H$ :	Thickness of tailings mud
$e$ :	Porosity ratio
$\Delta\sigma$ :	Increment of stress
$u_1(z)$ :	Termination pore water pressure as a function of depth $z$
$u_0(z)$ :	Initial pore water pressure as a function of depth $z$
$t_2$ :	Termination time
$t_1$ :	Initial time
$c_v$ :	Coefficient of consolidation
$U_z$ :	Saturation
$B_n$ :	Coefficients to be determined

$A_n$ : Coefficients to be determined  
 $\sigma_0$ : Initial total stress  
 $\sigma^f$ : Effective vertical stress  
 $\varepsilon_z$ : Strain in the  $z$  direction  
 $\gamma_w$ : Bulk density of water  
 $\gamma_s$ : Saturated bulk density of tailings dam  
 $\gamma^f$ : Buoyancy unit weight of tailings material  
 $v_z$ : The actual velocity along the flow direction in the tailings dam  
 $p_w$ : Water pressure  
 $m_v$ : Coefficient of volume compressibility  
 $i_z$ : Hydraulic gradient in the  $z$  direction  
 $H_1$ : The total height of tailings mud plus static water level  
 $F_z$ : The drag resistance force on the pore wall of a unit volume in the  $z$  direction.

## Conflicts of Interest

The authors declare that they have no conflicts of interest.

## Acknowledgments

This paper is supported by the Open Research Fund of State Key Laboratory of Geomechanics and Geotechnical Engineering, Institute of Rock and Soil Mechanics, Chinese Academy of Sciences, (Grant no. Z013009), the National Key Research and Development Program of China (Project no. 2017YFC0804601), the National Natural Science Foundation of China (Grant nos. 51764020; 51741410; 51234004), and the Natural Science Foundation of Yunnan Province (Grant no. 2015FB130). The authors would like to thank them for providing the financial support for conducting this research.

## References

- [1] K. Terzaghi, *Theoretical Soil Mechanics*, John Wiley & Sons, New York, NY, USA, 1943.
- [2] R. L. Schiffman and J. R. Stein, "One-dimensional consolidation of layered systems," *Journal of the Soil Mechanics and Foundations Division*, vol. 96, no. 4, pp. 1499–1504, 1970.
- [3] R. E. Olson, "Consolidation under time-dependent loading," *Journal of the Geotechnical Engineering Division*, vol. 103, no. 1, pp. 55–60, 1977.
- [4] Y.-Q. Cai, X.-Y. Geng, and C.-J. Xu, "Solution of one-dimensional finite-strain consolidation of soil with variable compressibility under cyclic loadings," *Computers & Geosciences*, vol. 34, no. 1, pp. 31–40, 2007.
- [5] N. Mühling, S. S. Razouki, M. Datcheva, and T. Schanz, "Rigorous solution for 1-D consolidation of a clay layer under haversine cyclic loading with rest period," *SpringerPlus*, vol. 5, no. 1, article no. 1987, 2016.
- [6] A. Qin, D. Sun, and J. Zhang, "Semi-analytical solution to one-dimensional consolidation for viscoelastic unsaturated soils," *Computers & Geosciences*, vol. 62, pp. 110–117, 2014.
- [7] L. Wang, D. Sun, P. Li, and Y. Xie, "Semi-analytical solution for one-dimensional consolidation of fractional derivative viscoelastic saturated soils," *Computers & Geosciences*, vol. 83, pp. 30–39, 2017.
- [8] R. E. Gibson, "The Progress of Consolidation in a Clay Layer Increasing in Thickness with Time," *Géotechnique*, vol. 8, no. 4, pp. 171–182, 1958.
- [9] S. S. Razouki and T. Schanz, "One-dimensional consolidation under haversine repeated loading with rest period," *Acta Geotechnica*, vol. 6, no. 1, pp. 13–20, 2011.
- [10] S. S. Razouki, P. Bonnier, M. Datcheva, and T. Schanz, "Analytical solution for 1D consolidation under haversine cyclic loading," *International Journal for Numerical and Analytical Methods in Geomechanics*, vol. 37, no. 14, pp. 2367–2372, 2013.
- [11] M. S. Mahmoud and H. Deresiewicz, "Settlement of inhomogeneous consolidating soils—I: The single-drained layer under confined compression," *International Journal for Numerical and Analytical Methods in Geomechanics*, vol. 4, no. 1, pp. 57–72, 1980.
- [12] G. Zhu and J.-H. Yin, "Analysis and mathematical solutions for consolidation of a soil layer with depth-dependent parameters under confined compression," *International Journal of Geomechanics*, vol. 12, no. 4, pp. 451–461, 2012.
- [13] X. W. Tang, B. Niu, G. C. Cheng, and H. Shen, "Closed-form solution for consolidation of three-layer soil with a vertical drain system," *Geotextiles and Geomembranes*, vol. 36, pp. 81–91, 2013.
- [14] G.-X. Mei and Q.-M. Chen, "Solution of Terzaghi one-dimensional consolidation equation with general boundary conditions," *Journal of Central South University*, vol. 20, no. 8, pp. 2239–2244, 2013.
- [15] B. C. Hawlader, B. Muhunthan, and G. Imai, "State-dependent constitutive model and numerical solution of self-weight consolidation," *Géotechnique*, vol. 58, no. 2, pp. 133–141, 2008.
- [16] M. A. Rahalt and A. R. Vuez, "Analysis of settlement and pore pressure induced by cyclic loading of silo," *Journal of Geotechnical and Geoenvironmental Engineering*, vol. 124, no. 12, pp. 1208–1210, 1998.
- [17] E. H. Davis and G. P. Raymond, "A non-linear theory of consolidation," *Géotechnique*, vol. 15, no. 2, pp. 161–173, 1965.
- [18] E. Conte and A. Troncone, "Soil layer response to pore pressure variations at the boundary," *Géotechnique*, vol. 58, no. 1, pp. 37–44, 2008.
- [19] V. Pane and R. L. Schiffman, "A note on sedimentation and consolidation," *Géotechnique*, vol. 35, no. 1, pp. 69–72, 1985.
- [20] R. E. Gibson, "A heat conduction problem involving a specified moving boundary," *Quarterly of Applied Mathematics*, vol. 16, no. 4, pp. 426–430, 1959.
- [21] R. L. Schiffman, "Consolidation of soil under time-dependent loading and varying permeability," in *Proceedings of the Thirty-Seventh Annual Meeting of the Highway Research Board*, vol. 37, pp. 584–617, 1958.
- [22] K. S. He, Z. J. Shen, and X. X. Peng, "The comparison of large strain method using total and updated Lagrangian finite element formulation and small strain method," *Chinese Journal of Geotechnical Engineering*, vol. 22, no. 1, pp. 30–34, 2000.
- [23] G. Mesri and R. E. Olson, "Mechanisms controlling the permeability of clays," *Clays and Clay Minerals*, vol. 19, no. 3, pp. 151–158, 1971.
- [24] Y.-C. Zhuang, K.-H. Xie, and X.-B. Li, "Nonlinear analysis of consolidation with variable compressibility and permeability," *Journal of Zhejiang University (Engineering Science)*, vol. 6, no. 3, pp. 181–187, 2005.
- [25] E. Conte and A. Troncone, "Nonlinear consolidation of thin layers subjected to time-dependent loading," *Canadian Geotechnical Journal*, vol. 44, no. 6, pp. 717–725, 2007.